School of Molecular and Life Sciences

2D Colloidal Atomic-Thick Metal Chalcogenides: Synthesis, Growth Mechanisms and Applications

Yingping Pang

This thesis is presented for the Degree of
Doctor of Philosophy
of
Curtin University

July 2019

Declaration

To the best of my knowledge and belief this thesis contains no material previously published by any other person except where due acknowledgment has been made.

This thesis contains no material which has been accepted for the award of any other degree or diploma in any university.

Signature:

Date: 30/09/2019

Table of contents

Acknowledgements

The writing of the doctoral thesis has come to an end, and my academic life will continue to a new start as well. I will leave the campus and step into a new life journey. At the moment, there is a mixed feeling filling my heart. The last campus time of my life is a beautiful landscape on my long-life road. I will cherish this memory and commemorate it. I sincerely thank the teachers, family members and friends, on this road, who have accompanied me through all the trials and hardships. Your presence is also an important benchmark in this beautiful landscape. It is also written into my memory of life.

First of all, I would like to express my heartfelt thanks to my co-supervisor Dr. Guohua Jia. Two years ago, I was fortunate enough to get the opportunity to join Dr. Jia's research group. Dr. Jia's flashing idea, modesty and gentleness made me feel the true meaning of research and the warmth of home. The teacher's calm and inner peace attitude towards life, open and selfless temperament, rigorous and meticulous style of study, profound and extensive knowledge and vision have deeply influenced me. Dr. Jia has devoted a lot of efforts in the topic selection, writing, and revision of the thesis. The successful completion of the thesis is inseparable from Dr. Jia's wise tips and guidance. Here, I would like to express my sincere gratitude to Dr. Jia who has contributed unselfishly! Also, I really appreciate the patience and professional guidance of my instructor, Prof. Mark Buntine. My gratefulness and appreciation to Dr. Jia and Prof. Mark is beyond words.

Secondly, I would like to thank the group partners who have worked hard with me. We not only discussed each other concerning paper writing and experiment conducting, but also helped each other in life. Here, I am especially grateful to my friends Dechao Chen, Wei Chen, Fei Wang, Shaghraf and Jinyang Zhang. It is your company that makes my postgraduate career colourful and makes my life full of sunshine and hope. It is a fate that we get together in a big family. During this time, we learned together, made progress together, and encouraged together. I sincerely thank you and sincerely wish you all the best in your future work and life.

In addition, I would like to extend my gratefulness to Dr. Chao Su for your patiently emotional support in my bad times, intelligently valuable advices in my job seeking, and powerfully sensible ways in challenge overcoming as well.

Finally, I would like to thank my family members-my father and my mother. Your precious and selfless dedication is the premise and foundation for my successful completion of my studies. In the future life path, I will continue to work hard, constantly surpass, and use actual actions to repay you.

Time flies, youth is like a song. My time at Curtin University is ending. Looking back, all the sweat and tears, glory and failure have become so insignificant. Stepping out of the school and shouldering the mission, I will always follow five core values of Curtin University: "Integrity, Respect, Courage, Excellence, and Impact", and constantly strive to take every step, and strive for the high expectations of the alma mater! Live up to the splendour of youth.

Abstract

Impelled by the discovery and its fascinating properties of graphene, the pursuit of alternative materials of atomic thickness, identified as “2D materials”, is springing up. 2D materials are a kind of materials possessing lateral sizes ranging from one hundred nanometres to even a few micrometres while their thickness is only less than 5 nm. As an emerging class of materials, 2D materials can be obtained with a thickness of atomic precision, and the electrons are confined in the thickness direction due to the quantum confinement effect, which will generate some astonishing properties that is different from their bulk counterparts. These 2D materials have recently stimulated much interest among scientific communities and technological entities, owing to their intriguing properties and distinctive potential in the fields of energy storage, photothermal therapy, field-effect transistors and optoelectronic devices. Motivated by the compelling properties and innovative applications of such ultrathin 2D nanomaterials, it is highly desirable developing a strategy for fabrication of atomic-thick layers of 2D nanomaterials with well-defined morphology, which triggers numerous efforts among scientific communities.

In this thesis, we synthesized a family of colloidal 2D nanomaterials, with a special emphasis on heavy-metal-free and non-toxic materials including ZnSe, ZnS nanoplatelets and MoS_2, WS_2, ReS_2 nanosheets, for the study of their application in photodetectors and hydrogen evolution reaction (HER).

Chapter 1 gives a broad review on some reliable methods along with suitable characterization techniques of common 2D nanomaterials. In addition, the promising applications of these 2D nanomaterials in photoelectronic devices, catalysis, energy storage and conversion, as well as sensing are emphasized in detail.

Following the Chapter 1, Chapter 2 focuses on the main growth mechanisms related to the growth of 8 layers of 2D ZnSe, ZnS nanoplatelets, based on experimental results and the density functional theory (DFT) simulations. We investigate the surface energy and growth kinetics of wurtzite nanoplatelets to elucidate why nanoplatelets of wurtzite structure exhibit a uniform thickness of eight monolayers.

Chapter 3 presents in more details the fundamental optical properties of four kinds of nanoplatelets, including ZnSe, ZnS, $ZnSe_{0.50}S_{0.50}$, and $ZnSe_{0.25}S_{0.75}$. The synthesized ZnSe nanoplatelets exhibit an exceptional narrow emission spectrum with a full-width at half-maximum as sharp as 90 meV and a 1.9 ns radiative fluorescent lifetime at room temperature. ZnSe nanoplatelets-based ultraviolet (UV) photodetectors is fabricated using a simple solution process. The photo-induced current at 100 V is about 7 nA excited by the 365 nm UV light and about 1.5 nA by the 254 nm UV light, suggesting that the photodetector has a spectrum responsivity of about 3.5 mA W^{-1} at 365 nm and 0.6 mA W^{-1} at 254 nm, respectively. This study provides a solid basis for the further practical applications of ZnSe nanoplatelets in terms of lighting and displays, optoelectronics (photodetectors), as well as photocatalysis and photoelectrochemical catalysis.

Chapter 4 aims at providing structural engineering of a variety of 2D MoS_2, WS_2, ReS_2 nanosheets, and giving a comprehensive study of HER performance of MoS_2 at different calcination temperatures as well. The resulting monolayer MoS_2 nanosheets exhibited high electrochemical performance toward HER with superior catalytic activities as evidenced by small overpotentials of 179 mV in 1 M KOH at 10 mA cm^{-2}.

Chapter5, finally, gives the authors' view on the conclusions, recommendations, challenges and future opportunities in this promising research area.

List of Publications

1. **Yingping Pang**, Md Nasir Uddin, Wei Chen, Shaghraf Javaid, Emily Barker, Yunguo Li, Alexandra Suvorova, Martin Saunders, Zongyou Yin, Guohua Jia. Colloidal Single-Layer Photocatalysts for Methanol-Storable Solar H_2 Fuel. *Adv. Mater.* **2019**, *31*, 1905540.
2. **Yingping Pang**, Minyi Zhang, Dechao Chen, Wei Chen, Fei Wang, Shaghraf Javaid, Martin Saunders, Matthew R. Rowles, Lihong Liu, Shaomin Liu, Amit Sitt, Chunsen Li, Guohua Jia. Why Do Colloidal Wurtzite Semiconductor Nanoplatelets Have an Atomically Uniform Thickness of Eight Monolayers? *J. Phys. Chem. Lett.* **2019**, *10*, 3465–3471.
3. Guohua Jia, **Yingping Pang**, Jiajia Ning, Uri Banin, Botao Ji. Heavy-Metal-Free Colloidal Semiconductor Nanorods: Recent Advances and Future Perspectives. *Adv. Mater.* **2019**, *31*, 1900781.
4. Shaghraf Javaid, Xiaojie Li, Fei Wang, Wei Chen, **Yingping Pang**, Shaobin Wang, Guohua Jia, Franca Jones. Synthesis of Magnetically Separable Fe_3O_4–Au–CdS Kinked Heterotrimers Incorporating Plasmonic and Semiconducting Functionalities. *J. Mater. Chem. C* **2019**, *7*, 14517–14524.
5. Wei Chen, Amir Karton, Tanveer Hussian, Shaghraf Javaid, Fei Wang, **Yingping Pang**, Guohua Jia. Spontaneous Shape and Phase Control of Colloidal ZnSe Nanocrystal by Tailoring Se Precursor Reactivity. *CrystEngComm* **2019**, *21*, 2955–2961.
6. Shaghraf Javaid, Yunguo Li, Dechao Chen, Xiaomin Xu, **Yingping Pang**, Wei Chen, Fei Wang, Zongping Shao, Martin Saunders, Jean-Pierre Veder, Guohua Jia, Franca Jones. Spontaneous Formation of Heterodimer Au-Fe_7S_8 Nanoplatelets by a Seeded Growth Approach. *J. Phys. Chem. C* **2019**, *123*, 10604–10613.
7. Dechao Chen, Huayang Zhang, Yunguo Li, **Yingping Pang**, Zongyou Yin, Hongqi Sun, Lai-Chang Zhang, Shaobin Wang, Martin Saunders, Emily Barker, Guohua Jia. Spontaneous Formation of Noble- and Heavy-Metal-Free Alloyed Semiconductor Quantum Rods for Efficient Photocatalysis. *Adv. Mater.* **2018**, 1803351.

Patent

Guohua Jia, **Yingping Pang**, Fei Wang. Heavy-Metal-Free Metal Chalcogenide Nanoplatelets. International application No. PCT/AU2018/051304.

Conferences

1. 10th International Conference on Quantum Dots (QD 2018), Toronto, Canada. Selective Growth of Au onto ZnSe Nanorod Couples for Photocatalysis. **Poster**.
2. 4th International Conference on Two-Dimensional Materials and Technologies, Melbourne, Australia. Heavy-Metal-Free Quasi-2D Colloidal Semiconductor Nanoplatelets with Atomically Uniform Thickness. **Oral**.

Chapter 1: Two-Dimensional Nanocrystals: Synthesis, Characterization and Potential Applications

Abstract

Impelled by the discovery and its fascinating properties of graphene, the pursuit of alternative nanocrystals (NCs) of atomic thickness, identified as "2D NCs" is springing up. These ultrathin 2D NCs manifest many specific and fascinating physical, optical, chemical and electronic properties. In this Review, some reliable methods along with suitable characterization techniques are described. In addition, the promising applications of these 2D NCs in photoelectronic devices, catalysis, energy storage and conversion, as well as sensing are emphasized in detail.

Keywords: 2D NCs, synthesis, characterization, applications.

1.1 Introduction

The discovery of graphene combined with its fascinating properties,[1-5] has triggered the pursuit of a new family of two-dimensional (2D) nanocrystals (NCs) among numerous scientific communities. 2D NCs are a kind of materials possessing lateral sizes ranging from one hundred nanometres to even few micrometres while their thickness is only less than 5 nm.[6] To date, besides graphene, an enormous wide spectrum of atomically-thin 2D NCs, ranging from transition metal dichalcogenides (TMDs),[7-10] 2D carbides and nitrides (MXenes),[11] graphitic carbon nitride (g-C_3N_4),[12-14] layered metal oxides[15,16] to layered double hydroxides (LDHs)[16,17] emerge as new types of 2D NCs. These ultrathin 2D NCs, possessing ultrahigh surface area and ultrathin atomic thickness, manifest specific and fascinating physical, optical, chemical and electronic performance, which is superior to their bulk counterparts. Due to their strong quantum confinement of electrons and structural features, 2D NCs have exposed promising potential in electronic devices,[18-21] catalysis,[22-24] energy storage and conversion,[25,26] and sensing.[27,28]

In this Review, we firstly summarize the synthetic methods for 2D NCs, including insights on their advantages and limitations. Secondly, appropriate characterization techniques are briefly described. Moreover, the potential applications of these ultrathin 2D NCs, especially in electronics/optoelectronics, catalysis, batteries, supercapacitors, and sensing platforms are given in detail. Finally, conclusion remarks and outlooks are proposed.

1.2 Synthetic methods

Stimulated by the compelling thickness-dependent properties of ultrathin 2D NCs and the high demands for property modulations, many efforts have been contributed to the synthetic approaches for preparation of ultrathin 2D NCs. Till now, the existing reliable synthetic strategies for ultrathin 2D NCs are separated into two categories: top-down method and bottom-up method. The former method mainly includes micromechanical cleavage, mechanical force-assisted, ion exchange-assisted and ion intercalation-assisted liquid exfoliation.[29] In the process of exfoliation, the interlayer attraction of layered bulk parent crystals will be swelled and weakened into completely separated layers with the aid of mechanical sonication or chemical intercalation (Figure 1-1). In contrast, chemical vapour deposition (CVD) and wet-chemical syntheses belong to the bottom-up methods. In CVD and wet-chemical syntheses, chemical reaction occurred in specific experimental conditions, which, in principle, are more versatile for the formation of ultrathin 2D nanomaterials, especially for the non-layered NCs.

In this section, our discussion will narrow down to several preparation methods that are widely used or suitable to a wide range of material. Of note, the merits and limitations of the well-developed synthetic method are briefly discussed in the end with personal insights.

1.2.1 Top-down methods

1.2.1.1 Micromechanical cleavage

Impelled by the successful cleavage of graphene, micromechanical cleavage technique is evolving into a method of preparing a sheet-like material by peeling the layer structured bulk crystals using a Scotch tape. This method initially relies on the tape to weaken the interlayer van der Waals force of the bulk crystals. In general, the desired single- or few-layers of 2D NCs can be obtained by repeated exfoliation through this method (Figure 1-2).[30]

The micromechanical cleavage technique is applicable to produce 2D NCs with no defect and large lateral size. But surely the limitations of this method mainly lie in three aspects: the low production yield and the low production rate as well as lack of precise control over size and shape.

1.2.1.2 Mechanical Force-Assisted Liquid Exfoliation

In the mechanical force-assisted liquid exfoliation technique, bulk crystals are added in the liquid phase and then the appropriate mechanical force is applied. With the aid of mechanical force exfoliation, an ultrathin 2D NCs may also be obtained. On the basis of mechanical forces, mechanical force-assisted liquid exfoliation can be classified into sonication-assisted liquid exfoliation (SALE) (Figure 1-1) and shear force-assisted liquid exfoliation (SFALE). In SALE, prior to sonication, the layered bulk crystals are first added in a particular solvent for a period of time. After the sonic treatment, the strong ultrasonic induced produce "cavitation" phenomenon in liquid. The "cavitation" reaches into the interspace of layered bulk, the layered crystals are peeled into an ultrathin mono- or multilayer nanosheets followed by the bubble rupture. The peeling of the layered mass in the liquid can also be achieved by exerting a high shear rate in SFALE. As with the sonication-assisted liquid exfoliation, the selection of suitable solvents and polymers can reduce the loss of peeling energy and stabilize the peeled sheet in liquid, thus making the exfoliation process more efficient.

1.2.1.3 Ion Exchange-Assisted Liquid Exfoliation

The ion exchange idea arises from the use of larger radius ions to replace ions with relatively small radius in different layers with larger radii. After the ion exchange, the interlayer spacing of the lamellar crystals is greatly expanded, which weakens the connection between adjacent layers in the bulk crystals. Then the mechanical force is applied to obtain single- or few-layer NCs (Figure 1-1).

1.2.1.4 Ion Intercalation-Assisted Liquid Exfoliation

The ion intercalation-assisted liquid exfoliation is based on the idea of inserting cation ions with small ionic radius into the interspacing of layered bulk crystals. The interlayer spacing of ion-intercalated intermediate would be distinctly expanded and adjacent layers would be weakened under ion intercalation. Thus, the monolayer or multilayer NCs are easily obtained under a very short period of sonication time (Figure 1-1).

The aforementioned liquid exfoliation is promising method and applicable for the high-yield production of ultrathin 2D NCs. However, its disadvantages should never be overlooked. Note that for the method of liquid exfoliation in solvents, three aspects should be outlined: (1) The liquid exfoliation strategy is only suitable for

those parent bulk crystals which possess a layered structure; (2) Only when the solvent surface energy is matching to that of lamellar bulk materials, effective exfoliation can be achieved; (3) The exfoliated layers are not stable due to the absence of protection of ligands.

1.2.2 Bottom-up methods

Given that the limitations in liquid exfoliation, in contrast, wet chemical syntheses, belonging to the bottom-up approaches, in principle, are more versatile for the formation of ultrathin 2D nanomaterials, especially for the non-layered NCs. The bottom-up methods mainly include hydro/solvothermal synthesis, 2D-oriented attachment, and 2D-templated synthesis.

1.2.2.1 Hydro/solvothermal synthesis

Hydrothermal/solvothermal synthesis refers to the chemical reaction (with reaction medium of water/organic solvent) occurs in a sealed vessel with high temperature and pressure which is unachievable in an atmospheric condition. As a representative example, Xie and co-workers[31] employed this method for the preparation of few-layer defect-rich MoS_2 nanosheets with the assistance of excess thiourea.

1.2.2.2 2D-oriented attachment

In a 2D-oriented attachment mechanism, the 0D or 1D NCs are frequently employed as building blocks. In this mechanism, the building block NCs with closer proximity would tend to emerge or connect with each other and fuse together to form large-aspect-ratio 2D NCs. The whole attachment process is driven by sharing the common crystallographic facet between adjacent NCs in order to relieve and even eliminate the high energy facets and interfaces.[32-34] For instance, PbS nanosheets was successfully prepared used this method in Weller's group.[35]

1.2.2.3 2D-templated synthesis

2D-templated synthesis refers to the use of the pre-synthesized nanomaterials or bulk substrates as templates to confine/direct the growth of specific nanostructures.[36,37] In 2014, Dou and co-workers[38] used poly(ethylene oxide)-poly(propylene oxide)-poly(ethylene oxide) (P123) 2D assemblies in ethylene glycol as colloidal soft template to confine the material growth between two adjacent layers

(Figure 1-3). This 2D-templated synthesis offers a general manner for preparation of a wide range of metal oxide comprising TiO_2, ZnO, Co_3O_4, WO_3, Fe_3O_4, and MnO_2.

1.3 Characterization

Coincident with the speedy advancement of nanotechnology is the development of some effective means of characterization to reveal 2D NCs in terms of composition, size, thickness, crystallinity, etc. It is very important to understand the strong correlation between the structural features and functional characteristics of ultrathin 2D NCs, and to guide the rational synthesis of 2D NCs with targeted characteristics.

1.3.1 Optical microscopy

The visibility of ultrathin 2D NCs under an ordinary optical microscopy has greatly contributed to in-depth study of their properties and applications. This imaging is based on the interference of different surface reflected light. Optical microscope is based on the optical principle of reflected light at distinct surfaces to quickly determine the location, shape and thickness of 2D NCs.[39-41] The optical difference between the bare substrate and ultrathin 2D NCs is caused by the apparent perturbation of the light transmittance and the light path on the sample. Some ultrathin 2D NCs have been identified with monochromic light or silicon dioxide with continuously changed thicknesses.

1.3.2 Scanning probe microscopy

Scanning probe microscope (SPM) is, adopting electronic tunnelling effect, a cunning apparatus to detect the local surface properties of a single atomic layer, such as surface defects, surface remodelling, thickness and electronic band structures at high resolution.[42] According to a variety of different interactions between the probe and the sample, SPM can be divided into atomic force microscopy (AFM) frequently utilized for thickness measurement of 2D NCs and conductive atomic force microscopy (CAFM) for collecting topographic information on 2D NCs. The principle is briefly described below. The probe moves closer to the sample and a voltage is applied between the two. When the probe and the sample surface are separated by only a few tens of angstroms, the tunnelling effect creates a constant tunnelling current between the probe and the sample. The surface having a small ups and downs, even if only atomic distance, will also make the occurrence of thousands

of times changes in current. This information is then recorded into a computer and processed to display the sample topography image on the screen.

1.3.3 Scanning electron microscopy

In SEM, in principle, the inelastic scattering interaction between electrons and sample surface will generate secondary electrons employed to identify detail surface topology,[43] size, and shape. Even so, full structural information will be obtained combined SEM and other TEM, EDS, and AFM characterization techniques.

1.3.4 Transmission electron microscopy

TEM uses the accelerated/focused electron beam projected onto a very thin sample to characterize the size, crystallinity, phase, exposed facets, and growth direction of a thin material.[44] The collision between electrons and atoms in the sample results in three-dimensional angular scattering. Thus, images with different contrast can be formed to roughly estimate the thickness of the sample. The image after zoomed in and focused will be displayed on the imaging device (such as the phosphor screen, film, and photographic coupling components).

1.3.5 Raman spectroscopy

The optical properties of 2D NCs can be detected by Raman spectroscopy which delivers structural and electronic evidence with high spectral and spatial resolution.[45] The peak position, intensity and linewidth, may change significantly with increasing layers of 2D NCs. Using this spectral characteristic information, we can identify the accurate number of layers.

1.4 Applications

1.4.1 Electronic/optoelectronic devices

Ultrathin 2D NCs with single- or multi-layer thickness have become the focus of nanoelectronics because of their intriguing mechanical and electrical properties.[46-51] These 2D NCs with unique properties in terms of short-channel effects resistance and free of dangling bond make them suitable for electronic/optoelectronic devices. Many 2D NCs, such as TMDs, black phosphorus, g-C_3N_4 and van der Waals heterojunction have found their applications in the field of electronic/optoelectronic devices.[52-54]

1.4.2 Electrocatalysis

2D NCs have attractive characteristics such as highly exposed edge active sites, large specific surface areas, and easily accessible by other guest materials, making them well suited for energy storage and conversion applications. Correspondingly, these 2D NCs are also widely used as electrocatalytic catalysts in some important electrochemical catalytic systems including hydrogen evolution reaction (HER),[55] oxygen evolution reaction (OER),[56,57] oxygen reduction reaction (ORR),[58] as well as other important electrocatalytic areas.

1.4.3 Batteries

Energy and environmental issues have been the concern of human beings. To meet the growing energy needs while avoiding the depletion of resources and environment damage, rechargeable batteries came into being. 2D NCs possessing good stability, high chemical activity interface, shorter ion transport distance and excellent electron transport kinetics, are finding emerging potential in the field of lithium-ion battery (LIBs), sodium-ion battery (SIBs) lithium-sulfur battery and Li-O_2 battery (Figure1-4).

1.4.4 Sensing

In practical applications, it is urgent to promote the progress of simple and reliable sensing system for rapid detection of specific chemical or biological substances, such as gas molecules, toxic ions, chemical molecules, biological molecules, with high sensitivity, selectivity and stability. As sensing platforms, 2D NCs have been widely used in the construction of different sensing systems. Because of their excellent conductivity, high specific surface area, high sensitivity to external stimulants, excellent fluorescence quenching ability, and so on, 2D NCs have been widely used in the construction of different sensing systems. The current application of the sensor platform includes electrical sensors,[60] fluorescence sensors,[61] and electrochemical sensors.[62]

1.5 Concluding remarks and outlook

In this Review, the synthesis methods of ultrathin 2D NCs with specific functions are summarized. Then the characterization techniques of ultrathin 2D NCs along with their advantages and disadvantages are described. At the same time,

potential applications of ultrathin 2D NCs such as electronic/optoelectronic devices, electrocatalysis, batteries, and sensing platforms are also discussed.

In the past few decades, although the research of ultrathin 2D NCs has been developed by leaps and bounds, both from the basic research ground or technical field, there is still a gap between the yield, quality as well as quantity of 2D NCs and practical industry application. Moreover, the stability of 2D NCs has yet to be further improved. In addition, from the aspect of characterization, in-situ measurements, such as in-situ XRD, TEM and XPS, should be developed to understand the growth mechanism of ultrathin 2D NCs thoroughly.

1.6 Figures

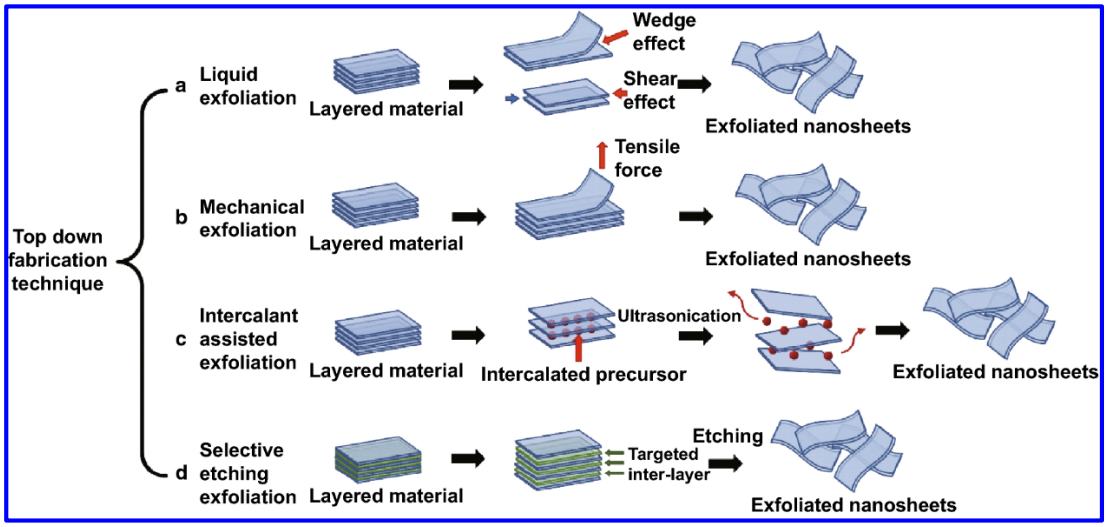

Figure 1-1. Schematic illustration of the main liquid exfoliation mechanisms.[29]
(Reproduced with permission. Copyright (2018) Springer Nature)

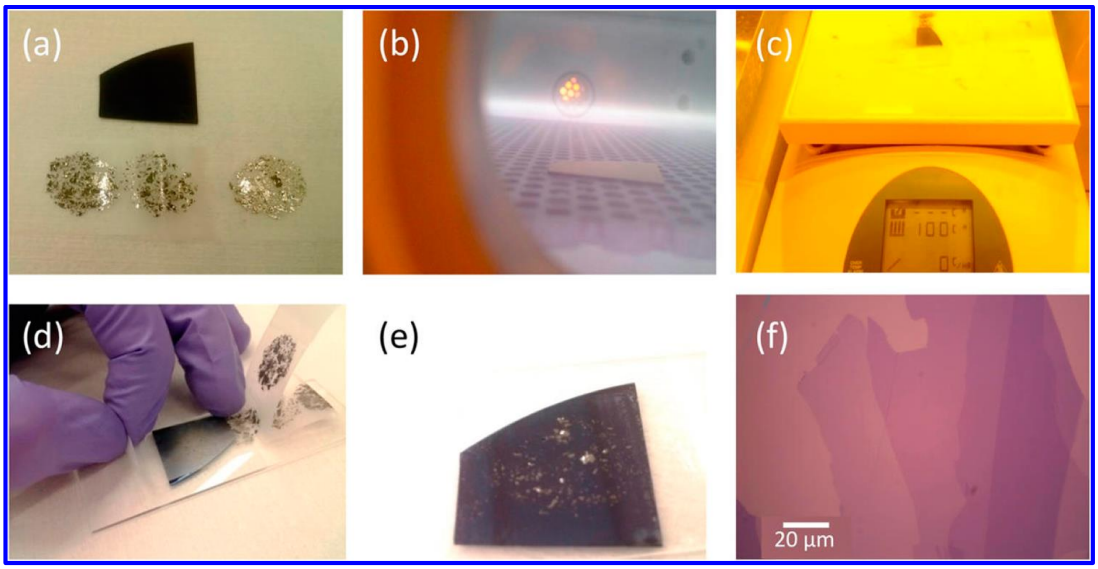

Figure 1-2. Schematic illustration of the typical process by the modified micromechanical cleavage method for exfoliation of graphene from graphite via Scotch tape.[30] (Reproduced with permission. Copyright (2015) American Chemical Society)

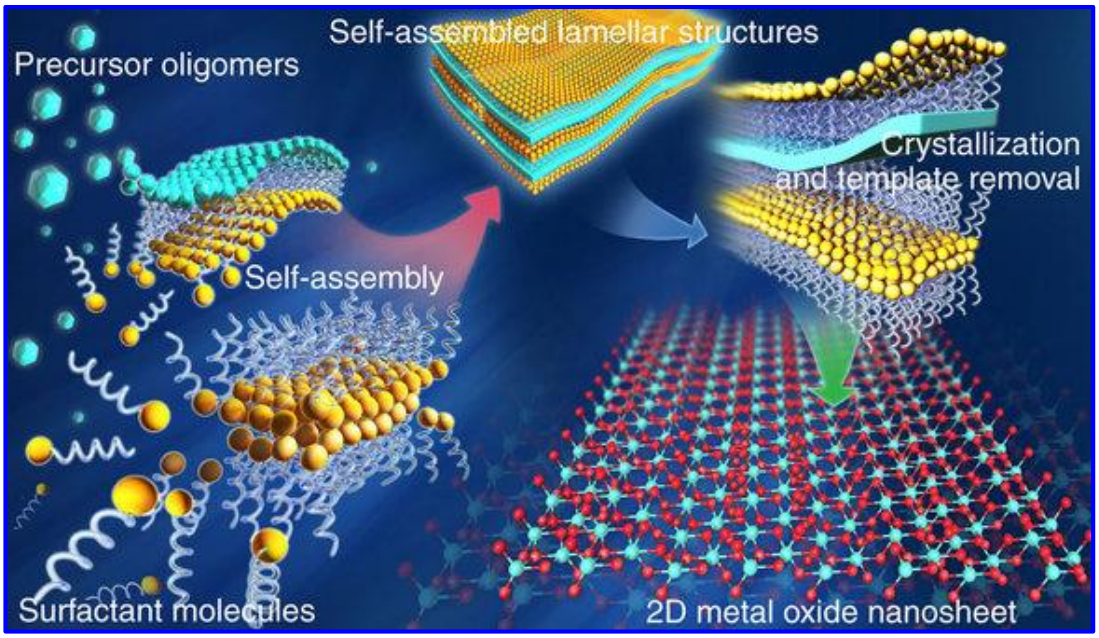

Figure 1-3. Schematic diagram of templated synthesis of 2D metal oxide nanosheets.[38] (Reproduced with permission. 2014, NATURE PUBLISHING GROUP)

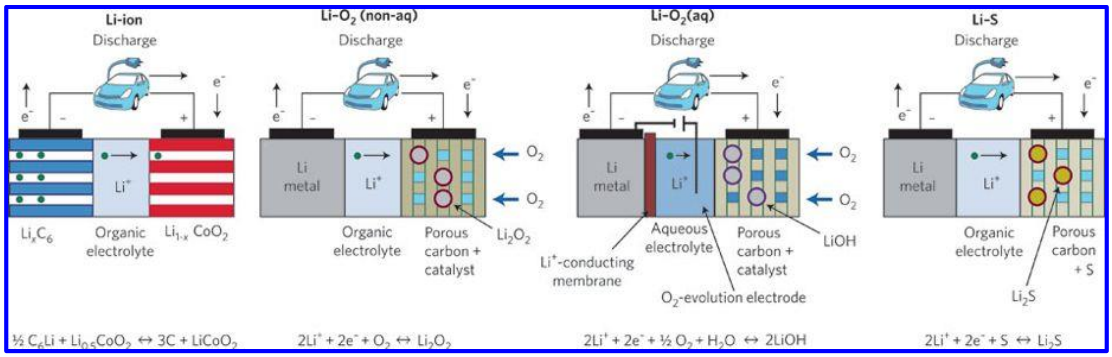

Figure 1-4. Schematic representations of Li-ion, Na-ion, Li–O_2, and Li–S batteries.[59] (Reproduced with permission. 2011, NATURE PUBLISHING GROUP)

1.7 References

(1) Novoselov, K. S.; Geim, A. K.; Morozov, S. V.; Jiang, D.; Zhang, Y.; Dubonos, S. V.; Grigorieva, I. V.; Firsov, A. A. Electric Field Effect in Atomically Thin Carbon Films. *Science* **2004**, *306*, 666−669.

(2) Zhang, Y.; Tan, Y.-W.; Stormer, H. L.; Kim, P. Experimental Observation of the Quantum Hall Effect and Berry's Phase in Graphene. *Nature* **2005**, *438*, 201−204.

(3) Geim, A. K.; Novoselov, K. S. The Rising of Graphene. *Nat. Mater.* **2007**, *6*, 183−191.

(4) Nair, R. R.; Blake, P.; Grigorenko, A. N.; Novoselov, K. S.; Booth, T. J.; Stauber, T.; Peres, N. M. R.; Geim, A. K. Fine Structure Constant Defines Visual Transparency of Graphene. *Science* **2008**, *320*, 1308−1308.

(5) Zhu, Y.; Murali, S.; Stoller, M. D.; Ganesh, K. J.; Cai, W.; Ferreira, P. J.; Pirkle, A.; Wallace, R. M.; Cychosz, K. A.; Thommes, M.; Su, D.; Stach, E. A.; Ruoff, R. S. Carbon-based Supercapacitors Produced by Activation of Graphene. *Science* **2011**, *332*, 1537−1541.

(6) Zhang, H. Ultrathin Two-Dimensional Nanomaterials. *ACS Nano* **2015**, *9*, 9451−9469.

(7) Tan, C. L.; Zhang, H. Two-Dimensional Transition Metal Dichalcogenide Nanosheet-Based Composites. *Chem. Soc. Rev.* **2015**, *44*, 2713−2731.

(8) Chhowalla, M.; Shin, H. S.; Eda, G.; Li, L. J.; Loh, K.; Zhang, H. The Chemistry of Two-Dimensional Transition Metal Dichalcogenide Nanosheets. *Nat. Chem.* **2013**, *5*, 263−275.

(9) Huang, X.; Zeng, Z. Y.; Zhang, H. Metal Dichalcogenide Nanosheets: Preparation, Properties and Applications. *Chem. Soc. Rev.* **2013**, *42*, 1934−1946.

(10) Lv, R.; Robinson, J. A.; Schaak, R. E.; Sun, D.; Sun, Y.; Mallouk, T. E.; Terrones, M. Transition Metal Dichalcogenides and Beyond: Synthesis, Properties, and Applications of Single- and Few-Layer Nanosheets. *Acc. Chem. Res.* **2015**, *48*, 56−64.

(11) Wang, X.; Kajiyama, S.; Iinuma, H.; Hosono, E.; Oro, S.; Moriguchi, I.; Okubo, M.; Yamada, A. Pseudocapacitance of MXene Nanosheets for High-Power Sodium-Ion Hybrid Capacitors. *Nat. Commun.* **2015**, *6*, 6544.

(12) Zhang, J.; Chen, Y.; Wang, X. Two-Dimensional Covalent Carbon Nitride Nanosheets: Synthesis, Functionalization, and Applications. *Energy Environ. Sci.* **2015**, *8*, 3092−3108.

(13) Ong, W.-J.; Tan, L.-L.; Ng, Y. H.; Yong, S.-T.; Chai, S.-P. Graphitic Carbon Nitride ($g\text{-}C_3N_4$)-Based Photocatalysts for Artificial Photosynthesis and Environmental Remediation: Are We a Step Closer to Achieving Sustainability? *Chem. Rev.* **2016**, *116*, 7159−7329.

(14) Zhi, C.; Bando, Y.; Tang, C.; Kuwahara, H.; Golberg, D. Large-Scale Fabrication of Boron Nitride Nanosheets and Their Utilization in Polymeric Composites with Improved Thermal and Mechanical Properties. *Adv. Mater.* **2009**, *21*, 2889−2893.

(15) Osadaab, M.; Sasaki, T. Exfoliated Oxide Nanosheets: New Solution to Nanoelectronics. *J. Mater. Chem.* **2009**, *19*, 2503−2511.

(16) Ma, R.; Sasaki, T. Two-Dimensional Oxide and Hydroxide Nanosheets: Controllable High-Quality Exfoliation, Molecular Assembly, and Exploration of Functionality. *Acc. Chem. Res.* **2015**, *48*, 136−143.

(17) Wang, Q.; O'Hare, D. Recent Advances in the Synthesis and Application of Layered Double Hydroxide (LDH) Nanosheets. *Chem. Rev.* **2012**, *112*, 4124−4155.

(18) Novoselov, K. S.; Geim, A. K.; Morozov, S. V.; Jiang, D.; Zhang, Y.; Dubonos, S. V.; Grigorieva, I. V.; Firsov, A. A. Electric Field Effect in Atomically Thin Carbon Films. *Science* **2004**, *306*, 666−669.

(19) Radisavljevic, B.; Radenovic, A.; Brivio, J.; Giacometti1, V.; Kis, A. Single-Layer MoS_2 Transistors. *Nat. Nanotechnol.* **2011**, *6*, 147−150.

(20) Yin, Z. Y.; Li, H.; Li, H.; Jiang, L.; Shi, Y. M.; Sun, Y. H.; Lu, G.; Zhang, Q.; Chen, X. D.; Zhang, H. Single-Layer MoS_2Phototransistors. *ACS Nano* **2012**, *6*, 74−80.

(21) Liang, L.; Li, K.; Xiao, C.; Fan, S.; Liu, J.; Zhang, W.; Xu, W.; Tong, W.; Liao, J.; Zhou, Y.; et al. Vacancy Associates-rich Ultrathin Nanosheets for High Performance and Flexible Nonvolatile Memory Device. *J. Am. Chem. Soc.* **2015**, *137*, 3102−3108.

(22) Song, F.; Hu, X. Exfoliation of Layered Double Hydroxides for Enhanced Oxygen Evolution Catalysis. *Nat. Commun.* **2014**, *5*, 4477.

(23) Voiry, D.; Yamaguchi, H.; Li, J.; Silva, R.; Alves, D. C. B.; Fujita, T.; Chen, M.; Asefa, T.; Shenoy, V. B.; Eda, G.; et al. Enhanced Catalytic Activity in Strained Chemically Exfoliated WS_2 Nanosheets for Hydrogen Evolution. *Nat. Mater.* **2014**, *12*, 850−855.

(24) Yang, S.; Gong, Y.; Zhang, J.; Zhan, L.; Ma, L.; Fang, Z.; Vajtai, R.; Wang, X.; Ajayan, P. M. Exfoliated Graphitic Carbon Nitride Nanosheets as Efficient Catalysts for Hydrogen Evolution Under Visible Light. *Adv. Mater.* **2013**, *25*, 2452−2456.

(25) Du, G.; Guo, Z.; Wang, S.; Zeng, R.; Chen, Z.; Liu, H. Superior Stability and High Capacity of Restacked Molybdenum Disulfide as Anode Material for Lithium Ion Batteries. *Chem. Commun.* **2010**, *46*, 1106−1108.

(26) Tsai, M. L.; Su, S. H.; Chang, J. K.; Tsai, D. S.; Chen, C. H.; Wu, C. I.; Li, L. J.; Chen, L. J.; He, J. H. Monolayer MoS_2 Heterojunction Solar Cells. *ACS Nano* **2014**, *8*, 8317−8322.

(27) Zhu, C.; Zeng, Z.; Li, H.; Li, F.; Fan, C.; Zhang, H. Single-Layer MoS_2-Based Nanoprobes for Homogeneous Detection of Biomolecules. *J. Am. Chem. Soc.* **2013**, *135*, 5998−6001.

(28) Perkins, F. K.; Friedman, A. L.; Cobas, E.; Campbell, P. M.; Jernigan, G. G.; Jonker, B. T. Chemical Vapor Sensing with Monolayer MoS_2. *Nano Lett.* **2013**, *13*, 668−673.

(29) Mukherjee, S.; Ren, Z.; Singh, G. Beyond Graphene Anode Materials for Emerging Metal Ion Batteries and Supercapacitors. *Nano-Micro Lett.* **2018**, *2150−5551*, 10:70.

(30) Huang, Y.; Sutter, E.; Shi, N. N.; Zheng, J.; Yang, T.; Englund, D.; Gao, H.-J.; Sutter, P. Reliable Exfoliation of Large-Area High-Quality Flakes of Graphene and Other Two-Dimensional Materials. *ACS Nano* **2015**, *9*, 10612−10620.

(31) Xie, J.; Zhang, H.; Li, S.; Wang, R.; Sun, X.; Zhou, M.; Zhou, J.; Lou, X. W.; Xie, Y. Defect-Rich MoS_2 Ultrathin Nanosheets with Additional Active Edge Sites for Enhanced Electrocatalytic Hydrogen Evolution. *Adv. Mater.* **2013**, *25*, 5807−5813.

(32) Wang, Z. W.; Schliehe, C.; Wang, T.; Nagaoka, Y.; Cao, Y. C.; Bassett, W. A.; Wu, H. M.; Fan, H. Y.; Weller, H. Deviatoric Stress Driven Formation of Large Single-Crystal PbS Nanosheet from Nanoparticles and in Situ Monitoring of Oriented Attachment. *J. Am. Chem. Soc.* **2011**, *133*, 14484−14487.

(33) Zhang, X. D.; Zhang, J. J.; Zhao, J. Y.; Pan, B. C.; Kong, M. G.; Chen, J.; Xie, Y. Half-Metallic Ferromagnetism in Synthetic Co_9Se_8 Nanosheets with Atomic Thickness. *J. Am. Chem. Soc.* **2012**, *134*, 11908−11911.

(34) Evers, W. H.; Goris, B.; Bals, S.; Casavola, M.; de Graaf, J.; van Roij, R.; Dijkstra, M.; Vanmaekelbergh, D. Low-Dimensional Semiconductor Superlattices Formed by Geometric Control over Nanocrystal Attachment. *Nano Lett.* **2013**, *13*, 2317−2323.

(35) Schliehe, C.; Juarez, B. H.; Pelletier, M.; Jander, S.; Greshnykh, D.; Nagel, M.; Meyer, A.; Foerster, S.; Kornowski, A.; Klinke, C.; Weller, H. Ultrathin PbS Sheets by Two-Dimensional Oriented Attachment. *Science* **2010**, *329*, 550−553.

(36) Fan, Z. X.; Zhang, H. Template Synthesis of Noble Metal Nanocrystals with Unusual Crystal Structures and Their Catalytic Applications. *Acc. Chem. Res.* **2016**, *49*, 2841−2850.

(37) Liu, Y. D.; Goebl, J.; Yin, Y. D. Templated Synthesis of Nanostructured Materials. *Chem. Soc. Rev.* **2013**, *42*, 2610−2653.

(38) Sun, Z.; Liao, T.; Dou, Y.; Hwang, S. M.; Park, M.-S.; Jiang, L.; Kim, J. H.; Dou, S. X. Generalized Self-assembly of Scalable Two-Dimensional Transition Metal Oxide Nanosheets. *Nat. Commun.* **2014**, *5*, 3813.

(39) Jung, I.; Pelton, M.; Piner, R.; Dikin, D. A.; Stankovich, S.; Watcharotone, S.; Hausner, M.; Ruoff, R. S. Simple Approach for High-Contrast Optical Imaging and Characterization of Graphene-Based Sheets. *Nano Lett.* **2007**, *7*, 3569−3575.

(40) Li, H.; Lu, G.; Yin, Z.; He, Q.; Li, H.; Zhang, Q.; Zhang, H. Optical Identification of Single- and Few-Layer MoS_2 Sheets. *Small* **2012**, *8*, 682−686.

(41) Li, H.; Wu, J.; Huang, X.; Lu, G.; Yang, J.; Lu, X.; Xiong, Q.; Zhang, H. Rapid and Reliable Thickness Identification of Two-Dimensional Nanosheets Using Optical Microscopy. *ACS Nano* **2013**, *7*, 10344−10353.

(42) Bottomley, L. A. Scanning Probe Microscopy. *Anal. Chem.***1998**, *70*, 425−476.

(43) Oatley, C. W.; Nixon, W. C.; Pease, R. F. W. Scanning Electron Microscopy. *Adv. Electron. Electron Phys.* **1966**, *21*, 181−247.

(44) Wang, Z. L. Transmission Electron Microscopy of Shape-Controlled Nanocrystals and Their Assemblies. *J. Phys. Chem. B* **2000**, *104*, 1153−1175.

(45) Zhang, X.; Qiao, X.-F.; Shi, W.; Wu, J.-B.; Jiang, D.-S.; Tan, P.-H. Phonon and Raman Scattering of Two-Dimensional Transition Metal Dichalcogenides from Monolayer, Multilayer to Bulk Material. *Chem. Soc. Rev.* **2015**, *44*, 2757−2785.

(46) Fiori, G.; Bonaccorso, F.; Iannaccone, G.; Palacios, T.; Neumaier, D.; Seabaugh, A.; Banerjee, S. K.; Colombo, L. Electronics Based on Two-Dimensional Materials. *Nat. Nanotechnol.* **2014**, *7*, 768−779.

(47) Chhowalla, M.; Jena, D.; Zhang, H. 2D Semiconductors for Transistors. *Nat. Rev. Mater.* **2016**, *1*, 16052.

(48) Wang, Q. H.; Kalantar-Zadeh, K.; Kis, A.; Coleman, J. N.; Strano, M. S. Electronics and Optoelectronics of Two-Dimensional Transition Metal Dichalcogenides. *Nat. Nanotechnol.* **2012**, *11*, 699−712.

(49) Lee, S.; Zhong, Z. Nanoelectronic Circuits Based on Two-Dimensional Atomic Layer Crystals. *Nanoscale* **2014**, *6*, 13283−13300.

(50) Schwierz, F.; Pezoldt, J.; Granzner, R. Two-Dimensional Materials and Their Prospects in Transistor Electronics. *Nanoscale* **2015**, *7*, 8261−8283.

(51) Lembke, D.; Bertolazzi, S.; Kis, A. Single-Layer MoS_2 Electronics. *Acc. Chem. Res.* **2015**, *48*, 100−110.

(52) Novoselov, K. S.; Jiang, D.; Schedin, F.; Booth, T. J.; Khotkevich, V. V.; Morozov, S. V.; Geim, A. K. Two-Dimensional Atomic Crystals. Proc. *Natl. Acad. Sci. U. S. A.* **2005**, *102*, 10451−10453.

(53) Salvatore, G. A.; Münzenrieder, N.; Barraud, C.; Petti, L.; Zysset, C.; Büthe, L.; Ensslin, K.; Tröster, G. Fabrication and Transfer of Flexible Few-Layers MoS_2 Thin Film Transistors to Any Arbitrary Substrate. *ACS Nano* **2013**, *7*, 8809−8815.

(54) Cheng, R.; Jiang, S.; Chen, Y.; Liu, Y.; Weiss, N.; Cheng, H.-C.; Wu, H.; Huang, Y.; Duan, X. Few-Layer Molybdenum Disulfide Transistors and Circuits for High-Speed Flexible Electronics. *Nat. Commun.* **2014**, *5*, 5143.

(55) Jaramillo, T. F.; Jørgensen, K. P.; Bonde, J.; Nielsen, J. H.; Horch, S.; Chorkendorff, I. Identification of Active Edge Sites for Electrochemical H_2 Evolution from MoS_2 Nanocatalysts. *Science* **2007**, *317*, 100−102.

(56) Trotochaud, L.; Ranney, J. K.; Williams, K. N.; Boettcher, S. W. Solution-Cast Metal Oxide Thin Film Electrocatalysts for Oxygen Evolution. *J. Am. Chem. Soc.* **2012**, *134*, 17253−17261.

(57) Chen, S.; Duan, J.; Jaroniec, M.; Qiao, S. Z. Three-Dimensional N-Doped Graphene Hydrogel/NiCo Double Hydroxide Electrocatalysts for Highly Efficient Oxygen Evolution. *Angew. Chem. Int. Ed.* **2013**, *52*, 13567−13570.

(58) Guo, D.; Shibuya, R.; Akiba, C.; Saji, S.; Kondo, T.; Nakamura, J. Active Sites of Nitrogen-Doped Carbon Materials for Oxygen Reduction Reaction Clarified Using Model Catalysts. *Science* **2016**, *351*, 361−365.

(59) Bruce, P. G.; Freunberger, S. A.; Hardwick, L. J.; Tarascon, J.-M. Li-O_2 and Li-S Batteries with High Energy Storage. *Nat. Mater.* **2012**, *11*, 19−29.

(60) Li, H.; Yin, Z. Y.; He, Q. Y.; Li, H.; Huang, X.; Lu, G.; Fam, D. W. H.; Tok, A. I. Y.; Zhang, Q.; Zhang, H. Fabrication of Single- and Multilayer MoS_2 Film-Based Field Effect Transistors for Sensing NO at Room Temperature. *Small* **2012**, *8*, 63−67.

(61) He, S.; Song, B.; Li, D.; Zhu, C.; Qi, W.; Wen, Y.; Wang, L.; Song, S.; Fang, H.; Fan, C. A Graphene Nanoprobe for Rapid, Sensitive, and Multicolor Fluorescent DNA Analysis. *Adv. Funct. Mater.* **2010**, *20*, 453−459.

(62) Bakker, E.; Telting-Diaz, M. Electrochemical Sensors. *Anal. Chem.* **2002**, *74*, 2781−2800.

Chapter 2: Why Do Colloidal Wurtzite Semiconductor Nanoplatelets Have an Atomically Uniform Thickness of Eight Monolayers? §

Abstract

Herein we employed a first-principles method based on density functional theory to investigate the surface energy and growth kinetics of wurtzite nanoplatelets to elucidate why nanoplatelets exhibit a uniform thickness of eight monolayers. We synthesized a series of wurtzite nanoplatelets (ZnSe, ZnS, ZnTe, and CdSe) with an atomically uniform thickness of eight monolayers. As a representative example, the growth mechanism of 1.39 nm thick (eight monolayers) wurtzite ZnSe nanoplatelets was studied to substantiate the proposed growth kinetics. The results show that the growth of the seventh- and eighth-layer along the $[11\bar{2}0]$ direction of ZnSe magic-size nanoclusters (0.99 nm, six monolayers) is accessible, whereas the growth of the ninth layer is unlikely to occur because the formation energy is large. This work not only gives insights into the synthesis of atomically uniform thick wurtzite semiconductor nanoplatelets but also opens up new avenues to their applications in light-emitting diodes, catalysis, detectors, and lasers.

Keywords: wurtzite semiconductor nanoplatelets, atomically uniform thickness, density functional theory, ZnSe.

2.1 Introduction

Being analogous to graphene and transition-metal dichalcogenides, atomically thin semiconductor nanocrystals are emerging as a class of intriguing materials with broad utility[1−8] because of the remarkable electronic properties of quantum wells such as giant oscillator strength,[3] exceptionally narrow fluorescence,[2,3] low lasing threshold,[9−11] and ultrafast exciton dynamics.[3,12−17] Nanoplatelets with excitons strongly confined along the thickness direction exhibit the electronic structure of quantum wells, and their optical and electronic properties are thickness-dependent. In this sense, thickness control of nanoplatelets is of significant importance as it not only can tune the geometry of the nanoparticles but also can provide a versatile approach to manipulate the optical and electronic properties with relevance to applications in optoelectronics, sensors, and lasers.

Thickness control with atomic precision has been successfully achieved in zinc blende semiconductor nanoplatelets, especially in CdSe nanoplatelets.[3,13] For example, Ithurria et al. prepared zinc blende CdSe, CdS, and CdTe nanoplatelets with well-defined thickness ranging from 4 to 11 monolayers by optimizing the synthetic conditions.[3] However, thickness control of wurtzite semiconductor nanoplatelets seems inaccessible. There are several reports on wurtzite CdSe,[2,18] ZnSe,[19] and CdTe[20] nanoplatelets, in which only eight-layer thick (∼1.4−1.6 nm) wurtzite nanoplatelets have been obtained. These studies indicate there is no such strategy to precisely tune the thickness of wurtzite semiconductor nanoplatelets, and the reason why these particles prefer to crystallize into eight-layer thick wurtzite nanoplatelets is still unknown.

Herein, besides ZnSe and CdSe, we expanded the palette of the family of wurtzite semiconductor nanoplatelets by synthesizing wurtzite ZnS and ZnTe nanoplatelets using wet-chemical synthetic approaches (see 2.2 for details).

2.2 Experimental section

2.2.1 Material synthesis

Synthesis of ZnSe nanopatelet: Monodispersed ZnSe nanoplatelets were synthesized using a one-pot synthetic method using a literature method with some modifications.[19] In a typical synthesis, 0.6 mmol of $Zn(NO_3)_2$ $6H_2O$ and 1.8 mmol of selenium powder were mixed with 10 mL of octylamine and 20 mL of oleylamine in

a 50 mL three-neck flask. The mixture was heated to 110 ℃ and kept at this temperature for 30 min. The temperature was then increased to 150-170 ℃ and kept at this temperature for a desired reaction time. The reaction was quenched by removal of the heating mantle. After cooling to room temperature, 30 mL crude reaction mixture was diluted with 20 mL of chloroform. 2 mL of TOP was added in order to extract the unreacted selenium. Methanol was added to precipitate the nanoparticles with the aid of centrifugation.

Synthesis of ZnS nanoplatelet: Monodispersed ZnS nanoplatelets were synthesized using a one-pot synthetic method. In a typical synthesis, $Zn(NO_3)_2$ $6H_2O$ (0.3 mmol, 89 mg) and sulfur (0.9 mmol, 28.9 mg) were mixed with 5 mL of octylamine and 10 mL of oleylamine in a 50 mL three-neck flask. The mixture was heated to 110 ℃ and kept at this temperature for 30 min. The temperature was then held at 170 ℃ for 6 h, before removal of the heating mantel and cooled down to room temperature. The product solution was diluted in chloroform, and the nanoplatelets were precipitated by adding methanol with the aid of centrifugation.

Synthesis of ZnTe nanoplatelet: Monodispersed ZnTe nanoplatelets were synthesized using a one-pot hot-injection method. In a typical synthesis, $Zn(NO_3)_2$ $6H_2O$ (0.3 mmol, 89 mg) was mixed with 3.224 g of dodecylamine and 16 mL of oleylamine in a 50 mL three-neck flask. When the mixture was heated to 60 ℃, 2 mL of tributylphosphine-Te (TBP-Te, 0.5 M) was injected, and then the reaction temperature was increased to 120 ^{o}C. After at 120 ^{o}C for 2 hrs, the temperature was then held at 200 ℃ for 30 min, before removal of the heating mantel and cooled down to room temperature. The product solution was diluted in chloroform, and the nanoplatelets were precipitated by adding methanol with the aid of centrifugation.

Synthesis of CdSe nanoplatelet: Monodispersed CdSe nanoplatelets were synthesized using a one-pot synthetic method using a literature method.[2]

2.2.2 Materials characterization

Ultraviolet-visible (UV-vis) absorption spectroscopy: UV-vis absorption spectroscopy was performed on a Perkin Elmer Lambda 35 UV/VIS Spectrometer using quartz cuvettes.

Powder X-ray diffraction (XRD) patterns: XRD patterns were obtained using Cu Kα (λ=1.5406 Å) photons from an X'per PRO (PANalytical) X-ray diffractometer

operated at 40 kV and 40 mA. The crude solutions of nanoplatelet samples were diluted in chloroform and precipitated by methanol with the aid of centrifugation. After repeating this procedure for three times, the powders were further diluted by a small amount of toluene and deposited as a thin layer on a low-background scattering silicon substrate.

Electron microscopy measurement: Transmission electron microscopy (TEM) was performed using a JEOL 2100 transmission electron microscope. High-resolution TEM (HRTEM), high angle annular dark field scanning transmission electron microscopy (HAADF-STEM) were performed on a FEI Titan G2 80-200 high-resolution transmission electron microscope. Samples for electron microscopy measurement were prepared by placing a drop of nanoparticle solution in chloroform on top of a copper grid coated with an amorphous carbon film.

2D small-angle X-ray scattering (SAXS): SAXS data were collected using a Bruker MetalJet Nanostar SAXS instrument over a scattering range of 0.008-0.348 $Å^{-1}$. The beam had a wavelength of 1.34 Å, and a 300-um diameter. Data were collected with a fixed sample for 10 minutes, with the background for 2 minutes. The radially averaged and background-corrected data were modelled using Irena[21] with a unified fit model[22] for the small-angle scattering and Lorentzian diffraction peaks.

2.3 Results and discussion

Figure 2-1 compares the transmission electron microscopy (TEM) image, high-angle annular dark field-scanning transmission electron microscopy (HAADF-STEM) image, and absorption spectra of four wurtzite nanoplatelets. All samples exhibt uniform size distributions with a rectangle shape (Figure 2-1a-h), although corner truncation is observed in CdSe nanoplatelets (Figure 2-1g,h). The regular rectangular shape of ZnS and ZnS nanoplatelets is different from CdSe nanoplatelets with an unusual rectangular shape synthesized in the presence of Br^- species.[18] This is because Br^- can regulate the growth rate of CdSe nanoplatelets by modulating the relative surface energies of the facets of CdSe nanoplatelets as these facets may have different binding affinities to Br^-, whereas, in our case, the addition of Br^- species is unlikely to affect the growth and final morphology of ZnSe nanoparticles (Figure A1-1)[23] since the morphology and adsorption position in UV-vis spectrum of intermediates is unchanged with or without Br^- addition (Figures 2-3B and A1-1a). Interestingly, TEM measurements on nanoplatelets standing on their edges reveal a

uniform thickness of ~1.4−1.6 nm for four kinds of nanoplatelets (insets in Figure 2-1a,c,e,g). The uniform thickness of ZnSe and ZnS was further confirmed by atomic force microscopy (AFM) measurement (Figure 2-2a,b, Figure A1-2). Sizing histograms of the thickness on both ZnS (Figure A1-2c) and ZnSe (Figure A1-2d) show that those nanoplatelets have an average thickness around 1.4 nm, which provide further evidence on the 8-monolayer uniform thickness of wurtzite nanoplatelets.

The contrast of ZnSe and ZnS nanoplatelets in HAADF-STEM images is very homogeneous, indicating a uniform flat rectangular shape (Figure 2-1b,d). A close inspection of some individual ZnSe nanoplatelets (Figure 2-1d) reveals evidently hollow features and patches. In Figure A1-3, we can see more clearly such features of hollowness and patchworks, indicating nanoplatelets may have formed by oriented attachment (see the following section for details).[1,24,25] All four wurtzite nanoplatelets show distinct absorption exciton peaks in the range from ultraviolet to visible, which are consistent with their respective band gap energies (Figure 2-1i). The absorption spectra for ZnSe, ZnTe, and CdSe nanoplatelets show distinct light hole−electron (lh-e) and heavy hole−electron (hh-e) transitions, typical of the electronic structure of quantum wells (Figure 2-1i). However, these transitions are not resolved for ZnS nanoplatelets, possibly because of their small spin−orbit splitting, because the spin−orbit coupling is found to decrease with decreasing the atomic number of the chalcogens of ZnX (X = Te, Se, S).[26] We also have performed additional photoluminescence measurements of our materials after ligand exchange with tributylphosphine. The PL spectra of the ZnS and ZnSe nanoplatelets (Figure A1-4) show a narrow emission band at 296 and 349 nm, respectively. As ZnTe nanoplatelets are very unstable and sensitive to air, ZnTe nanoplatelets do not show any luminescence.

X-ray diffraction patterns of ZnS, ZnS, and CdSe nanoplatelets can be satisfactorily assigned to the standard wurtzite phase (Figure A1-5a). As ZnTe nanoplates are extermely unstable under ambient conditions, XRD measurement of ZnTe nanoplatelets is not accessible. The selected area of electron diffraction of ZnTe nanoplatelets, however, can be well indexed to the diffractions of the wurtzite ZnTe (Figure A1-5b). High-resolution TEM (HRTEM) measurements (Figure 2-2c,d) show that the ZnSe and ZnS nanoplatelets are single crystalline. Lattice plane spacings extracted from fast Fourier transform (FFT) analyses of selected areas are

0.339 nm ($10\bar{1}0$) and 0.322 nm (0002) for ZnSe (inset in Figure 2-2c), and 0.317 ($1\bar{0}10$) and 0.299 nm (0002) for ZnS nanoplatelets (inset in Figure 2-2d), typical of the wurtzite structure. The sharp feature of the (0002) plane in the XRD patterns (Figure A1-5a) indeed corroborates the lateral long axis direction. The above structural characterizations verify that these four nanoplatelets crystallize into the wurtzite structure. It also enables us to work out the schematic of a single nanoplatelet with the wurtzite structure (Figure A1-5c).

In the following section, we use wurtzite ZnSe nanoplatelets as an illustrative example to study their growth mechanism. We combine experimental results with the density functional theory (DFT) simulations to reveal why these 2D nanoparticles tend to form eight-layer thick wurtzite nanoplatelets. As the reaction evolved for 2 min at 150 ^{o}C, bundled nanowires were obtained (Figure 2-3a1, 2-3a2, Figure A1-6). The bundle is composed of several nanowires with a uniform width of ~0.99 nm (inset in Figure A1-6a), which is manifested by a band gap absorption at 323 nm in UV-vis spectra (**1** in Figure 2-3e). The elemental composition of ZnSe nanowires was analysed by inductively coupled plasma−optical emission spectrometry (ICP-OES), confirming that the molar ratio of Zn and Se of the nanowires is 1:1 (Table 2-1 and Figure A1-7). Actually, these nanowires are assembles formed directly from the self-assembly of their respective nanoclusters. Both ZnSe and ZnS nanoclusters display distinct exciton peaks at 310/323 nm and 258/270 nm, respectively (Figure 2-3e, Figure A1-8f).[27,28] As the reaction proceeded for 4 min for ZnSe and 2 min for ZnS at 150 ^{o}C, the bundled nanowires became fused and fragmented (Figure 2-3b1, 2-3b2, Figure A1-9), and a slight shift to 325 nm is observed in the absorption spectrum (**2** in Figure 2-3e). In addition to the already existing peaks of the nanowires, the absorption spectrum (**2** in Figure 2-3e) indicates the formation of thicker species corresponding to an absorption onset at 348 nm. This increase in thickness of the small lateral size nanoplatelets already formed is confirmed by the higher contrast they exhibit in comparison to the fused nanowires in HAADF-STEM measurements (Figure 2-3b2, Figure A1-6). Maintaining the reaction for 30 min at 150 ^{o}C converted the fused nanowires into small lateral size nanoplatelets completely (Figure 2-3c1, 2-3c2) with a significant increase in the thickness from 0.99 nm to 1.39 nm. This is also indicated by two distinct sharp peaks at 348 nm and 331 nm (**3** in Figure 2-3e) and the disappearance of the peak at 325 nm in the absorption

spectrum. Continuing the reaction at this temperature for 2 h produced nearly monodisperse nanoplatelets (Figure 2-3d1, 2-3d2). The corresponding absorption spectrum of nanoplatelets (**4** in Figure 2-3e) is identical to that of the proceeding small lateral size nanoplatelets (**3** in Figure 2-3e), proving that nanoplatelets formed directly from small lateral size nanoplatelets by oriented attachment along the lateral direction without increasing the thickness.

It is worth noting that some nanoplatelets show hollow and patchy features (Figure 2-3d2, Figure A1-3), which corroborates that the formation of nanoplatelets of the wurtzite structure is based on the oriented attachment mechanism.[1,24,25] Our mechanistic studies on the formation of ZnS nanoplatelets with wurtzite structure (Figure A1-8) show similar results, demonstrating the generality of the proposed growth mechanism for wurtzite nanoplatelets.

As each nanowire component of the bundled nanowires has an extremely small diameter, i.e., 0.99 nm, it is hard to resolve the crystalline structures of each nanowire. This is because specifically focusing the electron beam of the field emission electron microscope on such a small nanowire may lead to its decomposition because of beam damage. In this sense, we utilized a non-destructive method, small-angle X-ray scattering (SAXS), as a powerful tool to understand the interactions between individual nanocrystal building blocks and the origin of their collective properties. This technique enables us to understand how single amine (oleylamine) or a mixture of two primary amines (octylamine and oleylamine) will affect the stacking of nanocrystal building blocks (either nanowires or nanoplatelets). Table 2-2 summarizes the SAXS model parameter values for the bundled nanowires (Figure 2-3f) and stacked nanoplatelets (Figure 2-3h). The SAXS patterns show two main peaks, which correspond to the first and second order diffractions from the same structure within each sample. The first diffraction peak in Figure 2-3f is 0.1273 $Å^{-1}$, which corresponds to a 4.94 nm of centre-to-centre distance (Figure 2-3g). Considering the thickness of each nanowire is 0.99 nm, a spacing of 3.95 nm between two adjacent nanowires was obtained. This distance is less than the sum of the length of two oleylamine ligands of 4.2 nm, suggesting oleylamine ligands on adjacent surface of nanowires are tightly buckled (Figure 2-3g).[29-33]A center-to-center distance of 4.60 nm (diffraction peak at 0.1366 $Å^{-1}$) was derived in Figure 2-3h, and therefore, the spacing between each two adjacent nanoplatelets is 3.21 nm considering the thickness of each nanoplatelet is 1.39 nm (Figure 2-3i). This spacing

(3.21 nm) corresponds to the sum of the chain length of an oleylamine (2.0 nm) and an octylamine (1.2 nm), suggesting the amine chains on the surface of nanoplatelets are less buckled (Figure 2-3i). Figure A1-10 summarizes the changes of the dimensions of nanoplatelets as a function of reaction time. TEM and SAXS measurements suggest that the increases of the thickness of 0.99 nm for the nanowires and 1.39 nm for the nanoplatelets may involve monomer diffusion and reconstruction.

To further establish the proposed mechanism and in particular to elucidate why nanoplatelets of wurtzite structure exhibit the uniform thickness of ~1.39 nm (equivalent to eight layers of the $(11\bar{2}0)$ plane of wurtzite ZnSe and ZnS), we employed the first-principles method based on DFT[34-36] to study the surface energy and growth kinetics of nanoplatelets (Figures A1-11, A1-12). The non-polar surface of $(11\bar{2}0)$ has the lowest surface energy (Figure 2-4a, Table 2-3) and hence is an expected dominant facet that determines the final morphology of the nanoplatelets. Two equivalent non-polar facets of $(10\bar{1}0)$A and $(1\bar{1}00)$A are also highly stable (inset of Figure 2-4a), and they are the terminated facets of the $[10\bar{1}0]$ and $[1\bar{1}00]$ directions, respectively. The polar facets of both (0002) and $(000\bar{2})$ have larger surface energy than any of the nonpolar surfaces over almost the entire thermodynamically allowed range (Figure 2-4a). This, in turn, leads to the fast growth of the system along [0002] (c-axis of the wurtzite structure). All of this leads to the formation of nanoplatelets with well-defined facets, as is illustrated schematically in Figure A1-5c. Our calculation results also show that ZnSe monomers always have much higher binding energy on the surfaces of nanoplatelets than alkylamine ligands, and thus, the ZnSe nanocrystals' growth is unlikely inhibited by the binding of ligands (Table 2-4 and Figures A1-13−A1-15).

We will now discuss the growth kinetics and illustrate why ZnSe nanoplatelets exhibit a uniform thickness of 1.39 nm. We used the nanowire model with a diameter of ~0.99 nm periodically repeating along the *c*-axis (Figure 2-4b) to investigate the growth of the nanowires (Figure 2-5a-c, Figure A1-13).[37] Two growth pathways were considered: oriented fusion of nanowires (Figure 2-5a-c) and growth through ZnSe monomers diffusion and reconstruction (Figure 2-5d1, 2-5d2). A side-to-side horizontally oriented fusion along the $[1\bar{1}00]$ direction (Figure 2-5a) is expected to be the dominated growth process because it has the lowest formation energy compared

to any other process (Figure 2-5b, 2-5c, Table 2-4). This growth process continuously repeats itself and finally results in the formation of 0.99 nm thick fused nanowires. The ZnSe monomer diffusion and reconstruction process become the dominant process after the ZnSe nanowires are depleted by means of the fusion process (Figure 2-5d1, 2-5d2). To deposit the firstly additional layer along the $[11\bar{2}0]$ direction (thickness increases from 0.99 nm to 1.19 nm), the system is required to overcome a small energy barrier of 0.0359 eV (equivalent to 415 K) (Figure 2-5d, Table 2-4). This can be easily overcome by the thermal energy of the reaction system (150 ^{o}C, 423.15 K). Following the deposition of the first additional layer on the $(11\bar{2}0)$ surface, the second additional layer will spontaneously form (thickness increases from 1.19 nm to 1.39 nm) because of its negative formation energy of -0.2489 eV (Figure 2-5d, Table 2-4). However, when the thickness of the nanoplatelets reaches 1.39 nm, further deposition of any additional atomic layer along the $[11\bar{2}0]$ direction is inaccessible because its formation energy significantly increases to 0.0654 eV (760 K), which is far beyond the range of our experimental conditions (Figure 2-5d, Table 2-4). Actually, reaction at temperatures above 200 ^{o}C led to the conversion of ZnSe nanoplatelets into thick ZnSe nanowires (Figure A1-16).

The 1.39 nm thick nanoplatelets with a small lateral size will continue to form via oriented attachment along the $[1\bar{1}00]$ direction. Because of the high surface energy of $(1\bar{1}00)$B/$(10\bar{1}0)$B and the low formation energy of $(1\bar{1}00)$A and $(10\bar{1}0)$A, ZnSe monomers will diffuse and redeposit on the exposed $(1\bar{1}00)$B/ $(10\bar{1}0)$B to form the new $(1\bar{1}00)$A and $(10\bar{1}0)$A surfaces (Figure 2-5d2, Figure A1-17). Growth of any additional atomic layer on these surfaces to form $(1\bar{1}00)$B and $(10\bar{1}0)$B is very difficult due to the large formation energy of 0.8364 eV (Figure 2-5d, Figure A1-17) so the new surfaces of $(1\bar{1}00)$A and $(10\bar{1}0)$A would be the terminating surfaces in their corresponding directions (Figure A1-18). This explains why ZnSe nanoplatelets form such a rectangular shape with a uniform thickness of 1.39 nm. DFT calculations on the formation energies of diffusion and nuclei construction along the $[11\bar{2}0]$ direction for three additional layers for ZnS, CdSe, and ZnTe nanoplatelets have a trend similar to that of ZnSe nanoplatelets. Similarly, ZnS, CdSe, and ZnTe nanoplatelets (Figures A1-19−A1-21) also undergo similar growth behaviour, starting from intermediate products with nanowire morphology and presenting a

uniform thickness of eight monolayers along the [11$\bar{2}$0] direction (see the Appendix 1 for details).

2.4 Conclusions

To summarize, a family of wurtzite nanoplatelets with eight-layer thickness with atomic precision were prepared, and wurtzite ZnSe nanoplatelets were used as a representative to study the growth mechanism. The combination of experimental results with DFT simulations reveals that the formation of eight-layer thick wurtzite nanoplatelets is kinetically favourable, whereas the formation energy for the growth of wurtzite nanoplatelets thicker than eight layers is too large to be accessed by the entire thermodynamically allowed range of nanoplatelet growth.

2.5 Tables and Figures

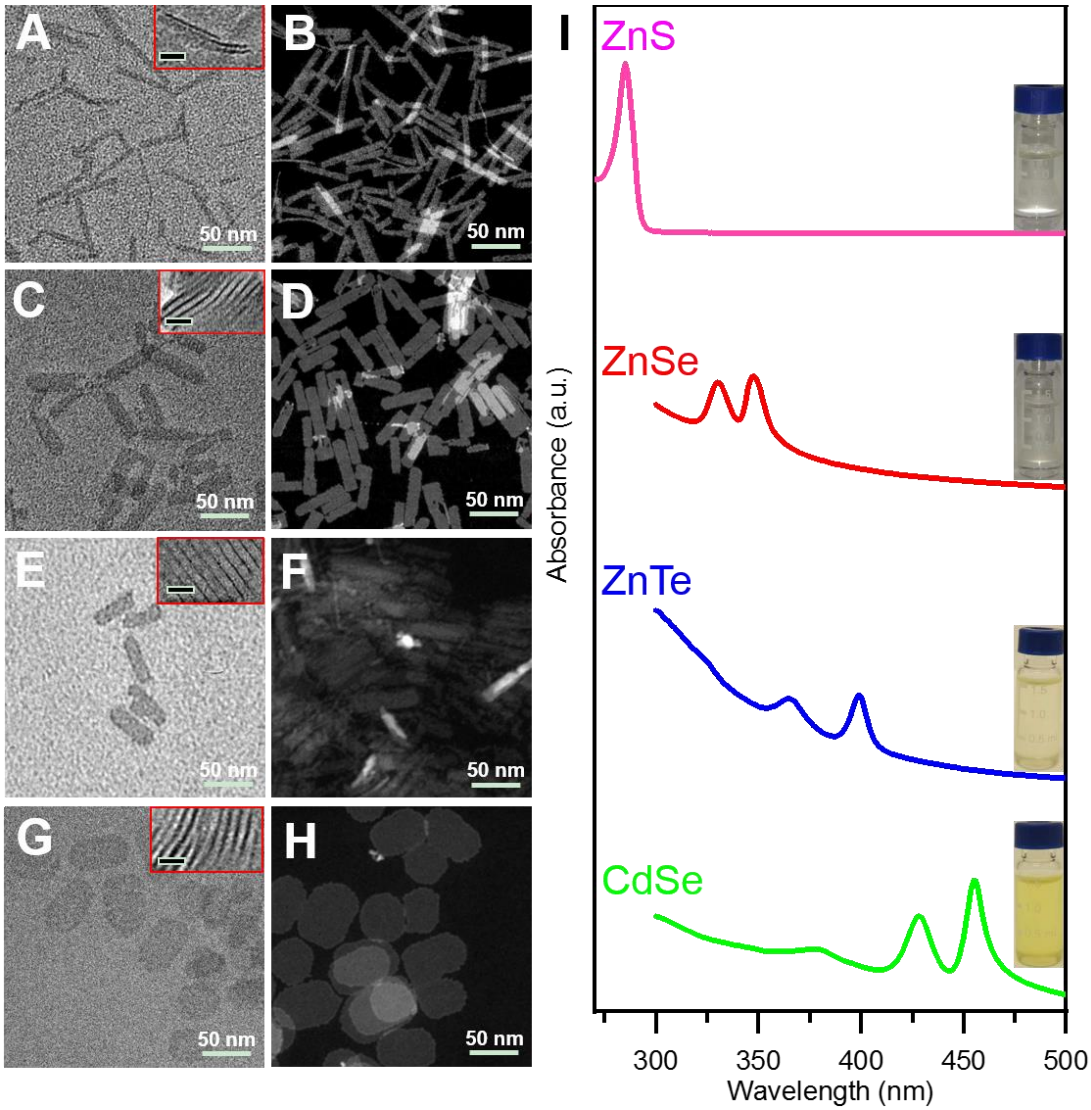

Figure 2-1. TEM images of (**A**) ZnS, (**C**) ZnSe, (**E**) ZnTe, and (**G**) CdSe nanoplatelets. HAADF-STEM images of (**B**) ZnS, (**D**) ZnSe, (**F**) ZnTe, and (**H**) CdSe nanoplatelets. **I**, UV−vis optical spectra of ZnS, ZnSe, ZnTe, and CdSe nanoplatelets. Insets in panel I are the photographs of ZnS, ZnSe, ZnTe, and CdSe nanoplatelets dispersed in toluene, showing good dispersity of the nanoparticles.

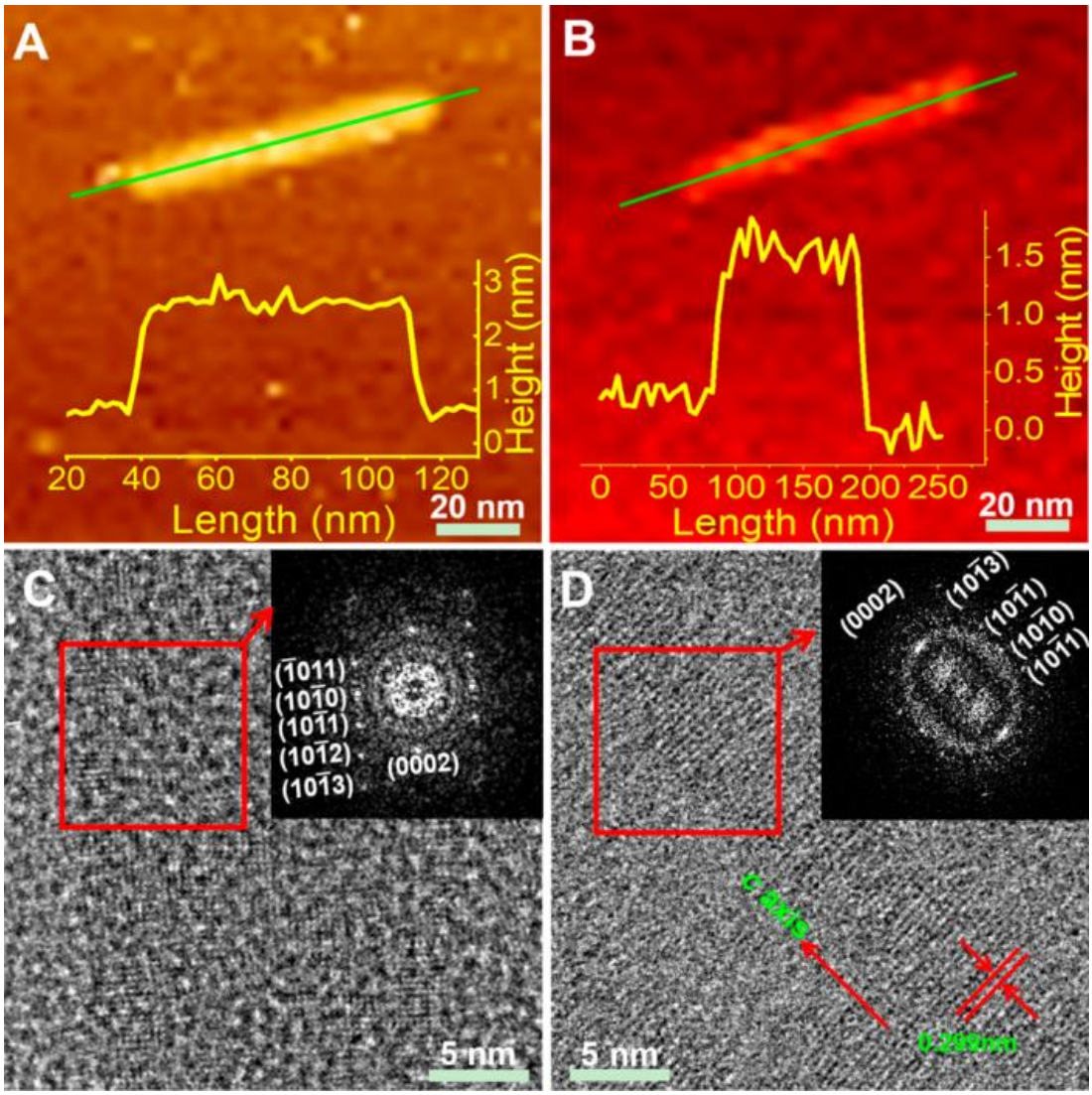

Figure 2-2. AFM images (top) and the cross-sectional height analysis (bottom) along the long lateral direction of an individual (**A**) ZnSe and (**B**) ZnS nanoplatelet. HRTEM images of (**C**) ZnSe and (**D**) ZnS nanoplatelets. Insets in panels C and D marked by red rectangles are the FFT analysis of a selected area of ZnSe and ZnS nanoplatelets, revealing the crystallographic relation.

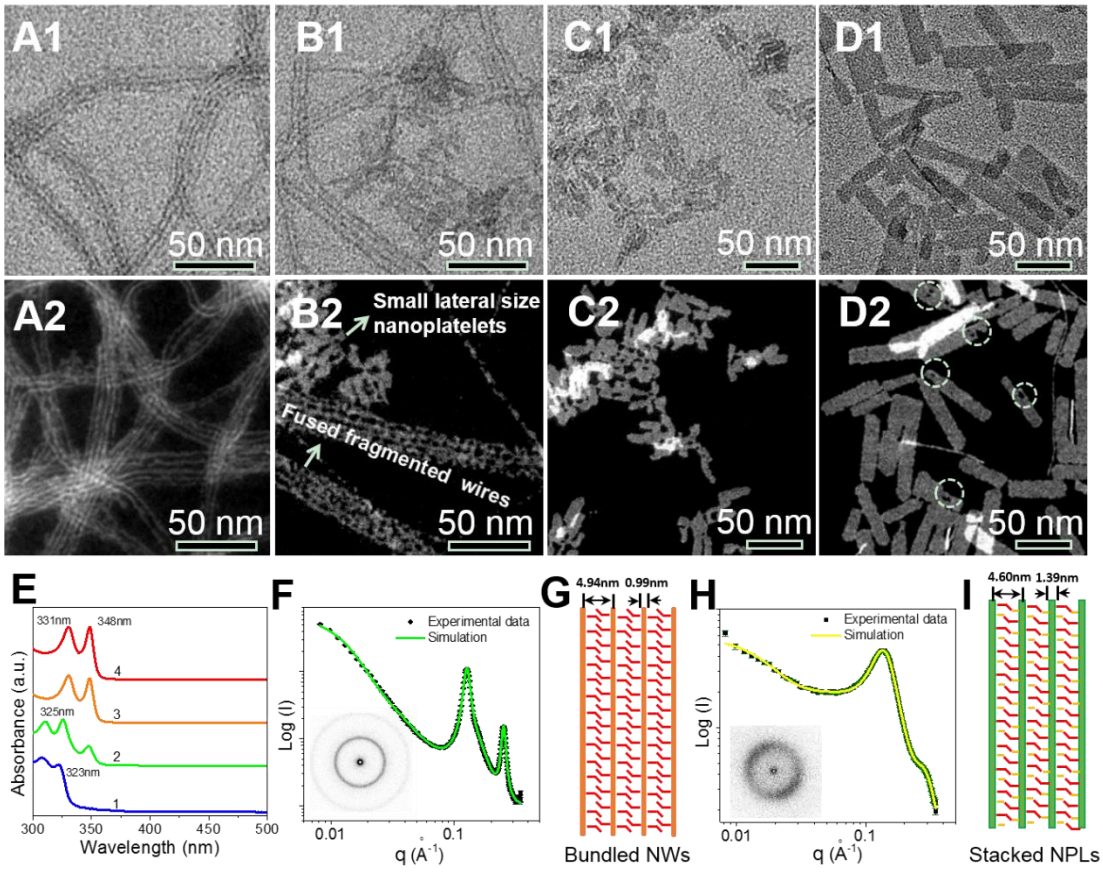

Figure 2-3. A, TEM (A1-D1) and **B**, HAADF-STEM (A2-D2) images of intermediates with controlled the reaction time at 150 ℃: (A1 and A2) 2 min, (B1 and B2) 4 min, (C1 and C2) 30 min, and (D1 and D2) 2 h. **E**, Absorption spectra of ZnSe nanocrystals at different growth stages. **F**, SAXS pattern and **G**, schematic illustration of bundled NWs. **H**, SAXS pattern and **I**, schematic illustration of stacked NPLs. Insets in panels F and H show 2-D SAXS patterns. Red and orange lines in panels G and I correspond to oleylamine and octylamine, respectively.

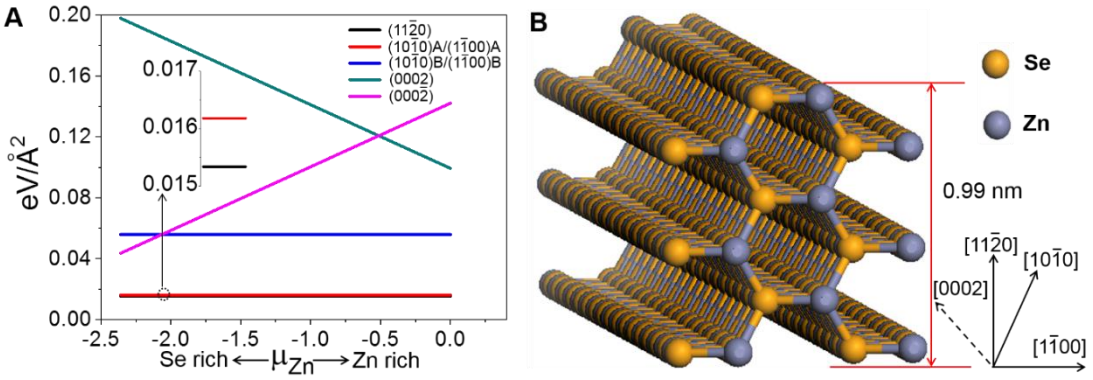

Figure 2-4. A, Surface energy as a function of the chemical potential $\Delta\mu_{Zn}$ of ZnSe slab surface. Inset shows the zoomed-in view of the highlighted area marked by a dashed circle. **B**, Schematic illustration of the nanowire model showing the initial thickness of the nanowires is 0.99 nm.

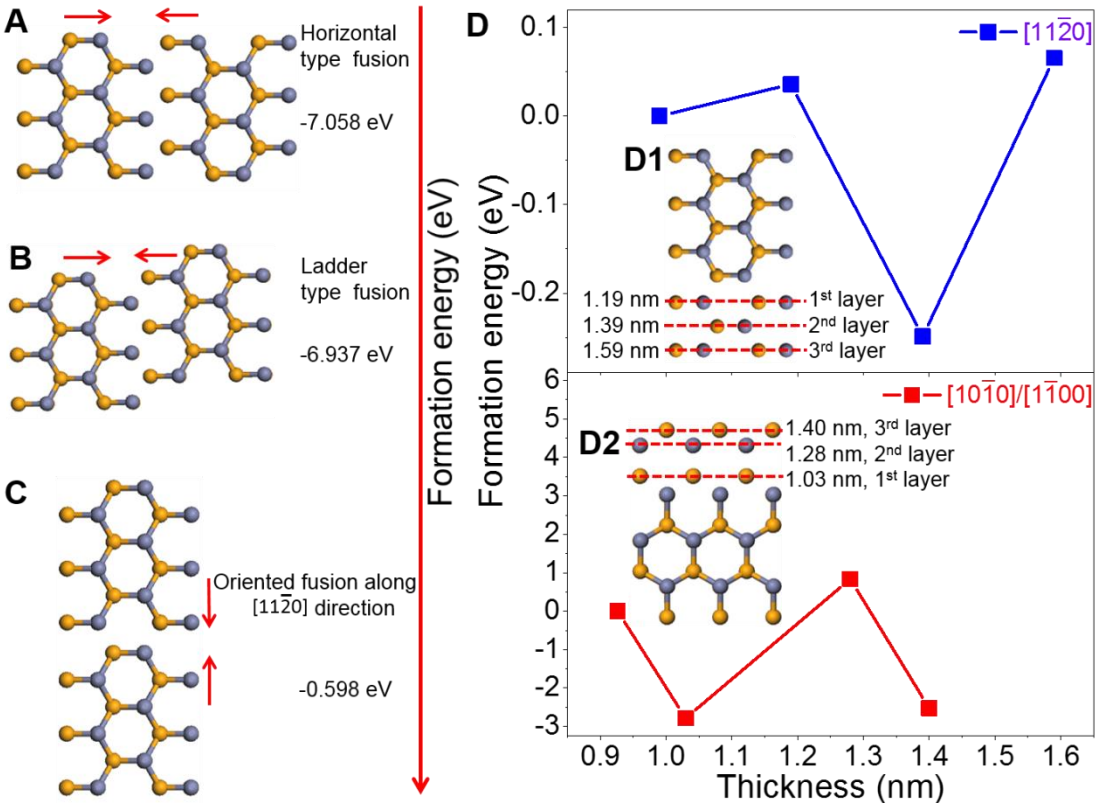

Figure 2-5. A, Horizontal-type oriented fusion of nanowires along the $[1\bar{1}00]$ direction. **B**, Ladder-type oriented fusion of nanowires along the $[\bar{1}100]$ direction. **C**, Oriented fusion along the $[11\bar{2}0]$ direction. **D**, Formation energies of diffusion and nuclei construction along the $[11\bar{2}0]$ and $[1\bar{1}00]$ directions for three additional layers, corresponding to D1 and D2, respectively. The optimized structures corresponding to A, B, D1, and D2 are shown in Figure A1-18.

Table 2-1. Determination of ZnSe nanowires composition using ICP-OES.

Se (mg/L)	Zn (mg/L)	Se (mmol/L)	Zn (mmol/L)	Molar ratio Zn:Se
107.510	95.340	1.361572	1.458018	0.933851
106.443	94.155	1.348059	1.439897	0.936219
105.242	94.146	1.332848	1.439768	0.925738
31.881	27.807	0.403768	0.425249	0.949485
32.324	28.325	0.409369	0.433165	0.945066
32.481	28.331	0.411356	0.43326	0.949443
13.608	11.718	0.172342	0.179203	0.961714
13.589	11.676	0.172097	0.178552	0.963847
13.724	11.508	0.173808	0.175993	0.987588

Table 2-2. SAXS model parameter values for bundled nanowires and stacked nanoplatelets. G and P are the Guinier and Porod constants. Rg is the radius of gyration. UF is Unified Fit. LP is Lorentzian Peak. *values were fixed during refinement.

Parameter	Sample 1	Sample 2
UF1 G	0.192(3)	7.4(4)
UF1 R_g (Å)	13.4(3)	141(2)
UF1 P	4*	2.33(2)
UF2 G	0.39(4)	
UF2 R_g (Å)	102(5)	
UF2 P	4*	
LP1 intensity	0.383(4)	1.028(13)
LP1 position ($Å^{-1}$)	0.1366(2)	0.12730(7)
LP1 width ($Å^{-1}$)	0.0420(6)	0.00958(13)
LP2 intensity	0.0320(7)	0.141(2)
LP2 position ($Å^{-1}$)	0.2817(11)	0.25283(9)
LP2 width ($Å^{-1}$)	0.086(4)	0.01429(13)
LP3 intensity		0.095(3)
LP3 position ($Å^{-1}$)		0.1386(6)
LP3 width ($Å^{-1}$)		0.0448(9)

Table 2-3. The surface energy (eV) of $(11\bar{2}0)$, $(10\bar{1}0)$A/$(1\bar{1}00)$A and $(10\bar{1}0)$B/$(1\bar{1}00)$B facets as a function of thickness of nanoplatelets.

	6 layers	7 layers	8 layers	10 layers
$(11\bar{2}0)$	0.0158	0.0153	0.0153	-
$(10\bar{1}0)$A/$(1\bar{1}00)$A	0.0166	-	0.0161	0.0161
$(10\bar{1}0)$B/$(1\bar{1}00)$B	0.0564	-	0.0557	0.0557

Table 2-4. The binding energy of alkylamine ligands and ZnSe monomers adsorption on different sites of exposed surfaces of the ZnSe nanostructure.

	Top-Zn	Top-Se	Bridge	Hcp	Monomer
$(11\bar{2}0)$	-0.9273	0.0435	-0.0323	-0.9317	-1.8565
$(10\bar{1}0)$A/$(1\bar{1}00)$A	-0.7396	-0.0379	-0.8577	-0.8876	-1.7029
$(10\bar{1}0)$B/$(1\bar{1}00)$B	-1.1160	0.0064	-1.1160	-2.9506	-3.7583
(0002)	-5.1486	-	-4.6258	-3.8125	-5.6899
$(000\bar{2})$	-	-1.4489	-1.4494	-1.4514	-3.5373

Note: details on different sites of exposed surfaces of ZnSe nanostructure are depicted in Figure A1-8.

Table 2-5. The formation energy (in eV) of diffusion and stacking process and fuse process along [11$\bar{2}$0] direction and [1$\bar{1}$00] direction, respectively.

	Diffusion process			Fuse process	
	7th-layer	8th-layer	9th-layer	-	
[11$\bar{2}$0]	0.0359	-0.2489	0.0654	-0.5979	
[1$\bar{1}$00]	-2.7828	0.8364	-2.5247	-7.0577 (Horizontal)	-6.9369 (ladder)

2.6 References

(1) Schliehe, C.; Juarez, B. H.; Pelletier, M.; Jander, S.; Greshnykh, D.; Nagel, M.; Meyer, A.; Foerster, S.; Kornowski, A.; Klinke, C.; Weller, H. Ultrathin PbS Sheets by Two-Dimensional Oriented Attachment. *Science* **2010**, *329*, 550–553.

(2) Son, J. S.; Wen, X.-D.; Joo, J.; Chae, J.; Baek, S.-il.; Park, K.; Kim, J. H.; An, K.; Yu, J. H.; Kwon, S. G.; Choi, S.-H.; Wang, Z.; Kim, Y.-W.; Kuk, Y.; Hoffmann, R.; Hyeon, T. Large-Scale Soft Colloidal Template Synthesis of 1.4 nm Thick CdSe Nanosheets. *Angew. Chem. Int. Ed.* **2009**, *48*, 6861–6864.

(3) Ithurria, S.; Tessier, M. D.; Mahler, B.; Lobo, R. P. S. M.; Dubertret, B.; Efros, Al. L. Colloidal Nanoplatelets with Two-Dimensional Electronic Structure. *Nat. Mater.* **2011**, *10*, 936–941.

(4) Tang, Z.; Zhang, Z.; Wang, Y.; Glotzer, S. C.; Kotov, N. A. Self-Assembly of CdTe Nanocrystals into Free-Floating Sheets. *Science* **2006**, *314*, 274–278.

(5) Riedinger, A.; Ott, F. D.; Mule, A.; Mazzotti, S.; Knüsel, P. N.; Kress, S. J. P.; Prins, F.; Erwin, S. C.; Norris, D. J. An Intrinsic Growth Instability in Isotropic Materials Leads to Quasi-Two-Dimensional Nanoplatelets. *Nat. Mater.* **2017**, *16*, 743–748.

(6) Liu, Y.-H.; Wang, F.; Wang, Y.; Gibbons, P. C.; Buhro, W. E.Lamellar Assembly of Cadmium Selenide Nanoclusters into Quantum Belts. *J. Am. Chem. Soc.* **2011**, *133*, 17005–17013.

(7) Chen, Y.; Chen, D.; Li, Z.; Peng, X.Symmetry-Breaking for Formation of Rectangular CdSe Two-Dimensional Nanocrystals in Zinc-Blende Structure. *J. Am. Chem. Soc.* **2017**, *139*, 10009–10019.

(8) Gerard, C.; Das, R.; Mahadevan, P.; Sarma, D. D. Effective Mass-Driven Structural Transition in a Mn-Doped ZnS Nanoplatelet. *J. Phys. Chem. Lett.* **2013**, *4*, 1023–1027.

(9) Grim, J. Q.; Christodoulou, S.; Di Stasio, F.; Krahne, R.; Cingolani, R.; Manna, L.; Moreels, I. Continuous-Wave Biexciton Lasing at Room Temperature Using Solution-Processed Quantum Wells. *Nat. Nanotech.* **2014**, *9*, 891–895.

(10) Yang, Z.; Pelton, M.; Fedin, I.; Talapin, D. V.; Waks, E. A Room Temperature Continuous-Wave Nanolaser Using Colloidal Quantum Wells. *Nat. Commun.* **2017**, *8*, 143.

(11) She, C.; Fedin, I.; Dolzhnikov, D. S.; Dahlberg, P. D.; Engel, G. S.; Schaller, R. D.; Talapin, D. V. Red, Yellow, Green, and Blue Amplified Spontaneous Emission and Lasing Using Colloidal CdSe Nanoplatelets. *ACS Nano* **2015**, *9*, 9475–9485.

(12) Rowland, C. E.; Fedin, I.; Zhang, H.; Gray, S. K.; Govorov, A. O.; Talapin, D. V.; Schaller, R. D. Picosecond Energy Transfer and Multiexciton Transfer Outpaces Auger Recombination in Binary CdSe Nanoplatelet Solids. *Nat. Mater.* **2015**, *14*, 484–489.

(13) Cho, W.; Kim, S.; Coropceanu, I.; Srivastava, V.; Diroll, B. T.; Hazarika, A.; Fedin, I.; Galli, G.; Schaller, R. D.; Talapin, D. V. Direct Synthesis of Six-Monolayer (1.9 nm) Thick Zinc-Blende CdSe Nanoplatelets Emitting at 585 nm. *Chem. Mater.* **2018**, *30*, 6957–6960.

(14) Wu, K.;Li, Q.; Jia, Y.; McBride, J. R.; Xie, Z.-X.; Lian, T. Efficient and Ultrafast Formation of Long-Lived Charge-Transfer Exciton State in Atomically Thin Cadmium Selenide/Cadmium Telluride Type-II Heteronanosheets. *ACS Nano* **2015**, *9*, 961–968.

(15) Ithurria, S.; Bousequet, G.; Dubertret, B. Continuous Transition from 3D to 1D Confinement Observed during the Formation of CdSe Nanoplatelets. *J. Am. Chem. Soc.* **2011**, *133*, 3070–3077.

(16) Baghani, E.; O'Leary, S. K.; Fedin, I; Talapin, D. V.; Pelton, M. Auger-Limited Carrier Recombination and Relaxation in CdSe Colloidal Quantum Wells. *J. Phys. Chem. Lett.* **2015**, *6*, 1032–1036.

(17) Kunneman, L. T.; Tessier, M. D.; Heuclin, H.; Dubertret, B.; Aulin, Y. V.; Grozema, F. C.; Schins, J. M.; Siebbeles, L. D. A. Bimolecular Auger Recombination of Electron-Hole Pairs in Two-Dimensional CdSe and CdSe/CdZnS Core/Shell Nanoplatelets. *J. Phys. Chem. Lett.* **2013**, *4*, 3574–3578.

(18) Gerdes, F.; Navío, C.; Juárez, B. H.; Klinke, C. Size, Shape, and Phase Control in Ultrathin CdSe Nanosheets. *Nano Lett.* **2017**, *17*, 4165–4171.

(19) Park, H.; Chung, H.; Kim, W. Synthesis of Ultrathin Wurtzite ZnSe Nanosheets. *Mater. Lett.* **2013**, *99*, 172–175.

(20) Sun, H.; Wang, F.; Buhro, W. E. Tellurium Precursor for Nanocrystal Synthesis: Tris(dimethylamino)phosphine Telluride. *ACS Nano*, **2018**, *12*, 12393–12400.

(21) Ilavsky, J.; Jemian, P. R. Irena: Tool Suite for Modeling and Analysis of Small-Angle Scattering. *J. Appl. Cryst.* **2009,** *42*, 347–353.

(22) Beaucage, G. Approximations Leading to a Unified Exponential/Power-Law Approach to Small-Angle Scattering. *J. Appl. Cryst.* **1995,** *28*, 717–728.

(23) Luo, Y. R. *Comprehensive Handbook of Chemical Bond Energies;* CRC Press: Boca Raton, FL, 2007.

(24) Wang, Z.; Schliehe, C.; Wang, T.; Nagaoka, Y.; Cao, Y. C.; Bassett, W. A.; Wu, H.; Fan, H.; Weller. H. Deviatoric Stress Driven Formation of Large Single-Crystal PbS Nanosheet From Nanoparticles and in Situ Monitoring of Oriented Attachment. *J. Am. Chem. Soc.* **2011**, *133*, 14484–14487.

(25) Penn, R. L.; Banfield, J. F. Imperfect Oriented Attachment: Dislocation Generation in Defect-Free Nanocrystals. *Science* **1998**, *281*, 969−971.

(26) Karazhanov, S. Zh.; Ravindran, P.; Kjekshus, A.; Fjellvåg, H.; Svensson, B. G. Electronic Structure and Optical Properties of ZnX (X=O, S, Se, Te): A Density Functional Study. *Phys. Rev. B* **2007**, *75*, 155104.

(27) Gao, D.; Hao, X.; Rowell, N.; Kreouzis, T.; Lockwood, D. J.; Han, S.; Fan, H.; Zhang, H.; Zhang, C.; Jiang, Y.; Zeng, J.; Zhang, M.; Yu, K. Formation of Colloidal Alloy Semiconductor CdTeSe Magic-Size Clusters at Room Temperature. *Nat. Commun.* **2019**, *10,* 1674.

(28) Wang, L.; Hui, J.; Tang, J.; Rowell, N.; Zhang, B.; Zhu, T.; Zhang, M.; Hao, X.; Fan, H.; Zeng, J.; Han, S.; Yu, K. Precursor Self-Assembly Identified as a General Pathway for Colloidal Semiconductor Magic-Size Clusters. *Adv. Sci.* **2018**, *5*, 1800632.

(29) Jia, G.; Sitt, A.; Hitin, G. B.; Hadar, I.; Bekenstein, Y.; Amit, Y.; Popov, I.; Banin, U. Couples of Colloidal Semiconductor Nanorods Formed by Self-Limited Assembly. *Nat. Mater.* **2014**, *13*, 301–307.

(30) Wang, Z.; Wen, X.-D.; Hoffmann, R.; Son, J. S.; Li, R.; Fang, C.-C.; Smilgies, D.-M.; Hyeon, T. Reconstructing a Solid-Solid Phase Transformation Pathway in CdSe Nanosheets with Associated Soft Ligands. *Proc. Natl. Acad. Sci. USA* **2010**, *107*, 17119–17124.

(31) Jia, G.; Banin, U. A General Strategy for Synthesizing Colloidal Semiconductor Zinc Chalcogenide Quantum Rods. *J. Am. Chem. Soc.* **2014**, *136*, 11121–11127.

(32) Chen, D.; Zhang, H.; Li, Y.; Pang, Y.; Yin, Z.; Sun, H.; Zhang, L.-C.; Wang, S.; Saunders, M.; Barker, E.; Jia, G. Spontaneous Formation of Noble- and Heavy-Metal-Free Alloyed Semiconductor Quantum Rods for Efficient Photocatalysis. *Adv. Mater.* **2018**, *30*, 1803351.

(33) Jia, G.; Pang, Y.; Ning, J.; Banin, U.; Ji, B. Heavy-Metal-Free Colloidal Semiconductor Nanorods: Recent Advances and Future Perspectives. *Adv. Mater.* **2019**, *31*, 1900781.

(34) Kresse, G.; Furthmüller, J. Efficient Iterative Schemes for *ab initio* Total-Energy Calculations Using a Plane-Wave Basis Set. *Phys. Rev. B* **1996**, *54*, 11169–11186.

(35) Blöchl, P. E. Projector Augmented-Wave Method. *Phys. Rev. B* **1994**, *50*, 17953–17979.

(36) Perdew, J. P.; Burke, K.; Ernzerhof, M. Generalized Gradient Approximation Made Simple. *Phys. Rev. Lett*. **1996**, *77*, 3865−3868.

(37) Wang, Y.; Zhou, Y.; Zhang, Y.; Buhro, W. E. Magic-Size II–VI Nanoclusters as Synthons for Flat Colloidal Nanocrystals. *Inorg. Chem.* **2015**, *54*, 1165−1177.

Author contribution statement: Y.P. and G.J. conceived the original idea of this work. Y.P. conducted the experiments. M.Z. performed the theoretical calculations. Y.P. wrote the manuscript with support from G.J. M.R. set up SAXS measurements and analysed data. L.L. conducted the ICP-OES measurement. All authors provided critical comments on the manuscript.

Every reasonable effort has been made to acknowledge the owners of copyright material. I would be pleased to hear from any copyright owner who has been omitted or incorrectly acknowledged.

Chapter 3: Heavy-Metal-Free Atomic-Thick Quasi-Two-Dimensional Colloidal Semiconductor Nanoplatelets for Photodetectors

Abstract

Atomic-thick quasi-two-dimensional (2D) colloidal semiconductor nanoplatelets continue to advance multidisciplinary research field owing to their intriguing size-dependent optical and electronic properties. Despite intensive exploration given to these 2D materials, the synthesis of heavy-metal-free semiconductor nanoplatelets is still at primitive stages. The growth mechanism, electronic and optical properties behind their highly anisotropic shape and precisely controlled atomic thickness remains unclear. Here a robust approach is reported that produces over ten-grams of zinc chalcogenide nanoplatelets with atomically uniform thickness under ambient conditions. The experimental results showed a previously unknown mechanism for the formation of nanoplatelets, which consists of fusion of bundled nanowires, followed by monomer diffusion and reconstructions, and finally oriented attachment, is revealed. The synthesized ZnSe nanoplatelets exhibit an exceptional narrow emission spectrum with full-width at half-maximum as sharp as 90 meV and a 1.9 ns radiative fluorescent lifetime at room temperature. ZnSe nanoplatelets-based ultraviolet (UV) photodetectors is fabricated using a simple solution process. This provides a solid basis for the further applications of ZnS and ZnSe nanoplatelets for lighting, display, photodetectors, electronics, catalysis, solar cells, and imaging.

Keywords: ZnS and ZnSe nanoplatelets, heavy-metal-free, atomic thickness, luminescence, ultraviolet photodetectors.

3.1 Introduction

In 2004, graphene, the ultra-thin carbon film of monoatomic layer, was born, which triggered the frenetic pursuit of two-dimensional nanomaterials by scientific research and industry.[1-3] Impelled by the discovery and fascinating properties of graphene,[1,4-7] the pursuit of atomic-thick forms of alternative materials, identified as "2D materials", is springing up. 2D materials are a kind of materials possessing lateral sizes ranging from one hundred nanometers to even a few micrometers while their thickness is only less than 5 nm.[8] So far, there are mainly three types of two-

dimensional materials: (1) Single-atom elemental 2D materials (Xenes);[2] (2) Transition metal carbides and nitrides (MXenes);[9,10] (3) Transition metal disulfide (TMDs).[11-15] There are also other two-dimensional materials such as hexagonal tantalum nitride,[16-18] metal organic frameworks (MOFs),[19,20] covalent organic frameworks (COFs),[21,22] layered double hydroxides (LDHs),[23-25] and oxides.[24-26] The above materials have common metrics that they are single or multi-layer structures obtained by stripping two-dimensional layered inorganic crystal materials, and the layers are mainly connected by weak forces such as van der Waals forces. As an emerging class of materials, 2D materials can be obtained with a thickness of atomic precision, and the electrons are confined in the thickness direction due to the quantum confinement effect, which will generate some astonishing properties that is different from their bulk counterparts. Being analogous to graphene and transition metal dichalcogenides, atomically thin semiconductor nanocrystals are emerging as a class of intriguing materials with broad utility[27-34] due to the remarkable electronic properties of quantum wells such as giant oscillator strength,[29] exceptionally narrow fluorescence,[28,29] low lasing threshold[35-37] and ultrafast exciton dynamics.[29,38-43] Motivated by the compelling properties and innovative applications of such ultrathin 2D nanomaterials, various synthetic methods have been developed. Generally speaking, the existing strategies are separated into two categories: top-down method and bottom-up method. The former method mainly includes mechanical forced- or ion intercalation-assisted liquid exfoliation.[44] In the process of exfoliation, the interlayer attraction of layered bulk parent crystals will be swelled and weakened into completely separated layers with the aid of mechanical sonication or chemical intercalation. The aforementioned liquid exfoliation is promising and applicable for the high-yield production of ultrathin 2D nanomaterials. However, its disadvantages should never be overlooked. Note that for the method of liquid exfoliation in solvents, three aspects should be outlined: (1) The liquid exfoliation strategy is only suitable for those parent bulk crystals which possess a layered structure; (2) Only when the surface energy of the solvent is matching to that of the layered bulk materials, effective exfoliation can be achieved; (3) The exfoliated layers are not stable for the absence of protection of ligands. In contrast, colloidal syntheses, as one of the bottom-up approaches, in principle, are more versatile for the formation of ultrathin 2D nanomaterials, especially for the non-layered NCs. In this regard, developing a strategy for fabrication of atomic-thick layers of non-layered compounds triggers

numerous efforts among scientific communities. Despite intense efforts over past 10 years, currently semiconductor nanocrystals still face several challenging issues: (i) the growth mechanism of nanoplatelets with wurtzite structure remains unclear although there are several mechanistic studies on nanoplatelets with zinc blende structure;[28,31-33,41] (ii) most reported nanoplatelets contain highly toxic heavy-metal ions such as cadmium[28-33,35-41] and lead;[27,45-47] (iii) the synthesis usually utilizes toxic organic phosphines as ligands/solvents and produces only small quantities of a few tens to a few hundreds of milligrams;[27,29,31-33,35,41,45] (iv) the synthesis require tedious multistep reactions [e.g. preparation and purification of the seeds, hot injection of precursor at elevated temperatures], and rigorous experimental conditions [e.g. oxygen- and moisture-free environments], and suffer from batch-to-batch variability.[29-33,35-41] All of the above issues impede their large-scale production and commercialization.

We report on a facile, scalable, robust and phosphine-free one-pot wet-chemical approach for fabricating free-standing heavy-metal-free colloidal zinc chalcogenide nanoplatelets with atomically uniform thickness under ambient conditions.

3.2 Experimental section

Chemicals. Zinc nitrate hexahydrate ($Zn(NO_3)_2$ $6H_2O$,), zinc chloride ($ZnCl_2$), zinc acetate dihydrate ($Zn(CH_3COO)_2$ $2H_2O$), zinc iodide (ZnI_2), selenium powder, sulfur powder, hexylamine, octylamine, decylamine, dodecylamine, hexadecylamine, oleylamine, oleic acid, 1-octadecene (ODE), trioctylphosphine (TOP), anhydrous chloroform and anhydrous methanol were purchased from Sigma Aldrich. All chemicals were used without further purification.

3.2.1 Synthesis of nanoplatelets

All syntheses were carried out under inert atmosphere using standard Schlenk techniques. Then the same syntheses were also conducted under ambient conditions in order to investigate if the synthesis of nanoplatelets is sensitive to oxygen and moisture. The quality of the products obtained under ambient conditions is the same as that obtained using standard Schlenk techniques. Therefore, in the following experiments, all the syntheses were carried out under ambient conditions unless otherwise stated.

ZnSe nanoplatelets synthesis: Monodisperse ZnSe nanoplatelets were synthesized using a one-pot synthetic method using a literature method with some modifications.[48] In a typical synthesis, 0.6 mmol $Zn(NO_3)_2$ $6H_2O$ and 1.8 mmol selenium powder were mixed with 10 mL octylamine and 20 mL oleylamine in a 50 mL three-neck flask. The mixture was heated to 110 ℃ and kept at this temperature for 30 min. The temperature was then increased to 150-170 ℃ and kept at this temperature for a desired reaction time. The reaction was quenched by removal of the heating mantle. After cooling to room temperature, 30 mL crude reaction mixture was diluted with 20 mL chloroform. 2 mL TOP was added in order to extract the unreacted selenium. Methanol was added to precipitate the nanoparticles with the aid of centrifugation. Same experimental conditions were used with other short-chain alkylamines except that oleylamine was replaced with octylamine (Table 3-1). $Zn(NO_3)_2$ $6H_2O$ has also been replaced by other zinc precursors, i.e. $ZnCl_2$, $Zn(ac)_2$ $2H_2O$, ZnI_2, to prepare ZnSe nanoplatelets, as detailed in Table 3-1.

Up-scaled synthesis of ZnSe nanoplatelets under ambient conditions: The synthetic procedure for up-scaled synthesis of ZnSe nanoplatelets was conducted under ambient conditions. In this synthesis, $Zn(NO_3)_2$ $6H_2O$ (100 mmol, 29.7 g) and selenium powder (300 mmol, 23.7 g) were mixed with 120 mL octylamine and 240 mL oleylamine in a 500 mL three-neck flask using an oil bath as the heating source (Figure 3-1A). The mixture was heated to 110 ℃ and kept at this temperature for 30 min. The temperature was then increased to 150-170 ℃ and kept at this temperature for a desired reaction time. The reaction was quenched by removal of the heating mantle. After cooling to room temperature, the crude solution was diluted with chloroform. TOP was added in order to extract the unreacted selenium. Methanol was added to precipitate the nanoparticles with the aid of centrifugation. The precipitation was dried under 60 ^oC and 19.9 g powders were obtained (Figure 3-1C, 3-1D).

ZnS nanoplatelets synthesis: Monodisperse ZnS nanoplatelets were synthesized using a one-pot synthetic method. In a typical synthesis, $Zn(NO_3)_2$ $6H_2O$ (0.3 mmol, 89 mg) and sulfur (0.9 mmol, 28.9 mg) were mixed with 5 mL octylamine and 10 mL oleylamine in a 50 mL three-neck flask. The mixture was heated to 110 ℃ and kept at this temperature for 30 min. The temperature was then held at 170 ℃ for 6 h, before removal of the heating mantel and cooled down to room temperature. The

product solution was diluted in chloroform, and the nanoplatelets were precipitated by adding methanol with the aid of centrifugation.

Up-scaled synthesis of ZnS nanoplatelets under ambient conditions: In a typical synthesis, $Zn(NO_3)_2$ $6H_2O$ (100 mmol, 29.7 g) and sulfur powder (300 mmol, 9.6 g) were mixed with 120 mL octylamine and 240 mL oleylamine in a 500 mL three-neck flask using an oil bath as the heating source (Figure A2-1a). The mixture was heated to 110 ℃ and kept at this temperature for 30 min. The temperature was then held at 170 ℃ for 6 h, before removal of the heating mantel and cooled down to room temperature. The product solution was diluted in chloroform, and the nanoplatelets were precipitated by adding methanol with the aid of centrifugation. The precipitation was dried under 60 ºC and 15.9 g powders were obtained (Figure A2-1c, A2-1d).

Alloyed $ZnS_{0.75}Se_{0.25}$ nanoplatelet synthesis: The synthetic procedure for alloyed $ZnSe_{0.25}S_{0.75}$ nanoplatelets was the same as that for ZnS nanoplatelets, except a mixture of chalcogens containing selenium (0.15 mmol, 11.8 mg) and sulfur (0.45 mmol, 14.5 mg) were used.

Alloyed $ZnS_{0.50}Se_{0.50}$ nanoplatelet synthesis: The synthetic procedure for alloyed $ZnSe_{0.50}S_{0.50}$ nanoplatelets was the same as that for ZnS nanoplatelets, except a mixture of chalcogens containing selenium (0.45 mmol, 35.5 mg) and sulfur (0.45 mmol, 14.5 mg) were used.

3.2.2 Lateral size control of nanoplatelets

ZnSe nanoplatelets with a lateral size of 33.9±4.6 nm: In a typical synthesis, $Zn(NO_3)_2$ $6H_2O$ (0.3 mmol, 89 mg) and selenium powder (0.9 mmol, 71 mg) were mixed with 5 mL octylamine and 10 mL oleylamine in a 50 mL three-neck flask. The mixture was heated to 110 ℃ and kept at this temperature for 30 min. The temperature was then held at 170 ℃ for 60 min, before removal of the heating mantel and cooled down to room temperature. The product solution was diluted in chloroform, and the nanoplatelets were precipitated by adding methanol with the aid of centrifugation.

ZnSe nanoplatelets with a lateral size of 57.4±16 nm: The synthetic procedure for the synthesis of ZnSe nanoplatelets was the same as that for the typical synthesis of ZnSe nanoplatelets with a lateral size of 33.9±4.6 nm described above,

except that 5 mL octylamine was replaced by decylamine with the same and the temperature for reaction was held at 170 ℃ for 10 h.

ZnSe nanoplatelets with a lateral size of 76.9±19 nm: The synthetic procedure for the synthesis of ZnSe nanoplatelets was the same as that for the typical synthesis of ZnSe nanoplatelets with a lateral size of 33.9±4.6 nm described above, except that the temperature was held at 170 ℃ for 6 h.

ZnSe nanoplatelets with a lateral size of 84.2±12.5 nm: The synthetic procedure for the synthesis of ZnSe nanoplatelets was the same as that for the typical synthesis of ZnSe nanoplatelets with a lateral size of 33.9±4.6 nm described above, except that the temperature was held at 160 ℃ for 6 h.

ZnSe nanoplatelets with a lateral size of 98.3±12.2 nm: The synthetic procedure for the synthesis of ZnSe nanoplatelets was the same as that for the typical synthesis of ZnSe nanoplatelets with a lateral size of 33.9±4.6 nm described above, except that the reaction was conducted under ambient environment.

ZnSe nanoplatelets with a lateral size of 103.2±12.7 nm: The synthetic procedure for the synthesis of ZnSe nanoplatelets was the same as that for the typical synthesis of ZnSe nanoplatelets with a lateral size of 33.9±4.6 nm described above, except that ZnI_2 (0.3 mmol, 96 mg) was used.

3.2.3 Materials characterization

Ultraviolet-visible (UV-vis) absorption spectroscopy: UV-vis absorption spectroscopy was performed on a Perkin Elmer Lambda 35 UV/VIS Spectrometer using quartz cuvettes.

Fluorescence spectroscopy: fluorescence spectrum was obtained using an Agilent Cary Eclipse fluorescence spectrophotometer.

Powder X-ray diffraction (XRD) patterns: XRD patterns were obtained using Cu Kα (λ=1.5406 Å) photons from an X'per PRO (PANalytical) X-ray diffractometer operated at 40 kV and 40 mA. The crude solutions of nanoplatelet samples were diluted in chloroform and precipitated by methanol with the aid of centrifugation. After repeating this procedure for three times, the powders were further diluted by a small amount of toluene and deposited as a thin layer on a low-background scattering silicon substrate.

Electron microscopy measurement: Transmission electron microscopy (TEM) was performed using a JEOL 2100 transmission electron microscope. High-resolution

TEM (HRTEM), high angle annular dark field scanning transmission electron microscopy (HAADF-STEM) and STEM-energy dispersive X-ray spectroscopy (EDX) were performed on a FEI Titan G2 80-200 high-resolution transmission electron microscope. Samples for electron microscopy measurement were prepared by placing a drop of nanoparticle solution in chloroform on top of a copper grid coated with an amorphous carbon film.

Thermal gravimetric analysis (TGA)-differential thermal analysis (DTA): The analysis was performed on a TA Instruments SDT Q600 simultaneous TGA-DTA. Samples were prepared similar to those for XRD. Approximately 10 mg of sample was weighed into a 110 μL platinum crucible with a matched empty crucible as a reference. The sample was heated from ambient to 743 ℃ at 10 ℃ per minute in a nitrogen atmosphere flowing at 100 mL per min, and then the system cooled to 200 ℃. The system was heated to again 743 ℃ at 10 ℃ per minute in air flowing at 100 mL per min. The temperature scale of the instrument was calibrated using the melting points of 99.999% indium (156.5985 ℃), 99.99+% tin (231.93 ℃), 99.99+% zinc (419.53 ℃), 99.99% silver (961.78 ℃), and 99.999% gold (1064.18 ℃). The balance was calibrated over the temperature range used with standards provided by the instrument manufacturer. The heat flow between the pans was calibrated using a sapphire disk provided by the manufacturer. The cell constant was fine-tuned using the heat of fusion of zinc (113 J/g).

Photophysical measurements: Uncorrected steady-state emission spectra were recorded using an Edinburgh FLSP980-stm spectrometer equipped with a 450 W xenon arc lamp, double excitation and emission monochromators, a Peltier-cooled Hamamatsu R928P photomultiplier (185-850 nm). Emission spectra were corrected for source intensity (lamp and grating) and emission spectral response (detector and grating) by a calibration curve supplied with the instrument. Overall quantum yields were measured with the use of an integrating sphere coated with BenFlect. Fluorescence emission lifetimes (τ) were determined with the time-correlated single photon counting technique (TCSPC) with the same Edinburgh FLSP920 spectrometer using pulsed picosecond LEDs (EPLED 280 or EPLED 320, FHWM <800 ps) as the excitation source, with repetition rates between 10 kHz and 1 MHz, and the above-mentioned R928P PMT as detector. To record the fluorescence spectra at 77 K, the samples were placed in quartz tubes (2 mm diameter) and inserted in a

special quartz Dewar filled with liquid nitrogen. To measure the fluorescence spectra at different temperatures from 77 K to 287 K, the samples were placed in quartz cuvettes in a liquid nitrogen cryostat (Oxford Instrument). All the solvents used in the preparation of the solutions for the photophysical investigations were of spectrometric grade. Experimental uncertainties are estimated to be ±10% for lifetimes and ±20% for quantum yields.

3.2.4 Fabrication of photodetectors

The ZnSe nanoplatelet powers were dispersed in toluene (10 mg mL^{-1}) with sonication (Figure A2-25). Interdigitated electrode arrays on quartz substrates were cleaned subsequently with detergent water, acetone and isopropanol for 30 minutes with sonication, then blow dried with nitrogen and treated with oxygen plasma. The size and geometry of the interdigitated electrodes are shown in Figure A2-26. 10 μL ZnSe/toluene was dropped on the cleaned interdigitated electrode and the solvent was evaporated at room temperature. The sample was then baked at 300 ℃ in nitrogen for 30 min.

3.3 Results and discussion

In comparison to the standard Schlenk techniques for the preparation of colloidal nanoparticles that require moisture- and oxygen-free environments, our synthesis of zinc chalcogenide nanoplatelets were conducted under ambient conditions using an easily accessible experimental apparatus containing a hot plate, an oil bath and a flask (Figure 3-1A, Figure A2-1a). The purification of the crude solutions (Figure 3-1B, Figure A2-1b) yields substantial amounts of dried zinc chalcogenide nanoplatelet powders, i.e. 19.9 g ZnSe (Figure 3-1C, 3-1D) and 15.9 g ZnS (Figure A2-1c, A2-1d), with yield of 71.3% for ZnSe nanoplatelets and 82.1% for ZnS nanoplatelets, which are about three orders of magnitude larger than the amount of nanoparticles obtained in a conventional synthesis (see supporting information). In these experiments, a mixture of oleylamine and a short-chain alkylamine (e.g. hexylamine, octylamine and decylamine) was used as both solvent and surfactant, which provides a mild reducing environment and ensures slow growth kinetics, making the scalable one-pot synthesis of nanoplatelets possible under ambient conditions. As shown in Figure A2-2 and A2-3, monodisperse ZnSe nanoplatelets were also obtained in the syntheses in which a variety of amines and

zinc precursors were used, demonstrating the robustness of this synthetic route (Table 3-1). Thermal gravimetric analysis-differential thermal analysis (TGA-DTA) (Figure A2-4) results reveal the amine ligands contribute approximately 49wt% of the total collected mass. This value is much higher than the ligand loss of spherical nanoparticles, which is ~20wt%.[49-51] This is because of the larger surface to volume ratio of the platelets with respects to spheres, and also because flat, extended facets of nanoplatelets can support more ligand interaction through better surface contact than curved facets in spherical particles.[52,53]

Transmission electron microscopy (TEM) images of the products show nearly monodisperse rectangular nanoplatelets with length ranging from 30 nm to 100 nm and width 4 nm to 18 nm (Figure 3-1E, 3-1H, Figure A2-5, A2-6). TEM measurements on nanoplatelets standing on their edges reveal a uniform thickness of ~1.39 nm (insets in Figure 3-1E, 3-1H). This was further confirmed by atomic force microscopy (AFM) measurement (Figure 3-1G, 3-1J, Figure A2-7). The contrast of ZnSe and ZnS nanoplatelets in high angle annular dark field-scanning transmission electron microscopy (HAADF-STEM) images is very homogenous, indicating a uniform flat rectangular shape (Figure 3-1F, 3-1I, Figure A2-5). A close inspection of some individual ZnSe nanoplatelets (Figure 3-1I, Figure A2-8) reveals evidently hollow feature and patches, indicating nanoplatelets may have formed by oriented attachment (see the following section for details).[27,47,54] STEM-energy-dispersive X-ray (EDX) element maps (Figure A2-9) of zinc chalcogenide nanoplatelets show that both Zn and chalcogens are evenly distributed throughout the structures with an approximately stoichiometric ratio (Figures A2-10−A2-12, Table 3-2), being consistent with their chemical compositions.

High-resolution TEM (HRTEM) measurements (Figure 3-1K, Figures A2-13−A2-15) show that the nanoplatelets are crystalline. Lattice plane spacings extracted from fast Fourier transform (FFT) analyses of selected areas are 0.339 nm ($10\bar{1}0$) and 0.322 nm (0002) for ZnSe (Figure 1L, Figure A2-13), and 0.317 ($10\bar{1}0$) and 0.299 nm (0002) for ZnS nanoplatelets (Figure A2-14, A2-15), typical of the wurtzite structure. Selected area electron diffraction (SAED) patterns of nanoplatelets in Figure 3-1M and Figure A2-14c show a set of well-defined rings indexed to wurtzite ZnSe and ZnS, respectively. Fourier filtering (Figure A2-16) of both ($10\bar{1}0$) and (0002) planes can be used to enhance the visibility of the platelets

against the amorphous carbon background of the TEM grid. It shows both $(10\bar{1}0)$ and (0002) planes on an individual nanoplatelet (Figure A2-16). XRD patterns of ZnSe and ZnS (Figure 3-1N) match with the wurtzite structure but clearly show a slight shift to higher angles in comparison with each standard XRD pattern. This is likely a result of the contraction of the ZnSe and ZnS lattices because of the high compressive stress, i.e. 1.38 GPa for ZnSe and 5.91 GPa for ZnS (see Supporting Information for details), exerted by surface-passivating amine ligands.[28,55] The gigapascal compressive stress exerted by surface ligands may also explain the twisting of ZnSe nanoplatelets along the long lateral direction (Figure A2-17).[56,57] The sharp feature of the (0002) plane in the XRD patterns (Figure 3-1N) indeed corroborates the lateral long-axis direction. The structural characterizations allow us to work out the schematic of a single nanoplatelet with wurtzite structure (Figure 3-1O).

The growth mechanism of zinc blende semiconductor nanoplatelets such as CdSe has been interpreted differently by several research groups, wherein lateral extension of the pre-existing seed[33,41] and intrinsic growth instability[31] have been proposed to explain the formation of anisotropic shape of nanoplatelets from the isotropic crystal structure. In wurtzite CdSe nanoplatelets, it was proposed that the platelets form by assembly/attachment of preformed clusters within the soft template lamellar structures.[28,32] We herein study the intermediate products of wurtzite ZnSe and ZnS nanoplatelets to understand how they form. When the reaction proceeds for 2 min at 150 ^{o}C, bundled ZnSe nanowires formed (Figure 3-2A). With the reaction for 4 min at 150 ^{o}C, a mixture containing fused fragmented nanowires and small lateral size ZnSe nanoplatelets came into being (Figure 3-2B). When nanoplatelets react for 30 min at 150 ^{o}C, small lateral size ZnSe is obtained (Figure 3-2C). Finally, the reaction of 2 h at 150 ^{o}C yields monodisperse ZnSe nanoplatelets (Figure 3-2D). In our experiments, we find no evidence of template growth, but a previously unknown growth mechanism is illustrated. The schematic illustration of the formation of ZnSe nanoplatelets is shown in Figure 3-2E. Initially, bundles of nanowires are formed; the bundles then fuse and fragmented, and then convert into nanoplatelets with small lateral size via monomer diffusion and reconstruction; finally, the proceeding small lateral size nanoplatelets assemble via oriented attachment into nanoplatelets.

Nanoplatelets have a giant oscillator strength transition, which will be manifested by a significantly short exciton radiative decay time.[29,58] To this end, we performed ligand exchange using tributylphosphine (TBP) or trioctylphosphine (TOP) to increase the fluorescence quantum yield by passivating the surface traps of nanoplatelets (Figure A2-18, A2-19, also see Appendix 2 for details). We synthesized alloyed $ZnS_{1-x}Se_x$ (x=0.25, 0.50) nanoplatelets to further tailor the band gap of nanoplatelets (Figure 3-3A, 3-3B), which enables tuning the fluorescent emission between 296 nm and 349 nm (Figure 3-3C, 3-3D). The absorption spectra for ZnSe and $ZnS_{0.50}Se_{0.50}$ nanoplatelets show distinct light hole-electron (lh-e) and heavy hole-electron (hh-e) transitions, typically of the electronic structure of quantum wells (Figure 3-3C). However, these transitions are not resolved for ZnS and $ZnS_{0.75}Se_{0.25}$ nanoplatelets, possibly because their small spin-orbit splitting, since the spin-orbit coupling is found to decrease with decreasing the atomic number of the chalcogens of ZnX (X=Te, Se, S).[59] This finding is in consistence with that for CdS nanoplatelets whose lh-e and hl-e transitions are also not resolved because of the small spin-orbit splitting of the valance bands.[3] The emission spectra of nanoplatelets shows extremely narrow emission bands with full-width at half-maximum (FWHM) as sharp as 90 meV for ZnSe nanoplatelets (Figure 3-3D, Table 3-3), suggesting atomically flat and extended surfaces of these quantum wells.

The fluorescence emission band of ZnSe nanoplatelets continue to shift to lower energy as the temperature decreases from room temperature to 77 K (Figure 3-3E, Figure A2-20). The fluorescence lifetimes for zinc chalcogenide nanoplatelets are ~2 ns at room temperature (Figure 3-3F) and are slightly shorter at 77 K (Figure A2-21). Such lifetimes are more than two orders of magnitude faster than that for spherical ZnSe nanoparticles[60] and are only about a half of that of CdSe nanoplatelets.[29] In addition, we have conducted additional experiment to study the effect of hollow and size feature on the PL and lifetime of the nanoplatelets. In the reaction, we took several aliquots. We checked it by UV-vis, PL, TEM and STEM measurement. In Figure A2-22b,c, the aliquot contains more bundled nanowires than small nanoplatelets. The emission is very low, originating from surface defects, and we cannot measure the lifetime of bundled nanowires. For small nanoplatelets (Figure A2-22d-f), the emission is at 361 nm, and the lifetime is 0.4 ns and 2 ns, showing a double exponential decay (inset in Figure A2-22d). In summary, the small nanoplatelets showed same order of magnitude lifetime decay, with ZnSe, ZnS, and

their alloyed structures. The extremely short fluorescence lifetimes can be attributed to the giant oscillator strength transition of quantum wells with strong spatial confined excitons.[58]

Both ZnS and ZnSe nanoplatelet powders show excellent stability and dispersity. After being kept under ambient light for 8 months, TEM measurements on the powder samples of both ZnS (Figure A2-23) and ZnSe (Figure A2-24) nanoplatelets show that the nanoplatelets retain their original morphology without any aggregation. The aged powder samples of both ZnS and ZnSe nanoplatelets can be readily dispersed into toluene solution, showing the sharp features of the absorption exciton peaks similar to the as-synthesized nanoplatelets, although a 2 nm red-shift of the first exciton peak is observed.

Photo responses to 365 nm and 254 nm UV light were studied for ZnSe nanoplatelets. Devices were prepared with interdigitated electrodes on quartz substrates according to a procedure described in the experimental section, in which ZnSe nanoplatelets were dispersed in toluene (10 mg mL^{-1}) with sonication (Figure A2-25). The size and geometry of the interdigitated electrodes are shown in Figure A2-26. A microscopic optical image of the active device area is presented in Figure 3-4A. The gap between two neighboring electrodes is 10 μm. Current-Voltage characteristics were obtained by sweeping the voltage from -100 V to 100 V at 1 V/step with and without UV light irradiation. As shown in Figure 3-4B, the device has obvious photo-induced current for both wavelengths. Figure 3-4C and 3-4D show the transient responses of the photodetector to 365 nm and 254 nm UV light, respectively. In both cases, the device currents exhibit a steep rise and fall with a response time of about 0.3 seconds (Figure A2-27a-d) upon turning on and off the UV light. The photo-induced current at 100 V is about 7 nA excited by the 365 nm UV light and about 1.5 nA by the 254 nm UV light, suggesting that the photodetector has a spectrum responsivity of about 3.5 mA W^{-1} at 365 nm and 0.6 mA W^{-1} at 254 nm, respectively. In comparison, commercial gallium phosphide (GaP)-based UV detectors have a responsivity of about 90 mA W^{-1} at 365 nm and 30 mA W^{-1} at 254 nm, respectively.[61] Nonetheless, the fabrication of the GaP UV detectors usually requires high temperature and high vacuum processes and expensive single-crystalline epitaxial substrates. The simple solution process in our ZnSe nanoplatelet UV detectors can eventually lead to scalable manufacturing of large area and low-cost devices in both rigid and flexible substrates.

3.4 Conclusions

To summarize, we have synthesized 1.4 nm atomic thick, air stable, scalable ZnSe, ZnS nanoplatelets via a one-pot heat-up method. The resulting nanoplatelets exhibit strong confinement effects as well as exceptional narrow emission spectrum with full-width at half-maximum as sharp as 90 meV and a 1.9 ns radiative fluorescent lifetime at room temperature. ZnSe nanoplatelets-based ultraviolet (UV) photodetectors has a spectrum responsivity of about 3.5 mA W^{-1} at 365 nm and 0.6 mA W^{-1} at 254 nm, respectively. This work will offer some idea on the rational synthesis of other semiconductors, providing a solid basis for the further emerging light applications.

3.5 Tables and Figures

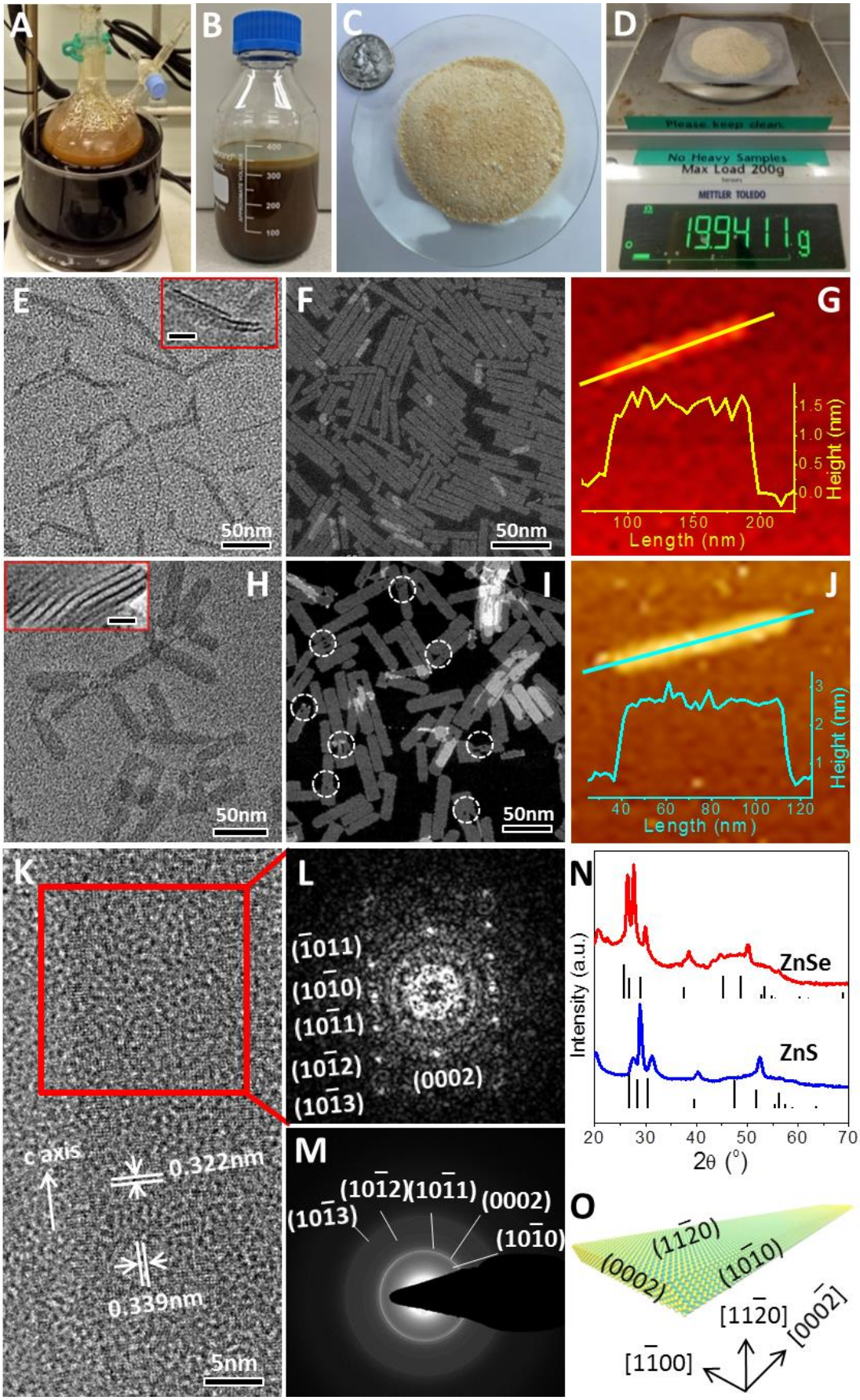

Figure 3-1. One-pot ultralarge scale synthesis under ambient conditions and structural characterizations of zinc chalcogenide nanoplatelets. Reaction setup **A**, and crude solution **B**, of ZnSe nanoplatelets. **C**,**D**, Photographs of a dried powder sample showing the Petri dish containing 19.9 g ZnSe nanoplatelets. A US quarter dollar coin is given in (C) for comparison. **E**, TEM image of ZnS nanoplatelets. **F**, HAADF-STEM image of ZnS nanoplatelets. **G**, AFM image (top) and the cross-section height analysis (bottom) along the long lateral direction of an individual ZnS nanoplatelet. **H**, TEM image of ZnSe nanoplatelets. Insets in (E, H) show nanoplatelets standing on their edges, revealing their uniform thickness of ~1.39 nm. Scale bars of Insets in (E, H) are 5 nm. **I**, HAADF-STEM image of ZnSe nanoplatelets. Hollow feature and patches of nanoplatelets are highlighted by dashed circles in (I). **J**, AFM image (top) and the cross-section height analysis (bottom) along the long lateral direction of an individual ZnSe nanoplatelet. **K**, HRTEM image of ZnSe nanoplatelets. (L, FFT image of a selected area in (K) marked by a red rectangle, revealing the crystallographic relation. The arrow in (K) indicating the orientation of the long axis of ZnSe nanoplatelets is parallel to the crystallographic *c*-axis of the wurtzite structure. **M**, SAED pattern of ZnSe nanoplatelets showing a set of distinct rings indexed to a wurtzite phase. **N**, XRD patterns of ZnSe and ZnS nanoplatelets indicating all diffraction peaks shift to high angle with respect to their respective standard XRD patterns. The standard XRD patterns for wurtzite ZnSe and ZnS are presented for reference. **O**, Schematic illustration of a single ZnSe nanoplatelet, revealing the predominant basal $(11\bar{2}0)$ facet, the side $(10\bar{1}0)$ and (0002) facets.

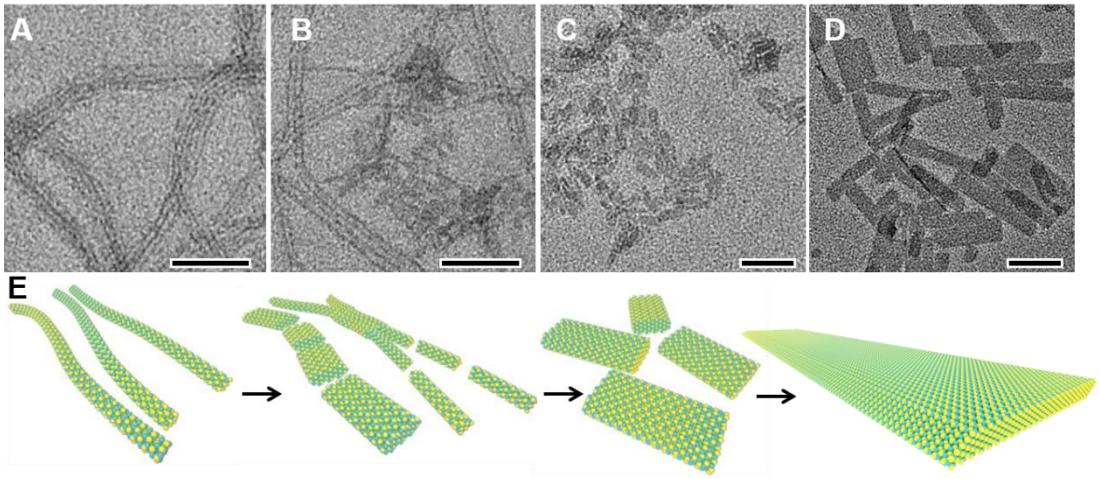

Figure 3-2. Mechanistic study of the formation of wurtzite ZnSe nanoplatelets. TEM (A-D) images. **A**, 2 min at 150 ^{o}C yielding bundled ZnSe nanowires. **B**, 4 min at 150 ^{o}C yielding a mixture containing fused fragmented nanowires and small lateral size ZnSe nanoplatelets. **C**, 30 min at 150 ^{o}C yielding small lateral size ZnSe nanoplatelets. **D**, 2 h at 150 ^{o}C yielding monodisperse ZnSe nanoplatelets. All scale bars are 50 nm. **E**, Schematic illustration of the formation of ZnSe nanoplatelets: initially, bundles of nanowires are formed; the bundles then fuse and fragmented, and then convert into nanoplatelets with small lateral size via monomer diffusion and reconstruction; finally, the proceeding small lateral size nanoplatelets assemble via oriented attachment into nanoplatelets.

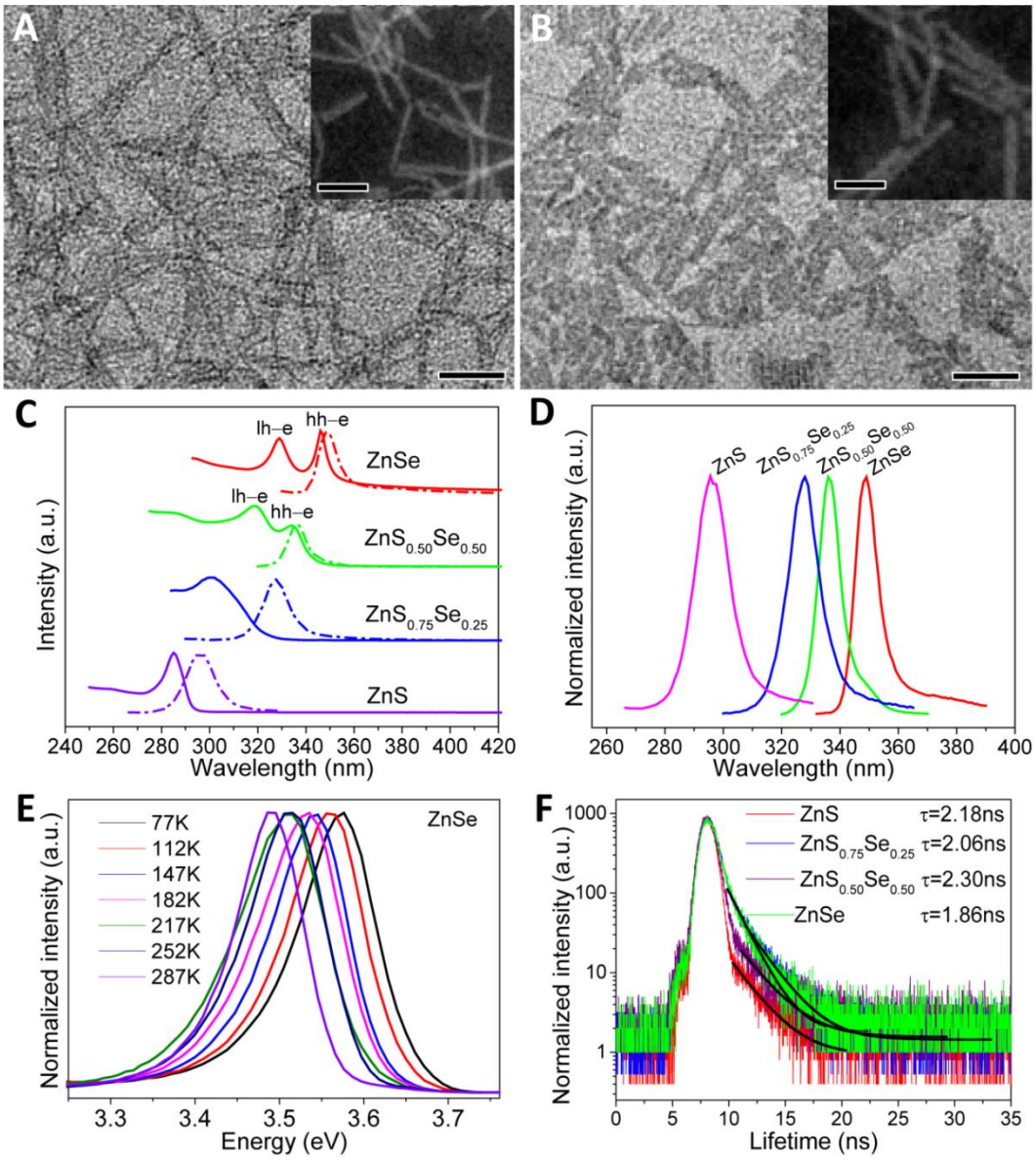

Figure 3-3. Optical spectroscopy of zinc chalcogenide nanoplatelets. A, TEM and HAADF-STEM (inset) images of $ZnS_{0.75}Se_{0.25}$ nanoplatelets. **B**, TEM and HAADF-STEM (inset) images of $ZnS_{0.50}Se_{0.50}$ nanoplatelets. All scale bars are 50 nm. **C**, Comparison of absorption (solid lines) and fluorescence emission (dash-dotted lines) spectra of zinc chalcogenide nanoplatelets. The light hole-electron and heavy hole-electron transitions are marked as lh-e and hh-e, respectively. **D**, Normalized fluorescence emission spectra of zinc chalcogenide nanoplatelets showing the tunability of the emission wavelengths from 296 nm to 349 nm. The FWHMs for ZnSe, $ZnS_{0.50}Se_{0.50}$, $ZnS_{0.75}Se_{0.25}$, and ZnS are 9 nm, 9 nm, 13 nm, and 14 nm, respectively. **E**, Normalized fluorescence emission spectra of ZnSe nanoplatelets for different temperatures. **F**, Fluorescence lifetimes of zinc chalcogenide nanoplatelets at room temperature.

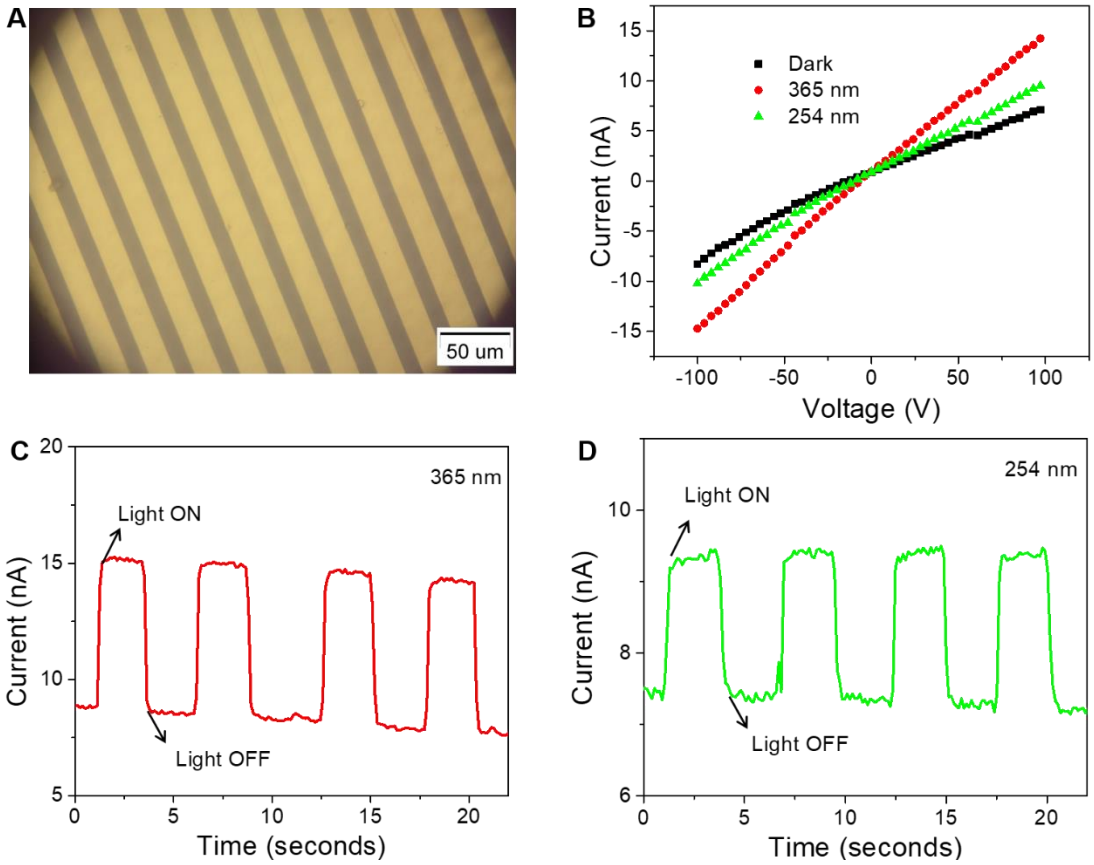

Figure 3-4. ZnSe nanoplatelet-based photodetectors. A, A microscopic image showing the active area of one photodetector. **B**, Current-Voltage characteristics of one photodetector measured at dark, with 365 nm (500 μW cm^{-2}) and 254 nm (650 μW cm^{-2}) UV light irradiation, respectively. Transient responses of the photodetector with light ON and OFF and 100 V biasing for **C**, 365 nm UV light and **D**, 254 nm UV light.

Table 3-1. Summary of the syntheses of ZnSe nanoplatelets.

Zinc Source	Primary Amines	Reaction Temperature	Reaction Time	First Exciton Peak	Thickness
$Zn(NO_3)_2$ $6H_2O$	Hexylamine	120 °C	6 h	-	-
	Octylamine	170 °C	2 min-6 h	348 nm	1.39 nm
	Decylamine	170 °C	2-6 h	348 nm	1.39 nm
	Oleylamine	170 °C	2-10 h	348 nm	1.39 nm
	Hexylamine + Oleylamine	120 °C	2-12 h	348 nm	1.39nm
	Octylamine + Oleylamine	170 °C	2 min-6 h	348 nm	1.39 nm
	Decylamine + Oleylamine	170 °C	10 min-1.5 h	348 nm	1.39 nm
$ZnCl_2$	Octylamine + Oleylamine	170 °C	2 h-6 h	348 nm	1.39 nm
$Zn(ac)_2$ $2H_2O$	Octylamine + Oleylamine	170 °C	10 min-10 h	348 nm	1.39 nm
ZnI_2	Octylamine + Oleylamine	170 °C	10 min-6 h	348 nm	1.39 nm
$ZnCl_2$ + ZnI_2	Decylamine + Oleylamine	170 °C	10 min-6 h	348 nm	1.39 nm

Note: The synthesis using hexylamine as the solvent produced white powders without any distinct absorption features associated with ZnSe.

Table 3-2. STEM-EDX spectroscopy analyses of zinc chalcogenide nanoplatelets.

Sample	Zn at%	S at%	Se at%
ZnS	47.3	52.7	
ZnSe	45.5		54.5
$ZnS_{0.75}Se_{0.25}$	58.7	28.6	12.7

Table 3-3. Optical properties of zinc chalcogenide nanoplatelets.

Sample	Exciton peak/nm		PL peak/nm	FWHM/ meV (nm)	Lifetime/ns		PLQY
	lh-e	hh-e			RT	77K	
ZnSe (Toluene +TBP)	330	349	349	90 (9)	1.86	1.76	0.03%
ZnSe (TBP)	330	349	349	90 (9)	4.25	3.00	0.73%
$ZnS_{0.50}Se_{0.50}$ (Toluene +TBP)	319	334	336	145 (9)	2.30	1.75	0.23%
$ZnS_{0.75}Se_{0.25}$ (Toluene +TBP)	-	301	328	145 (13)	2.06	1.76 (τ_1) 3.92(τ_2)	0.28%
ZnS (TOP)	-	284	296	199 (14)	2.18	2.12	-

Note: lh-e: light hole-electron; hh-e: heavy hole-electron.

The fluorescent emission lifetime curve for $ZnS_{0.75}Se_{0.25}$ (Toluene +TBP) at 77 K show a bi-exponential decay, with τ_1= 1.76 ns and τ_2=3.92 ns.

3.6 References

(1) Novoselov, K. S.; Geim, A. K.; Morozov, S. V.; Jiang, D.; Zhang, Y.; Dubonos, S. V.; Grigorieva, I. V.; Firsov, A. A. Electric Field Effect in Atomically Thin Carbon Films. *Science* **2004**, *306*, 666−669.

(2) Novoselov, K. S.; Fal′ko, V. I.; Colombo, L.; Gellert, P. R.; Schwab, M. G.; Kim, K. A Roadmap for Graphene. *Nature* **2012**, *490*, 192−200.

(3) Schwierz, F. Graphene Transistors. *Nat Nanotechnol.* **2010**, *5*, 487−496.

(4) Zhang, Y.; Tan, Y.-W.; Stormer, H. L.; Kim, P. Experimental Observation of the Quantum Hall Effect and Berry's Phase in Graphene. *Nature* **2005**, *438*, 201−204.

(5) Geim, A. K.; Novoselov, K. S. The Rising of Graphene. *Nat. Mater.* **2007**, *6*, 183−191.

(6) Nair, R. R.; Blake, P.; Grigorenko, A. N.; Novoselov, K. S.; Booth, T. J.; Stauber, T.; Peres, N. M. R.; Geim, A. K. Fine Structure Constant Defines Visual Transparency of Graphene. *Science* **2008**, *320*, 1308−1308.

(7) Zhu, Y. W. *et al.* Carbon-based Supercapacitors Produced by Activation of Graphene. *Science* **2011**, *332*, 1537−1541.

(8) Zhang, H. Ultrathin Two-Dimensional Nanomaterials. *ACS Nano* **2015**, *9*, 9451−9469.

(9) Naguib, M.; Gogotsi, Y. Synthesis of Two-Dimensional Materials by Selective Extraction. *Acc. Chem. Res.* **2015**, *48*, 128−135.

(10) Wang, X.; Kajiyama, S.; Iinuma, H.; Hosono, E.; Oro, S.; Moriguchi, I.; Okubo, M.; Yamada, A. Pseudocapacitance of MXene Nanosheets for High-Power Sodium-Ion Hybrid Capacitors. *Nat. Commun.* **2015**, *6*, 6544.

(11) Layers Najmaei, S.; Yuan, J.; Zhang, J.; Ajayan, P.; Lou, J. Synthesis and Defect Investigation of Two-Dimensional Molybdenum Disulfide Atomic Layers. *Acc. Chem. Res.* **2015**, *48*, 31−40.

(12) Tan, C. L.; Zhang, H. Two-Dimensional Transition Metal Dichalcogenide Nanosheet-Based Composites. *Chem. Soc. Rev.* **2015**, *44*, 2713−2731.

(13) Chhowalla, M.; Shin, H. S.; Eda, G.; Li, L. J.; Loh, K.; Zhang, H. The Chemistry of Two-Dimensional Transition Metal Dichalcogenide Nanosheets. *Nat. Chem.* **2013**, *5*, 263−275.

(14) Huang, X.; Zeng, Z. Y.; Zhang, H. Metal Dichalcogenide Nanosheets: Preparation, Properties and Applications. *Chem. Soc. Rev.* **2013**, *42*, 1934−1946.

(15) Lv, R.; Robinson, J. A.; Schaak, R. E.; Sun, D.; Sun, Y.; Mallouk, T. E.; Terrones, M. Transition Metal Dichalcogenides and Beyond: Synthesis, Properties, and Applications of Single- and Few-Layer Nanosheets. *Acc. Chem. Res.* **2015**, *48*, 56−64.

(16) Zhang, J.; Chen, Y.; Wang, X. Two-Dimensional Covalent Carbon Nitride Nanosheets: Synthesis, Functionalization, and Applications. *Energy Environ. Sci.* **2015**, *8*, 3092−3108.

(17) Ong, W.-J.; Tan, L.-L.; Ng, Y. H.; Yong, S.-T.; Chai, S.-P. Graphitic Carbon Nitride ($g\text{-}C_3N_4$)-Based Photocatalysts for Artificial Photosynthesis and Environmental Remediation: Are We a Step Closer to Achieving Sustainability? *Chem. Rev.* **2016**, *116*, 7159−7329.

(18) Zhi, C.; Bando, Y.; Tang, C.; Kuwahara, H.; Golberg, D. Large-Scale Fabrication of Boron Nitride Nanosheets and Their Utilization in Polymeric Composites with Improved Thermal and Mechanical Properties. *Adv. Mater.* **2009**, *21*, 2889–2893.

(19) Zhao, M.; Huang, Y.; Peng, Y.; Huang, Z.; Ma, Q.; Zhang, H. Two-dimensional Metal–Organic Framework Nanosheets: Synthesis and Applications. *Chem. Soc. Rev.* **2018**, *47*, 6267–6295.

(20) Zhao, M.; Lu, Q.; Ma, Q.; Zhang, H. Two‐Dimensional Metal-Organic Framework Nanosheets. *Small Methods* **2017**, *1*, 1600030.

(21) Evans, A. M.; Parent, L. R.; Flanders, N. C.; Bisbey, R. P.; Vitaku, E.; Kirschner, M. S.; Schaller, R. D.; Chen, L. X.; Gianneschi, N. C.; Dichtel, W. R. Seeded Growth of Single-Crystal Two-Dimensional Covalent Organic Frameworks. *Science* **2018**, *361*, 52–57.

(22) Zhan, X.; Chen, Z.; Zhang, Q. Recent Progress in Two-Dimensional COFs for Energy-Related Applications. *J. Mater. Chem. A* **2017**, *5*, 14463−14479.

(23) Wang, Q.; O'Hare, D. Recent Advances in the Synthesis and Application of Layered Double Hydroxide (LDH) Nanosheets. *Chem. Rev.* **2012**, *112*, 4124−4155.

(24) Ma, R.; Sasaki, T. Two-Dimensional Oxide and Hydroxide Nanosheets: Controllable High-Quality Exfoliation, Molecular Assembly, and Exploration of Functionality. *Acc. Chem. Res.* **2015**, *48*, 136−143.

(25) ten Elshof, J. E.; Yuan, H.; Rodriguez, P. G. Two-Dimensional Metal Oxide and Metal Hydroxide Nanosheets: Synthesis, Controlled Assembly and Applications in Energy Conversion and Storage. *Adv. Energy Mater.* **2016**, 1600355.

(26) Osadaab, M.; Sasaki, T. Exfoliated Oxide Nanosheets: New Solution to Nanoelectronics. *J. Mater. Chem.* **2009**, *19*, 2503–2511.

(27) Schliehe, C.; Juarez, B. H.; Pelletier, M.; Jander, S.; Greshnykh, D.; Nagel, M.; Meyer, A.; Foerster, S.; Kornowski, A.; Klinke, C.; Weller, H. Ultrathin PbS Sheets by Two-Dimensional Oriented Attachment. *Science* **2010**, *329*, 550–553.

(28) Son, J. S.; Wen, X.-D.; Joo, J.; Chae, J.; Baek, S.-il; Park, K.; Kim, J. H.; An, K.; Yu, J. H.; Kwon, S. G.; Choi, S.-H.; Wang, Z.; Kim, Y.-W.; Kuk, Y.; Hoffmann, R.; Hyeon, T. Large-Scale Soft Colloidal Template Synthesis of 1.4 nm Thick CdSe Nanosheets. *Angew. Chem. Int. Ed.* **2009**, *48*, 6861–6864.

(29) Ithurria, S.; Tessier, M. D.; Mahler, B.; Lobo, R. P. S. M.; Dubertret, B.; Efros, Al. L. Colloidal Nanoplatelets with Two-Dimensional Electronic Structure. *Nat. Mater.* **2011**, *10*, 936–941.

(30) Tang, Z.; Zhang, Z.; Wang, Y.; Glotzer, S. C.; Kotov, N. A. Self-Sssembly of CdTe Nanocrystals into Free-Floating Sheets. *Science* **2006**, *314*, 274–278.

(31) Riedinger, A.; Ott, F. D.; Mule, A.; Mazzotti, S.; Knüsel, P. N.; Kress, S. J. P.; Prins, F.; Erwin, S. C.; Norris, D. J. An Intrinsic Growth Instability in Isotropic Materials Leads to Quasi-Two-Dimensional Nanoplatelets. *Nat. Mater.* **2017**, *16*, 743–748.

(32) Liu, Y.-H.; Wang, F.; Wang, Y.; Gibbons, P. C.; Buhro, W. E. Lamellar Assembly of Cadmium Selenide Nanoclusters into Quantum Belts. *J. Am. Chem. Soc.* **2011**, *133*, 17005–17013.

(33) Chen, Y.; Chen, D.; Li, Z.; Peng, X. Symmetry-Breaking for Formation of Rectangular CdSe Two-Dimensional Nanocrystals in Zinc-Blende Structure. *J. Am. Chem. Soc.* **2017**, *139*, 10009–10019.

(34) Gerard, C.; Das, R.; Mahadevan, P.; Sarma, D. D. Effective Mass-Driven Structural Transition in a Mn-Doped ZnS Nanoplatelet. *J. Phys. Chem. Lett.* **2013**, *4*, 1023–1027.

(35) Grim, J. Q.; Christodoulou, S.; Di Stasio, F.; Krahne, R.; Cingolani, R.; Manna, L.; Moreels, I. Continuous-Wave Biexciton Lasing at Room Temperature Using Solution-Processed Quantum Wells. *Nat. Nanotechnol.* **2014**, *9*, 891–895.

(36) Yang, Z.; Pelton, M.; Fedin, I.; Talapin, D. V.; Waks, E. A Room Temperature Continuous-Wave Nanolaser Using Colloidal Quantum Wells. *Nat. Commun.* **2017**, *8*, 143.

(37) She, C.; Fedin, I.; Dolzhnikov, D. S.; Dahlberg, P. D.; Engel, G. S.; Schaller, R. D.; Talapin, D. V. Red, Yellow, Green, and Blue Amplified Spontaneous Emission and Lasing Using Colloidal CdSe Nanoplatelets. *ACS Nano* **2015**, *9*, 9475–9485.

(38) Rowland, C. E.; Fedin, I.; Zhang, H.; Gray, S. K.; Govorov, A. O.; Talapin, D. V.; Schaller, R. D. Picosecond Energy Transfer and Multiexciton Transfer Outpaces Auger Recombination in Binary CdSe Nanoplatelet Solids. *Nat. Mater.* **2015**, *14*, 484–489.

(39) Cho, W.; Kim, S.; Coropceanu, I.; Srivastava, V.; Diroll, B. T.; Hazarika, A.; Fedin, I.; Galli, G.; Schaller, R. D.; Talapin, D. V. Direct Synthesis of Six-Monolayer (1.9 nm) Thick Zinc-Blende CdSe Nanoplatelets Emitting at 585 nm. *Chem. Mater.* **2018**, *30*, 6957–6960.

(40) Wu, K.;Li, Q.; Jia, Y.; McBride, J. R.; Xie, Z.-X.; Lian, T. Efficient and Ultrafast Formation of Long-Lived Charge-Transfer Exciton State in Atomically Thin Cadmium Selenide/Cadmium Telluride Type-II Heteronanosheets. *ACS Nano* **2015**, *9*, 961–968.

(41) Ithurria, S.; Bousequet, G.; Dubertret, B. Continuous Transition from 3D to 1D Confinement Observed during the Formation of CdSe Nanoplatelets. *J. Am. Chem. Soc.* **2011**, *133*, 3070–3077.

(42) Baghani, E.; O'Leary, S. K.; Fedin, I; Talapin, D. V.; Pelton, M. Auger-Limited Carrier Recombination and Relaxation in CdSe Colloidal Quantum Wells. *J. Phys. Chem. Lett.* **2015**, *6*, 1032–1036.

(43) Kunneman, L. T.; Tessier, M. D.; Heuclin, H.; Dubertret, B.; Aulin, Y. V.; Grozema, F. C.; Schins, J. M.; Laurens, D. A. SiebbelesBimolecular Auger Recombination of Electron-Hole Pairs in Two-Dimensional CdSe and CdSe/CdZnS Core/Shell Nanoplatelets. *J. Phys. Chem. Lett.* **2013**, *4*, 3574−3578.

(44) Nicolosi, V.; Chhowalla, M.; Kanatzidis, M. G.; Strano, M. S.; Coleman, J. N. Liquid Exfoliation of Layered Materials. *Science* **2013**, *340*, 1226419.

(45) Koh, W-k.; Dandu, N. K.; Fidler, A. F.; Klimov, V. I.; Pietryga, J. M.; Kilina, S. V. Thickness-Controlled Quasi-Two-Dimensional Colloidal PbSe Nanoplatelets. *J. Am. Chem. Soc.* **2017**, *139*, 2152–2155.

(46) Aerts, M.; Bielewicz, T.; Klinke, C.; Grozema, F. C.; Houtepen, A. J.; Schins, J. M.; Siebbeles, L. D. A. Highly Efficient Carrier Multiplication in PbS Nanosheets. *Nat. Commun.* **2014**, *5*, 3789.

(47) Wang, Z.; Schliehe, C.; Wang, T.; Nagaoka, Y.; Cao, Y. C.; Bassett, W. A.; Wu, H.; Fan, H.; Weller, H. Deviatoric Stress Driven Formation of Large Single-Crystal PbS Nanosheet from Nanoparticles and in Situ Monitoring of Oriented Attachment. *J. Am. Chem. Soc.* **2011**, *133*, 14484–14487.

(48) Park, H.; Chung, H.; Kim, W. Synthesis of Ultrathin Wurtzite ZnSe Nanosheets. *Mater. Lett.* **2013**, *99*, 172–175.

(49) Leatherdale, C. A.; Woo, W.-K.; Mikulec, F. V.; Bawendi, M. G. On the Absorption Cross Section of CdSe Nanocrystal Quantum Dots. *J. Phys. Chem. B* **2002**, *106*, 7619–7622.

(50) Williamson, C. B.; Nevers, D. R.; Hanrath, T.; Robinson, R. D. Prodigious Effects of Concentration Intensification on Nanoparticle Synthesis: A High-Quality, Scalable Approach. *J. Am. Chem. Soc.* **2015**, *137*, 15843−15851.

(51) Tong, L.; Lu, E.; Pichaandi, J.; Cao, P.; Nitz, M.; Winnik, M. A. Quantification of Surface Ligands on $NaYF_4$ Nanoparticles by Three Independent Analytical Techniques. *Chem. Mater.* **2015**, *27*, 4899−4910.

(52) Jones, M. R.; Macfarlane, R. J.; Prigodich, A. E.; Patel, P. C.; Mirkin, C. A. Nanoparticle Shape Anisotropy Dictates the Collective Behavior of Surface-Bound Ligands. *J. Am. Chem. Soc.* **2011**, *133*, 18865–18869.

(53) Glotzer, S. C. Nanotechnology: Shape Matters. *Nature* **2012**, *481*, 450–452.

(54) Penn, R. L.; Banfield, J. F. Imperfect Oriented Attachment: Dislocation Generation in Defect-Free Nanocrystals. *Science* **1998**, *281*, 969–971.

(55) Meulenberg, R. W.; Jennings, T.; Strouse, G. F. Compressive and Tensile Stress in Colloidal CdSe Semiconductor Quantum Dots. *Phys. Rev. B* **2004**, *70*, 235311.

(56) Jana, S.; de Frutos, M.; Davidson, P.; Abécassis, B. Ligand-Induced Twisting of Nanoplatelets and Their Self-Assembly into Chiral Ribbons. *Sci. Adv.* **2017**, *3*, e1701483.

(57) G. Jia, A. Sitt, G. B. Hitin, I. Hadar, Y. Bekenstein, Y. Amit, I. Popov, U. Banin, Couples of Colloidal Semiconductor Nanorods Formed by Self-Limited Assembly. *Nat. Mater.* **2014**, *13*, 301−307.

(58) Feldmann, J.; Peter, G.; Gobel, E. O.; Dawson, P.; Moore, K.; Foxon, C.; Elliott, R. J. Linewidth Dependence of Radiative Exciton Lifetimes in Quantum Wells. *Phys. Rev. Lett.* **1987**, *59*, 2337–2340.

(59) Karazhanov, S. Zh.; Ravindran, P.; Kjekshus, A.; Fjellvåg, H.; Svensson, B. G. Electronic Structure and Optical Properties of ZnX (X=O, S, Se, Te): A Density Functional Study. *Phys. Rev. B* **2007**, *75*, 155104.

(60) Eilers, J.; van Hest, J.; Meijerink, A.; de Mello Donega, C. Unravelling the Size and Temperature Dependence of Exciton Lifetimes in Colloidal ZnSe Quantum Dots. *J. Phys. Chem. C* **2014**, *118*, 23313−23319.

(61) Bouhdada, A.; Hanzaz, M. Electrical and Optical Proprieties of Photodiodes Based on ZnSe Material. *Appl. Phys. Lett.* **2003**, *83*, 171−173.

Author contribution statement: Y.P. and G.J. conceived the original idea of this work. Y.P. conducted the experiments. L.A.G. and M.M. performed the photophysical measurements. X.S. and Z.Y. fabricated the UV photodetector devices. M.S. assisted with HRTEM measurements and structural analysis. Y.P. wrote the manuscript with support from G.J. All authors provided critical comments on the manuscript.

Chapter 4: Colloidal Two-Dimensional Monolayer MoS_2 Nanosheets for Electrocatalytic H_2 Evolution

Abstract

Nanoparticle-based electrocatalytic hydrogen generation (HER) through water-splitting devices has attracted tremendous attention. As benchmark materials, two-dimensional MoS_2 nanosheets, owing to their low hydrogen adsorption free energy, has been considered to be a promising low-cost non-precious alternative electrocatalyst for largely enhanced electrocatalytic HER. However, the lower active-edge-site density of MoS_2 has, to a large extent, limited the overall catalytic performance towards HER. Herein, we report a new colloidal strategy to improve the HER performance by increasing the edge sites via decreasing the layers of MoS_2 nanosheets to monolayer. The resulting monolayer MoS_2 nanosheets exhibited high electrochemical performance toward HER with superior catalytic activity as evidenced by small overpotentials of 179 mV in 1 M KOH at 10 mA cm^{-2}. Additionally, our method is feasible at a large scale and general for the synthesis of other two kinds of high-quality monolayer WS_2 and ReS_2 nanosheets, generating a family of metal chalcogenide nanosheets with atomic thickness. The successful synthesis of large active sites and 2H phase structure in this work will put forward a new attempt for chasing efficient electrocatalysts for high-efficient hydrogen generation.

Keywords: electrocatalysts, hydrogen evolution reaction, MoS_2, 2H, nanosheets.

4.1 Introduction

With increasing energy exhaustion and deteriorating ecological environment, clean energy, such as hydrogen production via electrochemical water splitting holds great promise for green future as the cleanest renewable energy source.[1-5]However, the imperfection of the catalysts is the main hurdle driving the electrochemical water splitting reaction for hydrogen production. Pt and Pt-based materials, can serve as ideal catalysts achieving high catalytic activities, long-term stability and low cost for the hydrogen evolution reaction (HER),[6-7] but they are precious metals and scarce to be useful for large scale practical application.

Analogous to Pt-like catalyst, molybdenum disulfide (MoS_2) nanosheets has been considered to be a promising low-cost alternative, owing to its zero free energy of H

adsorption.[8-12] Unfortunately, MoS_2 nanosheets still suffers low active-edge-site density, limiting the overall catalytic performance towards HER in terms of catalytic activity and stability. It is highly desirable, for the sake of practical applications, to design a good catalyst with increased number of catalytically active sites, substantially improving the electrochemical HER activity.

The size and structure of the catalytic material determine the number of active sites for boosting its catalytic performance. Increasing the number of catalytically active sites is also an effective way to improve the electrocatalytic properties of materials. In this regard, an important strategy to improve the catalytic activity is increasing the number of edge sites by preparing the materials into nanoscale two-dimensional (2D) nanosheets with atomic thickness, efficiently exposing under-coordinated S sites. By reducing the size and making them into 2D shapes, the number of active sites of MoS_2 can be effectively increased, and consequently the catalytic efficiency of MoS_2 can be significantly improved.

Single layer MoS_2, as with layered transition metal dichalcogenides (TMDs), can be produced via exfoliation of bulk material. However, note that for the mechanical[13-14] and chemical[15-16] exfoliation routes producing small amounts of samples, they are not suitable for facile control over thickness distribution as well as lateral dimensions and uniformity. Although chemical vapor transport (CVT),[17-18] chemical vapour deposition (CVD),[19-21] and molecular beam epitaxy (MBE),[22] are useful for large-area and high-quality atomic MoS_2 nanostructures, they may result in substrate-confined nanostructures, limiting yield and transfer capabilities. In this regard, colloidal syntheses, as one of the bottom-up approaches, in principle, are more versatile for the formation of ultrathin high-yield, tuneable, and substrate-free 2D MoS_2 nanomaterials.

Altavilla *et al.* reported a wet-chemical synthesis of single and multilayer MoS_2 nanosheets using oleylamine as the surfactant/solvent at a temperature as high as the boiling point of oleylamine, i.e. 360 ^oC.[23] Since this growth temperature for MoS_2 nanosheets is at the boiling point of the surfactant, oleylamine ligands are more liable and prone to liberate from the surfaces of the nanoparticles, which in turn, leading to extensive stacking and undefined lateral sizes of MoS_2 nanosheets. One of the main drawbacks of this synthesis is that the single layer MoS_2 nanosheets prepared at 360 ^oC will automatically convert into multilayer MoS_2 nanosheets just by increasing the reaction time, making it difficult to prepare single layer MoS_2 nanosheets exclusively.

Furthermore, the growth mechanism underpinning the formation of single layer MoS_2 nanosheets is not yet known.

Herein, we demonstrated a robust, scalable stacking-hinderable colloidal strategy to not only enable exclusive single-layer growth mode for TMDs selectively sandwiched by surfactant molecules at a temperature of well below the boiling point of oleylamine, but also regulate the synergistic structural and size modulations of the nanosheets as efficient catalysts towards water splitting for hydrogen generation. Our strategy is a general process that can be further expanded to synthesize other two types of high-quality single-layer TMDs such as WS_2 and ReS_2 nanosheets. Single-layer MoS_2 nanosheet, with increasing active-edge-site density, shows high electrochemical performance toward HER with superior catalytic activity as evidenced by small overpotentials of 179 mV in 1 M KOH at 10 mA cm^{-2}. The successful synthesis of single-layered TMDs in this work in this work will put forward a new attempt for chasing efficient photocatalysts for high-efficiency methanol decomposition for hydrogen generation.

4.2 Experimental section

4.2.1 Material synthesis

Synthesis of single-layer MoS_2 nanosheets: In a typical synthesis of single-layer MoS_2 nanosheets, ammonium tetrathiomolybdate [$(NH_4)_2MoS_4$, 4 mmol] was mixed with 7 mL of oleylamine and 8 mL of ODE in a 50 mL three neck round bottom flask. The mixture was degassed at 110 ℃ for 30 min. Then, the temperature was raised to 280 ℃ under N_2 flow, and kept at this temperature for another 5 min. The temperature was cooled down to room temperature and a 15 mL mixture of toluene/methanol = 1:1 was added. The whole resulting product was centrifuged and washed three times with a 15 mL mixture of toluene/methanol = 1:1. The products were naturally dried in the glovebox. Then, the dried products was calcined in tubular furnace at 300, 350 ℃ and 400 ℃ for 2 h in N_2 gas atmosphere (heating rate: 2 ℃ min^{-1}).

Synthesis of single-layer WS_2 nanosheets: The single-layer WS_2 nanosheets were synthesized using the same method for MoS_2 nanosheets, except that $(NH_4)_2MoS_4$ was replaced by ammonium tetrathiotungstate [$(NH_4)_2WS_4$, 4 mmol].

Synthesis of single-layer ReS_2 nanosheets: The single-layer ReS_2 nanosheets were synthesized with the same method for MoS_2 nanosheets, except that $(NH_4)_2MoS_4$

was replaced by tetrabutylammonium tetrathiorhenate(VII) [$(C_4H_9)_4$-$NReS_4$, 0.1 mmol].

4.2.2 Material characterization

XRD patterns were acquired using a X'per PRO (PANalytical) X-ray diffractometer (40 kV, 40 mA) with Cu Kα radiation (λ=1.5406 Å). UV-vis absorption spectroscopy was carried out on a Perkin Elmer Lambda 35 UV/vis spectrometer. TEM images were taken with a JEOL 2100 transmission electron microscope at an acceleration voltage of 120 kV. HAADF-STEM, HRTEM and STEM-EDX images were obtained on a FEI Titan G2 80-200 high-resolution transmission electron microscope. AFM measurements was performed on a Bruker Dimension Icon atomic force microscope with a Bruker NCHVA probe. XPS data were collected on a Kratos Axis Ultra DLD spectrometer. The binding energy scale was calibrated for each sample by setting the main line of the C 1s spectrum to 284.8 eV. Each high-resolution spectrum was fitted with a Gaussian-Lorentzian (70%-30%) line shape using a Shirley background.

4.2.3 Electrochemical measurements

The overall electrochemical measurements of MoS_2 nanosheets was evaluated in a 1.0 M KOH electrolyte on a standard three-electrode electrochemical cell system equipped with a rotating disk electrode configuration (Pine Research Instrumentation). 5 mg of MoS_2 nanosheet and 1 mg of Super P conductive carbon were mixed in 450 μL of absolute ethanol and 50 uL of 5 wt% Nafion ultrasonically to form a homogeneous catalyst suspension. A 5 μL of catalyst suspension was then loaded onto a glass carbon (GC) electrode having a diameter of 3 mm (0.196 cm^2) with catalyst loading amount of 0.255 mg cm^{-2}. The working electrode before use was polished with α-Al_2O_3 powder having a particle size of about 0.05 μm. Before the test, nitrogen was introduced into the 1.0 M KOH electrolyte in order to remove residual organic matter and ions. A glassy carbon electrode supported with catalyst serve as working electrode, a Hg/HgO electrode being used as reference electrode and a graphite rod electrode was applied as the counter electrode. All the potential values were calibrated against the reversible hydrogen electrode (RHE) using the equation: E(RHE) = E(Hg/HgO) + 0.0591 × pH + 0.098 (V). The current density (*j*) was achieved by normalizing current values measured to the geometrical surface area of the GC. The HER overpotential (η), the gap between the applied potential and the

equilibrium potential (0V vs. RHE), was calculated based on the equation: η = 0 - E(RHE)(V). The Tafel plot was acquired based on Tafel equation ($\eta = b \log |j| + a$). The HER performance tested by linear sweep voltammetry (LSV, CHI 760E bipotentiostat) at a scan rate of 5 mV s^{-1} was carried out in an argon-saturated 1.0 M KOH. The N_2 gas flow was continuously passed over the electrolyte during the test to eliminate dissolved oxygen in the electrolyte.

4.2.4 Computational methods

Calculations were performed at the density functional theory (DFT) level by using the Vienna *Ab initio* Simulations Package (VASP)[24-26] and projected augmented wave (PAW) method[27-29] (with $1s^1$, $2s^22p^2$, $2s^22p^3$, $3s^23p^4$, $4d^55s^1$ as valence electrons for H, C, N, S and Mo, respectively). The exchange-correlation interaction was treated with different approximations including the local density approximation (LDA) and the generalized gradient approximation (GGA) parameterized by Perdew, Burke and Ernzerhof (PBE).[30] van der Waals interaction was treated by employing the empirical correction of Grimme (DFT-D2).[31] The cutoff energy of plane-wave basis was set to 600 eV. Brillouin zone was sampled by using a Gamma-centred ***k***-point set of 13×13×1 for 1H-MoS_2 and similar dense k-mesh was used for other structures. The total energy was able to converge within 1 meV/atom. The energy was converged within 10^{-4} eV/cell and the force was converged to less than 0.01 eV/Å for all structure relaxations. We firstly calculated the interlayer cohesion energy of MoS_2, from $E_{coh} = \left(E_{bulk} - nE_{single}\right)/n\mathrm{A}$, where E_{bulk} is the total energy of bulk MoS_2 (space group *R3m*, No. 160), E_{single} is the total energy of single-layer MoS_2, n is the number of layers in the bulk, and A is the area of basal plane per formula. The calculated E_{coh} by different methods are plotted in Fig. 2b. Then, we investigated the adsorption of NH_3 and H_2S molecules on single-layer MoS_2 in a 2×2×1 supercell. The occupancy number is determined by the number of molecules (N) on one side of MoS_2 single layer over the number of MoS_2 formulas (four) in the supercell. For each occupancy, we considered several configurations that are likely to happen. We calculated the adsorption energy for adsorbed molecules by $E_{ads} = \left(E_{MoS_2} + NE_{molecule} - E_{(MoS_2+molecule)}\right)$, which can be converted to the cohesion energy between MoS_2 and molecules by $\mathrm{E}_{coh} = E_{ads}/4\mathrm{A}$.

4.3 Results and discussion

Synthesis and characterizations of single-layer MoS_2 nanosheets. Single-layer MoS_2 nanosheets were synthesized by a one-pot colloidal wet-chemical approach (see 4.2.1 for detailed information). The thermal decomposition of the source precursor of ammonium tetrathiomolybdate [$(NH_4)_2MoS_4$)] at 280 ℃ in the presence of octadecane (ODE) and oleylamine exclusively produced single-layer MoS_2 nanosheets (Figure 4-1a). Purification of the crude solution produced substantial amount of dried MoS_2 nanosheets, i.e. 1.26 g with a yield of >95% (Figure A3-1), which are about two orders of magnitude larger than the amount of nanoparticles obtained in a conventional colloidal synthesis. The low-magnification transmission electron microscopy (TEM) image (Figure A3-2) showed that the products were deposited on the amorphous carbon film. The 2D features of the products are able to be resolved at a larger magnification. As shown in Figure 4-1a, roselike 2D MoS_2 nanosheets with distinct ripples and corrugations were clearly observed, demonstrating their ultrathin features. TEM measurements on nanosheets standing on their edges reveal a uniform thickness of ~0.6 nm (Figure 4-1a, inset), which is consistent with the thickness of the single-layer MoS_2 nanosheets.[32] Such single-layer nanosheets intertwined into a network structure owing to their ultrathin thickness. The atomic force microscopic (AFM) measurement further confirmed their uniform thickness of 0.6 nm corresponding to single-layer MoS_2 nanosheets (Figure 4-1b, Figure A3-3).

UV-vis absorption spectroscopy was measured to correlate the optical properties to the number of layers of MoS_2 nanosheets (Figure 4-1c). The UV-vis spectra in Figure 4-1c reveals that the as-synthesized nanosheets have two absorption peaks at A (600 nm) and B (401 nm). These two absorption peaks can be attributed to the direct-gap transition between the maxima of split valence bands and the minimum of the conduction band located at the *K* point of the Brillouin zone. The absorption peak at 401 nm of the products is in good agreement of that of single-layer MoS_2 nanosheets and is significantly different from that of the three-layer (416 nm) and five-layer (424 nm) MoS_2 nanosheets.[33] The as-prepared single-layer MoS_2 nanosheets could be easily re-dispersed in a variety of organic solvents ranging from chloroform, hexane to toluene for further use (Figure 4-1c, inset).

X-ray diffraction (XRD) measurement (Figure 4-1d) confirms the 2H phase of MoS_2 (JCPDS card no. 37-1492) of the products. Two obvious peaks at 33 ° and 56 ° can be well indexed to the (100) and (110) planes of 2H MoS_2. At the same time, the disappearance of the diffraction peak at 14.4 ° of the (002) lattice plane further proves the obtained products are single-layer MoS_2 nanosheets, which is in consistent with the reported experimental results.[34,35] X-ray photoelectron spectroscopy (XPS) analysis was performed to explore the surface conditions and valence state of the single-layer MoS_2 nanosheets. The XPS survey spectrum shows that Mo and S elements coexisted in the system (Figure A3-4). The high-resolution XPS spectra of the individual Mo_{3d} and S_{2p} charge states of MoS_2 nanosheets show that the XPS spectrum of Mo_{3d} can be resolved into four peaks at around 235.4 eV, 232.5 eV, 232 eV and 229 eV, respectively (Figure 4-1e). The strongest peaks located at 232 eV and 229 eV can be assigned to Mo^{4+} $3d_{3/2}$ and Mo^{4+} $3d_{5/2}$, respectively.[36,37] As Mo^{4+} $3d_{3/2}$ and Mo^{4+} $3d_{5/2}$ of 1T phase MoS_2 show characteristic XPS peaks at 228.2 and 231.2 eV, the absence of additional peaks at above energy indicates that the prepared MoS_2 is 2H phase instead of 1T phase.[36] The peaks at 235.4 eV and 232.5 eV match well with the binding energy of Mo^{6+} 3d. The high oxidation state of Mo may be attributed to presence of MoO_3 species, which is often observed in solution prepared MoS_2 nanosheets.[38] Two peaks (Figure 4-1f) located at 162.2 eV and 163.4 eV can be assigned to S $2p_{3/2}$ and S $2p_{1/2}$ of S(-2), respectively. The XPS results confirm the formation of the 2H phase MoS_2 nanosheets in terms of XPS peak positions and shapes for both Mo and S. The elemental mapping of MoS_2 nanosheets collected from high-angle annular dark-field (HAADF)-scanning TEM (STEM) reveals the homogeneous distribution of Mo (red) and S (green) through the whole nanosheets (Figure 4-1g-i). Both STEM-EDX mapping and EDX spectrum (Figure A3-5) further confirm the co-presence of both Mo and S in the obtained samples.

Growth mechanism of single-layer MoS_2 nanosheets. In this section, we will discuss how the thermal decomposition of single source precursor of ammonium tetrathiomolybdate [$(NH_4)_2MoS_4$] produce single layer MoS_2 nanosheets in the presence of oleylamine and ODE. Previous differential thermal analysis (DTA) and thermogravimetric analysis (TGA) indicate $(NH_4)_2MoS_4$ compound may decompose under vacuum by the following equation:[39]

$$(NH_4)_2MoS_4 \rightarrow MoS_2 + NH_3 + H_2S + S$$

Although the thermal decomposition of $(NH_4)_2MoS_4$ in oleylamine and ODE solutions may be very complex, the species formed in the reaction are similar to the products of the above equation. As MoS_2 has layered structures with relatively weak interlayer van der Waals interactions, whether thermal decomposition of MoS_2 produces single-layer or multi-layer sheets will mostly likely depend on how strong of the adhesion energy among the MoS_2 layers in comparison to the adsorption energy of molecules binding on MoS_2.[40]

Possible adsorbates are the product molecules NH_3 and H_2S and the surfactant oleylamine. Since oleylamine exhibits affinity to surfaces through the $-NH_2$ functional unit, we would expect a similar surface adsorption energy for both oleylamine and NH_3. Usually it can be modelled by NH_3. We therefore, investigated the effects of adsorbates on the interlayer cohesion of MoS_2 by comparing the interlayer cohesion strength of MoS_2 with the binding strength of NH_3 and H_2S on MoS_2 (See Methods for details). The calculated E_{coh} are plotted in Figure 4-2b and 4-2c. The calculated adsorption energy per NH_3 molecule at a sparse occupancy of 25% (0.126 eV/molecule) agrees with previous data of 0.127 eV/molecule.[41] Inset in Figure 4-2c shows the obtained most stable adsorption configurations for NH_3 and H_2S molecules on single-layer MoS_2. It should be noted that the obtained most stable configurations may not be the ground-state configurations, but for the ground state, the true adsorption energy should not be lower than the calculated ones. As can be seen in Figure 4-2b and 4-2c, the interlayer cohesion is very weak for MoS_2, which can be surpassed by the adsorption of either NH_3 or H_2S molecules. The binding between molecules and MoS_2 can only be further strengthened in case of the presence of both NH_3 and H_2S. Therefore, the presence of adsorbate like NH_3, H_2S and oleylamine can hinder the stacking growth of MoS_2 layers. Therefore, we attribute the exclusive formation of single-layer MoS_2 nanosheets to the effective and efficient interaction of adsorbate molecules between the MoS_2 interlayers. Such a scenario can be illustrated by the three-dimensional representation in Figure 4-2a.

Synthesis and characterizations of single-layer WS_2 and ReS_2 nanosheets. Importantly, our synthetic approach based on the decomposition of a single precursor is widely applicable. A series of nanocrystals of monolayer WS_2 and ReS_2 nanosheets were successfully synthesized. For example, when ammonium tetrathiomolybdate [$(NH_4)_2MoS_4$] was replaced by ammonium tetrathiotungstate

[$(NH_4)_2WS_4$], single-layer WS_2 nanosheets with an average thickness of 0.6 nm (Figure 4-3a-c, Figure A3-6) were synthesized. The high-resolution TEM image (Figure A3-7) shows that a lattice fringe of 0.309 nm, which corresponds to the (004) plane of WS_2 nanosheets. The diffraction peaks in the XRD pattern at 32.7 ° and 58.4 ° correspond to (100) and (110) planes of the 2H-WS_2 nanosheets, respectively (JCPDS card no. 08-0237) (Figure 4-3d). The XRD pattern of WS_2 nanosheets shows no crystal plane diffraction peak appearance at 14.4°, illustrating there is no stack along (002) plane, and thus proving the product is single layer WS_2 nanosheets, which are in consistent with the results obtained from the TEM, STEM and AFM characterizations (Figure 4-3a-c). The UV-vis absorption spectrum (Figure A3-8) does not show any obvious peak at 607 nm, which is in consistence with the previous results on single-layer WS_2 nanosheets.[42,43] The XPS survey scan (Figure A3-9), EDX spectrum (Figure A3-10) and STEM-EDX mapping (Figure A3-11) of the as-prepared nanosheets show W and S co-exist in the obtained nanosheets. Figure 4-3e and 4-3f show the high-resolution Mo 3d and S 2p XPS spectra of the single-layer WS_2 nanosheets. The characteristic W 4f energy peaks of the prepared single-layer WS_2 nanosheets are shown in Figure 4-3e. The presence of two characteristic peaks at 35.5 eV and 33.3 eV which correspond to $4f_{5/2}$ and W $4f_{7/2}$ of W^{4+}, respectively, confirm the formation of 2H-WS_2, as they are different from the characteristic peaks at 34 eV and 32 eV of 1T-WS_2. In addition, the XPS spectrum shows two weak peaks at ~36.3 eV and 39.2 eV, which can be assigned to the W-O species. The XPS peaks at 163.3 eV and 162.1 eV correspond to S $2p_{1/2}$ and S $2p_{3/2}$ respectively, of S (-2) (Figure 4-3f).[44]

Similarly, when single precursors such as tetrabutylammonium tetrathiorhenate(VII) [$(C_4H_9)_4$-$NReS_4$] were thermal decomposed in solutions containing oleylamine and ODE, the single-layer ReS_2 nanosheets (Figure 4-3g-l, Figures A3-12−A2-15) were also synthesized via the one-pot process, demonstrating the generality of this synthetic approach.

The as-prepared MoS_2 nanosheets are evaluated as electrocatalysts for HER in both acidic and basic aqueous solutions. During the HER test, we used a standard three-electrode electrochemical test system to evaluate the HER catalytic activity of the MoS_2 nanosheets (300 °C) at a N_2-saturated 0.5 M H_2SO_4 electrolyte. We also tested the electrocatalytic activity of a bare glassy carbon (GC) electrode without MoS_2 nanosheets as a comparative reference. Detailed measurements can be seen in

the section 4.2.3. All catalyst solutions were deposited and loaded on a glassy carbon electrode (diameter ca. 3 mm) for testing (loading amount of 0.255 mg cm^{-2}). The polarization curve of the sample in 0.5 M H_2SO_4 acid electrolyte is shown in Figure 4-4, and pure GC electrode exhibits poor HER activity. The HER catalytic activity of MoS_2 nanosheets is much better than that of GC electrode without catalyst but far away from satisfactory results.

Then we checked the HER activity of MoS_2 nanosheets in alkaline 1 M KOH electrolyte. The LSV plot of MoS_2 nanosheets obtained at different calcination temperatures (300 ^oC, 350 ^oC, 400 ^oC), denoted as MoS_2-300, MoS_2-350 and MoS_2-400, respectively, is shown in Figure 4.5a. As the calcination temperature increases MoS_2-400 exhibits the best HER catalytic activity. The overpotential is only 179 mV at the current density is below 10 mA cm^{-2}. Figure 4.5b shows Tafel plots of corresponding MoS_2-300, MoS_2-350 and MoS_2-400 electrocatalysts derived from the early stages of HER polarization curves. As shown in Figure 4.5b, MoS_2-300, MoS_2-350 and MoS_2-400 achieve similar Tafel slope of 110 mV per decade, confirming there was no significant change in the mechanism of HER reaction for three kinds of nanosheets-like electrocatalyst. We compared our materials to some of the other MoS_2-based catalysts in Table 4-1. From the table we can find that our samples show excellent HER catalytic activity. The high catalytic activity of MoS_2 nanosheets can be attributed to the facilitated electron transport by the removal of surface ligands.

4.4 Conclusions

In summary, we suggest that synergistic structural and size modulations of the MoS_2 nanosheets serve as an efficient strategy to improve the HER catalytic activity. The as-prepared single layer MoS_2 nanosheets consist of increasing active-edge-site density. Benefiting from the desirable nanostructure, these single layer MoS_2 nanosheets exhibit remarkable electrocatalytic activity for HER in basic solutions. Additionally, our method is scalable and general for the synthesis of WS_2 and ReS_2 nanosheets, generating a family of metal chalcogenide nanosheets with atomic thickness. This design opens up a new feasible and scalable avenue producing ultrathin single-layer nanosheet as a promising low-cost and high-performance catalyst for optimization of electrocatalytic activity for hydrogen production.

4.5 Tables and Figures

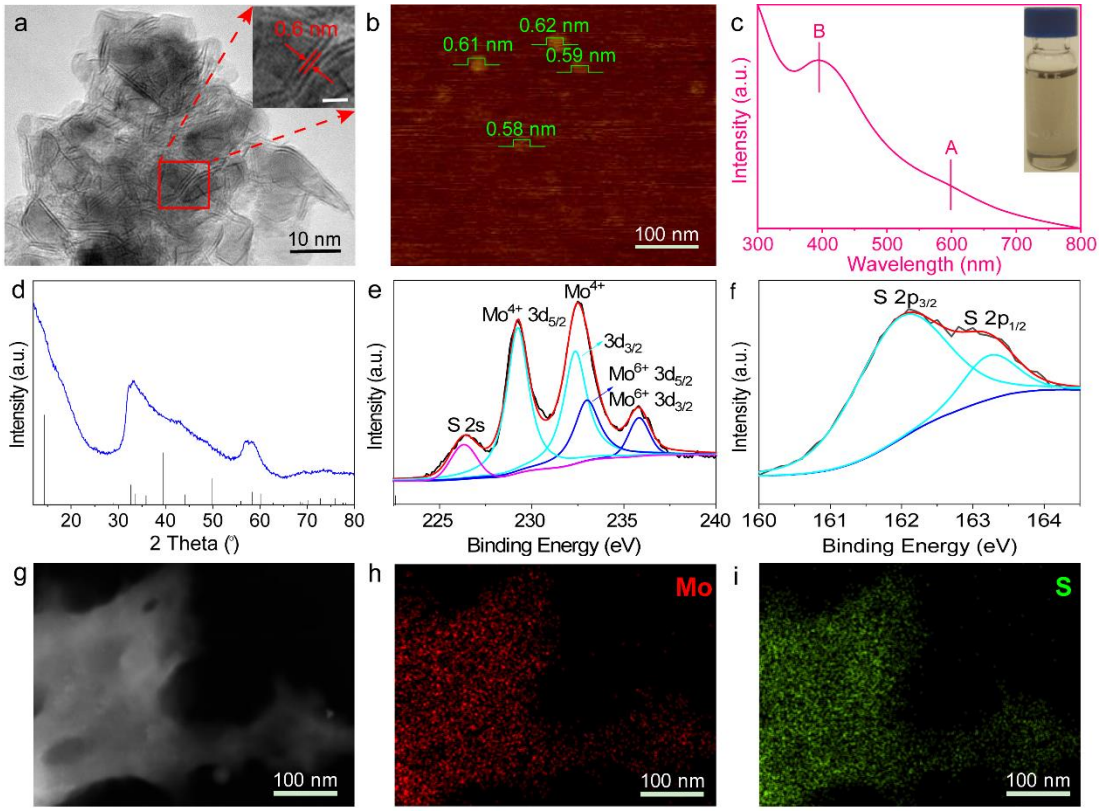

Figure 4-1. Characterizations of single-layer MoS_2 nanosheets. a, The high-magnification TEM image of single-layer MoS_2 nanosheets. Inset: Zoom in TEM image showing the thickness of MoS_2 nanosheets. Scale bar: 2 nm. **b**, AFM image shows the thickness of a single layer MoS_2 nanosheet. **c,** UV-vis absorption spectrum of single-layer MoS_2 nanosheets. Inset: Photograph of as-synthesized MoS_2 nanosheets dissolved in chloroform. **d**, XRD pattern of single-layer MoS_2 nanosheets assembled on a Si wafer. **e,f**, XPS spectra of (e) Mo_{3d}, and (f) S_{2p} of MoS_2 nanosheets. **g**, HAADF-STEM image of MoS_2 nanosheets. **h,i**, STEM-EDS elemental mapping of (h) Mo and (i) S of as-synthesized MoS_2 nanosheets.

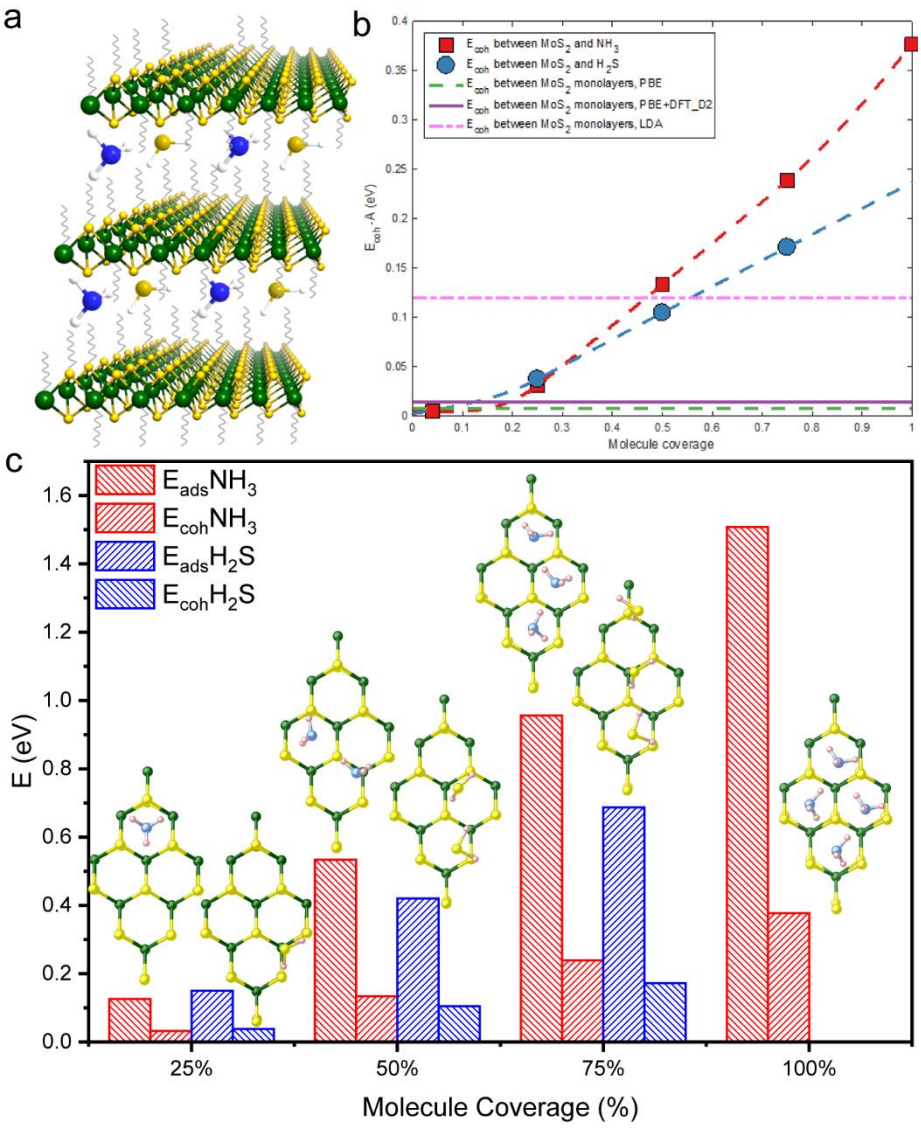

Figure 4-2. Growth mechanism of single-layer MoS_2 nanosheets. a, Three-dimensional representation of NH_3 and H_2S molecular intercalated between 3-layer MoS_2 nanosheets. **b**, Interlayer cohesion energy (E_{coh}) in bulk MoS_2 (*R3m*) and between single-layer MoS_2 nanosheets and molecules. A is the area of basal plane. Data at 4% is from the reference.[41] **c**, The converted cohesion energy (E_{coh}) and the adsorption energy (E_{ads}) for NH_3 and H_2S on basal plane of single-layer MoS_2 nanosheets with different molecule coverage. Inset: Configurations of NH_3 and H_2S molecules adsorbed on single-layer MoS_2 nanosheets. Mo, S, N and H are represented by green, yellow, blue and pink balls, respectively.

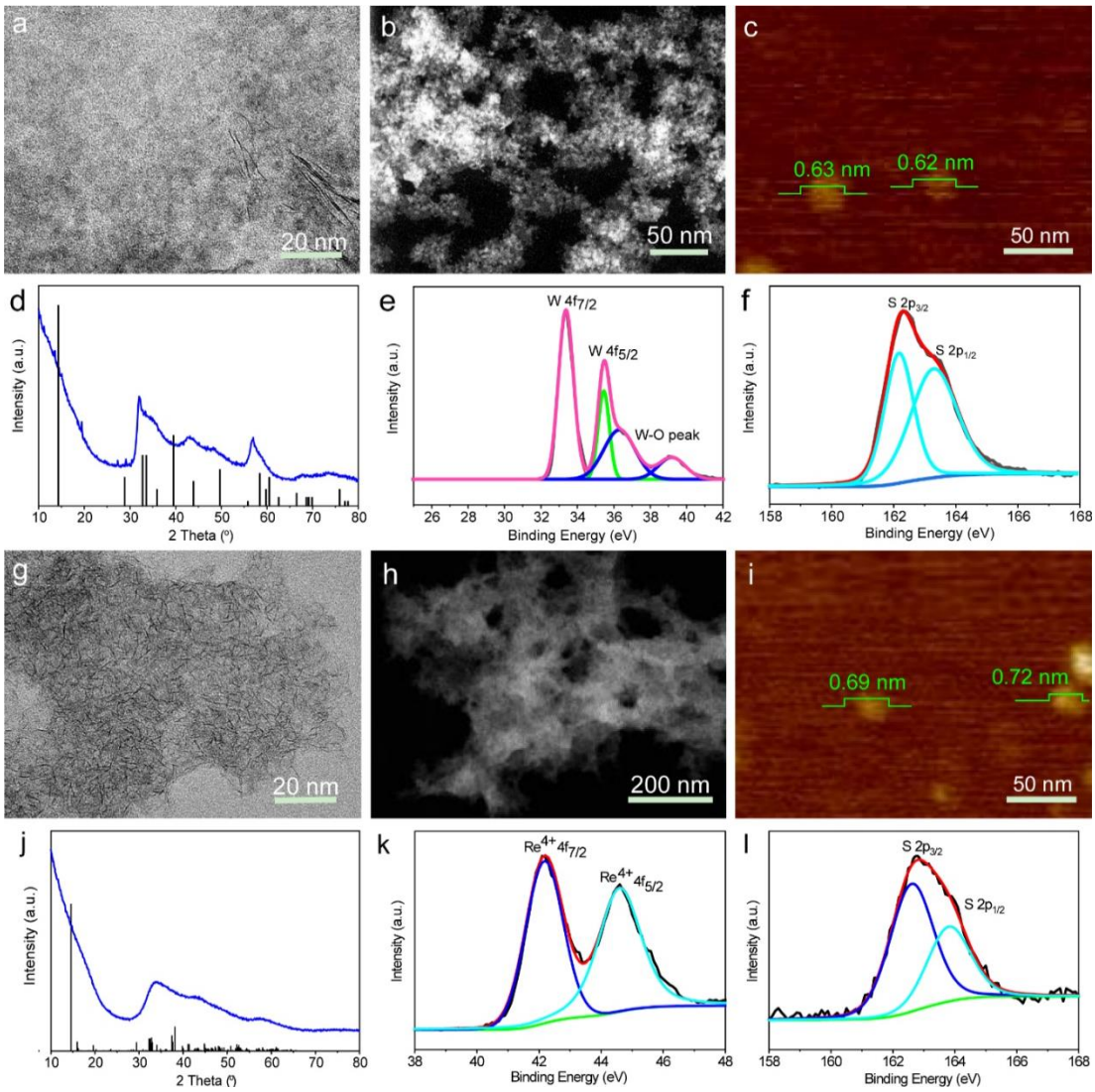

Figure 4-3. Characterizations of single-layer WS_2 and ReS_2 nanosheets. a, The high-magnification TEM image of WS_2 nanosheets. **b,** STEM image of WS_2 nanosheets. **c,** AFM image shows the thickness of a single layer WS_2 nanosheet. **d,** XRD pattern of WS_2 nanosheets assembled on a Si wafer. **e,f,** XPS spectra of (e) W_{4f}, and (f) S_{2p} of WS_2 nanosheets. **g,** The high-magnification TEM image of ReS_2 nanosheets. **h,** STEM image of ReS_2 nanosheets. **i,** AFM image showing the thickness of a single layer ReS_2 nanosheet. **j,** XRD pattern of ReS_2 nanosheets assembled on a Si wafer. **k,l,** XPS spectra of (k) Re_{4f}, and (l) S_{2p} of ReS_2 nanosheets.

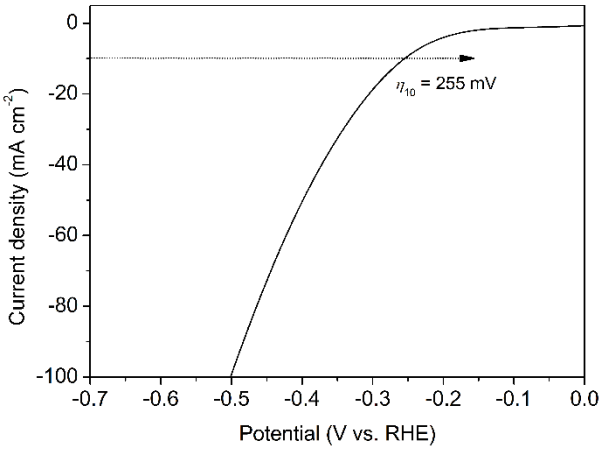

Figure 4-4. HER polarization curve of monolayer MoS_2 nanosheets in 0.5 M H_2SO_4.

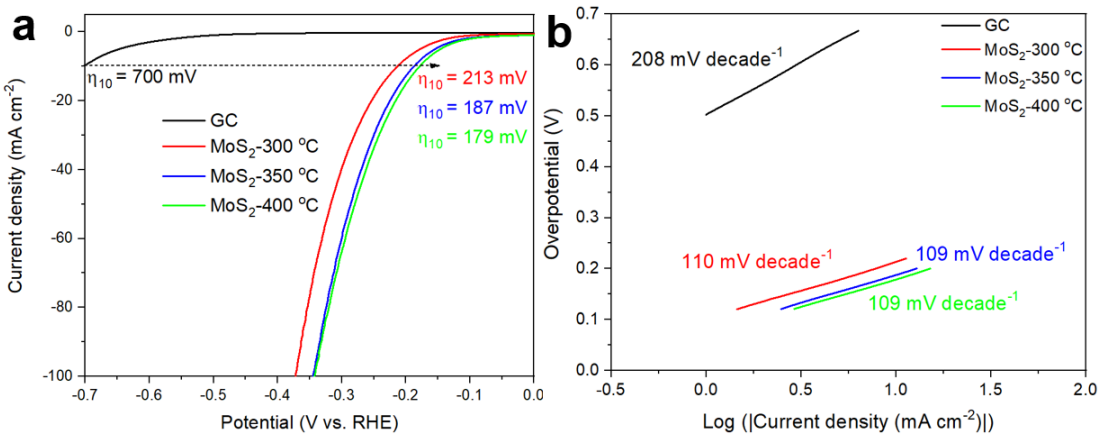

Figure 4-5. HER performance of MoS_2-300, MoS_2-350 and MoS_2-400 nanosheets in 1.0 M KOH. a, Polarization curves at 5 mV s^{-1}. **b**, Tafel plots of the corresponding electrocatalysts derived from the early stages of HER polarization curves.

Table 4-1. Summary of alkaline HER activity (in 1 M KOH) of MoS_2 catalysts reported in previous literature.

Entry	Catalyst	Overpotential at 10 mA cm^{-2}	Tafel slope	Ref.
1	MoS_2	370	124	[45]
2	in‐plane 1T–2H MoS_2	~280 320 at 20 mA cm^{-2}	65	[46]
3	Edge-terminated and interlayer-expanded MoS_2 (R-MoS_2)	111	105	[47]
4	MoS_2/CC	187	145	[48]
5	defect-rich MoS_2 (GC)	189	98	[49]
6	2D MoS_2 (GC)	95	68	[50]
7	MoS_2	308	201	[51]
8	n-type MoS_2 single crystal	760	(1M NaOH)	[52]
9	3D macroporous MoS_2 thin film on Mo foil (MoS_2/Mo)	184	87	[53]
10	MoS_2 nanosheet-300 ^oC	213	110	This work
11	MoS_2 nanosheet-350 ^oC	187	109	This work
12	MoS_2 nanosheet-400 ^oC	179	109	This work

4.6 References

(1) Lewis, N. S.; Nocera, D. G. Powering the Planet: Chemical Challenges in Solar Energy Utilization. *Proc. Natl Acad. Sci. USA* **2006**, *103*, 15729−17573.

(2) Walter, M. G.; Warren, E. L.; McKone, J. R.; Boettcher, S. W.; Mi, Q.; Santori, E. A.; Lewis, N. S. Solar Water Splitting Cells. *Chem. Rev.* **2010**, *110*, 6446−6473.

(3) Cook, T. R.; Dogutan, D. K.; Reece, S. Y.; Surendranath, Y.; Teets, T. S.; Nocera, D. G. Solar Energy Supply and Storage for the Legacy and Nonlegacy Worlds. *Chem. Rev.* **2010**, *110*, 6474−6502.

(4) Dresselhaus, M. S.; Thomas, I. L. Alternative Energy Technologies. *Nature* **2001**, *414*, 332−337.

(5) Turner, J. A. Sustainable Hydrogen Production. *Science* **2004**, *305*, 972−974.

(6) Kye, J.; Shin, M.; Lim, B.; Jang, J.-W.; Oh, I.; Hwang, S. Platinum Monolayer Electrocatalyst on Gold Nanostructures on Silicon for Photoelectrochemical Hydrogen Evolution. *ACS Nano* **2013**, *7*, 6017−6023.

(7) Gray, H. B. Powering the Planet with Solar Fuel. *Nat. Chem.* **2009**, *1*, 7.

(8) Laursen, A. B.; Kegnæs, S.; Dahl, S.; Chorkendorff, I. Molybdenum Sulfides—Efficient and Viable Materials for Electro- and Photoelectrocatalytic Hydrogen Evolution. *Energy Environ. Sci.* **2012**, *5*, 5577−5591.

(9) Voiry, D.; Yamaguchi, H.; Li, J.; Silva, R.; Alves, D. C. B.; Fujita, T.; Chen, M.; Asefa, T.; Shenoy, V. B.; Eda, G.; Chhowalla, M. Enhanced Catalytic Activity in Strained Chemically Exfoliated WS_2 Nanosheets for Hydrogen Evolution. *Nat. Mater.* **2013**, *12*, 850−855.

(10) Merki, D.; Hu, X. Recent Developments of Molybdenum and Tungsten Sulfides as Hydrogen Evolution Catalysts. *Energy Environ. Sci.* **2011**, *4*, 3878−3888.

(11) Kibsgaard, J.; Jaramillo, T. F.; Besenbacher, F. Building an Appropriate Active-Site Motif into a Hydrogen-Evolution Catalyst with Thiomolybdate $[Mo_3S_{13}]^{2-}$ Clusters. *Nat. Chem.* **2014**, *6*, 248−253.

(12) Kibsgaard, J.; Chen, Z.; Reinecke, B. N.; Jaramillo, T. F. Engineering the Surface Structure of MoS_2 to Preferentially Expose Active Edge Sites for Electrocatalysis. *Nat. Mater.* **2012**, *11*, 963−969.

(13) Larentis, S.; Fallahazad, B.; Tutuc, E. Field-Effect Transistors and Intrinsic Mobility in Ultra-Thin $MoSe_2$ Layers. *Appl. Phys. Lett.* **2012**, *101*, 223104.

(14) Tongay, S.; Zhou, J.; Ataca, C.; Liu, J.; Kang, J. S.; Matthews, T. S.; You, L.; Li, J.; Grossman, J. C.; Wu, J. Broad-Range Modulation of Light Emission in Two-Dimensional Semiconductors by Molecular Physisorption Gating. *Nano Lett.* **2013**, *13*, 2831−2836.

(15) Bissessur, R.; Xu, H., Nanomaterials Based on Molybdenum Diselenide. *Mater. Chem. Phys.* **2009**, *117*, 335−337.

(16) Zheng, J.; Zhang, H.; Dong, S.; Liu, Y.; Tai Nai, C. N.; Suk Shin, H. S.; Jeong, H. Y.; Liu, B.; Loh, K. P. High Yield Exfoliation of Two-Dimensional Chalcogenides Using Sodium Naphthalenide. *Nat. Commun.* **2014**, *5*, 2995.

(17) Kong, D.; Wang, H.; Cha, J. J.; Pasta, M.; Koski, K. J.; Yao, J.; Cui, Y. Synthesis of MoS_2 and $MoSe_2$ Films with Vertically Aligned Layers. *Nano Lett.* **2013**, *13*, 1341−1347.

(18) Wang, H.; Kong, D.; Johanes, P.; Cha, J. J.; Zheng, G.; Yan, K.; Liu, N.; Cui, Y. $MoSe_2$ and WSe_2 Nanofilms with Vertically Aligned Molecular Layers on Curved and Rough Surfaces. *Nano Lett.* **2013**, *13*, 3426−3433.

(19) Lu, X.; Utama, M. I. B.; Lin, J.; Gong, X.; Zhang, J.; Zhao, Y.; Pantelides, S. T.; Wang, J.; Dong, Z.; Liu, Z.; Zhou, W.; Xiong, Q. Large-Area Synthesis of Monolayer and Few-Layer $MoSe_2$ Films on SiO_2 Substrates. *Nano Lett.* **2014**, *14*, 2419−2425.

(20) Wang, X.; Gong, Y.; Shi, G.; Chow, W. L.; Keyshar, K.; Ye, G.; Vajtai, R.; Lou, J.; Liu, Z.; Ringe, E.; Tay, B. K.; Ajayan, P. M. Chemical Vapor Deposition Growth of Crystalline Monolayer $MoSe_2$. *ACS Nano* **2014**, *8*, 5125−5131.

(21) Zhang, W.; Huang, Z.; Zhang, W.; Li, Y. Two-Dimensional Semiconductors with Possible High Room Temperature Mobility. *Nano Research* **2014**, *7*, 1731−1737.

(22) Zhang, Y.; Chang, T.-R.; Zhou, B.; Cui, Y.-T.; Yan, H.; Liu, Z.; Schmitt, F.; Lee, J.; Moore, R.; Chen, Y.; Lin, H. Jeng, H.-T.; Mo, S.-K.; Hussain, Z.; Bansil, A.; Shen, Z.-X. Direct Observation of the Transition from Indirect to Direct Bandgap in Atomically Thin Epitaxial $MoSe_2$. *Nat. Nanotechnol.* **2013**, *9*, 111−115.

(23) Altavilla, C.; Sarno, M.; Ciambelli, P. A Novel Wet Chemistry Approach for the Synthesis of Hybrid 2D Free-Floating Single or Multilayer Nanosheets of MS_2@oleylamine (M=Mo, W). *Chem. Mater.* **2011**, *23*, 3879–3885.

(24) Tsai, C.; Abild-Pedersen, F.; Nørskov, J. K. Tuning the MoS_2 Edge-Site Activity for Hydrogen Evolution via Support Interactions. *Nano Lett.* **2014**, *14*, 1381−1387.

(25) Kresse, G.; Joubert, D. From Ultrasoft Pseudopotentials to the Projector Augmented-Wave Method. *Phys. Rev. B* **1999**, *59*, 1758−1775.

(26) Blöchl, P. E. Projector Augmented-Wave Method. *Phys. Rev. B* **1994**, *50*, 17953−17979.

(27) Kresse, G.; Furthmüller, J. Efficiency of Ab-initio Total Energy Calculations for Metals and Semiconductors Using a Plane-Wave Basis Set. *Comput. Mater. Sci.* **1996**, *6*, 15−50.

(28) Kresse, G.; Furthmüller, J. Efficient Iterative Schemes for Ab Initio Total-Energy Calculations Using a Plane-Wave Basis Set. *Phys. Rev. B* **1996**, *54*, 11169−11186.

(29) Kresse, G.; Hafner, J. Ab Initio Molecular Dynamics for Open-Shell Transition Metals. *Phys. Rev. B* **1993**, *48*, 13115−13118.

(30) Perdew, J. P.; Burke, K.; Ernzerhof, M. Generalized Gradient Approximation Made Simple. *Phys. Rev. Lett.* **1996**, *77*, 3865−3868.

(31) Grimme, S. Semiempirical GGA-Type Density Functional Constructed with a Long-Range Dispersion Correction. *J. Comput. Chem.* **2006**, *27*, 1787−1799.

(32) Böker, T.; Severin, R.; Müller, A.; Janowitz, C.; Manzke, R.; Voß, D.; Krüger, P.; Mazur, A.; Pollmann, J. Band Structure of MoS_2, $MoSe_2$, and α-$MoTe_2$: Angle-Resolved Photoelectron Spectroscopy and Ab Initio Calculations. *Phys. Rev. B* **2001**, *64*, 235305.

(33) Zhou, M.; Zhang, Z.; Huang, K.; Shi, Z.; Xie, R.; Yang, W. Colloidal Preparation and Electrocatalytic Hydrogen Production of MoS_2 and WS_2 Nanosheets with Controllable Lateral Sizes and Layer Numbers. *Nanoscale* **2016**, *8*, 15262−15272.

(34) Jung, W.; Lee, S.; Yoo, D.; Jeong, S.; Miró, P.; Kuc, A.; Heine, T.; Cheon, J., Colloidal Synthesis of Single-Layer MSe_2 (M = Mo, W) Nanosheets via Anisotropic Solution-Phase Growth Approach. *J. Am. Chem. Soc.* **2015**, *137*, 7266−7269.

(35) Guan, G.; Zhang, S.; Liu, S.; Cai, Y., Low, M., Teng, C. P.; Phang, I. Y.; Cheng, Y.; Duei, K. L.; Srinivasan, B. M.; Zheng, Y.; Zhang, Y.-W.; Han, M.-Y.

Protein Induces Layer-by-Layer Exfoliation of Transition Metal Dichalcogenides. *J. Am. Chem. Soc.* **2015**, *137*, 6152−6155.

(36) Yin, Y.; Han, J.; Zhang, Y.; Zhang, X.; Xu, P.; Yuan, Q.; Samad, L.; Wang, X.; Wang, Y.; Zhang, Z. Zhang, P.; Cao, X.; Song, B.; Jin, S. Contributions of Phase, Sulfur Vacancies, and Edges to the Hydrogen Evolution Reaction Catalytic Activity of Porous Molybdenum Disulfide Nanosheets. *J. Am. Chem. Soc.* **2016**, *138*, 7965–7972.

(37) Liu, Y.; Yu, Y-X.; Zhang, W-D. MoS_2/CdS Heterojunction with High Photoelectrochemical Activity for H_2 Evolution under vVisible Light: The Role of MoS_2. *J. Phys. Chem. C* **2013**, *117*, 12949–12957.

(38) Weber, T.; Muijsers, J. C.; van Wolput, J. H. M. C.; Verhagen, C. P. J.; Niemantsverdriet, J. W. Basic Reaction Steps in the Sulfidation of Crystalline MoO_3 to MoS_2, as Studied by X-Ray Photoelectron and Infrared Emission Spectroscopy. *J. Phys. Chem.* **1996**, *100*, 14144−14150.

(39) Prasad, T.P.; Diemann, E.; Müller, A. Thermal decomposition of $(NH_4)_2MoO_2S_2$, $(NH_4)_2MoS_4$, $(NH_4)_2WO_2S_2$ and $(NH_4)_2WS_4$. *J. Inorg. Nucl. Chem.* **1973**, *35*, 1895−1904.

(40) Li, Y., Li, Y-L., Sa, B. & Ahuja R. Review of two-dimensional materials for photocatalytic water splitting from a theoretical perspective. *Catal. Sci. Technol.* **27**, 545−559 (2017).

(41) Zhao, S., Xue, J. & Kang, W. Gas Adsorption on MoS_2 Monolayer from First-Principles Calculations. *Chem. Phys. Lett.* **2014**, *595−596*, 35−42.

(42) Wang, H.; Yuan, H.; Hong, S. S.; Li, Y.; Cui, Y. Physical and Chemical Tuning of Two-Dimensional Transition Metal Dichalcogenides. *Chem. Soc. Rev.* **2015**, *44*, 2664−2680.

(43) Zeng, H.; Cui, X. An Optical Spectroscopic Study on Two-Dimensional Group-VI Transition Metal Dichalcogenides. *Chem. Soc. Rev.* **2015**, *44*, 2629−2642.

(44) Mahler, B.; Hoepfner, V.; Liao, K.; Ozin, G. A. Colloidal Synthesis of 1T-WS_2 and 2H-WS_2 Nanosheets: Applications for Photocatalytic Hydrogen Evolution. *J. Am. Chem. Soc.* **2014**, *136*, 14121−14127.

(45) Zhao, G.; Lin, Y.; Rui, K.; Zhou, Q.; Chen, Y.; Dou, S. X.; Sun, W. Epitaxial Growth of $Ni(OH)_2$ Nanoclusters on MoS_2 Nanosheets for Enhanced Alkaline Hydrogen Evolution Reaction. *Nanoscale* **2018**, *10*, 19074−19081.

(46) Wang, S.; Zhang, D.; Li, B.; Zhang, C.; Du, Z.; Yin, H.; Bi, X.; Yang, S. Ultrastable in-Plane 1T–2H MoS_2 Heterostructures for Enhanced Hydrogen Evolution Reaction. *Adv. Energy Mater.* **2018**, *8*, 1801345.

(47) Anjum, M. A. R.; Jeong, H. Y.; Lee, M. H.; Shin, H. S.; Lee, J. S. Efficient Hydrogen Evolution Reaction Catalysis in Alkaline Media by All-in-One MoS_2 with Multifunctional Active Sites. *Adv. Mater.* **2018**, *30*, 1707105.

(48) Liu, J.; Wang, J.; Zhang, B.; Ruan, Y.; Wan, H.; Ji, X.; Xu, K.; Zha, D.; Miao, L.; Jiang, J. Mutually Beneficial Co_3O_4@MoS_2 Heterostructures as a Highly Efficient Bifunctional Catalyst for Electrochemical Overall Water Splitting. *J. Mater. Chem. A* **2018**, *6*, 2067−2072.

(49) Zhang, L.-F.; Ke, X.; Ou, G.; Wei, H.; Wang, L.-N.; Wu, H. Defective MoS_2 Electrocatalyst for Highly Efficient Hydrogen Evolution through a Simple Ball-Milling Method. *Sci. China Mater.* **2017**, *60*, 849−856.

(50) Kong, X.; Shen, X.; Zhang, C.; Oliaee, S. N.; Peng, Z. Engineering Active Sites of Two-Dimensional MoS_2 Nanosheets for Improving Hydrogen Evolution. *Inorg. Chem. Front.* **2016**, *3*, 1376−1380.

(51) Zhang, J.; Wang, T.; Liu, P.; Liu, S.; Dong, R.; Zhuang, X.; Chen, M.; Feng, X. Engineering Water Dissociation Sites in MoS_2 Nanosheets for Accelerated Electrocatalytic Hydrogen Production. *Energy Environ. Sci.* **2016**, *9*, 2789−2793.

(52) Wiensch, J. D.; John, J.; Velazquez, J. M.; Torelli, D. A.; Pieterick, A. P.; McDowell, M. T.; Sun, K.; Zhao, X.; Brunschwig, B. S.; Lewis, N. S. Comparative Study in Acidic and Alkaline Media of the Effects of pH and Crystallinity on the Hydrogen-Evolution Reaction on MoS_2 and $MoSe_2$. *ACS Energy Lett.* **2017**, *2*, 2234−2238.

(53) Pu, Z.; Liu, Q.; Asiri, A. M.; Luo, Y.; Sun, X.; He, Y. 3D Macroporous MoS_2 Thin Film: In Situ Hydrothermal Preparation and Application as a Highly Active Hydrogen Evolution Electrocatalyst at All pH Values. *Electrochim. Acta* **2015**, *168*, 133−138.

Author contribution statement: G. J. and Y.P. conceived the project, designed the experiments and G. J. supervised the research. Y.P. conducted synthesis, materials characterization and analysis. X.X. performed the HER testing. Y.L. performed the DFT simulations. A.S. and M.S assisted with HRTEM measurements and structural

analysis. Y.P., G.J. and Y.L. wrote the manuscript. All authors discussed the data, mechanisms, and commented on the manuscript.

Every reasonable effort has been made to acknowledge the owners of copyright material. I would be pleased to hear from any copyright owner who has been omitted or incorrectly acknowledged.

Chapter 5: Conclusions and Recommendations

5.1 Conclusions

In this thesis, we mainly focus on 2D atomic-thick metal chalcogenide nanomaterials. A series of 2D metal chalcogenides, including ZnS, ZnSe, MoS_2, WS_2 and ReS_2, were synthesized and their intrinsic properties or potential applications in photodetection and HER were also systematically investigated.

The conclusion for each chapter is summarized as follows:

Firstly, Chapter 1 gives an overview of the state-of-the-art of 2D metal chalcogenide nanomaterials in terms of their synthetic methods and characterization means. The applications ranging from electronic/optoelectronic devices, electrocatalysis, and batteries to sensing were emphasized as well.

Secondly, Chapter 2 offers an idea why these 2D ZnSe, ZnS, ZnTe and CdTe nanoplatelets have a uniform thickness of 1.4 nm, being of 8 layers. We conducted corresponding experiments coupled with DFT calculation to certify this idea. The major advance of this work lies on the theoretical explanation of the growth of several wurtzite semiconductors into atomically precise eight monolayers, employing the first-principles method based on DFT to investigate the surface energy. It was found that, from the perspective of formation energy, the 7th layer and 8th layer growth along the [11-20] direction of ZnSe nanoclusters is accessible (formation energy is achievable in the reaction temperature) while the 9th layer growth is unlikely to occur (formation energy is too high). Therefore, the ZnSe nanoplatelets would be grown into a precise eight monolayers. Together, this work provides insight into the fundamental understanding of controlling the thickness of several wurtzite materials.

Following by Chapter 1 and Chapter 2, Chapter 3 mainly presents the scalable synthesis of ZnS and ZnSe nanoplatelets, achieving 10-gram scale production. Also, the optical properties of ZnS, ZnSe, and their alloyed $ZnSe_{0.50}S_{0.50}$, and $ZnSe_{0.25}S_{0.75}$ were investigated in detail. The ZnSe nanoplatelets-based ultraviolet (UV)

photodetectors in this work shed light on the future applications of 2D nanoplatelets in optoelectronics.

Chapter 4 focused on the current hot materials transitional metal dichalcogenides (TMDs). In this chapter, a series of 2D TMDs of MoS_2, WS_2, ReS_2 nanosheets were prepared at a large scale. The resulting monolayer MoS_2 nanosheets exhibited superior HER catalytic activity as evidenced by small overpotentials of 179 mV in 1 M KOH at 10 mA cm^{-2}. This work will put forward a new attempt for chasing efficient electrocatalysts for high-efficient hydrogen generation.

5.2 Recommendations

The work of this thesis focuses on the efficient construction of 2D atomic-thick metal chalcogenides (ZnSe, ZnS, ZnTe, MoS_2, WS_2, ReS_2) and the adjustment of their structure and electronic properties for photodetectors and HER electeocatalysis. Based on the above research foundation, aiming to exert and improve the photoelectric and electeocatalytic performance of such 2D atomic-thick metal chalcogenides, there are still some works worthy of further research and exploration:

1. Most research works follow now with interest in increasing on the number of the catalytically active sites of 2D layered TMDs, such as MoS_2, WS_2, ReS_2, but how to develop the reaction active sites of their basal planes to the greater extent still faces a huge challenge. In future work, the active sites of the basal planes of MoS_2, WS_2, ReS_2, and other layered TMDs can be further increased by constructing defects and ion doping on the basal planes to enhance the electrocatalytic activity of HER. Then we can study the specific kinetic process and reaction mechanism of electrocatalytic HER under such conditions. If a breakthrough can be made in this respect, the structure-performance relationship of the 2D layered TMDs will be more clearly understood, and thus it is helpful to design more efficient HER electrocatalysts of 2D TMDs.

2. For non-layered metal chalcogenide systems, such as ZnSe, ZnS, and ZnTe, the construction of heterojunction systems has become an emerging direction, but how to break through the bottleneck of the photoelectric and catalytic performance of single-

component 2D metal chalcogenide compounds is a huge challenge. In future, ongoing efforts can be made in search of methods for systematic control of structural features and properties of 2D metal chalcogenides to produce core/shell metal chalcogenides, alloyed/doped metal chalcogenides, metal-semiconductor heterostructures, and self-assembly of metal chalcogenides to further enhance their potential applications, such as lighting and displays, optoelectronics and catalysis.

In short, the growth of 2D metal chalcogenides seems to be simple, yet, there are still many complex processes and mechanisms that have not been revealed. Through the trinity of the experiment, characterization, and simulation, we are able to understand the mechanism of 2D metal chalcogenides growth, and provide effective technical guidance for the reproducibility and batch production of 2D metal chalcogenides with specific functions.

Stimulated by the great stride in the synthesis, and properties related to 2D metal chalcogenides nanomaterials, explosive progress has been achieved in these kinds of materials, from fundamental study and practical applications.

Great development of 2D metal chalcogenides is often accompanied by new challenges. First, from the sustainable and eco-friendly development point of view, green chemistry is highly desired. We should put our emphasis on heavy metal-free green zinc-based semiconductor NPL alternatives, converting from the study of the conventional cadmium chalcogenides. Second, from the material synthesis point of view, a general and method should be developed to meet the industry requirement of high-yield and massive production of 2D metal chalcogenides. Third, from the characterization point of view, the growth mechanism of ultrathin 2D metal chalcogenides should be further in-situ explored and identified with in situ characterization techniques, such as in situ XRD, in situ TEM and in situ XPS. Finally, from the application point of view, another critical challenge in this field lies in the development of reliable methods to stabilize these 2D metal chalcogenides, including tuning the parameter windows from surfactant molecules to kinetics control and thermodynamics control of the chemical reaction.

Appendix 1: Supplementary information of Chapter 2

Mechanistic study of the formation of ZnS nanoplatelets

We characterize the intermediate products by the combination of TEM techniques with absorption spectroscopy to investigate the growth mechanism of ZnS nanoplatelets. As the reaction evolved for 10 min at 90 ^{o}C, we obtained bundled ZnS nanowires (Figure A1-8a), which manifests a band gap at 270 nm (Figure A1-8f). As the reaction proceeded for 1 min at 110 ^{o}C, bundled nanowires were partially fragmented (Figure A1-8b), and the absorption onset slight shifts to 272 nm (Figure A1-8f). In additional to the existing peaks, the absorption spectrum in Figure A1-8f indicates the formation of thicker species with an absorption onset at 283 nm. This suggests that some fragmented species already convert into thick ones via monomer diffusion and reconstruction. As the reaction evolved for 10 min at 110 ^{o}C (Figure A1-8c), this conversion finished as the absorption onset corresponding to the fragmented species vanished (Figure A1-8f). A further reaction at 170 ^{o}C for 30 min produced nanoplatelets with hollow and patchy features (Figure A1-8d). The absorption onset at 283 nm (Figure A1-8f) is identical to the proceeding species. This further corroborates that the mechanism on the formation of nanoplatelets with wurtzite structure, as proposed in the main article. As the reaction proceeded for 2 h at 170 ^{o}C, we obtained uniform ZnS nanoplatelets (Figure A1-8e) manifesting an absorption onset at 283 nm (Figure A1-8f). The mechanistic study clearly reveals that the monomer diffusion and reconstruction are accompanied by a thickness increase of the species, which is followed by oriented attachment that lead to the formation of monodisperse ZnS nanoplatelets. This further demonstrates the generality of the growth mechanism of nanoplatelets with wurtzite structure, as discussed in the main article.

Computation details

We employed the first principles method based on the density functional theory (DFT) and the first principles pseudopotential method to investigate the growth mechanism of ZnSe nanoplatelets. The DFT calculations were carried out by the Vienna Ab Initio Simulation Package (VASP) code[3,4] with the projector-augmented wave (PAW) method using the Perdew-Burke-Ernzerhof (PBE) exchange-correlation functional.[5,6] The plane wave cutoff was set as 500 eV, with the total energy convergence at 10^{-6} eV for the self-consistent iterations. The Gaussian smearing method with σ = 0.05 eV was considered for Brillouin-zone integration and the geometry optimizations were stopped until the forces on the atoms were < 0.01 eV/Å.

Figure A1-11 presents the mainly growth directions of ZnSe nanoplatelets. Perpendicular to the viewing plane is the [0002] direction (being parallel to the *c*-axis of wurtzite ZnSe) and this direction corresponds to the three index [002] direction. The dominant surface is $(11\bar{2}0)$ along the $[11\bar{2}0]$ direction, which corresponds to the three index (110) surface. The direction that intersects $[11\bar{2}0]$ with an angle of 30 degree is $[10\bar{1}0]$ direction. Along this direction, there are two different surface structures such as $(10\bar{1}0)$A and $(10\bar{1}0)$B, which correspond to the three index surfaces (100)A and (100)B, respectively. Another growth direction perpendicular to $[11\bar{2}0]$ direction is $[1\bar{1}00]$. This direction corresponds to the three index $[1\bar{1}0]$ direction. Along this direction, there are two different surface structures of $(1\bar{1}00)$A and $(1\bar{1}00)$B, both of which correspond to the three index (100) surface. Note the

surface structure of $(1\bar{1}00)$A is equivalent to that of $(10\bar{1}0)$A whereas the surface structure of $(1\bar{1}00)$ is equivalent to that of $(10\bar{1}0)$B.

Surface energy

We used the finite-sized slab technique to calculate the surface energy of ZnSe nanoplatelets. The slab models were built from the wurtzite ZnSe crystal structure determined by Korneeva.[7] The lattice parameters of bulk ZnSe, optimised with a $12\times12\times6$ *k*-point grid, were a = b = 3.996 Å, c = 6.626 Å, which are in good agreement with the experimental values. According to the exposed surfaces of wurtzite ZnSe nanoplatelets, five different surfaces were studied: three non-polar surfaces of $(11\bar{2}0)$, $(10\bar{1}0)$A/$(1\bar{1}00)$A and $(10\bar{1}0)$B/$(1\bar{1}00)$B, and two polar surfaces (Zn-terminated (0002) and Se-terminated $(000\bar{2})$) (Figure A1-12). All these slab models in periodical super cell were separated by a vacuum region of 20 Å thick. Each slab of nonpolar surface models contains four zinc and four selenium atoms within each Zn-Se layer in a repeated slab configuration. As for the polar surface models, each one contains eight zinc or eight selenium atoms within each Zn-Se layer in a repeated slab configuration. Reasonable slab models were constructed by testing the slab thickness, as illustrated in Table S2. The surface free energy of the particular slab with a repeated geometry is given by the following equation:

$$\sigma = \left(E_{slab} - \sum_i n_i \mu_i\right) / 2A$$

Where n_i and μ_i are the number of atoms and the chemical potential of the i^{th} constituent of the slab, respectively, A is the surface area and E_{slab} is the total energy of the particular slab. The factor of 2 accounts for two equivalent surfaces in the particular slab. The surface energies of non-polar surface were found to converge with slab thickness and were converged to <0.001 eV/Å^2 with respect to eight-layer slab thickness. We therefore used the eight-layer thick ZnSe slabs for studying the

surface energies of $(11\bar{2}0)$ surface and of $(10\bar{1}0)/(1\bar{1}00)$ surfaces with $3\times6\times1$ and $6\times3\times1$ Monkhorst-Pack *k*-point grid, respectively.

Special care should be taken in the computational treatment of the polar surface, in particular to avoid the buildup of an overall artificial dipole field. Here, we adopted symmetric structures of the nine-layer slab model for the Zn-terminated (0002) and Se-terminated $(000\bar{2})$ surfaces, as shown in Figure A1-12.[8] The surface free energy equation is a thermodynamic function of the chemical potential of the constituent in the slab.[9] Therefore, the surface energy is governed by the chemical potentials of the constituents of the slab, i.e. μ_{Zn} and μ_{Se}. Invoking equilibrium of ZnSe bulk, $\mu_{Zn}+\mu_{Se} = E_{bulk}^{ZnSe}$, the dependence of the surface free energy on the chemical potential can be further simplified by eliminating μ_{Se}, leading to a dependence of the surface free energy on μ_{Zn} only. We restrict the values of μ_{Zn} to $E_{bulk}^{Zn} + \Delta H_f[ZnSe] \leq \mu_{Zn} \leq E_{bulk}^{Zn}$, i.e. $\Delta H_f[ZnSe] \leq \Delta\mu_{Zn} = \mu_{Zn} - E_{bulk}^{Zn} \leq 0$, according to the thermodynamically allowed ranges. These ranges are determined by the assumed constraints, $\mu_{Zn} \leq E_{bulk}^{Zn}$ and $\mu_{Se} \leq E_{bulk}^{Se}$, which means that the Zn and Se do not crystallize on the surface. Moreover, the formation enthalpy of bulk ZnSe was given by $\Delta H_f[ZnSe] = E_{bulk}^{ZnSe} - \mu_{Zn} - \mu_{Se}$. We have calculated the surface energies as a linear function of μ_{Zn}, $-2.360\ eV \leq \Delta\mu_{Zn} \leq 0$, as shown in Figure 3a in the main article. The chemical potential $\Delta\mu_{Zn} = 0$, i.e. $\mu_{Zn} = E_{bulk}^{Zn}$, represents the Zn-rich condition while $\Delta\mu_{Zn} = -2.360$ eV represents the Se-rich condition. Our surface energy calculation results show that $(11\bar{2}0)$ surface is the dominant facet. The growth of ZnSe would be fast along $[000\bar{2}]$ (*c*-axis) and $[1\bar{1}00]$, and will terminate at $(000\bar{2})$ and $(10\bar{1}0)$A/$(1\bar{1}00)$A surfaces, respectively. These

preferred growing processes will finally result in the formation of ZnSe nanoplatelets with well-developed facets, as shown schematically in Figure A1-5c.

ZnSe monomer and alkylamine binding energies in the slab model

According to the experiment, the reaction solution for the growth of wurtzite ZnSe nanoplatelets contains the Zn cation, Se anion, and alkylamine ligand, which may directly affect the growth behavior of ZnSe nanoplatelets. Therefore, it is essential to investigate the binding behavior of alkylamine ligands and ZnSe monomer on the exposed surfaces of the ZnSe nanostructure. Here we also used the slab model with eight atomic layers separated by a vacuum space of 20 Å thick to study the features of molecule binding on the surfaces. The surface sizes of the models are the same as those for studying the surface energy above with similar *k*-point meshes. In order to suppress any long-ranged interference between Zn- and Se-terminated ends of the slab, the dangling bonds of the bottom atoms of ZnSe (0002) and $(000\bar{2})$ slab models were saturated by adding one monolayer of pseudo hydrogen atoms with nuclear charge Z = 1/2|*e*| and Z = 3/2|*e*|, respectively.

The binding energy is calculated as $E_{binding} = E_{tot}-E_{slab}-E_{amine}$ for alkylamine adsorption and $E_{binding} = (E_{tot}-E_{slab})/n-E_{Zn}-E_{Se}$ for ZnSe monomer adsorption. Where E_{tot} and E_{slab}, are the total adsorption energies of the system, the energy of the slab model without adsorption, respectively; E_{amine}, E_{Zn} and E_{Se} are the energies of the alkylamines, bulk Zn, and bulk Se, respectively; *n* is the number of ZnSe monomers. To simplify the calculations, methylamine served as a representative for alkylamines. For the adsorption of methylamine, we simulated four-symmetry adsorption sites such as top(Zn)-site, top(Se)-site, bridge-site, and hexagonal close packed (hcp)-site. For the ZnSe monomer, we consider ZnSe monomer adsorption on crystal space lattice site.

Table S4 shows the binding energies of the methylamine and ZnSe monomer adsorption states on different sites of each surface. Their adsorption optimized

structures were all presented on Figure A1-13. The most stable methylamine adsorption for each surface were listed as follow: (11 $\bar{2}$ 0) hcp-site with -0.9317 eV, (10$\bar{1}$0)A/(1$\bar{1}$00)A hcp-site with -0.8876 eV, (10$\bar{1}$0)B/(1$\bar{1}$00)B hcp-site with -2.9506 eV, (0002) with hcp-site with -3.8125 eV, (0002) top-site with -5.1486 eV and (000 $\bar{2}$) hcp-site with -1.4514 eV. By contrast, ZnSe monomer adsorption on the crystal space lattice site of each surface was (11 $\bar{2}$ 0) with -1.8565 eV, (10$\bar{1}$0)A/(1$\bar{1}$00)A with -1.7029 eV, (10$\bar{1}$0)B/(1$\bar{1}$00)B with -3.7583 eV, (0002) with -5.6899 eV and (000 $\bar{2}$) with -3.5373 eV. It is evident that ZnSe monomer adsorption states have much lower binding energy than that of methylamine adsorption. These results show that all the surfaces prefer to bind ZnSe monomer prior to the alkylamines. Therefore, the ZnSe growth is unlikely to be inhibited by the binding of alkylamines, and the epitaxial growth of all the surface will be promoted by the strong binding with ZnSe monomer. The surfaces of (10$\bar{1}$0)B/(1$\bar{1}$00)B, (0002) and (000 $\bar{2}$), which also have large surface energy, show large binding energies with ZnSe monomer. These surfaces will lead to the fast growth along *c*-axis and [1$\bar{1}$00] direction.

ZnSe monomer and alkylamines binding energy in nanowire model

As the diameter of initially formed zinc-alkylamine lamellar structure is determined by the template,[10] we used the ZnSe nanowire model with a diameter of ~0.99 nm to calculate the binding energy. Figure A1-14 shows the structure of the nanowire model. For the [11 $\bar{2}$ 0] direction, there are six atomic layers with a thickness of 0.99 nm whereas for the [1$\bar{1}$00] direction, the distance between two terminated (1$\bar{1}$00)B surfaces is 0.92 nm (Figure A1-14). It is to be noted that in the case of nanowire, it is periodic along the *c*-axis, and sufficient vacuum of 20 Å has been kept along the [11 $\bar{2}$ 0] and [1$\bar{1}$00] directions, and 8×1×1 Monkhorst-Pack *k*-point grid has been taken for the total energy calculations. These ZnSe nanowire models are built after careful consideration. In the first case, five or seven atomic layers along [11 $\bar{2}$ 0] direction have a thickness of 0.79 nm or 1.19 nm while in the second case the distance between (1$\bar{1}$00)B and (1$\bar{1}$00)A or two ($\bar{1}$100)A along [1$\bar{1}$00] direction are 1.04 nm and 1.17 nm, respectively. So distances in the latter case are far away from the diameter of the nanowires (0.9 nm in our experiment). So in the next section, we will use the nanowire models of the first case as the starting point to study the growth kinetics of ZnSe nanoplatelets.

As seen from Figure A1-15a, all average binding energies with different binding number of ZnSe monomer for (11 $\bar{2}$ 0) surface of the nanowire are below -2.3 eV. As for (1$\bar{1}$00)B surface, the average binding energy has a slight increasing trend, but all average binding energies with different binding number of ZnSe monomer are below -3.0 eV. Thus the nucleation may proceed on both (11 $\bar{2}$ 0) and (1$\bar{1}$00)B surfaces. In addition, we also studied binding behavior of octylamine and ZnSe monomer with

the nanowire model, which is similar to the behavior of the methylamine with slab models. The octylamine shows physisorption state neither on (11 $\bar{2}$ 0) nor (1$\bar{1}$00)B surface as the binding energies for (11 $\bar{2}$ 0) and (1$\bar{1}$00)B surfaces are -0.842 eV and -0.983 eV, respectively (Figure A1-15b). Overall, the ZnSe monomer shows much stronger binding behavior on both (11 $\bar{2}$ 0) and (1$\bar{1}$00)B surfaces than octylamine does and therefore nanowire prefers bind with ZnSe monomer. This behavior can promote the epitaxial growth along the [11 $\bar{2}$ 0] and [1$\bar{1}$00] directions.

Growth kinetics of ZnSe nanoplatelets

In this section, we will use the atomic scale step structures to study growth of ZnSe nanoplatelets.[11] The step structures and corresponding formation energies show the differences of surface morphologies and growth rate between two different surfaces. From this we proposed the effects of step structures and the formation energies on the formation of ZnSe nanoplatelets. Our atomic scale step model starts with the nanowire with a diameter of ~0.99 nm, as shown schematically in Figure A1-14.

As discussed above, the growth along [0002] (*c*-axis) is energetic and fast due to the large surface energy of the (0002) polar surface. The final morphology of ZnSe nanoplatelets may be mainly dominated by the growth behavior along the directions of [11$\bar{2}$0], [10$\bar{1}$0] and [1$\bar{1}$00], so we would mainly focused on growth behavior along these directions. There may be two possible growth pathways along these two directions (see Figure 5A-C, 5D1, 5D2 in the main article). One is that ZnSe monomers may diffuse onto the surface of the nanowire, then reconstruct and form the new surface layer. Thereafter more ZnSe monomers would repeat this process, resulting in layer-by-layer stacking, which increases the thickness of that direction. The other pathway is the oriented fuse between two or more nanowires followed by reconstruction which promotes the growth along the fuse direction. We studied both growth pathways along [11$\bar{2}$0] and [1$\bar{1}$00] direction, and elucidated why ZnSe nanoplatelets have a uniform thickness of 1.39 nm with (11$\bar{2}$0) as the dominated surface.

The formation energy can be defined and calculated as:

$$E_{\text{formation}} = E_{\text{total}} - E_{\text{tererac}} - n_{\text{Zn}}*\mu_{\text{Zn}} - n_{\text{Se}}*\mu_{\text{Se}}$$

Here, E_{total} and $E_{terrace}$ are the DFT total energies of the as-simulated step model and the pure terrace parts in the same model, and n_{Zn}, μ_{Zn}, n_{Se} and μ_{Se} are the number of Zn atoms and Se atoms in the system and their chemical potential, respectively. We assumethat the terrace parts of ZnSe nanocrystal always has the thermodynamic equilibrium conditions as $\mu_{Zn} + \mu_{Se} = E_{tererac}/n_{monomer}$. Here $n_{monomer}$ is the number of ZnSe monomers in terrace parts of ZnSe nanocrystal.

Then, we calculated the formation energy of new ZnSe nanostructures which were formed by layer-by-layer stacking along [11 $\bar{2}$ 0] and [1$\bar{1}$00] (Table S5). For the [11 $\bar{2}$ 0] direction, the formation energy of ZnSe nanostructure after stacking the first, second and third atomic layer is 0.0359 eV, -0.2489 eV and 0.0654 eV, which corresponds to the thickness of 1.19 nm, 1.39 nm and 1.59 nm along [11 $\bar{2}$ 0] direction, respectively. While for the [1$\bar{1}$00] direction, the formation energy of ZnSe nanostructures after stacking first, second and third atomic layer is -2.7828 eV, 0.8364 eV and -2.5247 eV, respectively. Furthermore, we also calculated the formation energy of new ZnSe nanostructure formed by oriented fuse between two nanowires along [11 $\bar{2}$ 0] and [1$\bar{1}$00] directions (Figure 5A-C in the main article). The formation energies are -7.058 eV, -6.937 eV, and -0.598 eV for the horizontal type [$\bar{1}$100] oriented direction, ladder type [1$\bar{1}$00] oriented direction and [11 $\bar{2}$ 0] oriented direction, respectively (see Figure 5A-C in the main article for the detailed fuse configurations). The optimized structures of all atomic scale step models in relation to the two growth pathways are illustrated in Figure A1-18.

Growth kinetics of ZnS, CdSe and ZnTe nanoplatelets

In this section, we used the same approach as conducted for ZnSe to study the reason why ZnS, CdSe and ZnTe nanoplatelets also present a uniform thickness of eight monolayers along [11 $\overline{2}$ 0] direction.

The experimental growth of wurtzite platelets shows that most wurtzite platelets with thickness of eight monolayers undergo the similar growing behavior as that of ZnSe. Most of them appear the intermediate products with nanowire morphology and six monolayers, which can dominate the following trend of growth. According to the theoretical study of growth behavior of ZnSe nanoplatelets above, the final thickness of ZnSe nanoplatelets corresponds to the lowest formation energy of eight monolayer and a sharp rise of formation energy of adding another atomic layer in diffusion process along [11 $\overline{2}$ 0] direction. Therefore, we also chose the nanowire with six monolayers as the atomic scale step model for the ZnS, CdSe and ZnTe, and study their diffusion process along the [11 $\overline{2}$ 0] direction through the formation energy when depositing more atomic layers as that of ZnSe above (Figure A1-19).

The calculated result of formation energy as shown schematically in Figure A1-19, which clearly show that all theZnS, CdSe and ZnTe have the similar growing trajectory as that of ZnSe in the diffusion process along [11 $\overline{2}$ 0] direction. From Figure A1-20, all the formation energies of eight monolayers of ZnS, CdSe and ZnTe are negative and lowest among the seven to nine depositing monolayer processes. Then for all of ZnS, CdSe and ZnTe, further deposition of any additional atomic layer to reach the nine layers are very difficult, because their formation energies all significantly increase to positive value. These imply that all the ZnS, CdSe and ZnTe are favor to stable with the thickness of eight monolayers along [11 $\overline{2}$ 0] direction. Furthermore, ZnS and CdSe can very easily to reach the thickness of eight layers as

their low formation energies of seven layers. However, distinguish to the ZnS and CdSe, ZnTe should overcome a little bit high energy barrier as the formation energy of seven layer is 0.095eV. In our opinion, ZnTe could reach the seven layers through other path, one of which might be the ladder fusion by the magic size or lateral size, whose thickness is six monolayers as shown in Figure A1-21. The formation energy of this attachment is very low of -6.15 eV. So the ladder type of fusion would be very favorable, and help to overcome the energy barrier of seven monolayer formation of ZnTe, and then finally reach the thickness of eight monolayers through the diffusion process. In summary, the ZnS, CdSe and ZnTe are favor to stable with the thickness of eight monolayers along [11 $\overline{2}$ 0] direction as that of ZnSe.

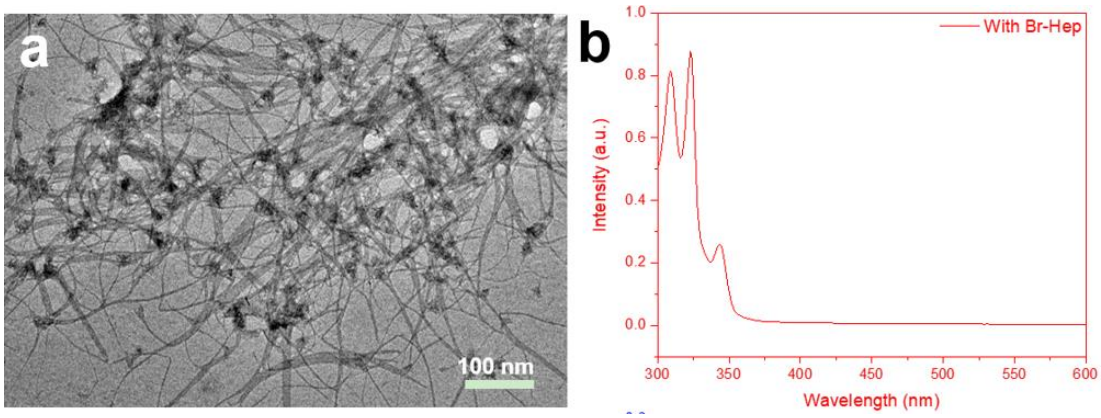

Figure A1-1. TEM image and UV-vis spectrum of the sample with adding Br-Hep. a, TEM image. **b**, UV-vis spectrum.

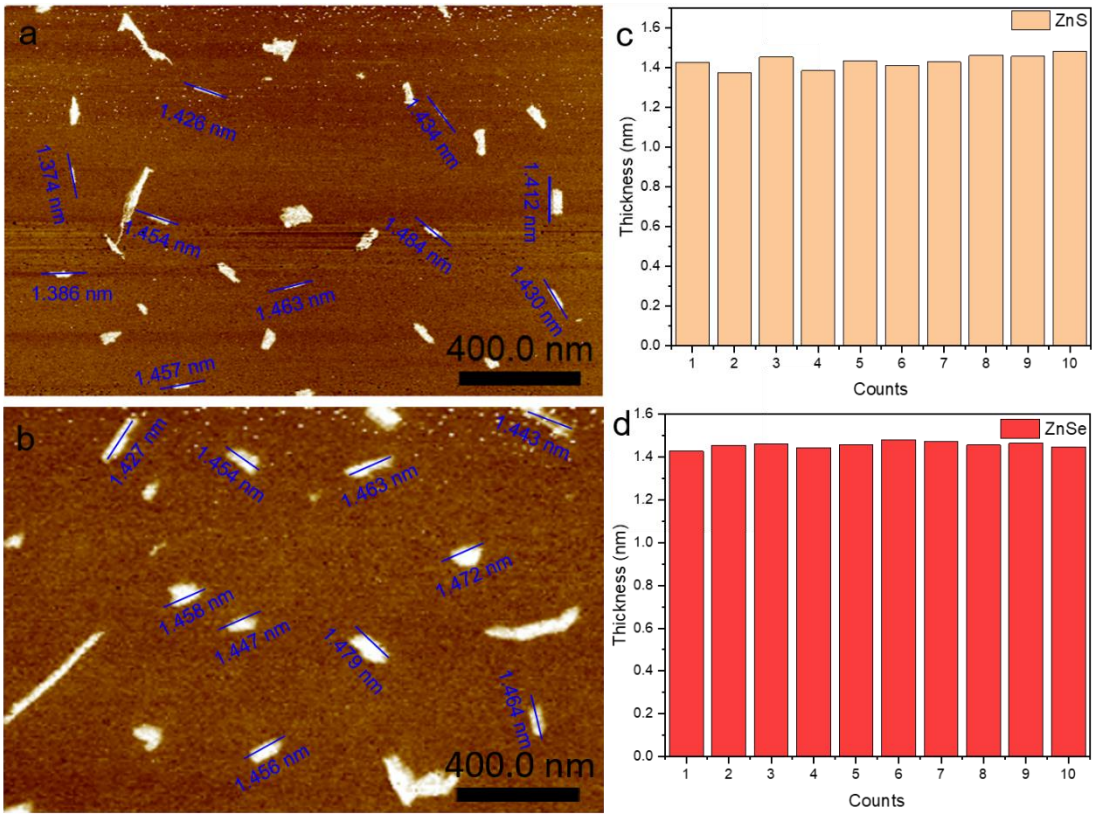

Figure. A1-2. AFM characterization of ZnS and ZnSe nanoplatelets. AFM images of **a**, ZnS and **b**, ZnSe nanoplatelets. Thickness histograms of **c**, ZnS and **d**, ZnSe nanoplatelets.

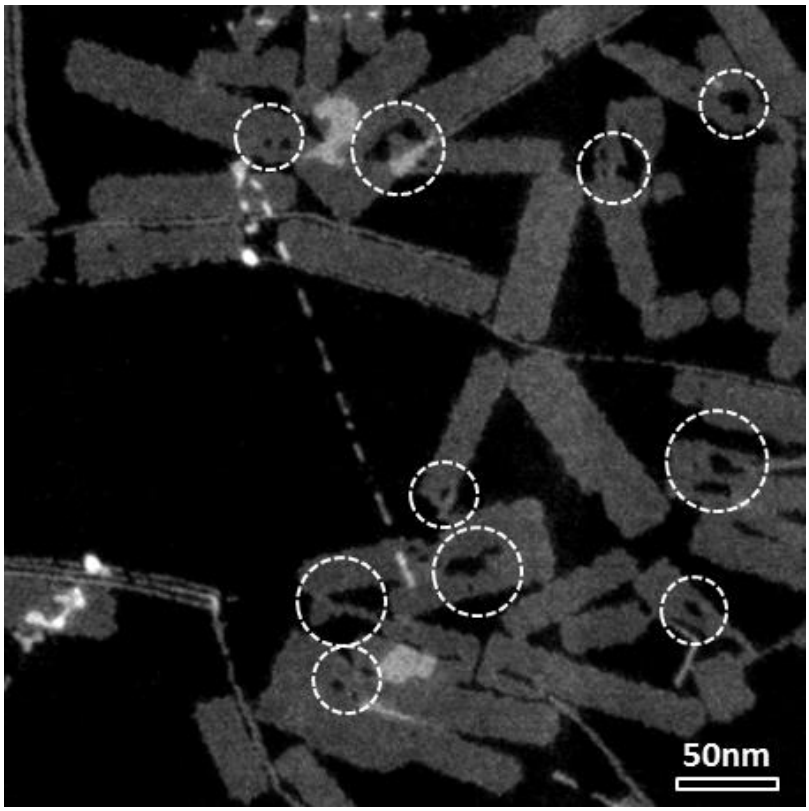

Figure A1-3. HAADF-STEM image of ZnSe nanoplatelets. Hollow feature and patches of nanoplatelets are highlighted by white dashed circles, indicating nanoplatelets may form from small nanoplatelets via oriented attachment.

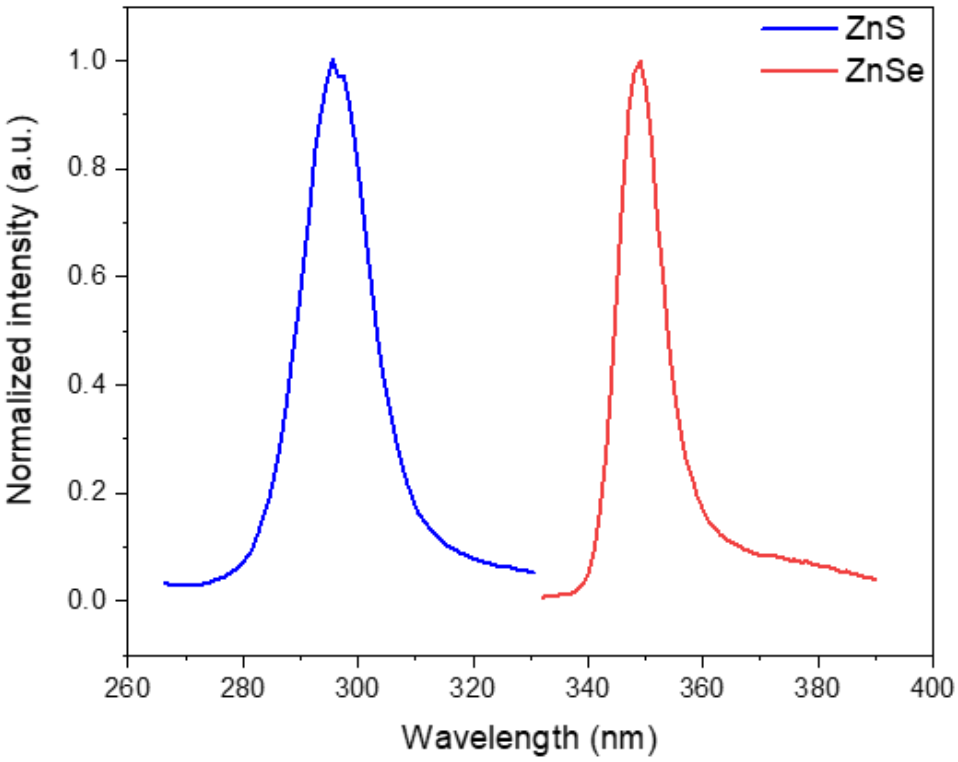

Figure A1-4. The photoluminescence spectra of ZnS (blue line) and ZnSe (red line) nanoplatelets.

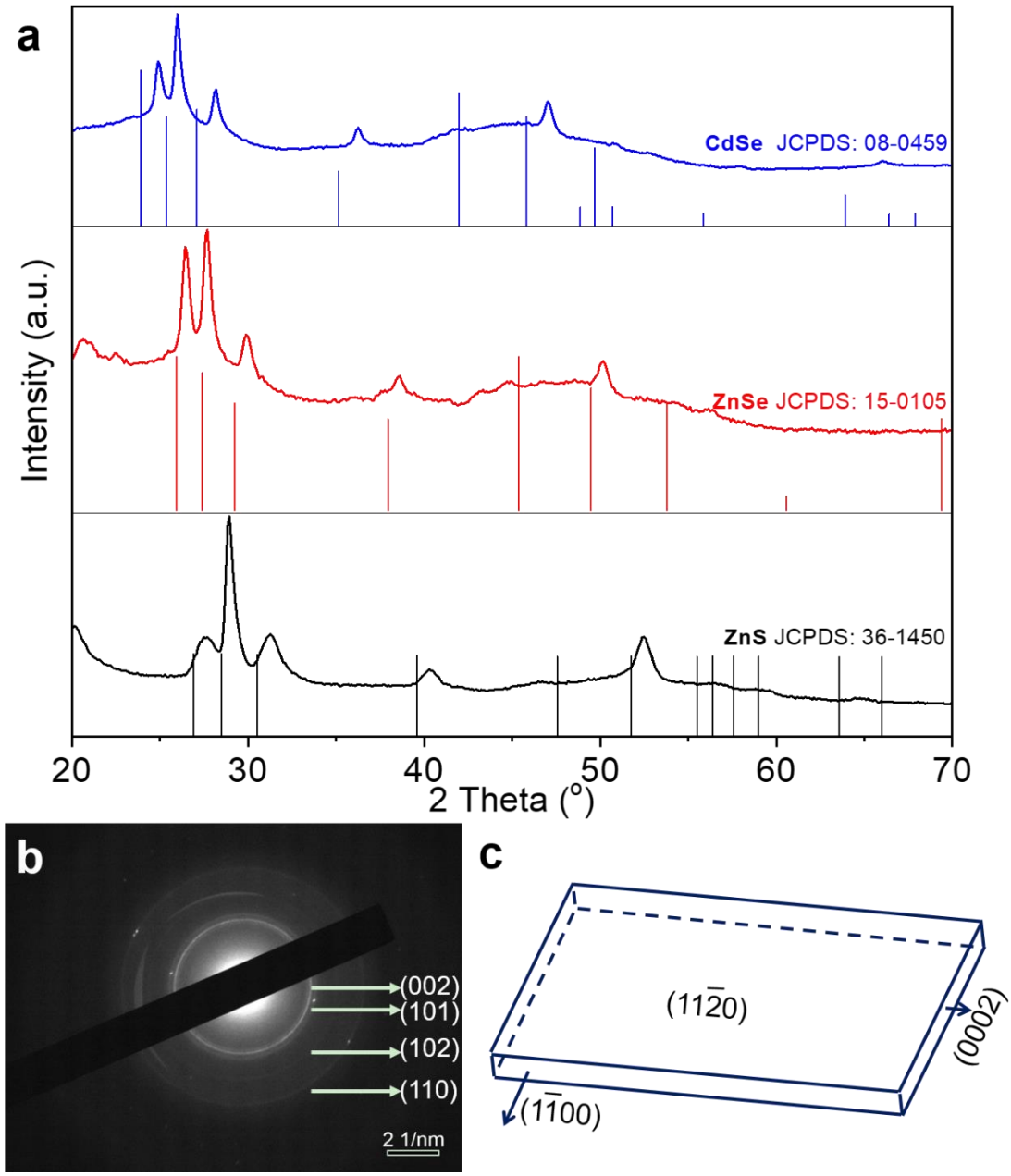

Figure A1-5. Structural characterization of nanoplatelets. a, XRD pattern of ZnS, ZnSe and CdSe nanoplatelets. **b**, SAED pattern of ZnTe nanoplatelets. **c**, Schematic illustration of a single ZnSe nanoplatelet, revealing the predominant basal (11$\bar{2}$0) facet, the side (10$\bar{1}$0) and (0002) facets.

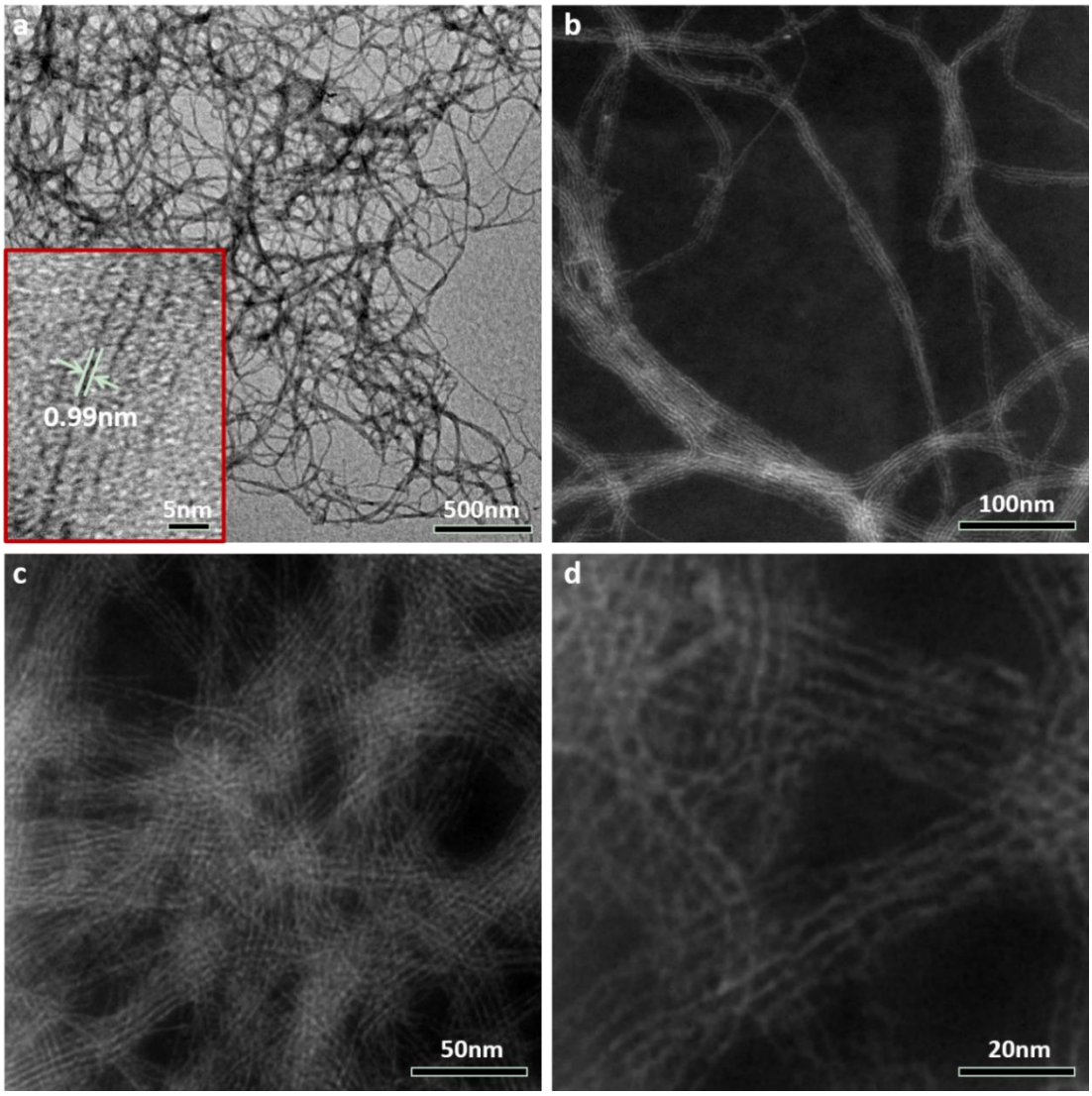

Figure A1-6. TEM and HAADF-STEM images of the sample obtained after the reaction evolved for 2 min at 150 ºC. a, TEM image showing the length scale of bundled wires is a few micrometers. Inset is the HRTEM image of bundled wires, showing the width of each wire is ~0.99 nm. **b-d**, HAADF-STEM image showing each bundled structure contains 2-6 individual wires with different magnifications.

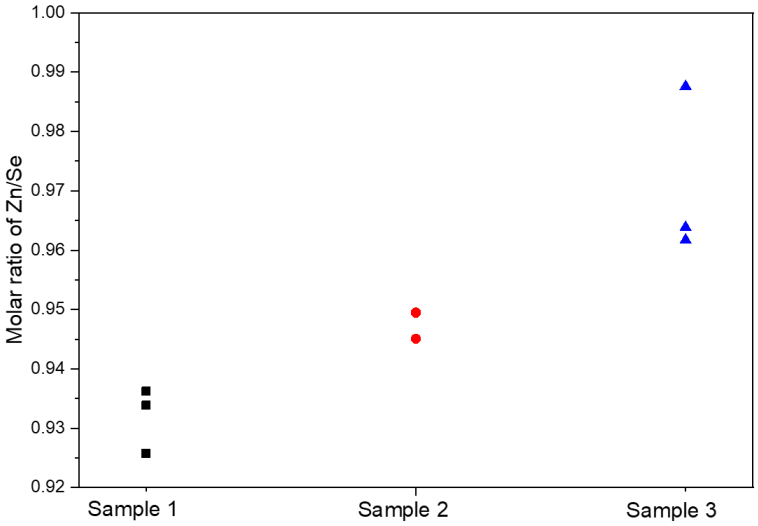

Figure A1-7. ICP-OES statistics of ZnSe bundled nanowires.

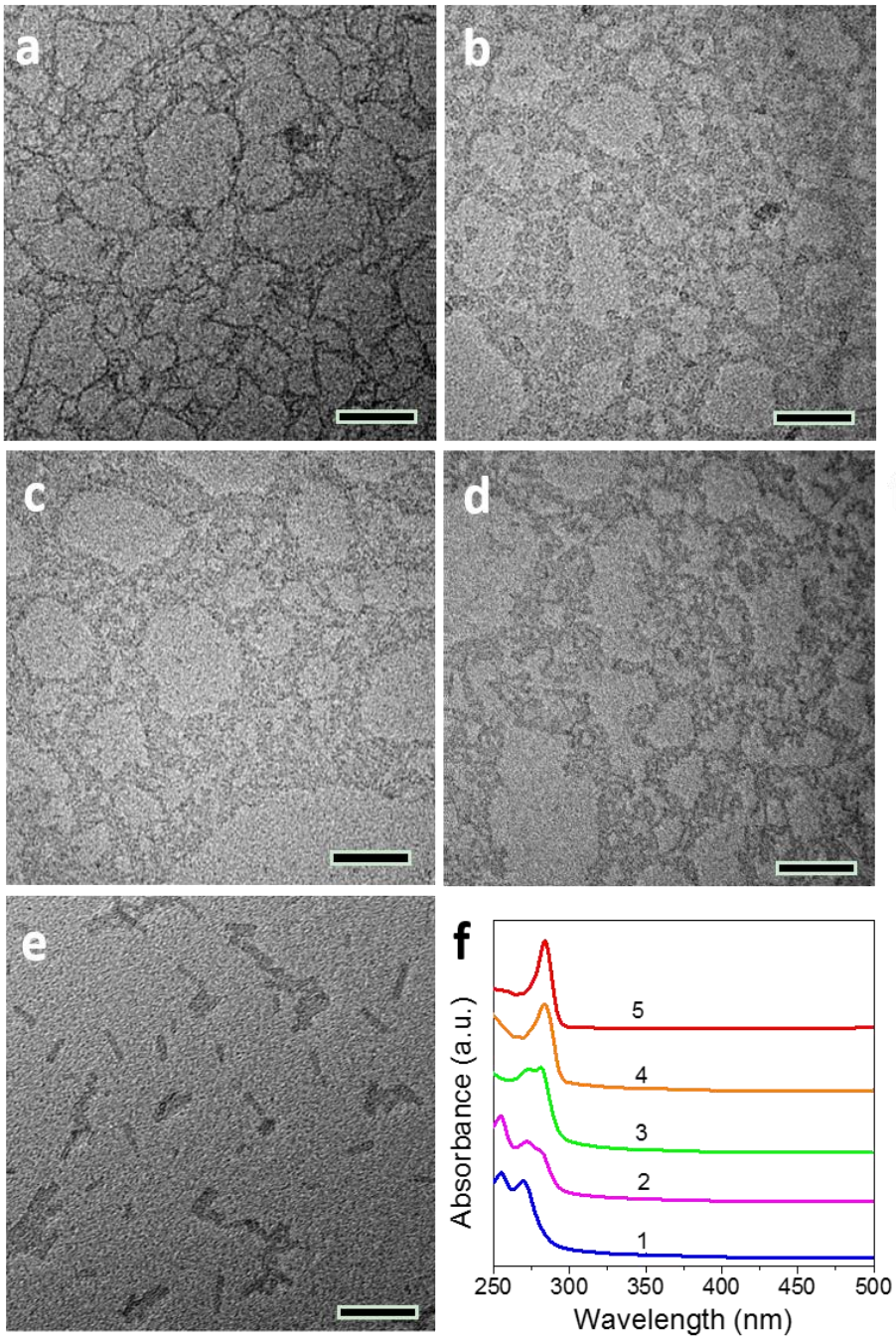

Figure A1-8. Mechanistic study of the formation of ZnS nanoplatelets. a-e, TEM images of ZnS nanoparticles. **a**, 10 min at 90 ^{o}C yielding bundled ZnS nanowires. **b**, 1 min at 110 ^{o}C yielding a mixture containing fragmented nanowires and small lateral size nanoplatelets. **c**, 10 min at 110 ^{o}C yielding small lateral size nanoplatelets. **d**, 30 minutes at 170 ^{o}C yielding nanoplatelets showing hollow and patchy features. **e**, 2 h at 170 ^{o}C yielding monodisperse ZnS nanoplatelets. **f**, Absorption spectra of ZnS nanocrystals at different growth stages showing the red-shift of the absorption onset, which is in consistence with the increase of the thickness of the nanocrystals. All scale bars are 50 nm.

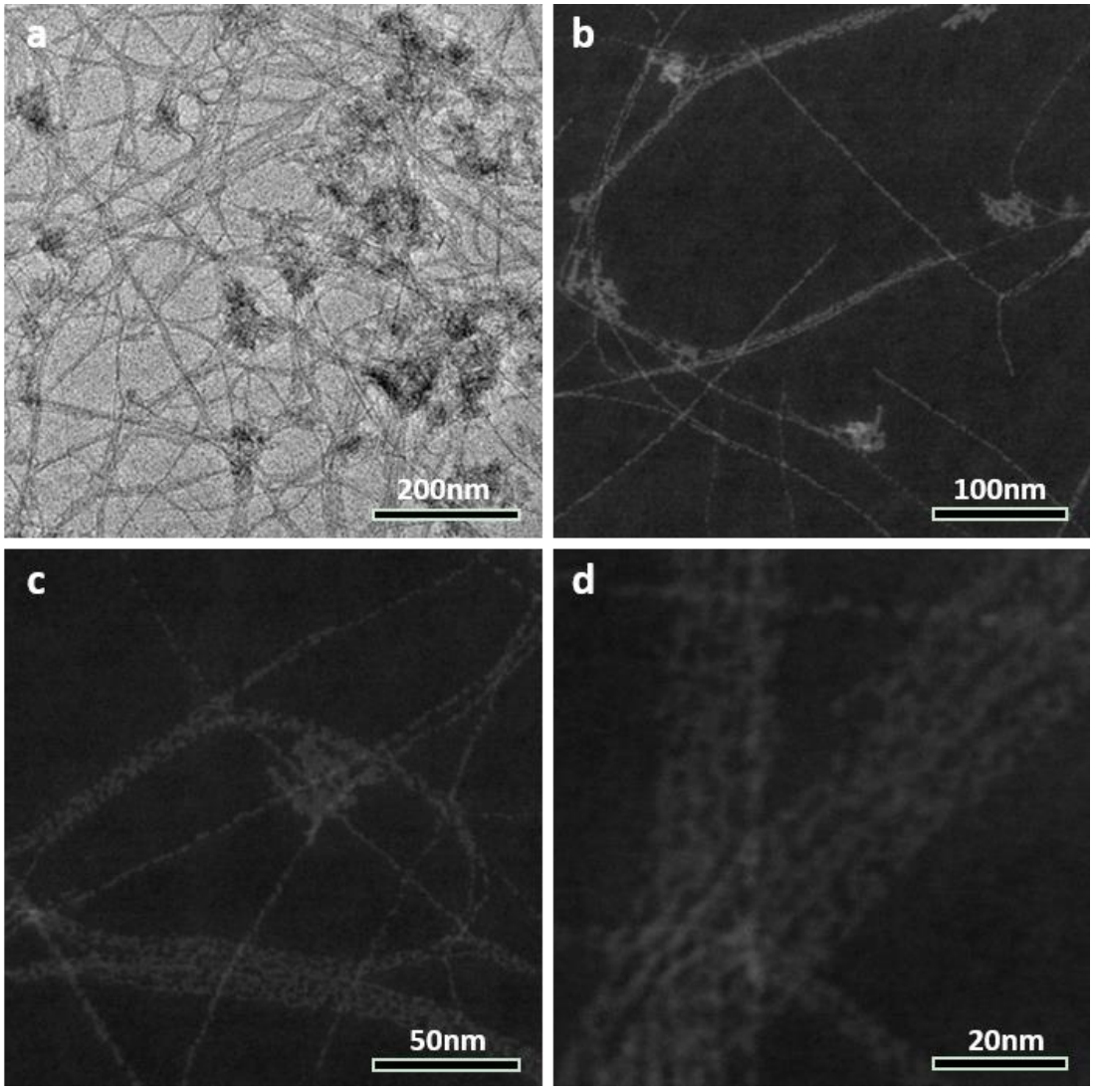

Figure A1-9. TEM and HAADF-STEM images of the sample obtained after the reaction evolved for 4 min at 150 ºC. a, TEM image showing the product contains both fused nanowires and nanoplatelets with small lateral size, with the former being the dominant phase. **b-d**, HAADF-STEM images confirming the fragmented feature of the fused nanowires with different magnifications. It also shows that the small lateral size nanoplatelets have larger contrast in comparison to fused fragmented nanowires, confirming the larger thickness of the nanoplatelets with small lateral size.

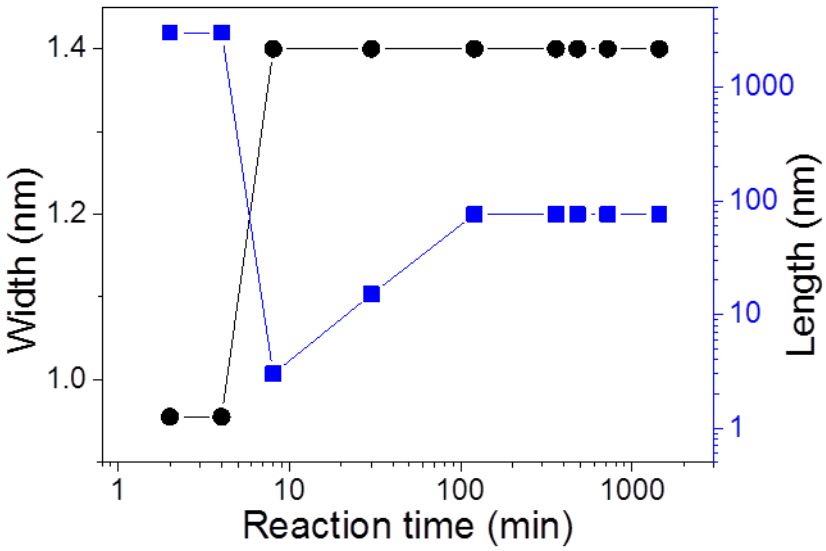

Figure A1-10. Thickness (black circles) and length (blue squares) of nanoplatelets as a function of reaction time at 150 ºC showing the increase of thickness of nanoplatelets from 0.99 nm to 1.39 nm via monomer diffusion and reconstruction.

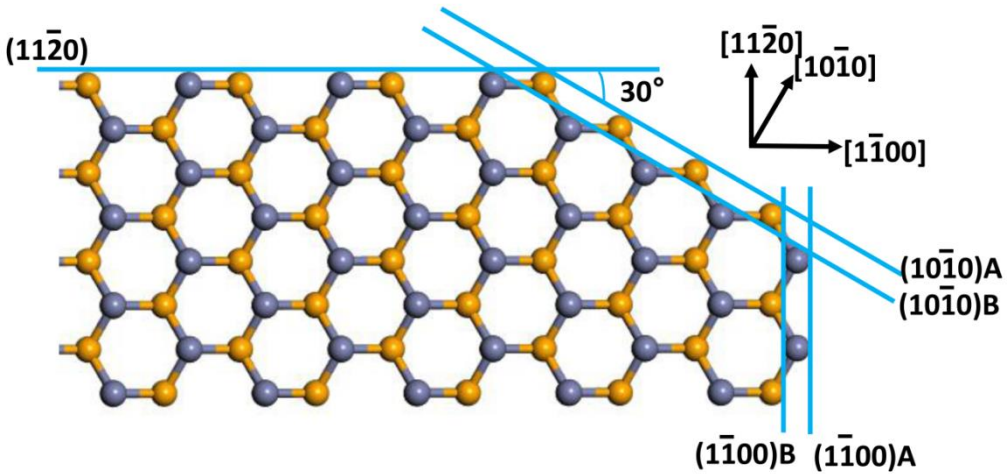

Figure A1-11. The growth directions of ZnSe nanoplatelets. Normal to the surface plane is the [0002] direction being parallel to the *c*-axis of the wurtzite structure of ZnSe. Note that the surface structure of (1$\bar{1}$00)A is equivalent to that of (10$\bar{1}$0)A whereas the surface structure of (1$\bar{1}$00) is equivalent to that of (10$\bar{1}$0)B.

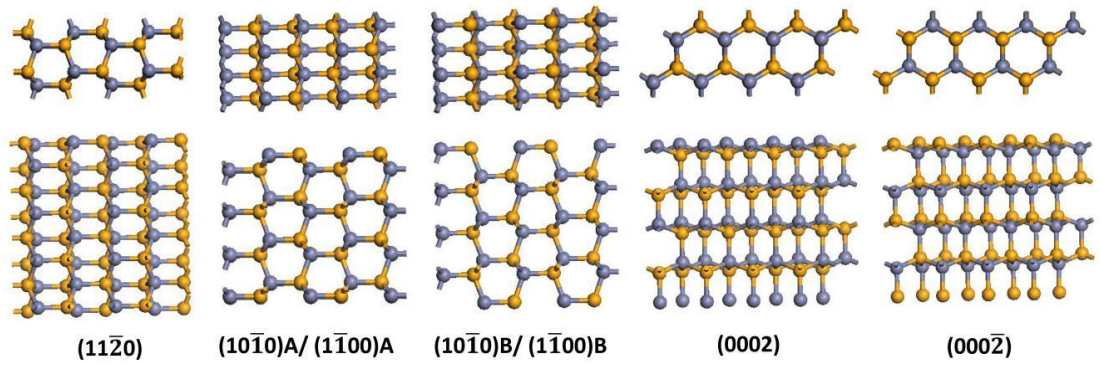

Figure A1-12. The slab model structures. The slab model structures of (11 $\bar{2}$ 0), (10$\bar{1}$0)A/(1$\bar{1}$00)A, (10$\bar{1}$0)B/(1$\bar{1}$00)B, Zn-terminated (0002) and Se-terminated (000 $\bar{2}$) surfaces. Top panel and bottom panel correspond to top-view and side view of the structures.

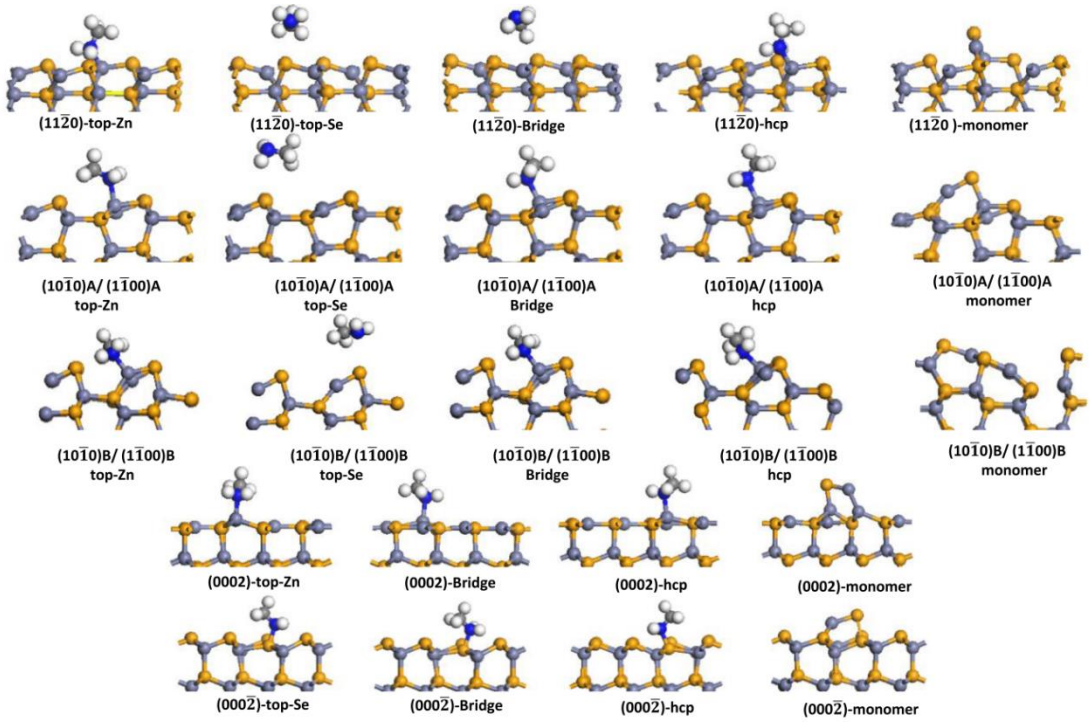

Figure A1-13. The optimized structures of alkylamine ligand and ZnSe monomers adsorption on different sites of exposed surfaces of the ZnSe nanostructure.

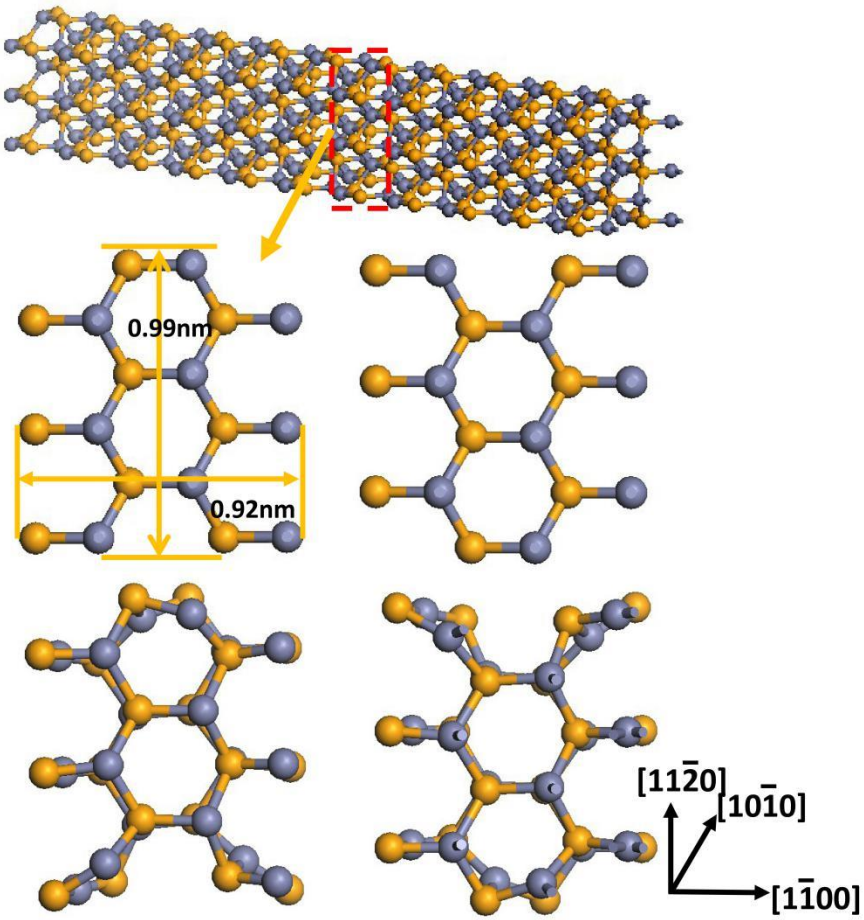

Figure A1-14. Optimized structures of nanowire models. Upper panel shows the three-dimensional (3-D) view of the nanowire model, middle panel gives side views of the two equivalent structures of the nanowire models, and the bottom panel presents the optimized structures of two equivalent structures of the nanowire models.

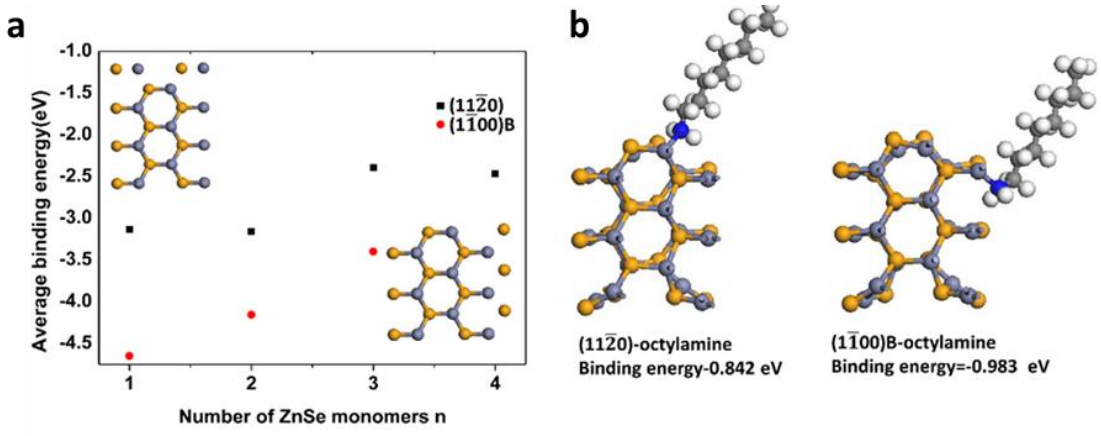

Figure A1-15. Binding behavior of monomers and octylamine ligand on (11 $\bar{2}$ 0) and (1$\bar{1}$00)B surface of nanowires. a, ZnSe monomer. **b**, Octylamine.

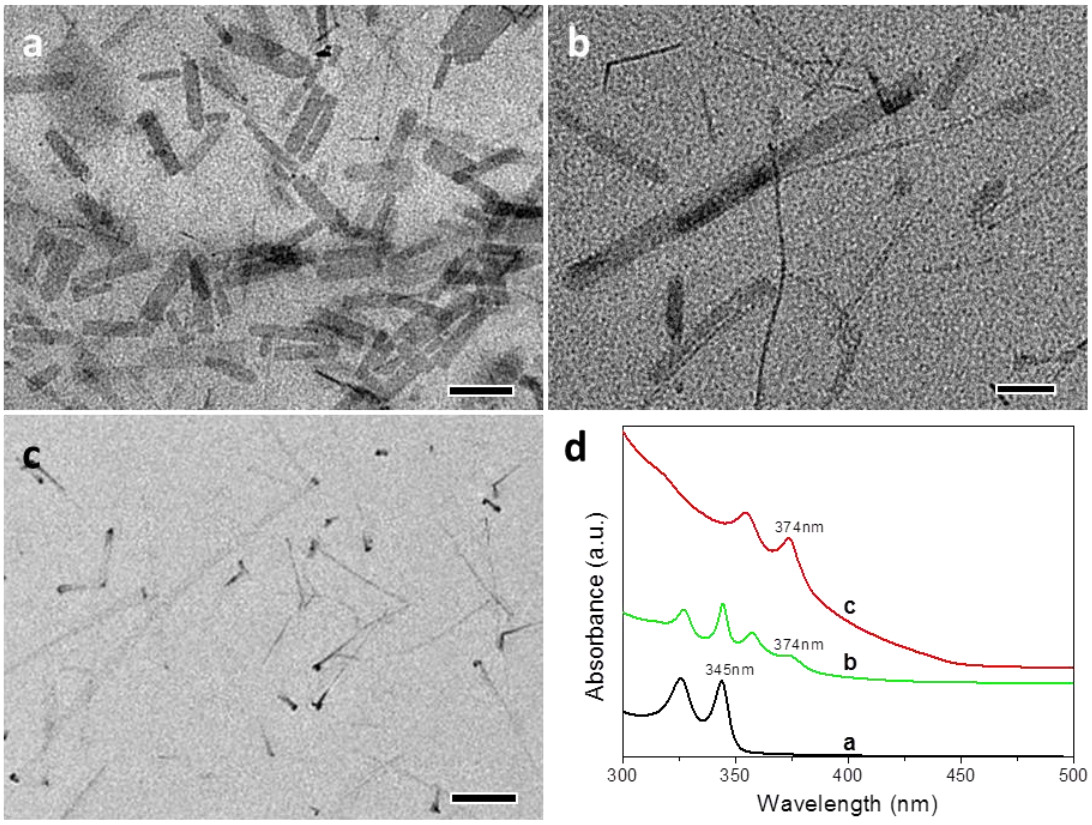

Figure A1-16. Evolution of ZnSe nanoplatelets at different reaction temperatures. a, TEM image of ZnSe nanoplatelets obtained after 90 min at 170 ^{o}C. **b**, TEM image of product obtained after 30 min at 200 ^{o}C showing a mixture containing both nanoplatelets and nanowires was obtained. **c**, TEM image of product obtained after 30 min at 220 ^{o}C showing thick nanowires were obtained. All scale bars are 100 nm. **d**, Absorption spectra of ZnSe nanoparticles.

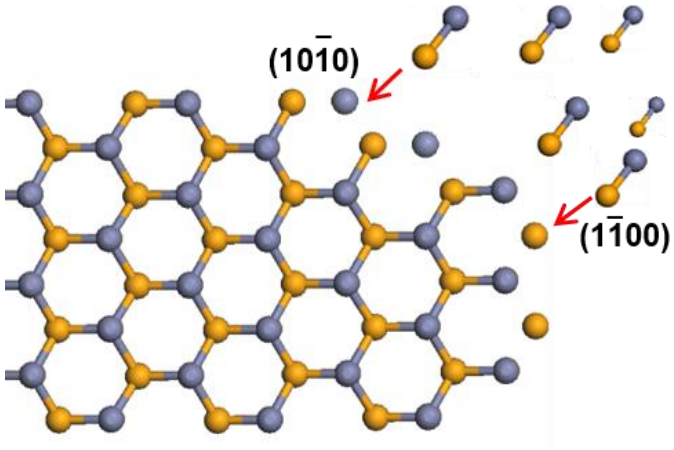

Figure A1-17. Diffusion and nuclei construction forming $(10\bar{1}0)$ and $(1\bar{1}00)$ terminated surfaces. The optimized structures corresponding to (Figure 1-5A, 1-5B, 1-5D1, and 1-5D2) were shown in Figure A1-15.

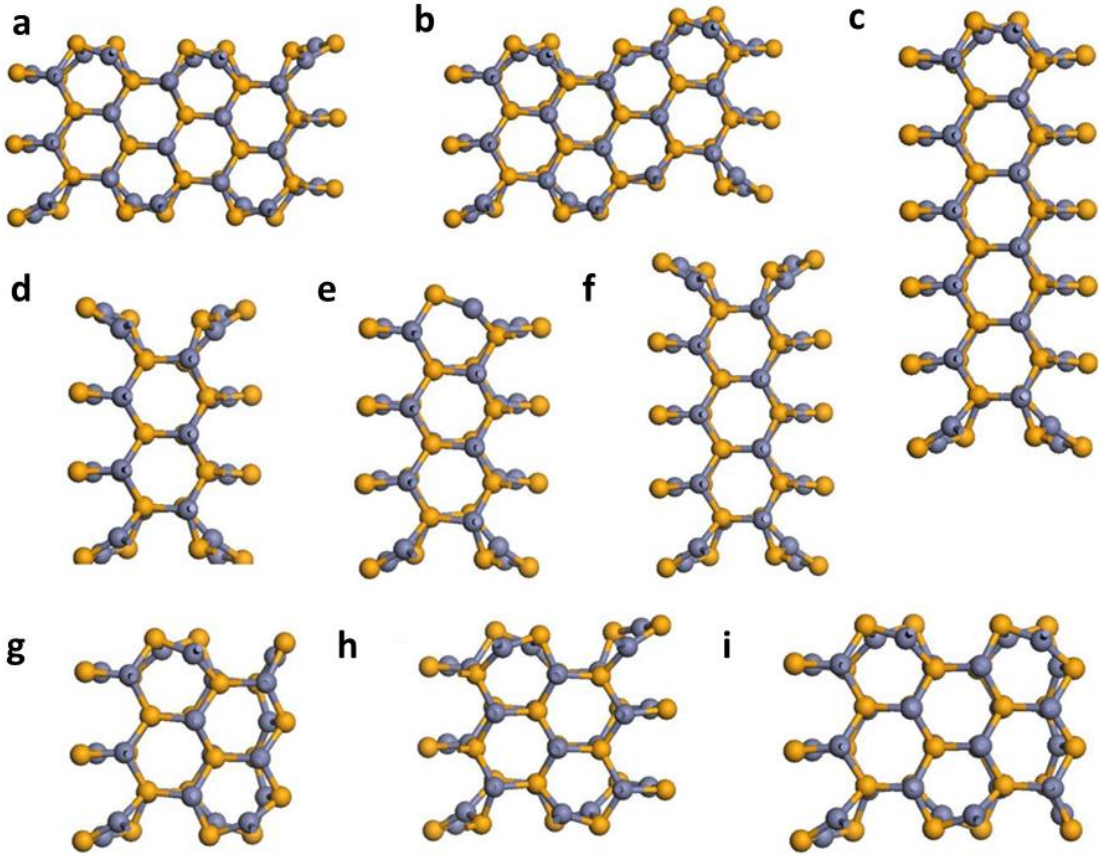

Figure A1-18. The optimized structures associated with the diffusion and nuclei construction during the formation of ZnSe nanoplatelets. Optimized structures corresponding to the figures in the main article: **a**, Figure 5A. **b**, Figure 5B. **c**, Figure 5C. **d**, Additional seven layers of Figure 5D1. **e**, Additional eight layers of Figure 5D1. **f**, Additional nine layers of Figure 5D1. **g**, Additional seven layers of Figure 5D2, **h**, Additional eight layers of Figure 5D2. **i**, Additional nine layers of Figure 5D2.

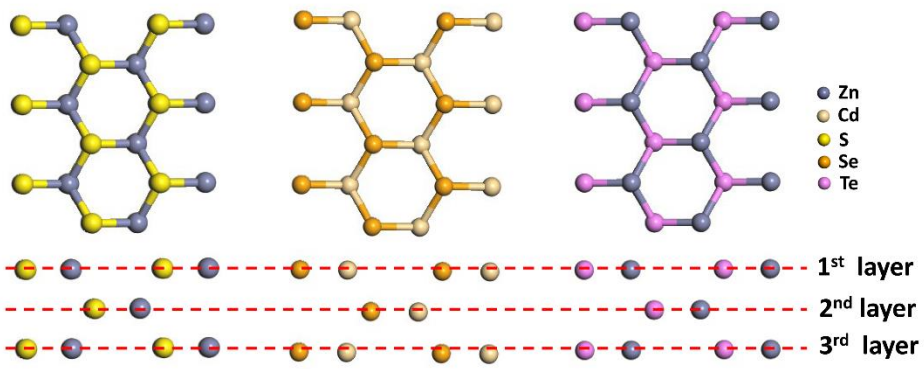

Figure A1-19. Formation energies of diffusion and nuclei construction of ZnS, CdSe and ZnTe along $[11\bar{2}0]$ for three additional layers.

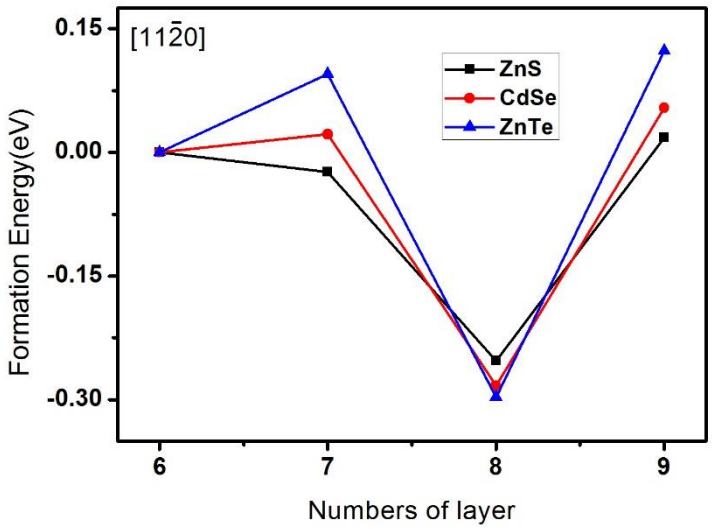

Figure A1-20. The calculated formation energy of ZnS, CdSe and ZnTe.

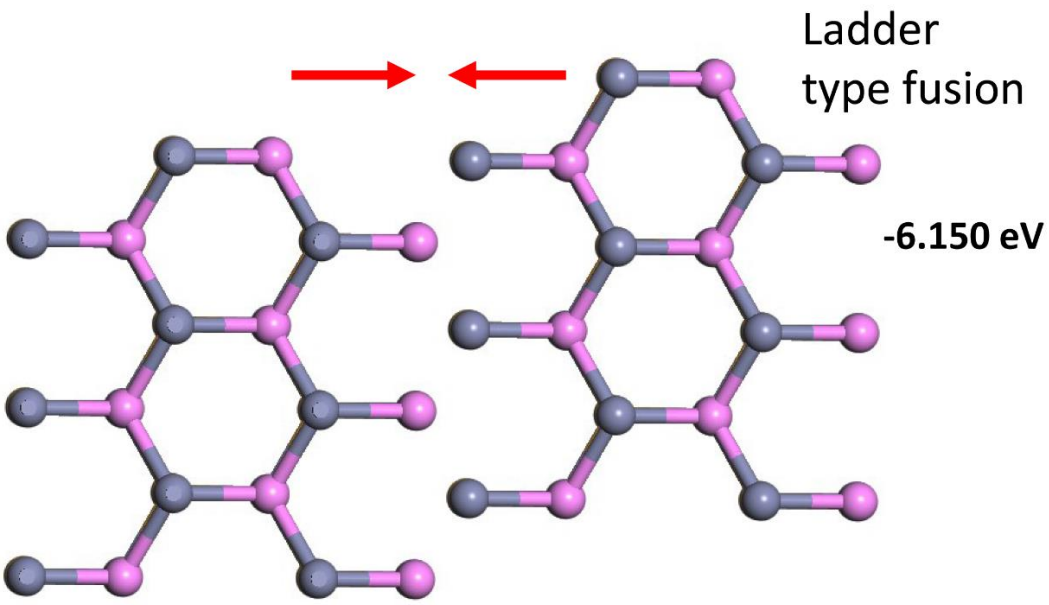

Figure A1-21. Ladder type-oriented fusion of ZnTe.

References

(1) Park, H.; Chung, H.; Kim, W. Synthesis of Ultrathin Wurtzite ZnSe Nanosheets. *Mater. Lett.* **2013**, *99*, 172−175.

(2) Son, J. S.; Wen, X.-D.; Joo, J.; Chae, J.; Baek, S.-il.; Park, K.; Kim, J. H.; An, K.; Yu, J. H.; Kwon, S. G.; Choi, S.-H.; Wang, Z.; Kim, Y.-W.; Kuk, Y.; Hoffmann, R.; Hyeon, T. Large-Scale Soft Colloidal Template Synthesis of 1.4 nm Thick CdSe Nanosheets. *Angew. Chem. Int. Ed.* **2009**, *48*, 6861−6864.

(3) Kresse, G.; Furthmüller, J. Efficient Iterative Schemes for *ab initio* Total-energy calculations using a plane-wave basis set. *Phys. Rev. B* ***1996***, *54*, 11169–11186.

(4) Kresse, G.; Furthmüller, J. Efficiency of ab-initio Total Energy Calculations for Metals and Semiconductors Using a Plane-Wave Basis Set. *Comput. Mater. Sci.* **1996**, *6*, 15−50.

(5) Blöchl, P. E. Projector Augmented-Wave Method. *Phys. Rev. B* **1994**, *50*, 17953−17979.

(6) Perdew, J. P.; Burke, K.; Ernzerhof, M. Generalized Gradient Approximation Made Simple. *Phys. Rev. Lett*. **1996**, *77*, 3865−3868.

(7) Korneeva, I. V. The Hexagonal Modification of Zinc Selenide. *Kristallografiya* **1961**, *6*, 630−631.

(8) Liu, P.-L.; Siao, Y.-J. Ab Initio Study on Preferred Growth of ZnO. *Scr. Mater.* **2011**, *64*, 483−485.

(9) Franchini, C.; Bayer, V.; Podloucky, R.; Parteder, G.; Surnev, S.; Netzer, F. P.*Phys. Rev. B* **2006**, *73*, 155402.

(10) Wang, Y.; Zhou, Y.; Zhang, Y.; Buhro, W. E. Magic-Size II-VI Nanoclusters as Synthons for Flat Colloidal Nanocrystals. *Inorg. Chem.* **2015**, *54*, 1165−1177.

(11) Zhu, R.; Zhao, Q.; Xu, J.; Chen, L.; Leprince-Wang, Y.; Yu, D. Formation Mechanism of Homo-Epitaxial Morphology on ZnO (000 ±1) Polar Surfaces. *CrystEngComm* **2013**, *15*, 4249−4254.

Appendix 2: Supplementary information of Chapter 3

Synthesis yield of ZnSe and ZnS nanoplatelets

For ZnSe:

We use $Zn(NO_3)_2$ $6H_2O$ (100 mmol, 29.7 g) and selenium powder (300 mmol, 23.7 g) as raw materials. The molar ratio of $Zn(NO_3)_2$ $6H_2O$: Se = 1 : 3. We assume that all of the $Zn(NO_3)_2$ $6H_2O$ is converted 100% to the product of ZnSe nanoplatelets, then the final ZnSe nanoplatelets is 100 mmol and the mass is approximately 14.435 g. In our experiment, when the ligand weight is considered, the final weight of ZnSe is 19.9411 g (see manuscript Figure 1D). In order to know the exact amount of ligand in our final product, we conduct thermal property analysis of ZnSe nanoplatelets (See Figure A2-4). As is shown in Figure A2-4a, TGA curves present a dominant weight loss of the samples (48.4% for ZnSe) in the temperature range of 150-460 ^oC accompanied by small endothermic peaks, as marked by red circles on the DTA curves. The weight loss and endothermic feature correspond to the evaporation of amine ligands.

So the actual weight of ZnSe is 19.9411 * (1 - 48.4%) = 10.290 g

The synthesis yield of ZnSe nanoplatelets is 10.290/14.435 = 71.3%

For ZnS:

We use $Zn(NO_3)_2$ $6H_2O$ (100 mmol, 29.7 g) and sulfur powder (300 mmol, 9.6 g) as raw materials. The molar ratio of $Zn(NO_3)_2$ $6H_2O$: S = 1 : 3. We assume that all of the $Zn(NO_3)_2$ $6H_2O$ is converted 100% to the product of ZnS nanoplatelets, then the final ZnS nanoplatelets is 100 mmol and the mass is approximately 9.746 g. In our experiment, when the ligand weight is considered, the final weight of ZnSe is 15.9098 g (see Figure A2-1D). In order to know the exact amount of ligand in our final product, we conduct thermal property analysis of ZnSe nanoplatelets. As is shown in Figure A2-4b, TGA curves present a dominant weight loss of the samples (49.7% for ZnS) in the temperature range of 150-460 ^oC accompanied by small endothermic peaks, as marked by red circles on the DTA curves. The weight loss and endothermic feature correspond to the evaporation of amine ligands.

So the actual weight of ZnSe is 15.9098 g* (1 – 49.7%) = 8.003 g

The synthesis yield of ZnSe nanoplatelets is 8.003/9.746 = 82.1%

Surface ligand exchange of nanoplatelets

Surface ligandexchange of {ZnSe[n-amine]$_x$} nanoplatelets with TBP: In a typical procedure, ZnSe powder (80 mg, 0.55 mmol) was dissolved in toluene (2 mL) with continuous sonication for 30 min, which led to the formation of the transparent solution. Then the clear and colorless solution was transferred to a glove box. In the glove box, TBP (1 mL) was added in the reaction mixture with constant stirring for 60 min at room temperature. The obtained product was directly used or diluted with toluene for further characterizations.

Surface ligand exchange of {ZnS$_{0.75}$Se$_{0.25}$[n-amine]$_x$} nanoplatelets with TBP: 0.5 mL crude solution of$ZnSe_{0.25}S_{0.75}$nanoplatelets was purified with the same purification procedure as that for ZnSe. The purified {$ZnS_{0.75}Se_{0.25}$[n-amine]$_x$} nanoplatelet solids were dispersed in toluene (0.5 mL) and then the solution was transferred to a glove box. In the glove box, TBP (0.25 mL) was added in the solution under constant stirring for 60 min at room temperature. The obtained product was directly used or diluted with toluene for further characterizations.

Surface ligand exchange of {ZnS$_{0.50}$Se$_{0.50}$[n-amine]$_x$} nanoplatelets with TBP: 0.5 mL crude solution of$ZnSe_{0.50}S_{0.50}$nanoplatelet was purified with the same purification procedure as that for ZnSe. The purified {$ZnS_{0.50}Se_{0.50}$[n-amine]$_x$} nanoplatelet solids were dispersed in toluene (0.5 mL) and then the solution was transferred to a glove box. In the glove box, TBP (0.25 mL) was added in the solution under constant stirring for 60 min at room temperature. The obtained product was directly used or diluted with toluene for further characterizations.

Surface ligand exchange of {ZnS[n-amine]$_x$} nanoplatelets with TOP: In a typical procedure, ZnS (2 mg, 0.02 mmol) was dissolved in toluene (0.5 mL) with continuous sonication for 30 min until the solution became transparent. Then the clear and colourless solution was transferred to a glove box. In the glove box, TOP (3.75 mL) was added in the solution with constant stirring for 120 min at room temperature. Then the temperature was raised to 50 ^oC and kept at this temperature for 40 min to remove the toluene before cooling down to the room temperature. The obtained product was directly used for further characterizations.

Surface ligand exchange of {ZnSe[n-amine]$_x$} nanoplatelets with TBP: In a typical procedure, ZnSe (2 mg, 0.014 mmol) was dissolved in toluene (0.5 mL) with continuous sonication for 30 min until the solution became transparent. Then the clear and colourless solution was transferred to a glove box. In the glove box, TBP

(3.75 mL) was added in the solution with constant stirring for 120 min at room temperature. Then the temperature was raised to 50 ^{o}C and kept at this temperature for 40 min to remove the toluene before cooling down to the room temperature. The obtained product was directly used for further characterizations.

ZnSe nanoplatelets synthesized using a variety of amine and zinc precursors

We have employed a variety of alkylamines (Figure A2-2) and zinc precursors (Figure A2-3) to investigate their effects on the formation of ZnSe nanoplatelets, as summarized in Table S1. When single amine including octylamine ($C_8H_{19}N$) (Figure A2-2c), decylamine ($C_{10}H_{23}N$) (Figure A2-2d), and oleylamine (Figure A2-2e), was used in the synthesis, densely stacked ZnSe nanoplatelets with lamellar structures were formed (Figure A2-2c-e). The synthesis using hexylamine as the solvent produced white powders without any distinct absorption features that are associated with ZnSe. A mixed solvent containing oleylamine with a short chain amine (e.g. hexylamime, octylamine and decylamine) in the synthesis produced nearly monodisperse ZnSe nanoplatelets with good dispersity (Figure A2-2f-h). Synthesis using different zinc precursors, i.e. $Zn(NO_3)_2$ $6H_2O$ (Figure A2-3a), ZnI_2 (Figure A2-3b), and $Zn(ac)_2$ $2H_2O$ (Figure A2-3c), also produced monodisperse ZnSe nanoplatelets. All of the obtained nanoplatelets show sharp absorption features with the first exciton peak at 348 nm (Figures A2-2b and A2-3d), indicating their uniform thickness of the basal plane of ZnSe nanoplatelets.

Thermal property analysis of nanoplatelets

Figure A2-4a and 4b show TGA-DTA curves of ZnS and ZnSe nanoplatelets, respectively. In the first scan conducted in N_2 from room temperature to 743 ^oC, TGA curves present a dominant weight loss of the samples (49.7% for ZnS and 48.4% for ZnSe) in the temperature range of 150-460 ^oC accompanied by small endothermic peaks, as marked by red circles on the DTA curves. The weight loss and endothermic feature correspond to the evaporation of decylamine (boiling point 220.5 ^oC)[1] and oleylamine (boiling point 350 ^oC)[2] ligands. Thermal property measurements conducted in air show a second weight loss (8.8% for ZnS and 20.6% for ZnSe) in the TGA curves which are accompanied by sharp exothermic peaks (635 ^oC for ZnS and 465 ^oC for ZnSe). Close inspections on the second weight loss and the exothermic feature suggest that zinc chalcogenide nanoplatelets convert into ZnO due to oxidation in air at elevated temperatures.

$$2ZnS + 3O_2 \rightarrow 2ZnO + 2SO_2\uparrow \text{ (Equation 1)}$$

Theoretical weight loss for ZnS based on Equation 1:

$$\frac{W_{ZnS}-W_{ZnO}}{W_{original\ powder}} = \frac{(1-49.7\%)*1-\frac{81.41}{97.47}*(1-49.7\%)*1}{1} = 8.3\%$$

$$2ZnSe + 3O_2 \rightarrow 2ZnO + 2SeO_2\uparrow \text{ (Equation 2)}$$

Theoretical weight loss for ZnSe based on Equation 2:

$$\frac{W_{ZnSe}-W_{ZnO}}{W_{original\ powder}} = \frac{(1-48.4\%)*1-\frac{81.41}{144.35}*(1-48.4\%)*1}{1} = 22.5\%$$

The values of measured weight loss for ZnS and ZnSe nanoplatelets conducted in air are 8.8% and 20.6%, being in consistent with those of the theoretical weight loss of 8.3% and 22.5%, respectively. This consistency confirms that the presence of the exothermic peaks on the DTA curves corresponds to the decomposition and oxidization of zinc chalcogenide nanoparticles in air at elevated temperatures. Compared with ZnSe nanoplatelets, ZnS nanoplatelets are more stable in air and they do not show evident oxidization below 560 ^oC.

TEM and HAADF-STEM characterizations of nanoplatelets

TEM (Figure A2-5a, A2-5c) and HAADF-STEM images (Figure A2-5b, A2-5d) of zinc chalcogenide nanoplatelets with a large population are used to illustrate the particles shown in Figure 3-1e, 3-1f, 3-1h and 3-1i in the main article are representative of the entire samples. Sizing histograms on both ZnS and ZnSe nanoplatelets (Figure A2-5e, A2-5f) show narrow size distributions.

Lateral size control of ZnSe nanoplatelets

Sizing histograms of ZnSe nanoplatelets (Figure A2-6) show narrow size distributions, indicating the monodispersity of ZnSe nanoplatelets.

Contraction of lattice of zinc chalcogenide nanoplatelets induced by surface ligands

In order to provide further insight on the amine ligand induced compressive stress that leads to the contraction of lattices of zinc chalcogenide nanoplatelets, we interpreted these results based on theory of elasticity.[3] For a linearly elastic material, the bulk modulus, K, is defined as the ratio of pressure increment, ΔP, required to induce unit change in volume per unit volume, $\Delta V/V$.

$$K = (\Delta P/((\Delta V)/V) \text{ (Equation 3)}$$

$$K = E/(3(1 - 2\nu)) \text{ (Equation 4)}$$

Wherein E is modulus of elasticity, ν is Poisson's ratio.

$$\Delta V/V = 3((\Delta a)/a) + 3((\Delta a)/a)^{\wedge 2} + ((\Delta a)/a)^{\wedge 3} \text{(Equation 5)}$$

If we ignore the terms with square and cubic of $\Delta a/a$ for small strain in Equation 5, we obtain the following equation.

$$\Delta P = (E/(1 - 2\nu))/((\Delta a)/a) \text{ (Equation 6)}$$

$E_{ZnSe(bulk)}$ = 67.2 GPa, $E_{ZnS(bulk)}$ = 74.5 GPa; ν_{ZnSe} = 0.28, ν_{ZnS} = 0.27.[4-7]

The d(0002) spacings calculated based on the XRD patterns in Figure 1n in the main article are d_{ZnSe} = 0.32206 nm, and d_{ZnS} = 0.29901 nm.

The d(0002) spacings in the standard XRD patterns of wurtzite ZnSe and for ZnS are 0.32501 nm and 0.31292 nm, respectively.

ΔP_{ZnSe} = 1.38 GPaΔP_{ZnS} = 5.91 GPa

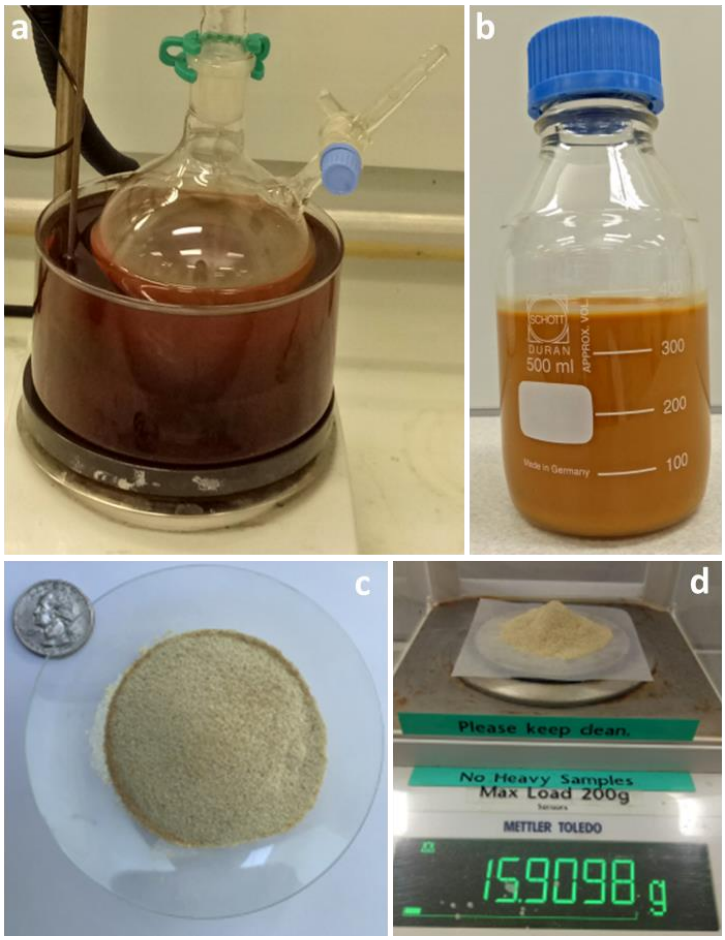

Figure A2-1. One-pot ultralarge scale synthesis of ZnS nanoplatelets under ambient conditions. a, Reaction setup. **b**, Crude solution. **c**,**d**, Photographs of a dried sample, showing the Petri dish containing 15.9 g ZnS nanoplatelets. A US quarter dollar coin is given in (**c**) for comparison.

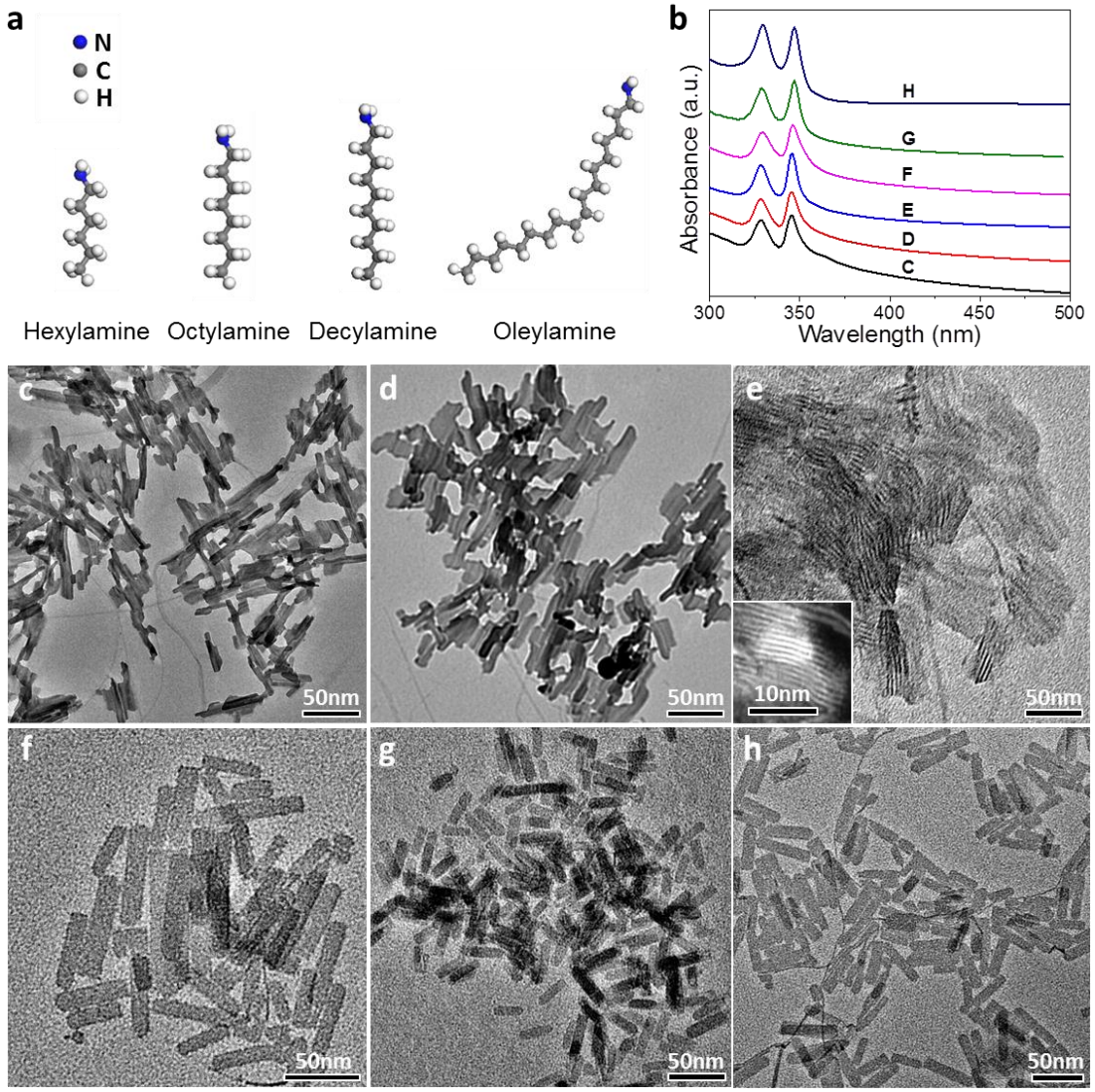

Figure A2-2. ZnSe nanoplatelets synthesized using different alkylamines. a, Schematic illustration of amines, including hexylamine ($C_6H_{15}N$), octylamine ($C_8H_{19}N$), decylamine ($C_{10}H_{23}N$) and oleylamine ($C_{18}H_{37}N$). **b**, Absorption spectra of ZnSe nanoplatelets with an absorption onset at 348-350 nm, suggesting the uniform thickness of nanoplatelets. **c-h**, TEM images of ZnSe nanoplatelets synthesized in (c) Octylamine, (d) Decylamine, (e) Oleylamine, (f) Hexylamine + oleylamine, (g) Octylamine + oleylamine, and (h) Decylamine + oleylamine. Inset in (e) is the HAADF-STEM image of ZnSe nanoplatelets, showing the nanoplatelets are standing on their edges with a uniform thickness of ~1.39 nm. For a mixed solvent, the volume ratio between the short amine and oleylamine for (f-h) is 1:2.

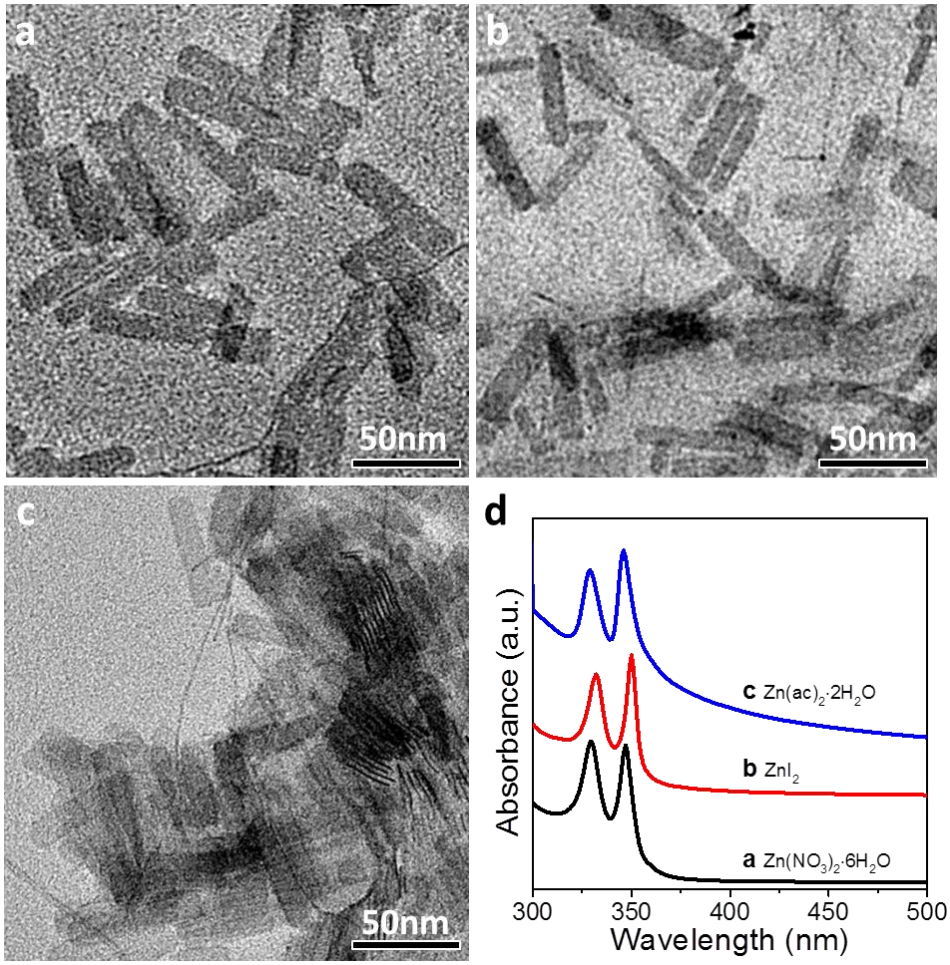

Figure A2-3. ZnSe nanoplatelets synthesized using different zinc precursors. a-c, TEM images of ZnSe nanoplatelets synthesized using **a**, $Zn(NO_3)_2$ $6H_2O$, **b**, ZnI_2, and **c**, $Zn(ac)_2$ $2H_2O$ as the zinc precursor. **d**, Absorption spectra of ZnSe nanoplatelets with the absorption onset at 348 nm, suggesting the uniform thickness of nanoplatelets.

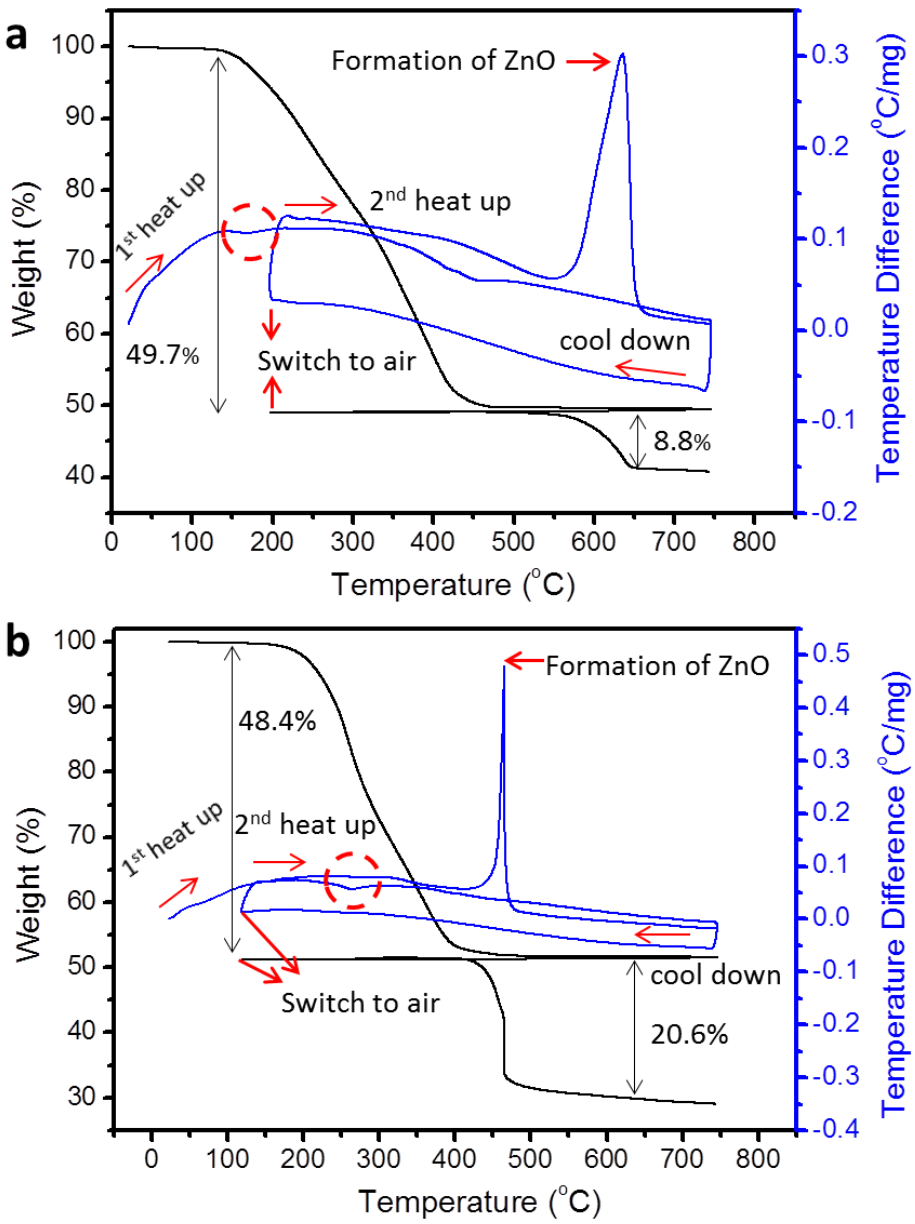

Figure A2-4. Thermal gravimetric analysis-differential thermal analysis (TGA-DTA) of nanoplatelets. a, ZnS. **b**, ZnSe. Each DTA plot contains two scans: the first scan starts from room temperature under N_2 and finishes at 743 °C, then the system cools down to a temperature below 200 °C, from which the second scans starts under air and finishes at 743 °C.

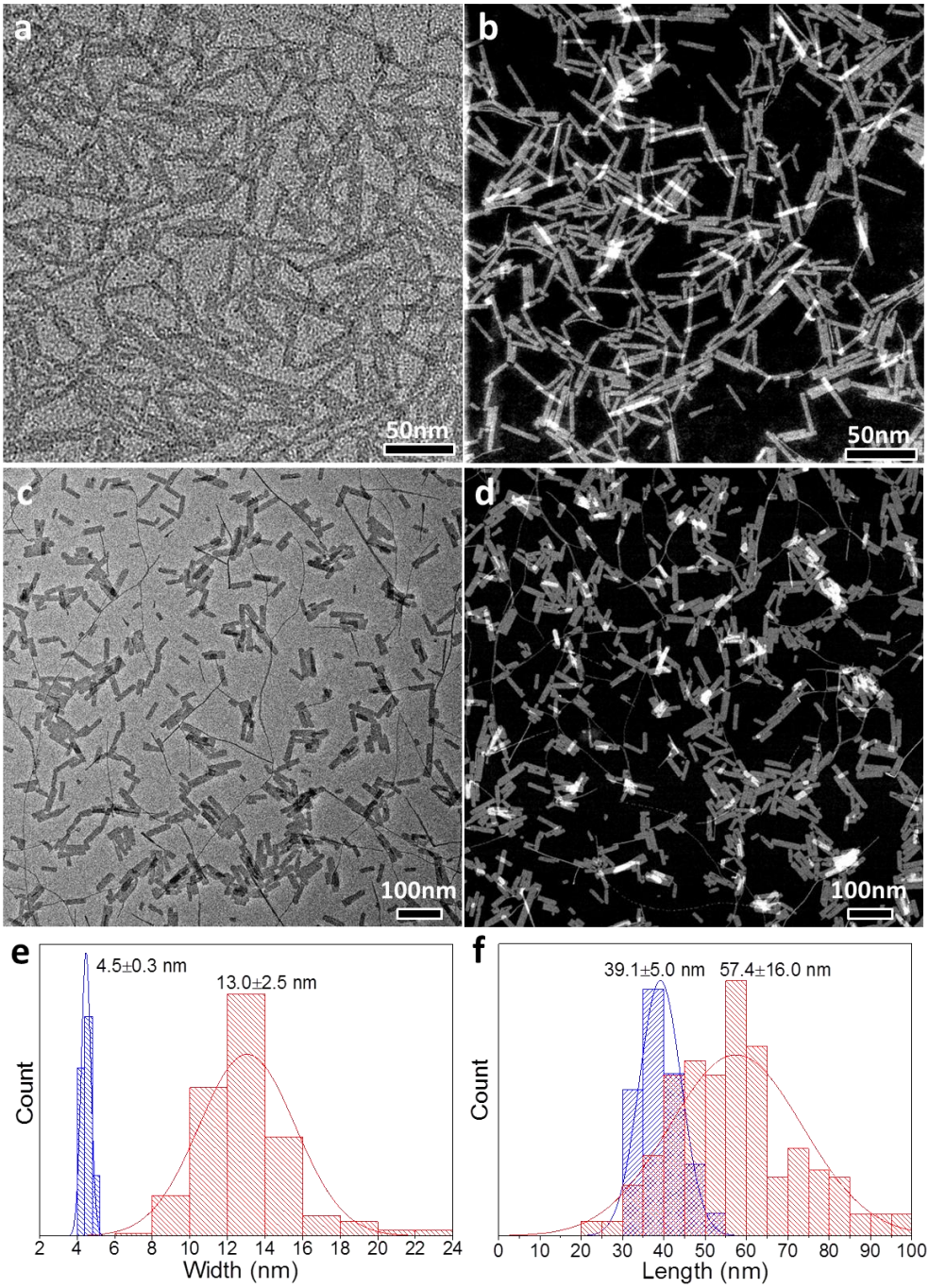

Figure A2-5. Electron microscopy images and sizing histograms of nanoplatelets. **a**, TEM image of ZnS nanoplatelets. **b**, HAADF-STEM image of ZnS nanoplatelets. **c**, TEM image of ZnSe nanoplatelets. **d**, HAADF-STEM image of ZnSe nanoplatelets. Size histograms (**e**) width and (**f**) length of nanoplatelets. Blue and red columns correspond to (a,b) ZnS and (c,d) ZnSe nanoplatelets, respectively.

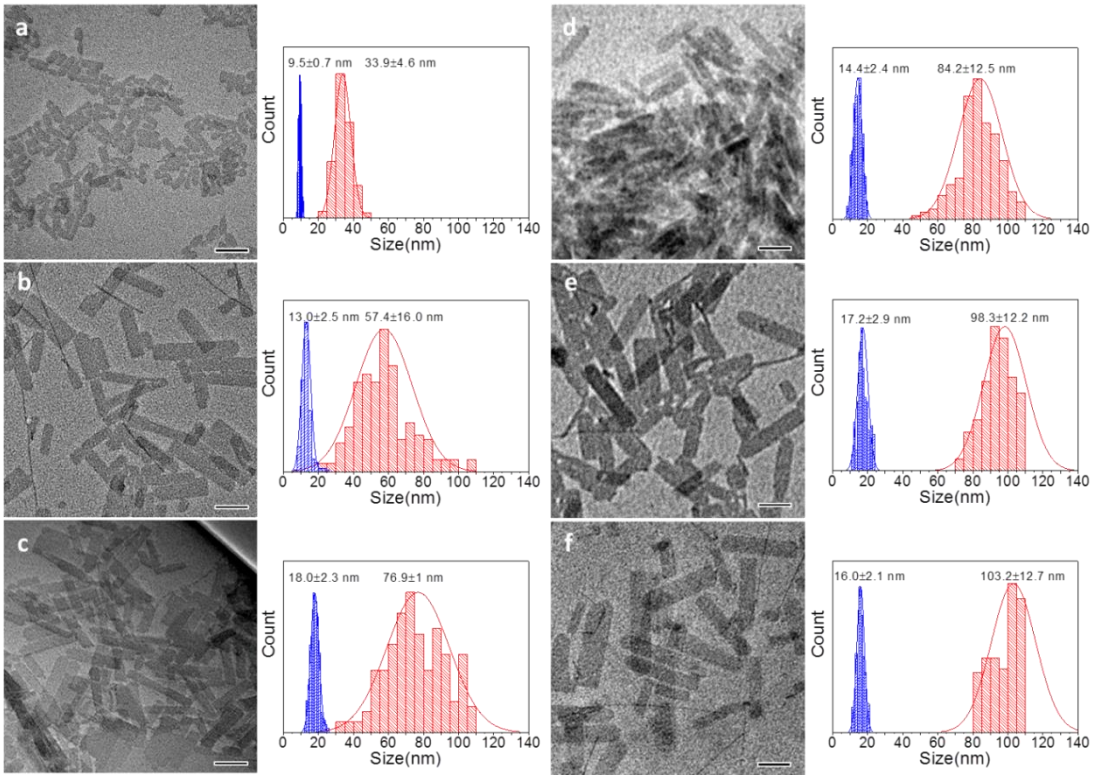

Figure A2-6. Lateral size control of ZnSe nanoplatelets. a, 9.5±0.7 nm × 33.9±4.6 nm. **b**, 13.0±2.5 nm × 57.4±16.0 nm. **c**, 18.0±2.3 nm × 76.9±17.9 nm. **d**, 14.4±2.4 nm × 84.2±12.5 nm. **e**, 17.2±2.9 nm × 98.3±12.2 nm. **f**, 16.0±2.1 nm × 103.2±12.7 nm. The sizing histogram of each sample is shown on right side of its TEM image. All scale bars are 50 nm.

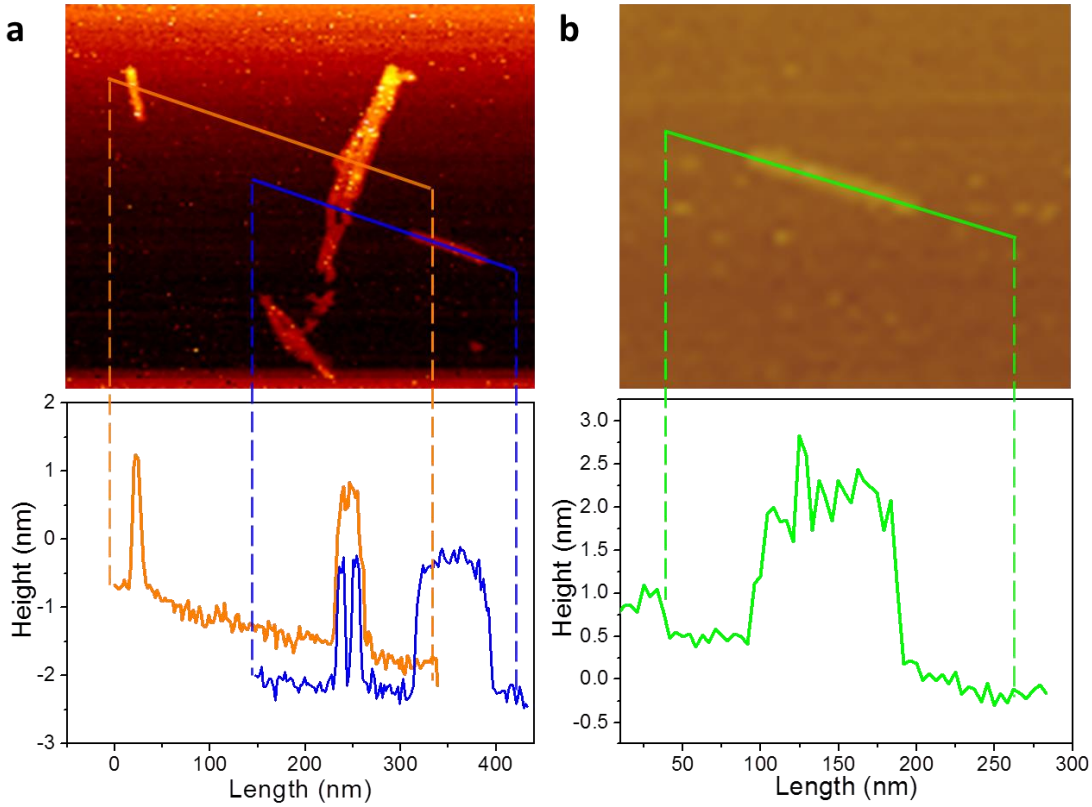

Figure A2-7. AFM images and cross-section height analyses of individual zinc chalcogenide nanoplatelets. a, ZnS. **b**, ZnSe. AFM images show the lateral elongation of ZnS and ZnSe nanoplatelets and the height analyses confirm the uniform thickness of ~1.39 nm for both ZnS and ZnSe nanoplatelets.

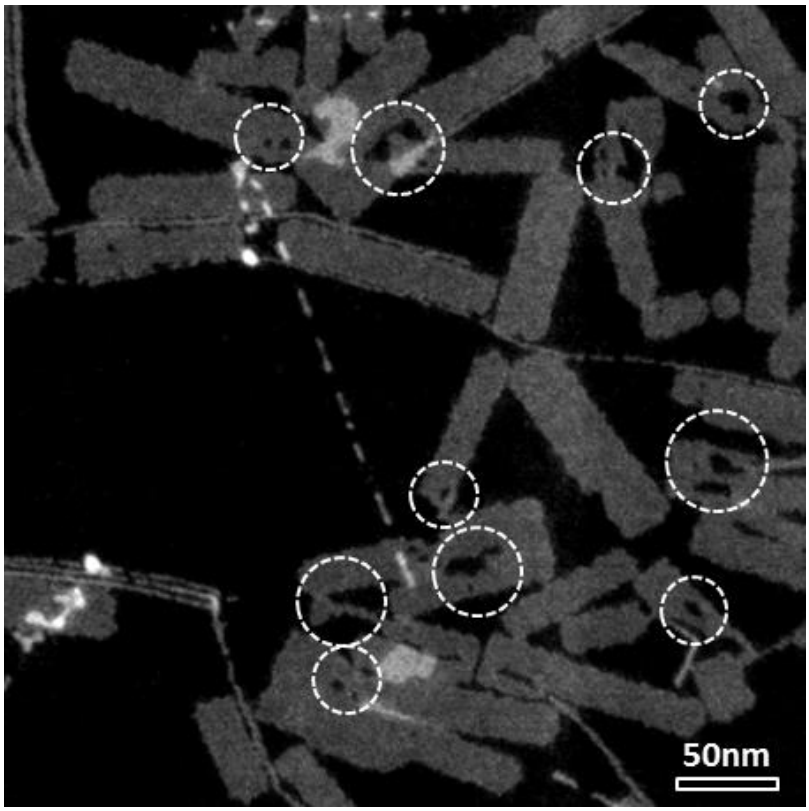

Figure A2-8. HAADF-STEM image of ZnSe nanoplatelets. Hollow feature and patches of nanoplatelets are highlighted by white dashed circles, indicating nanoplatelets may form from small nanoplatelets via oriented attachment.

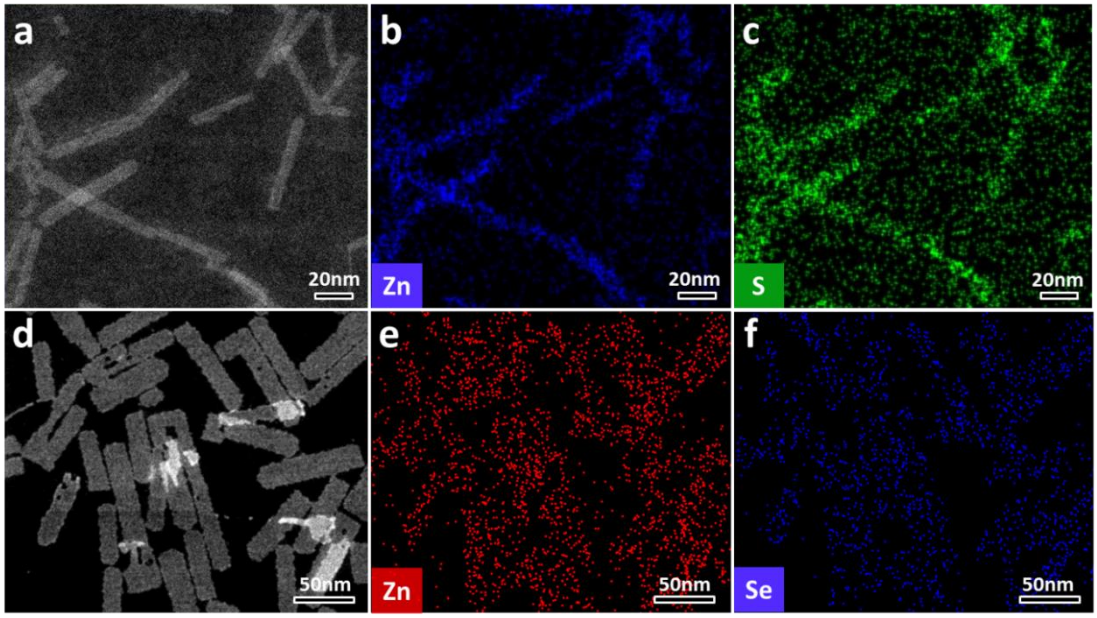

Figure A2-9. HAADF-STEM images and element maps of zinc chalcogenide nanoplatelets. a-c, ZnS nanoplatelets. **d-f**, ZnSe nanoplatelets.

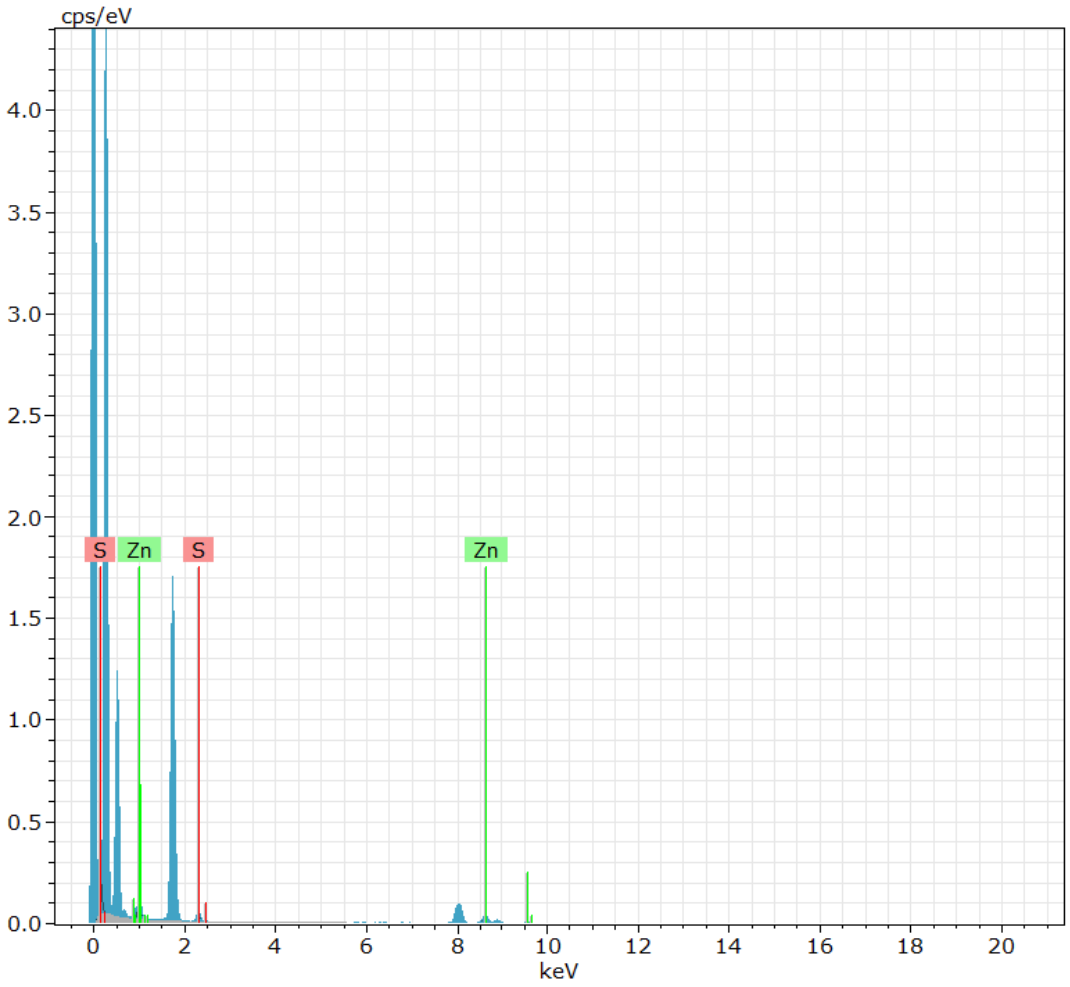

Figure A2-10. STEM-EDX spectrum of ZnS nanoplatelets.

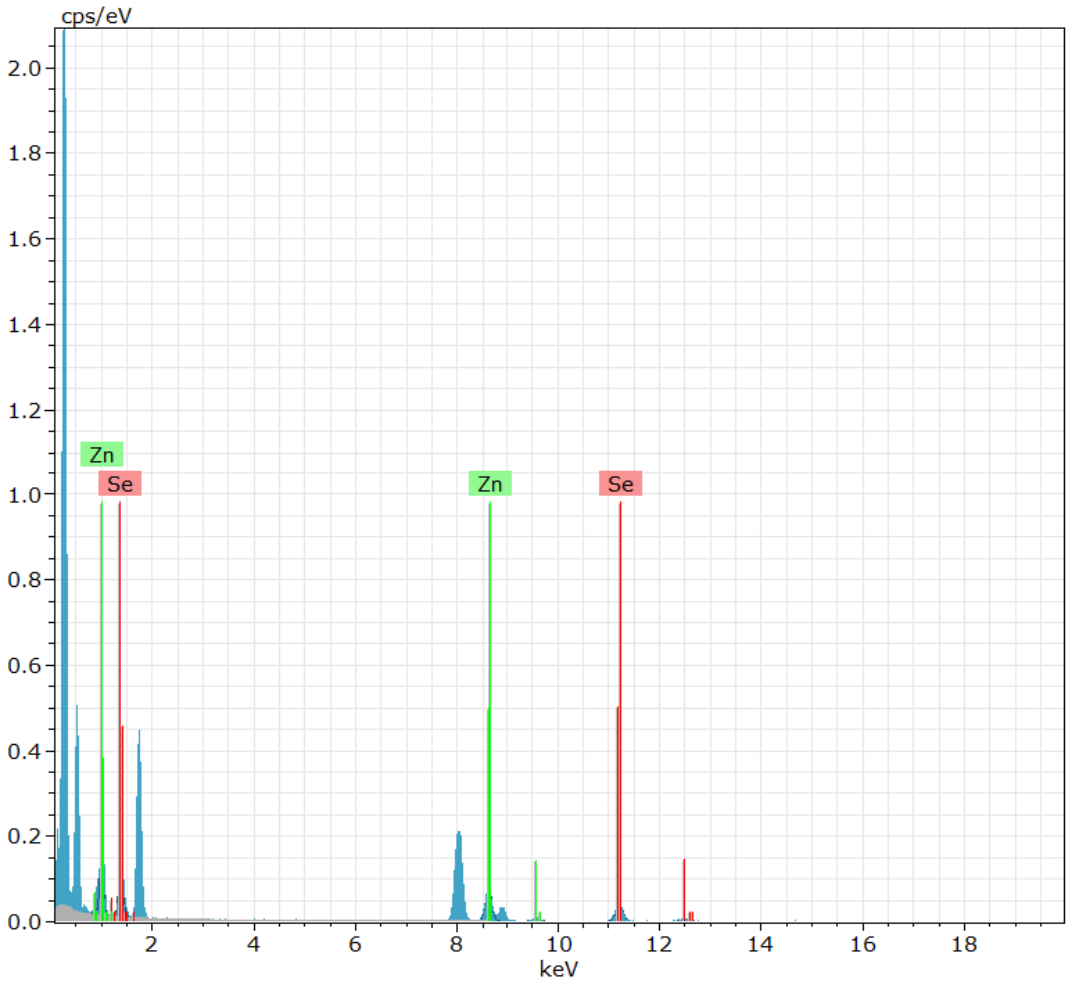

Figure A2-11. STEM-EDX spectrum of ZnSe nanoplatelets.

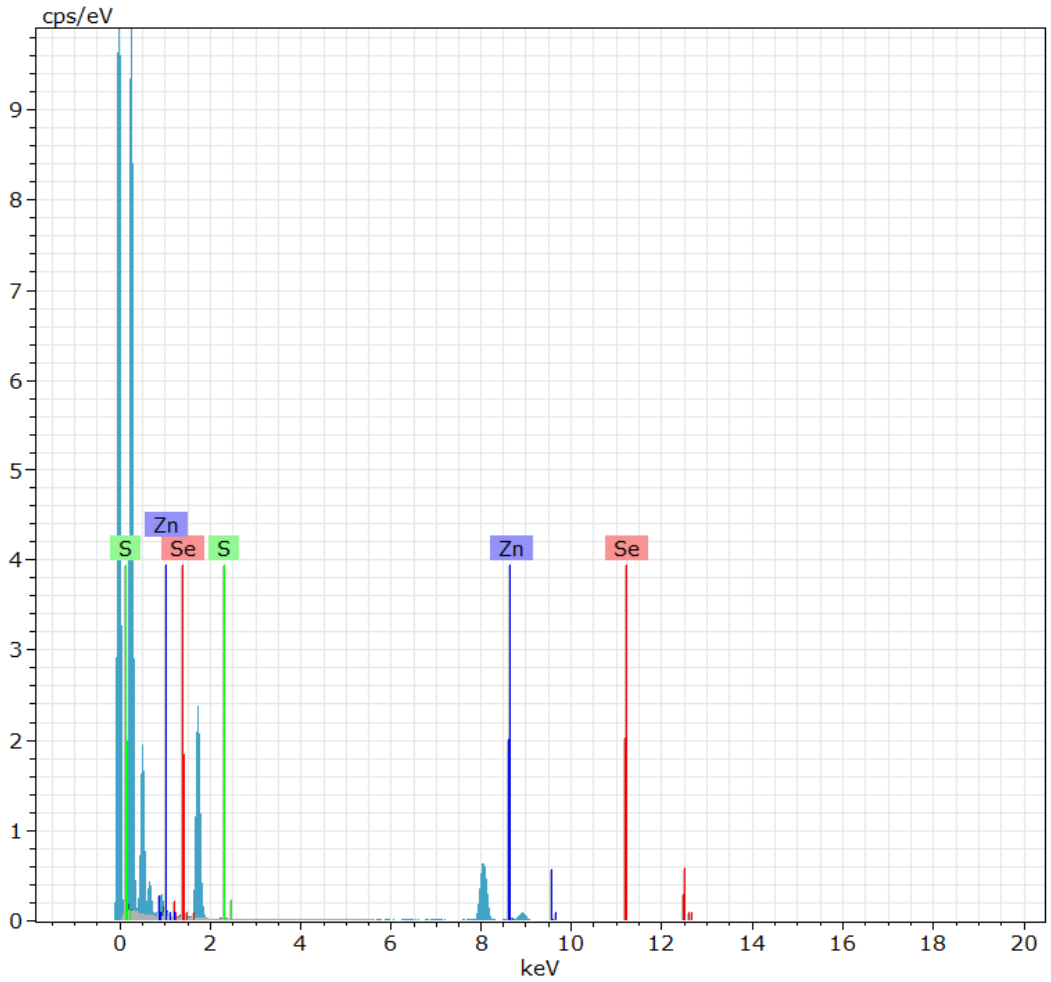

Figure A2-12. STEM-EDX spectrum of alloyed $ZnS_{0.75}Se_{0.25}$ nanoplatelets.

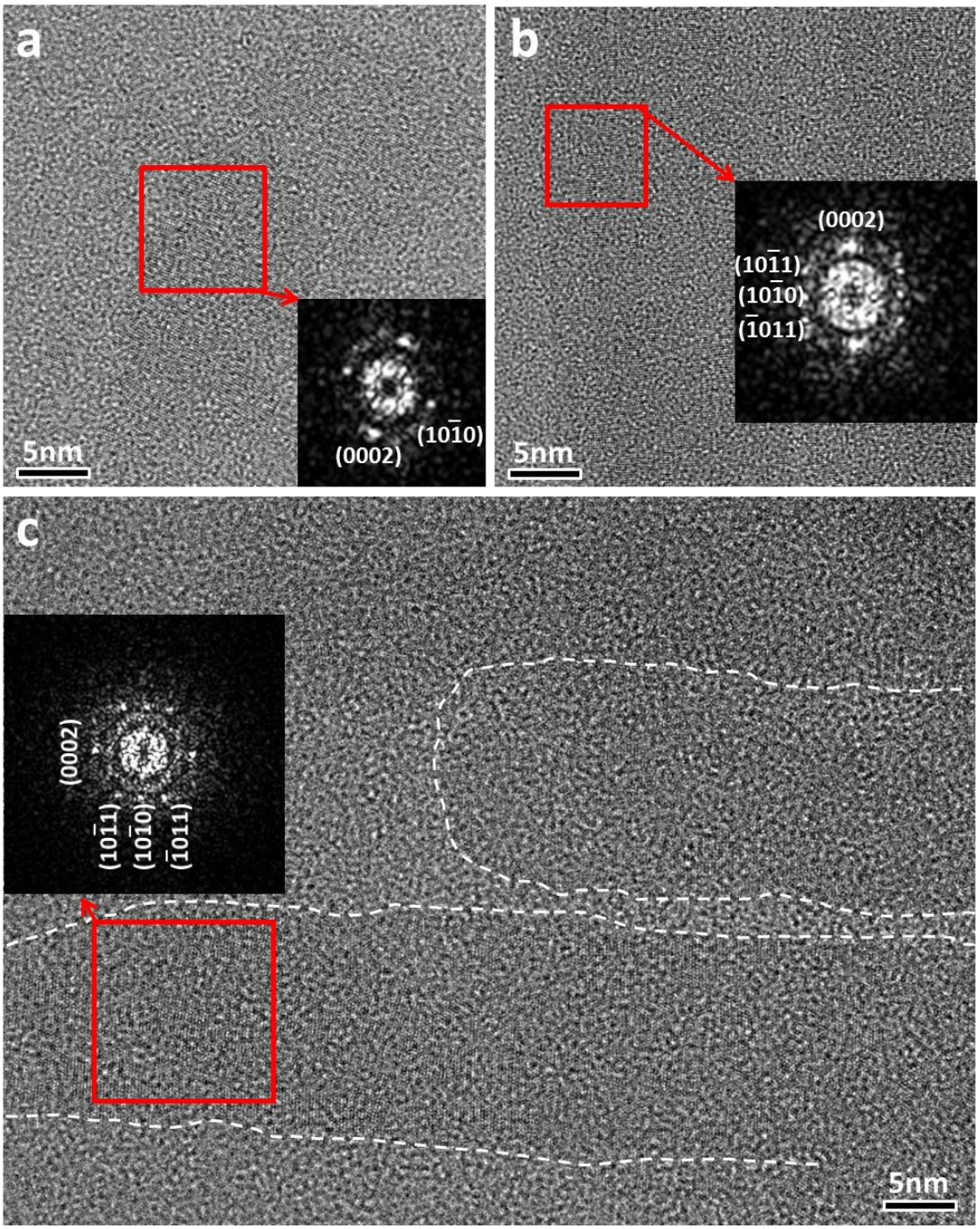

Figure A2-13. HRTEM images and FFT analyses of selected areas of ZnSe nanoplatelets. a-c, HRTEM images of ZnSe nanoplatelets. Inserts show FFT analyses of selected areas, as marked by red rectangles, revealing the crystallographic relations. White dashed lines in (c) are used to guide the boundary of each individual ZnSe nanoplatelet.

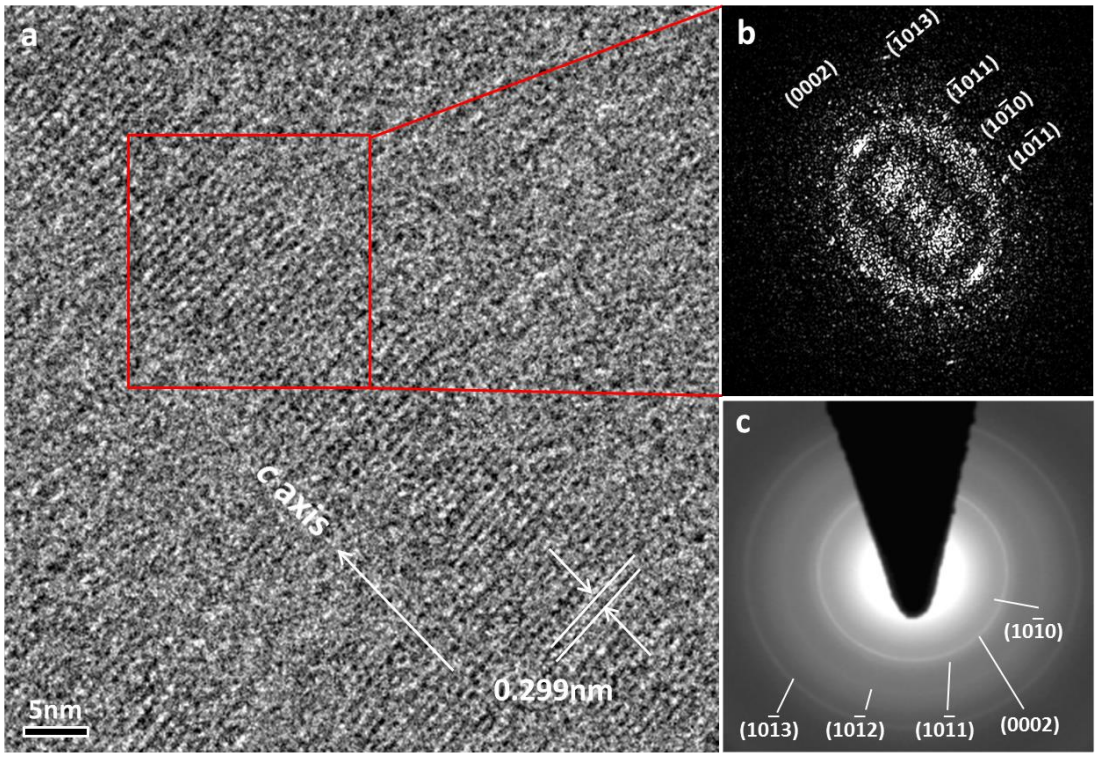

Figure A2-14. Structural characterization of ZnS nanoplatelets. a, HRTEM image. **b**, FFT analysis of a selected area in (a) marked by a red rectangle, revealing the crystallographic relation. The arrow in (a) indicates the orientation of the long axis of ZnS nanoplatelets is parallel to the crystallographic *c*-axis of the wurtzite structure. **c**, SAED patterns showing a set of well-defined rings indexed to wurtzite ZnS.

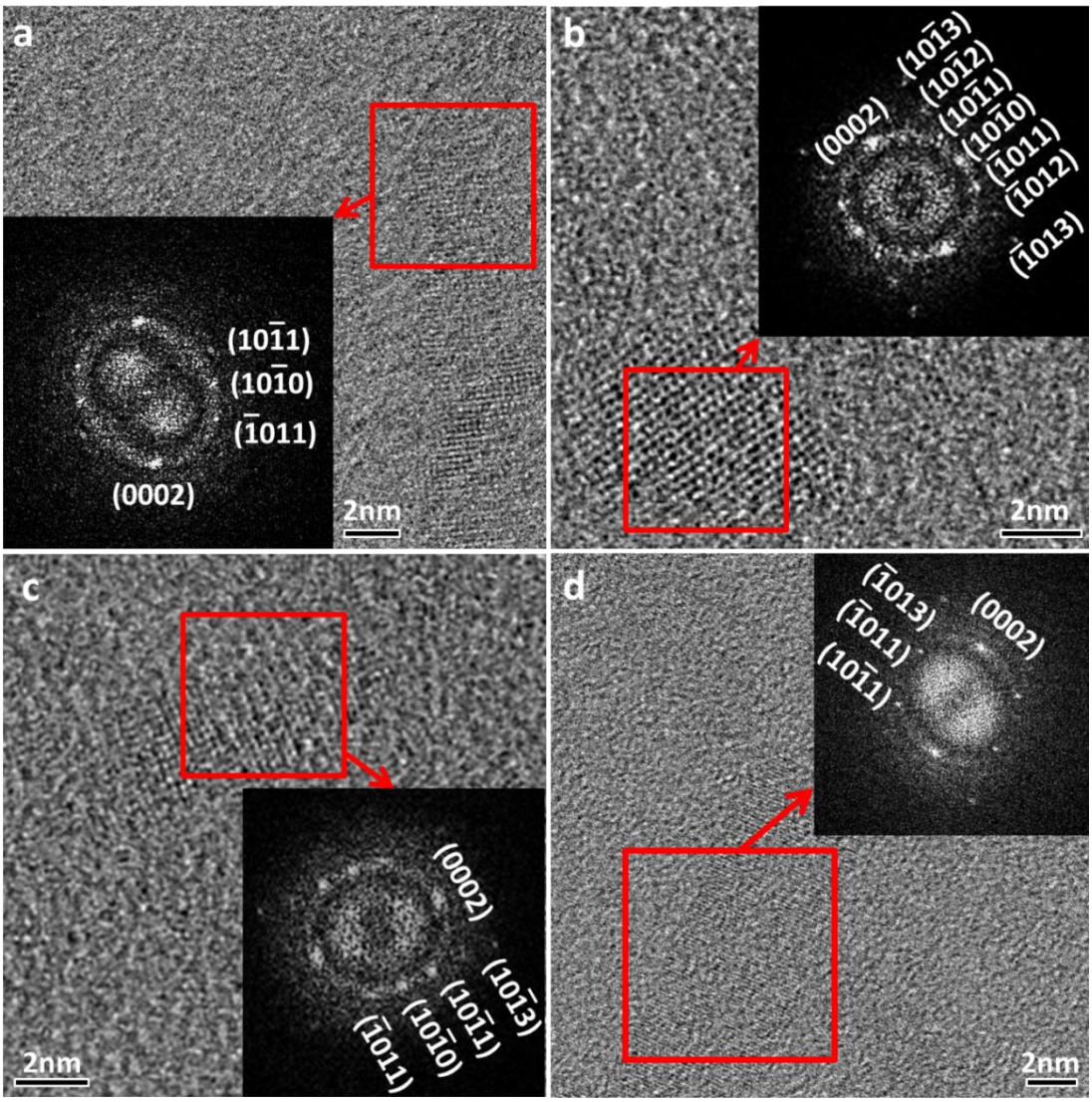

Figure A2-15. HRTEM images and FFT analyses of selected areas of ZnS nanoplatelets. a-d, HRTEM images of ZnS nanoplatelets. Inserts show FFT analyses of selected areas, as marked by red rectangles, revealing the crystallographic relations.

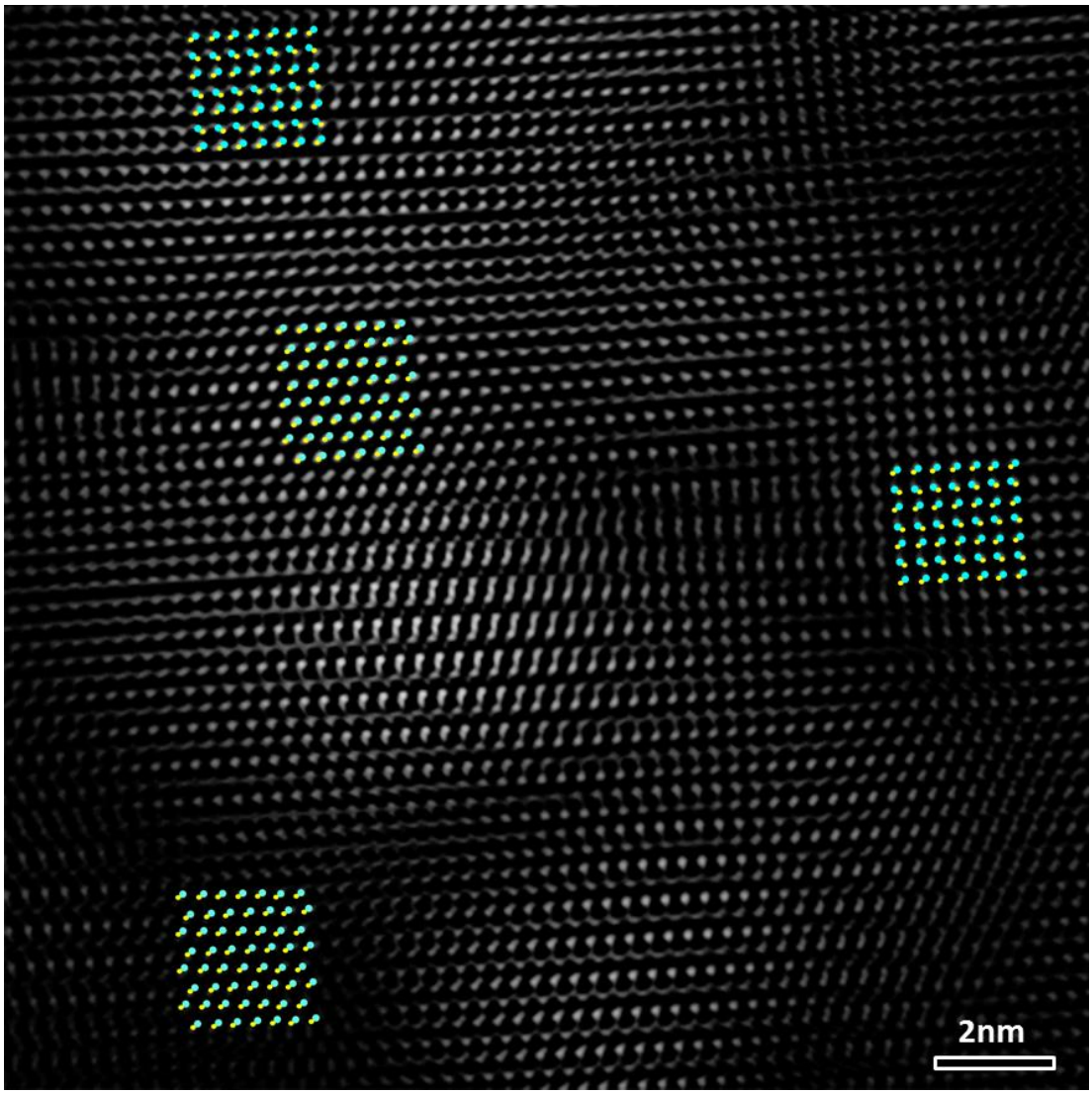

Figure A2-16. FFT reconstructed image of ZnSe nanoplatelets showing both zinc (yellow) and selenium (cyan) atoms are visible.

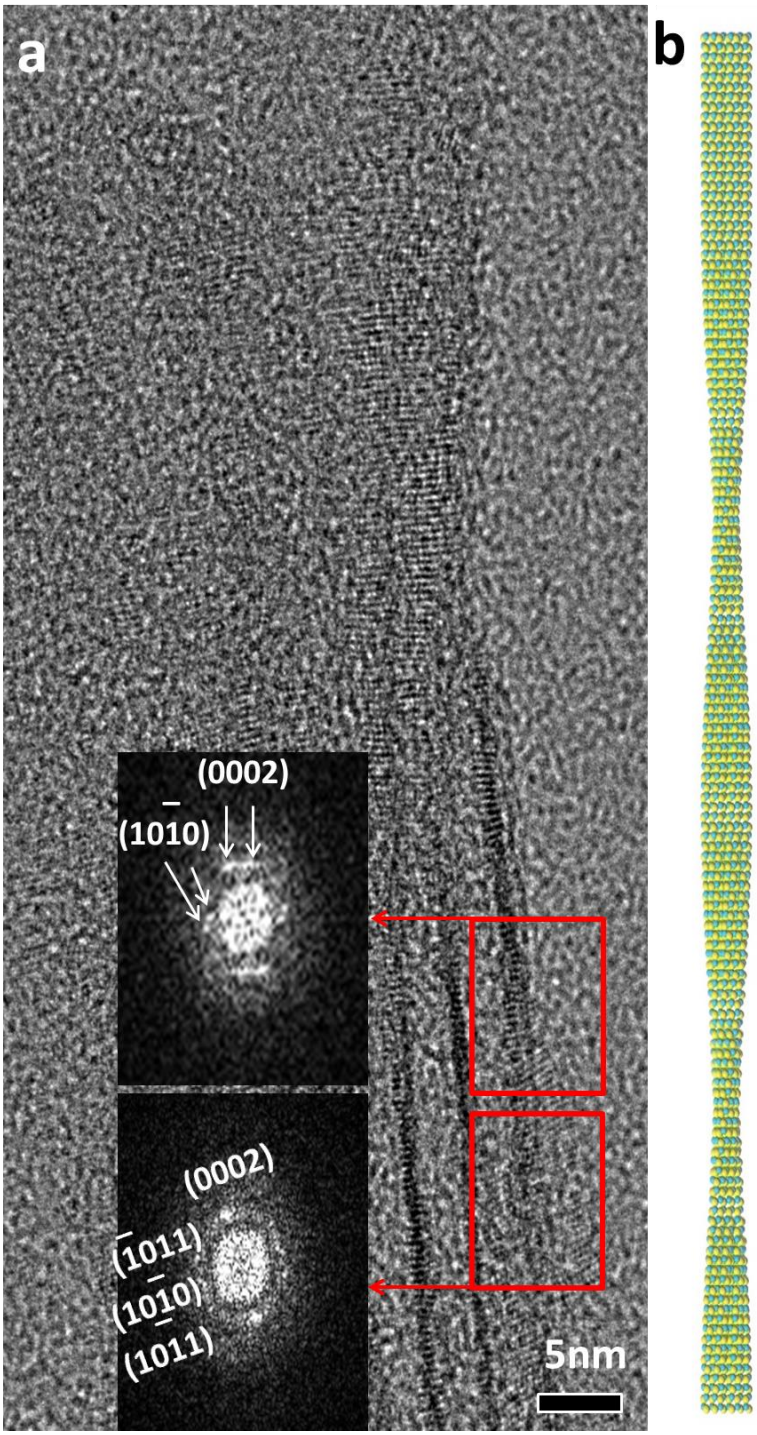

Figure A2-17. HRTEM image and FFT analyses of selected areas of twisted ZnSe nanoplatelets. a, HRTEM image of twisted ZnS nanoplatelets. Inserts show FFT ananlyses of selected areas, as marked by red rectangles, revealing the crystallographic relations. The presence of two sets of diffraction patterns are marked by arrows in inset (top) revealing different orientation of the lattice planes of an individual nanoplatelet due to the twisting. **b**, Scheme of a twisted nanoplatelet associated with (a).

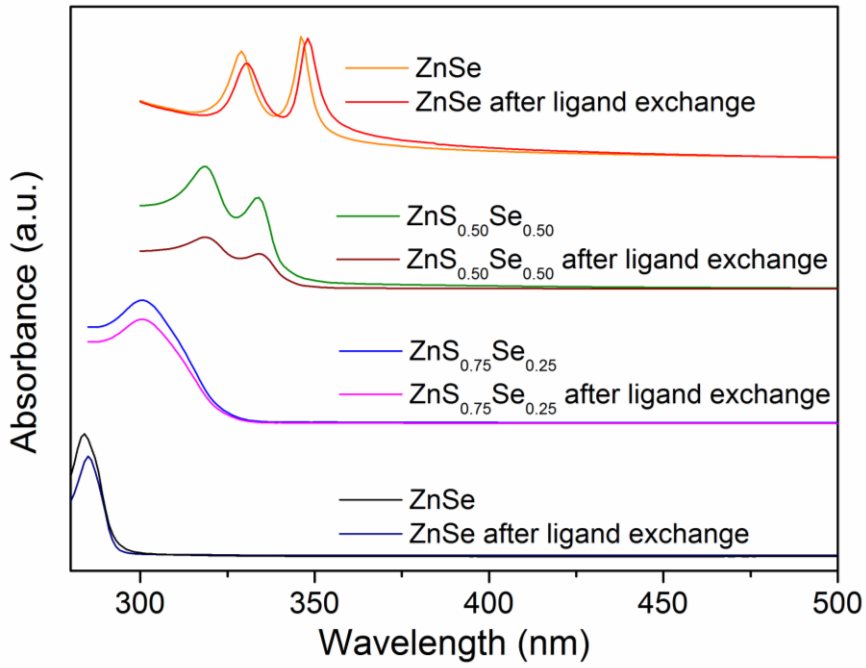

Figure A2-18. Comparison of absorption spectra of nanoplatelets before and after ligand exchange. TBP was used to substitute the surface passivating ligand of alkylamine for ZnSe and alloyed nanoplatelets whereas TOP was used ZnS nanoplatelets. The absorption spectra for all nanoplatelets retain the features of the original nanoplatelets after the surface ligand has been changed into TBP or TOP although a slight red-shift was observed.

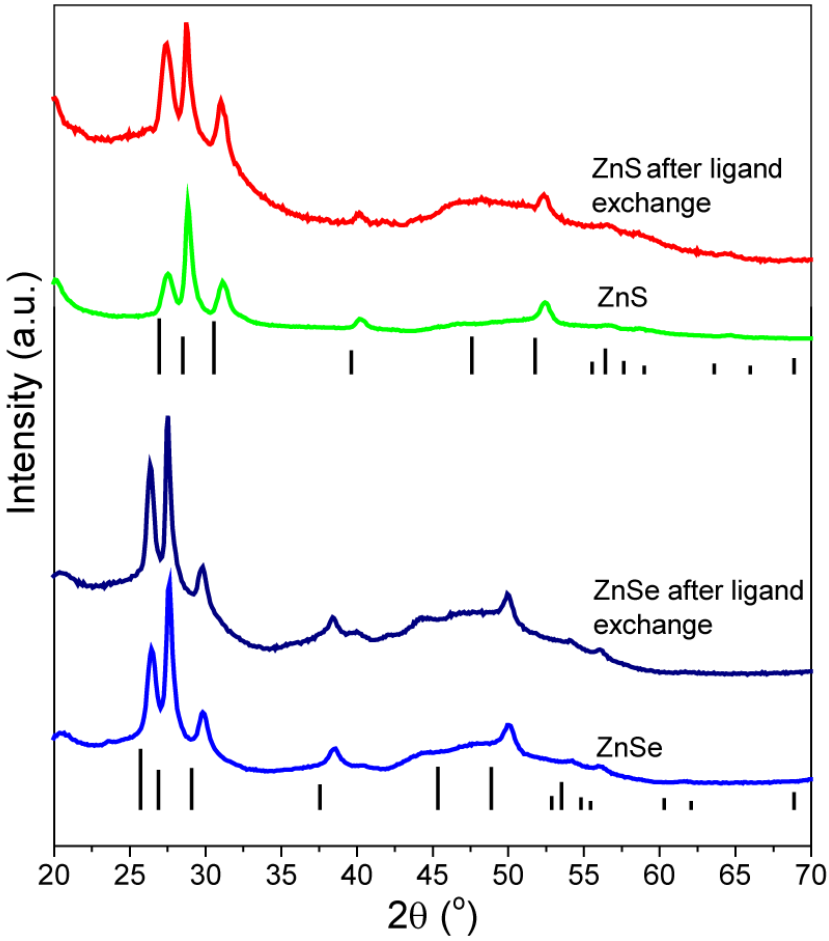

Figure A2-19. Comparison of XRD patterns of nanoplatelets before and after ligand exchange. TBP was used to substitute the surface passivating ligand of alkylamine for ZnSe nanoplatelets whereas TOP was used for the case of ZnS. The diffraction peaks in the XRD patterns for both ZnSe and ZnS after the surface ligand has been changed into TBP or TOP do not show any shift with respect to those of the original nanoplatelets. The standard XRD patterns for both wurtzite ZnSe and ZnS were given for reference.

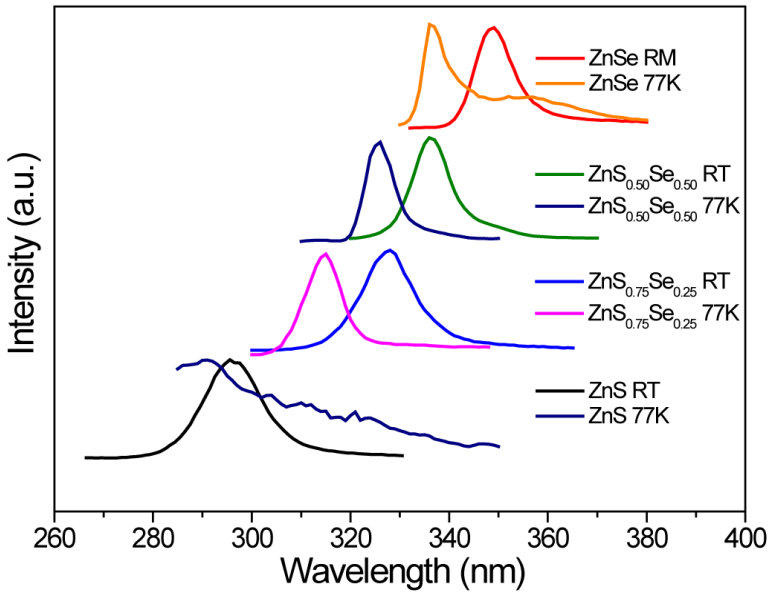

Figure A2-20. Fluorescence emission spectra of nanoplatelets at room temperature (RT) and 77 K. The fluorescence emission spectra for all nanoplatelets at RT are much broader than those at 77 K, with a shift to the lower energy due to thermal broadening.

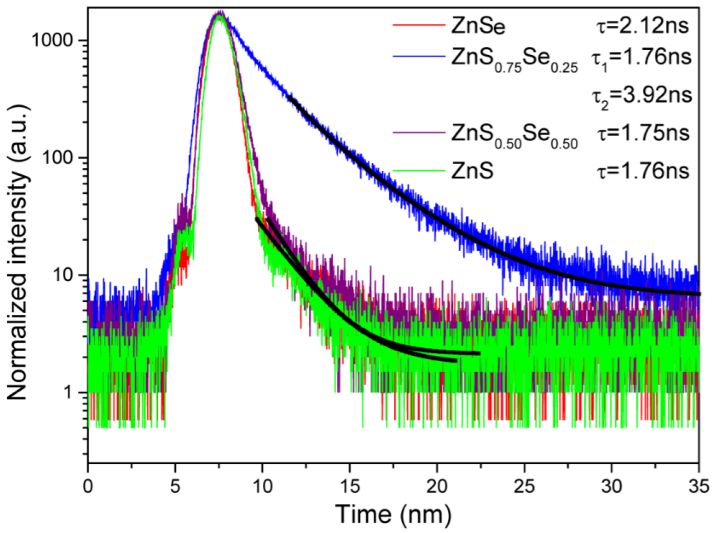

Figure A2-21. Fluorescence lifetime of zinc chalcogenide nanoplatelets at 77 K. The fluorescent emission lifetime curve for $ZnS_{0.75}Se_{0.25}$ (toluene + TBP) at 77 K show a bi-exponential decay, with $\boldsymbol{\tau}_1$= 1.76 ns and $\boldsymbol{\tau}_2$=3.92 ns.

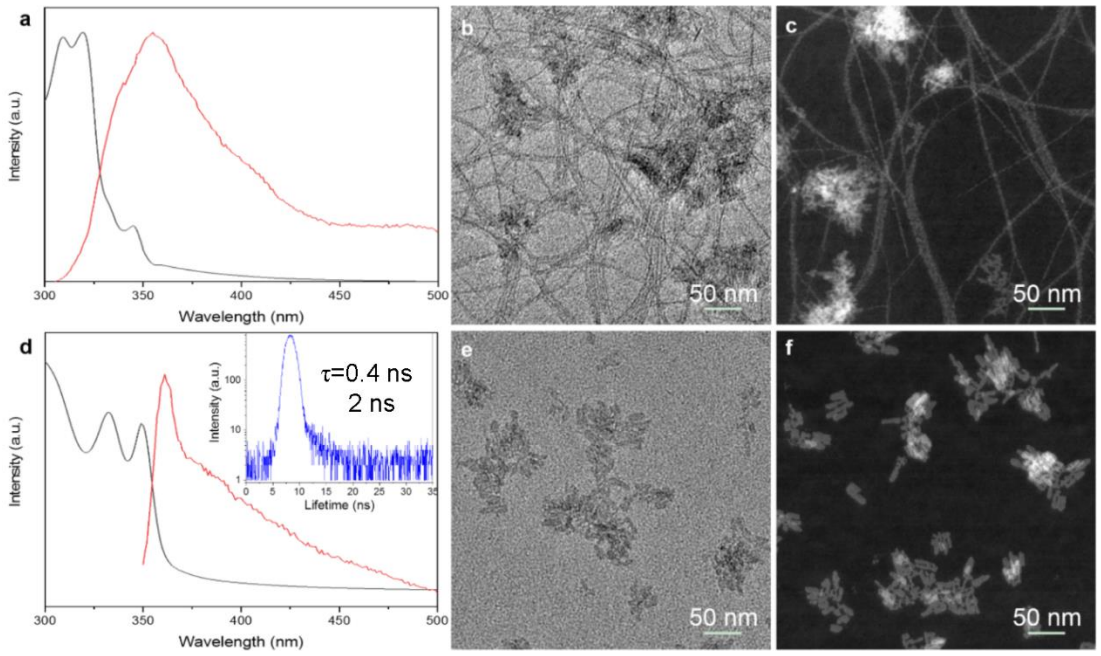

Figure A2-22. Optical spectroscopy, TEM and STEM images of ZnSe bundled wires and small nanoplatelets. a,d, Absorption (black lines) and fluorescence emission (red lines) **b,e**, TEM images and **c,f**, STEM images. Inset in d is the fluorescence lifetime of ZnSe small nanoplatelets at room temperature.

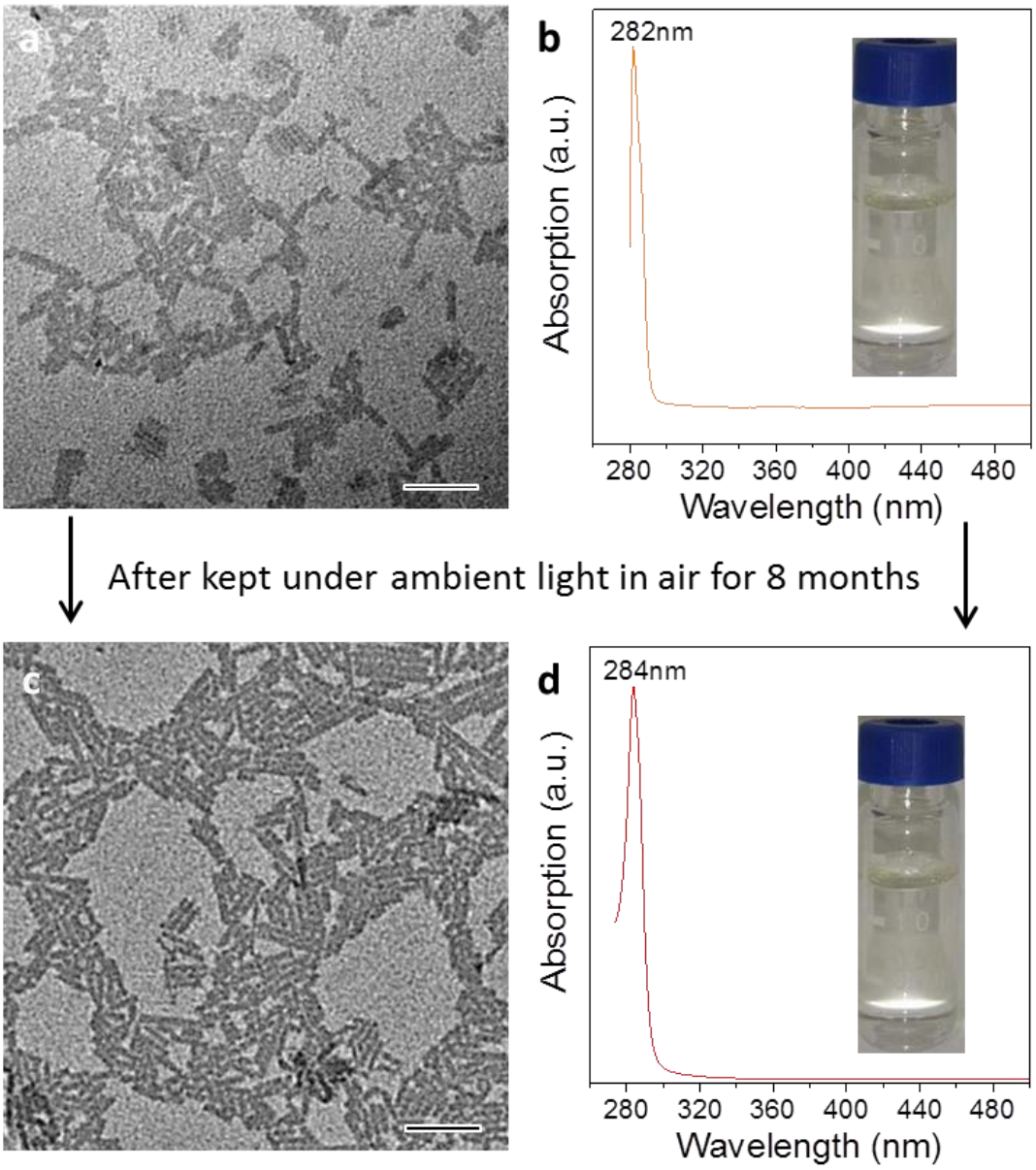

Figure A2-23. Stability of ZnS nanoplatelets under ambient conditions. a, TEM image of freshly made ZnS nanoplatelets. **b**, Absorption spectrum of freshly made ZnS nanoplatelets. Inset shows ZnS nanoplatelets dispersed in toluene. **c**, TEM image of ZnS nanoplatelets after keeping under ambient light in air for 8 months, showing the morphology of nanoplatelets was retained. **d**, Absorption spectrum of ZnS nanoplatelets after keeping under ambient light in air for 8 months, showing the sharp features of the absorption exciton peaks are preserved, although a 2 nm red-shift of the first exciton peak is observed. Inset shows ZnS nanoplatelets dispersed in toluene, showing good dispersity of the nanoparticles. All scale bars are 100 nm.

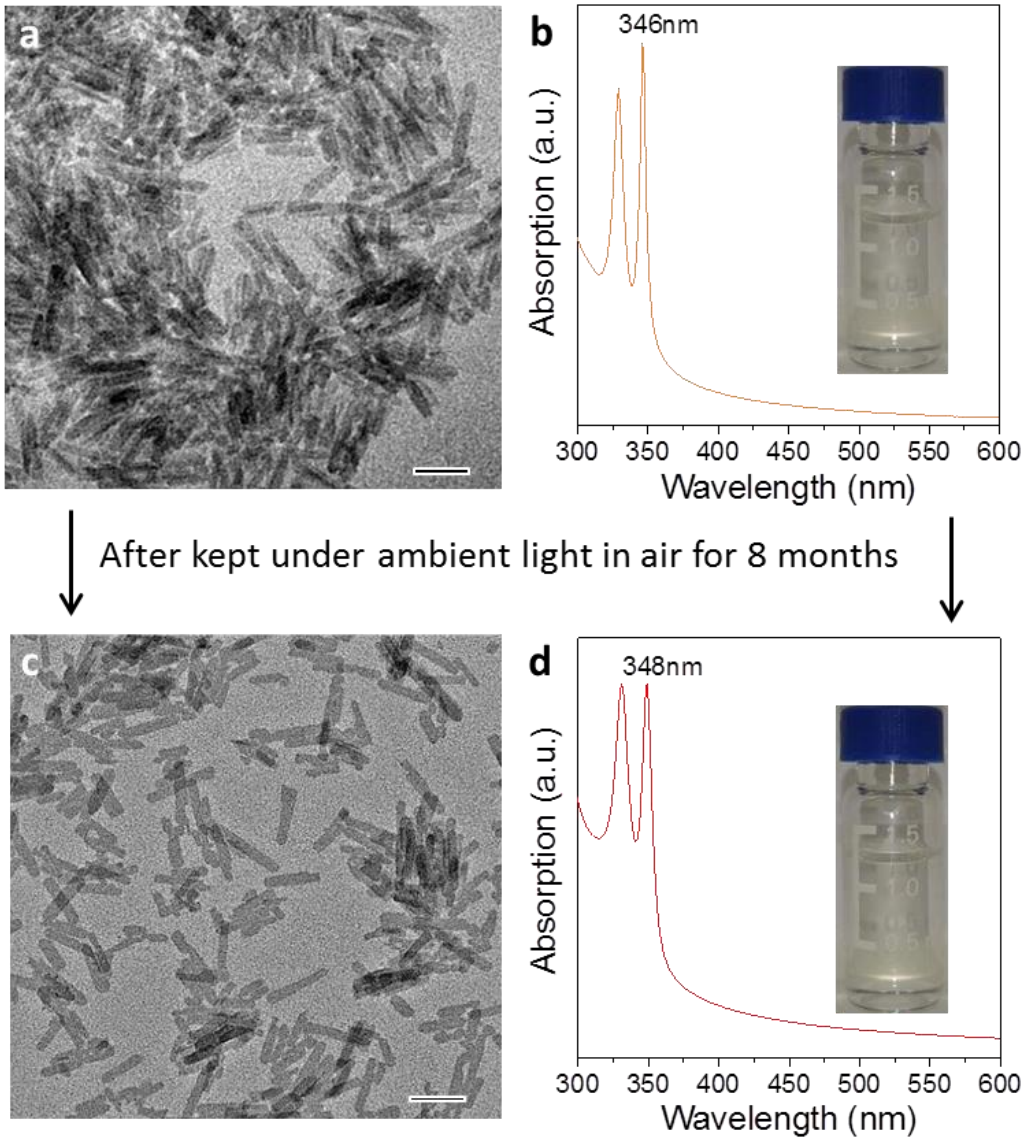

Figure A2-24. Stability of ZnSe nanoplatelets under ambient conditions. a, TEM image of freshly made ZnSe nanoplatelets. **b**, Absorption spectrum of freshly made ZnSe nanoplatelets. Inset shows ZnSe nanoplatelets dispersed in toluene. **c**, TEM image of ZnSe nanoplatelets after keeping under ambient light in air for 8 months, showing the morphology of nanoplatelets are retained. **d**, Absorption spectrum of ZnSe nanoplatelets after keeping under ambient light in air for 8 months showing the sharp features of the absorption exciton peaks are preserved, although a 2 nm red-shift of the first exciton peak is observed. Inset shows ZnSe nanoplatelets dispersed in toluene, showing good dispersity of the nanoparticles. All scale bars are 100 nm.

Figure A2-25. Photograph of ZnSe nanoplatelets dispersed in toluene solution.

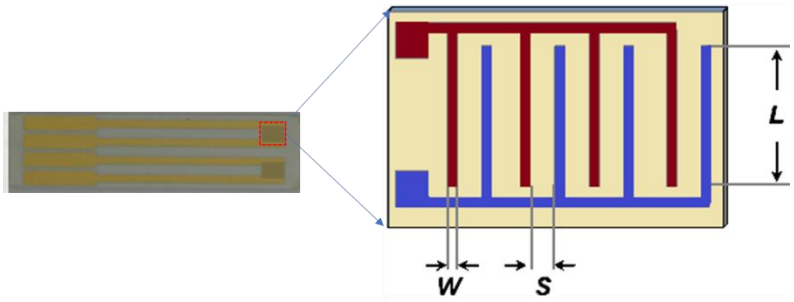

L = 1 mm, W (finger) = 20 µm, S (gap) = 10 µm

40 fingers in total: 20 for left contact and 20 for right contact.
The figures are made with 5 nm Cr adhesion layer and 150 nm Au.

FigureA2-26. Size and geometry of the interdigitated electrodes used in this work.

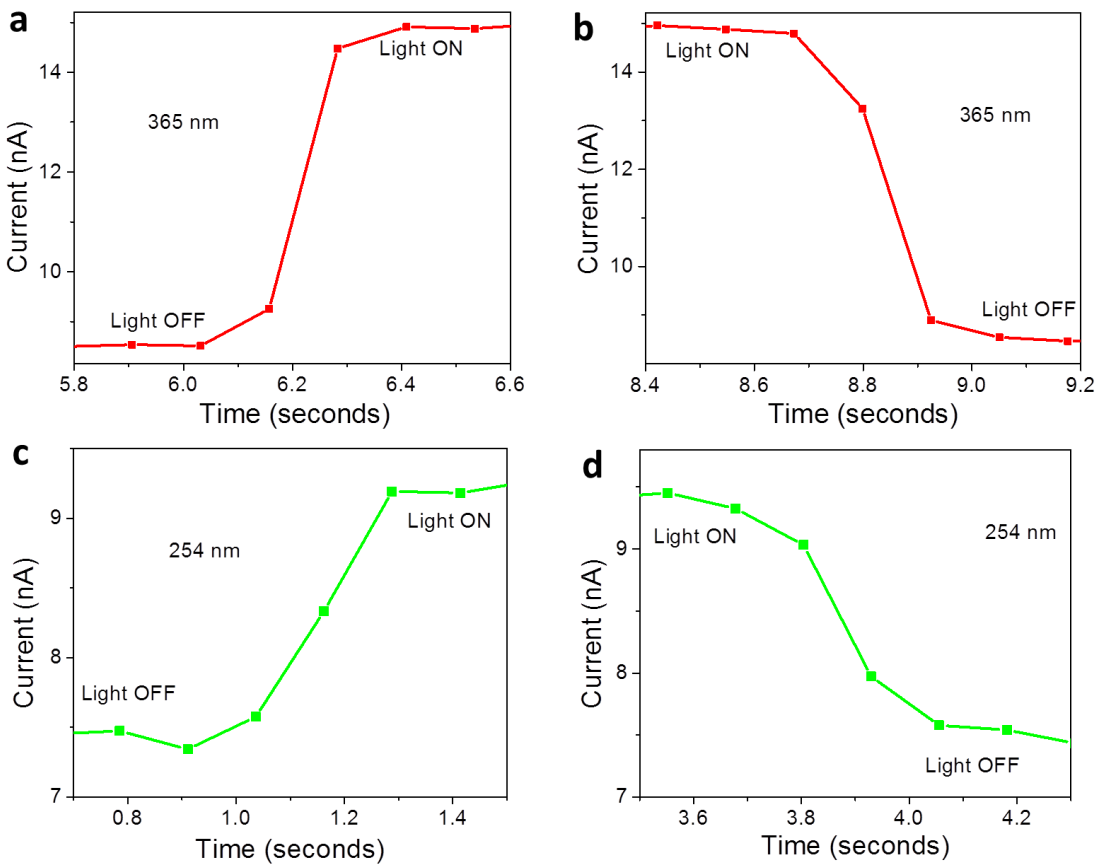

Figure A2-27. Transient responses of the ZnSe photodetector suggesting that the response time of current rise and fall is about 0.3 s when the UV light is switched on and off.

References

(1)Lide, D. R. *CRC Handbook of Chemistry and Physics.* 81st Ed., p.3–148, CRC Press, Boca Raton, FL 2000.

(2)http://www.chemicalbook.com/ChemicalProductProperty_US_CB4375298.aspx

(3)Timoshenko, S. P.; Goodier, J. N. *Theory of elasticity.* 3rd Ed., McGraw Hill, New York, 1970.

(4)Li, X.; Wang, X.; Xiong, Q.; Eklund, P. C. Mechanical Properties of ZnS Nanobelts. *Nano Lett.* **2005**, *5*, 1982–1986.

(5)Martin, R. M. Elastic Properties of ZnS Structure Semiconductors. *Phys. Rev. B* **1970**, *1*, 4005–4011.

(6)Casalia, R. A.; Christensenb, N. E. Elastic Constants and Deformation Potentials of ZnS and ZnSe under Pressure. *Solid State Commun.* **1998**, *108*, 793–798.

(7)Subbaiah, Y. P. V.; Prathap, P.; Reddy, K. T. R. Reddy, Structural, Electrical and Optical Properties of ZnS Films Deposited by Close-Spaced Evaporation. *Appl. Surf. Sci.* **2006**, *253*, 2409–2415.

Appendix 3: Supplementary information of Chapter 4

Figure A3-1. Photograph showing a weighing paper containing 1.26 g of single-layer MoS_2 nanosheets.

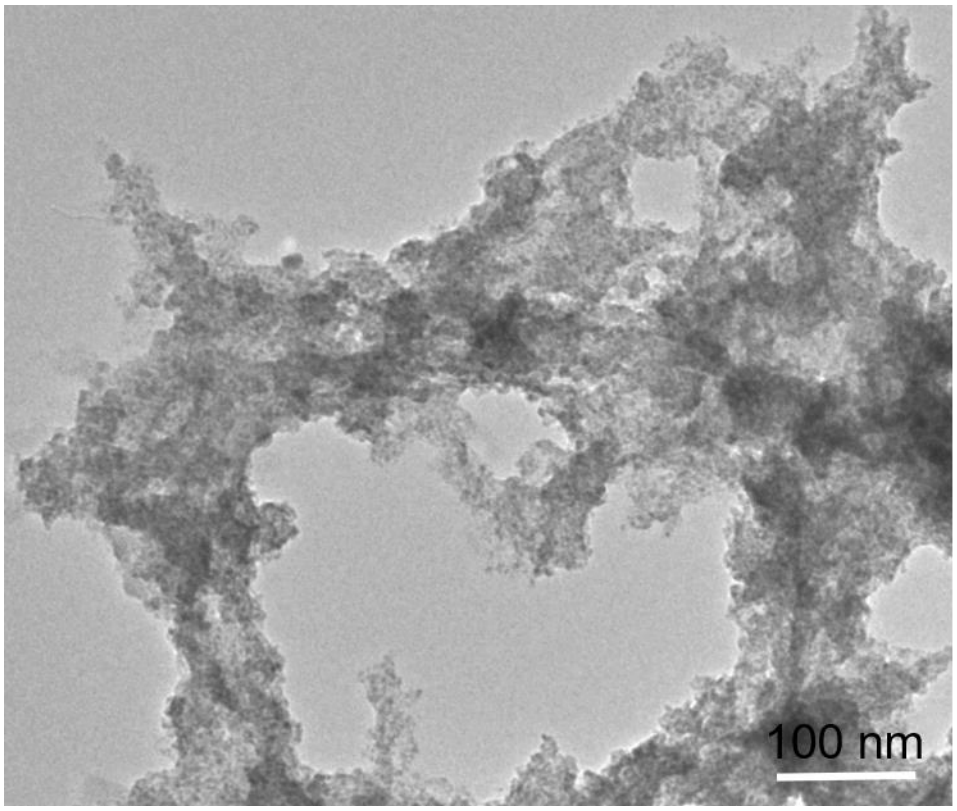

Figure A3-2. Low-magnification TEM image of single-layer MoS_2 nanosheets.

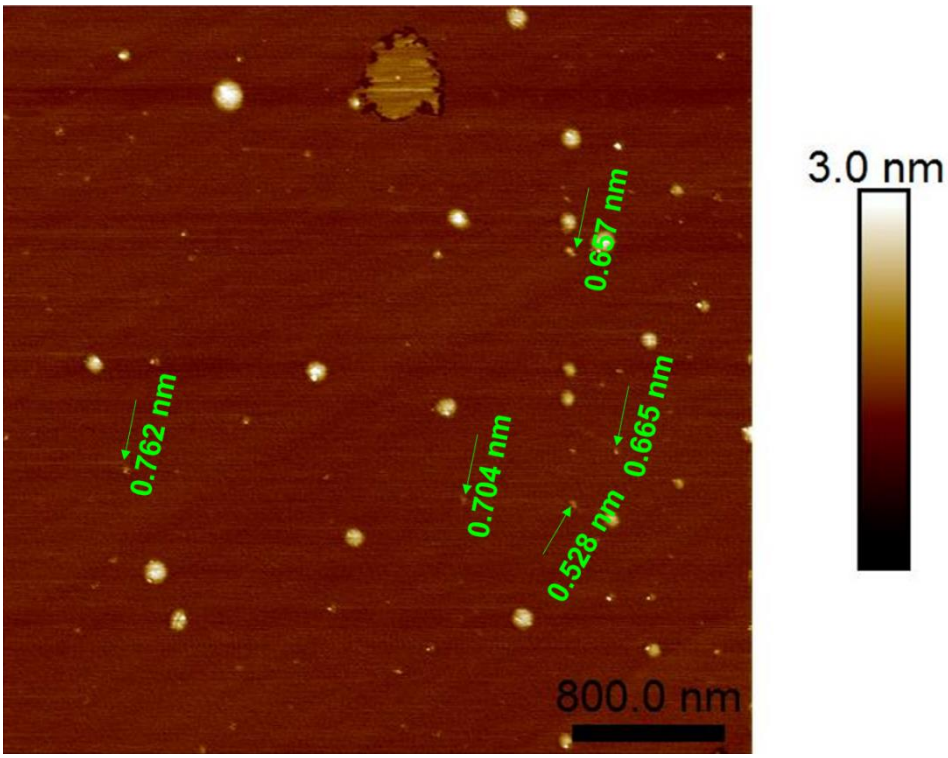

Figure A3-3. AFM image showing the uniform thickness of ~0.6 nm of five individual single-layer MoS_2 nanosheets.

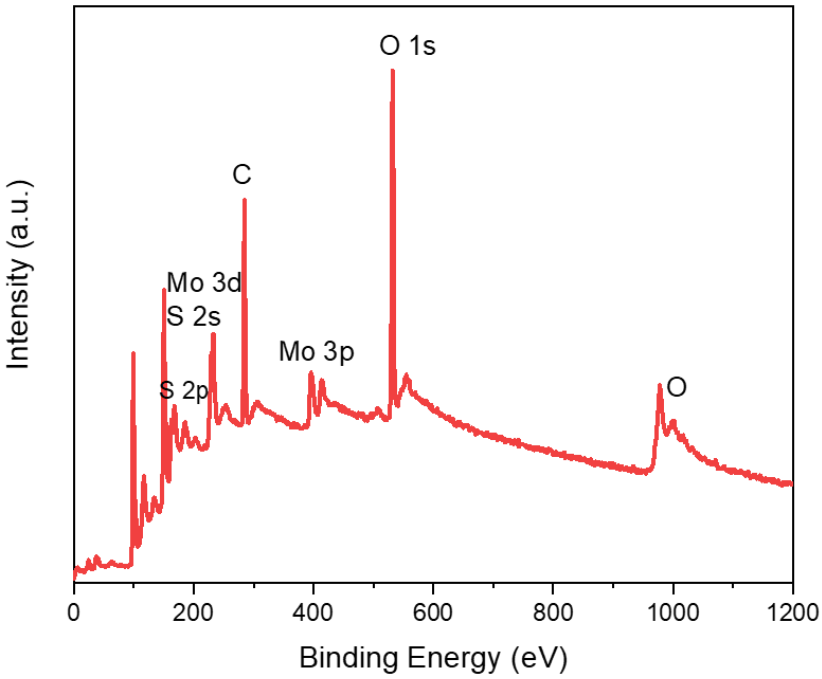

Figure A3-4. XPS survey spectrum of single-layer MoS_2 nanosheets.

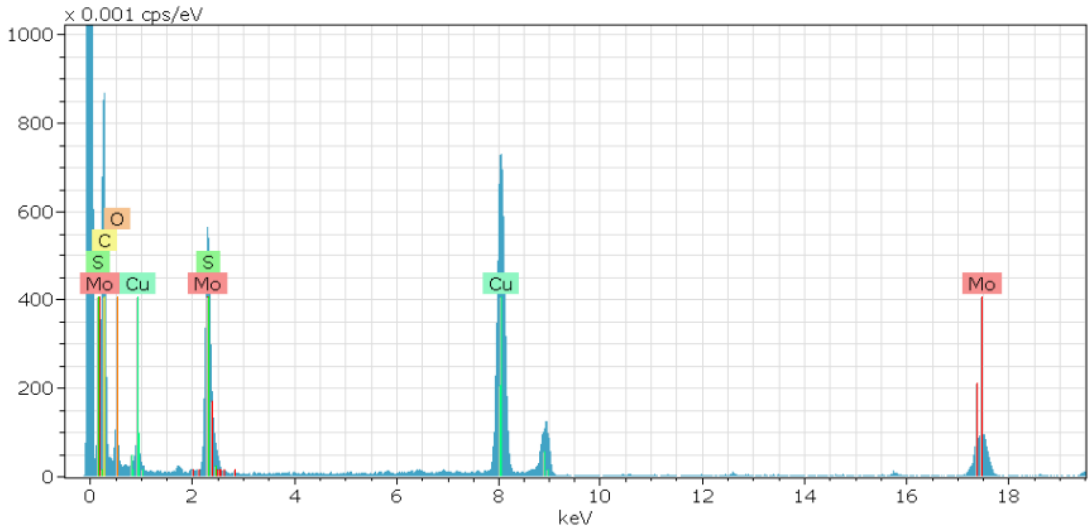

Figure A3-5. EDX spectrum of single-layer MoS_2 nanosheets.

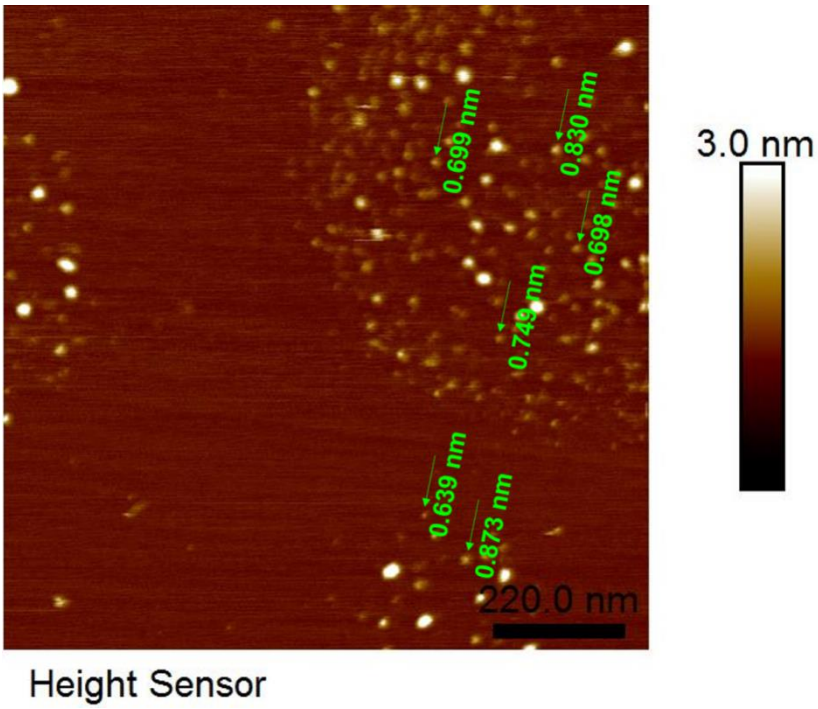

Figure A3-6. AFM image showing the thickness of individual single-layer WS_2 nanosheet.

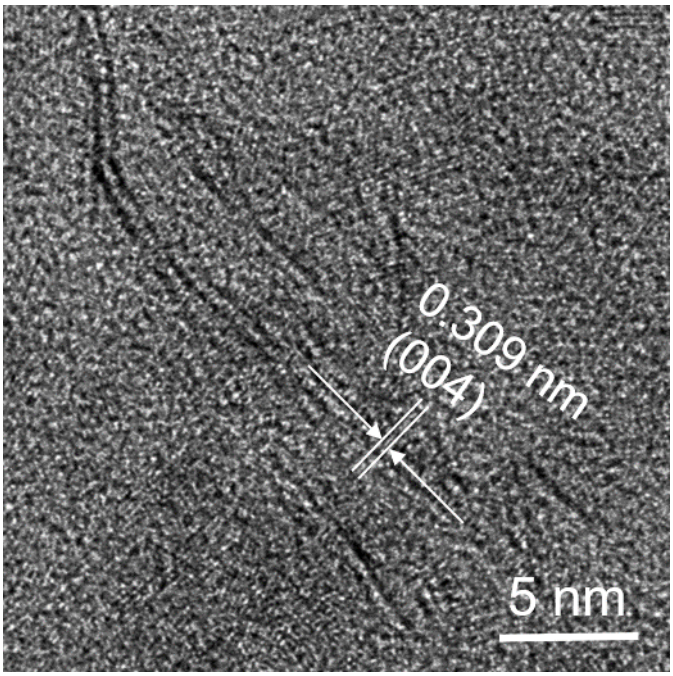

Figure A3-7. High-resolution TEM image of single-layer WS_2 nanosheets.

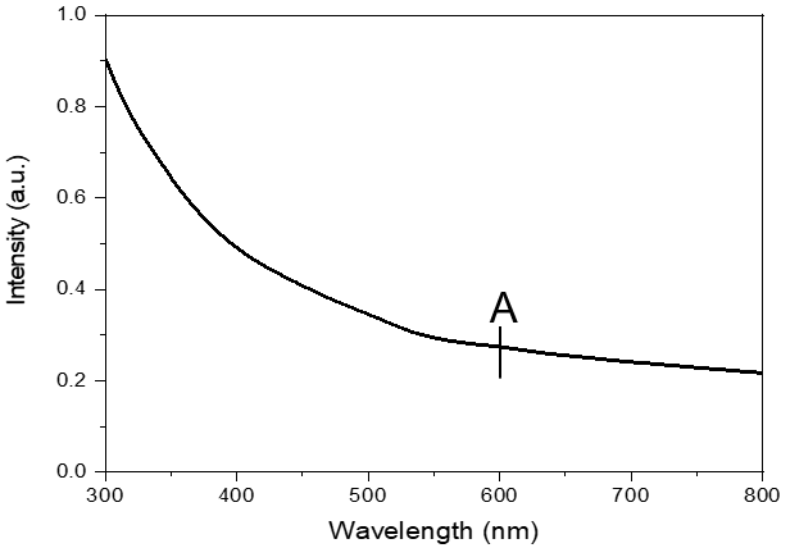

Figure A3-8. UV-vis absorption spectrum of single-layer WS_2 nanosheets.

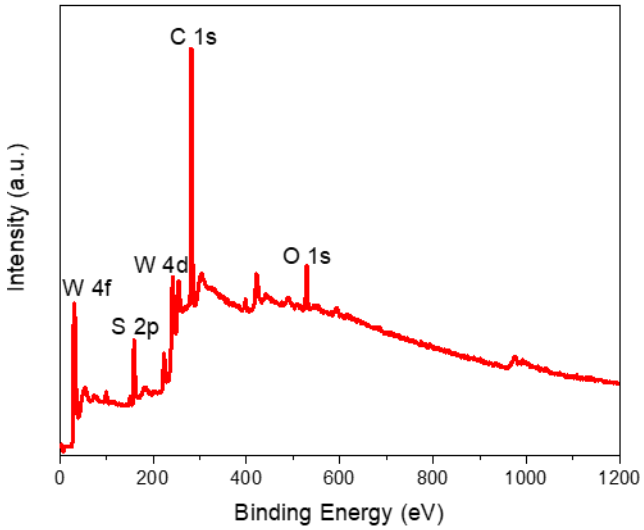

Figure A3-9. XPS survey spectrum of single-layer WS_2 nanosheets.

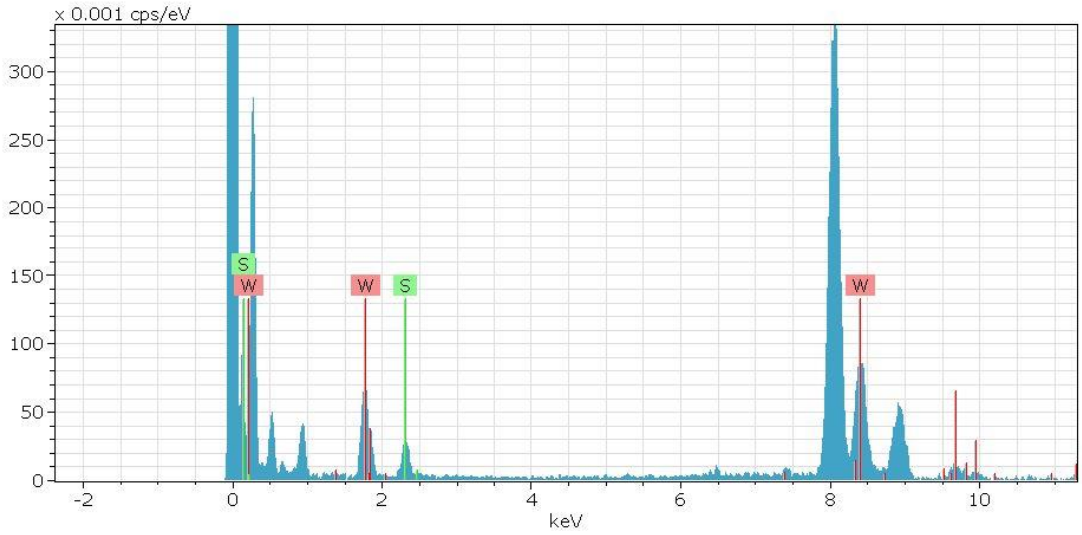

Figure A3-10. EDX spectrum of single-layer WS_2 nanosheets.

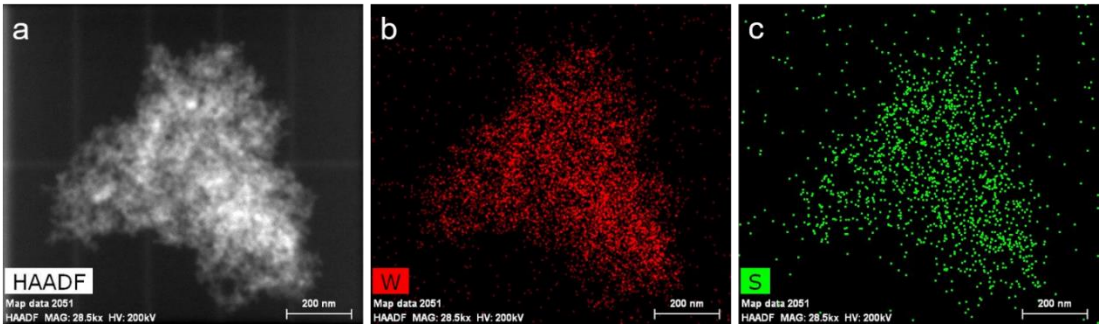

Figure A3-11. a, STEM image of single-layer WS_2 nanosheets. **b,c**, STEM-EDS elemental mapping of (b) W and (c) S of as-synthesized single-layer WS_2 nanosheets.

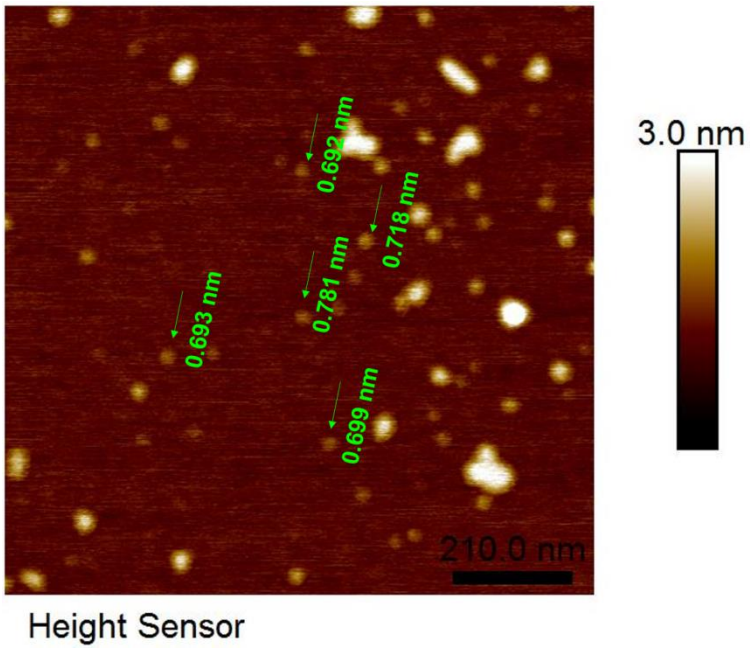

Figure A3-12. AFM image showing the thickness of ~0.6 nm of individual single-layer ReS_2 nanosheet.

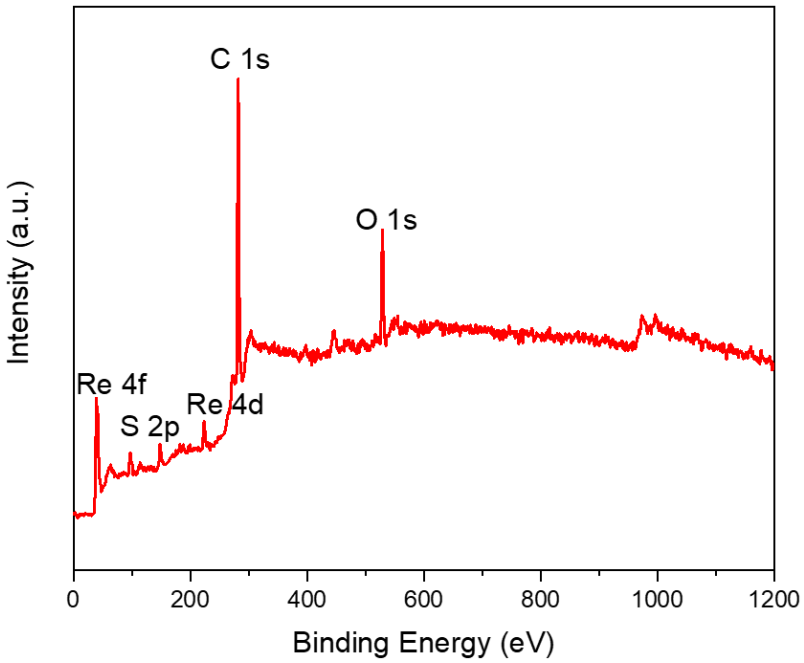

Figure A3-13. XPS survey spectrum of single-layer ReS_2 nanosheets.

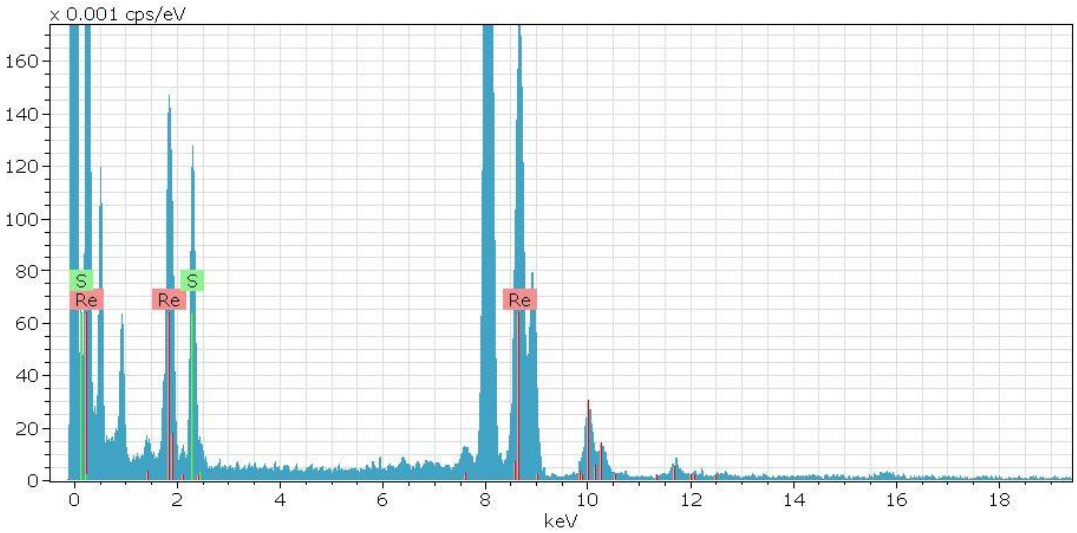

Figure A3-14. EDX spectrum of single-layer ReS_2 nanosheets.

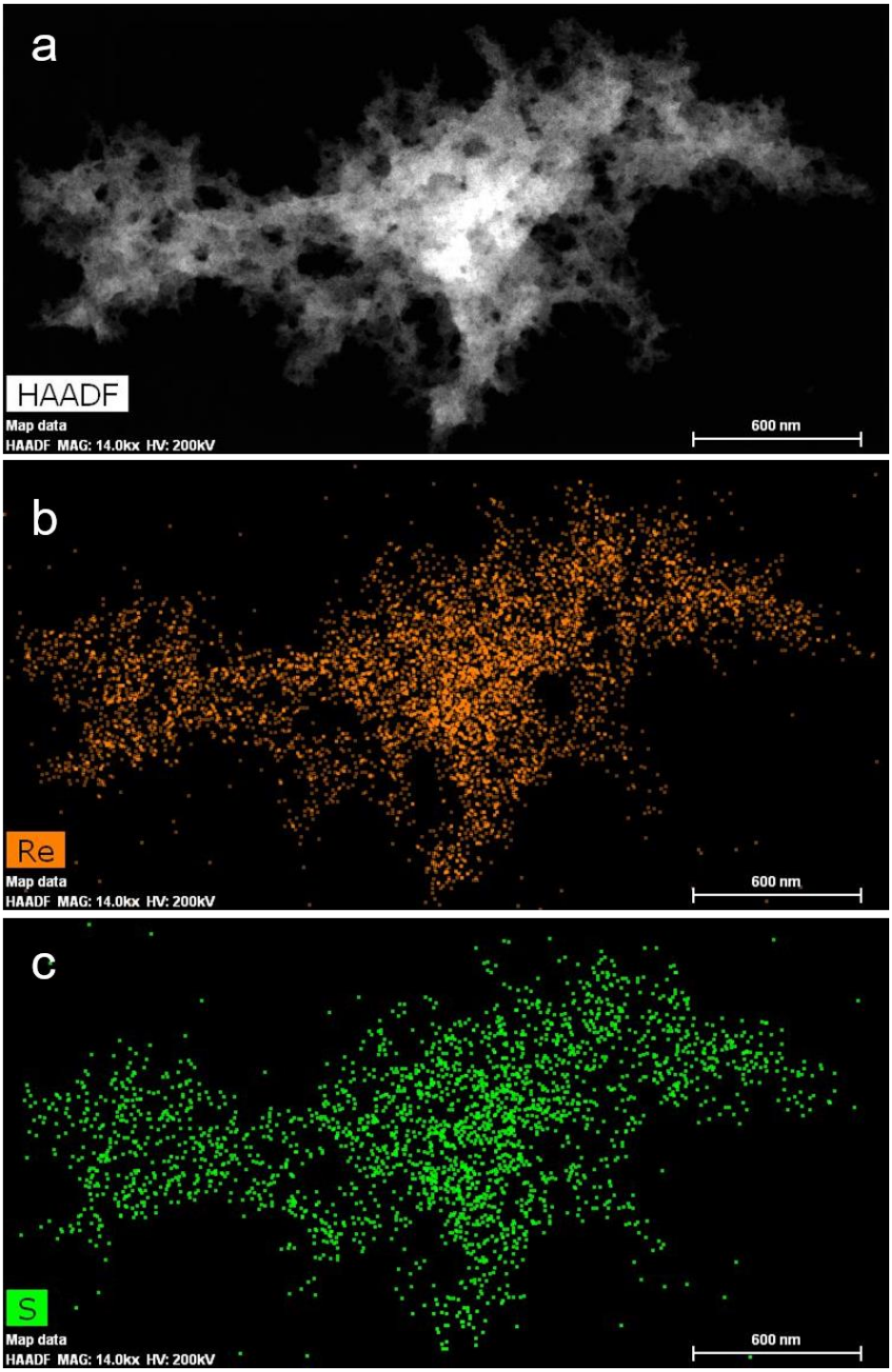

Figure A3-15. a, STEM image of single-layer ReS_2 nanosheets. **b,c**, STEM-EDS elemental mapping of (b) Re and (c) S of as-synthesized single-layer ReS_2 nanosheets.

Appendix 4: Statement of Contribution by Others

Statement of Contribution by Others

To Whom It May Concern I, [Yingping Pang], contributed (Y.P. designed and conducted the experiments. Y.P. wrote the manuscript and analysed the experimental data with support from G.J.) to the paper/publication entitled (Y. Pang, M. Zhang, D. Chen, W. Chen, F. Wang, Shaghraf Javaid, M. Saunders, M, Rowles, L. Liu, S. Liu, A. Sitt, C, Li, G. Jia, Why Do Colloidal Wurtzite Semiconductor Nanoplatelets Have an Atomically Uniform Thickness of Eight Monolayers? *J. Phys. Chem. Lett.* **2019**, *10, 12,* 3465-3471).

(Signature of Candidate)

I, as a Co-Author, endorse that this level of contribution by the candidate indicated above is appropriate.

Minyi Zhang
(Full Name of Co-Author 1) (Signature of Co-Author 1)

Dechao Chen
(Full Name of Co-Author 2) (Signature of Co-Author 2)

Wei Chen
(Full Name of Co-Author 3) (Signature of Co-Author 3)

Fei Wang
(Full Name of Co-Author 4) (Signature of Co-Author 4)

Shaghraf Javaid
(Full Name of Co-Author 5) (Signature of Co-Author 5)

Martin Saunders
(Full Name of Co-Author 6) (Signature of Co-Author 6)

Matthew R. Rowles
(Full Name of Co-Author 7) (Signature of Co-Author 7)

Lihong Liu
(Full Name of Co-Author 8) (Signature of Co-Author 8)

Shaomin Liu
(Full Name of Co-Author 9) (Signature of Co-Author 9)

Amit Sitt
(Full Name of Co-Author 10) (Signature of Co-Author 10)

Chunsen Li
(Full Name of Co-Author 11) (Signature of Co-Author 11)

Guohua Jia
(Full Name of Co-Author 12) (Signature of Co-Author 12)

Order Completed

Thank you for your order.

This Agreement between Curtin University -- Yingping Pang ("You") and Springer Nature ("Springer Nature") consists of your license details and the terms and conditions provided by Springer Nature and Copyright Clearance Center.

Your confirmation email will contain your order number for future reference.

printable details

License Number	4633400016835
License date	Jul 20, 2019
Licensed Content Publisher	Springer Nature
Licensed Content Publication	Nature Communications
Licensed Content Title	Generalized self-assembly of scalable two-dimensional transition metal oxide nanosheets
Licensed Content Author	Ziqi Sun, Ting Liao, Yuhai Dou, Soo Min Hwang, Min-Sik Park et al.
Licensed Content Date	May 12, 2014
Licensed Content Volume	5
Type of Use	Thesis/Dissertation
Requestor type	academic/university or research institute
Format	print and electronic
Portion	figures/tables/illustrations
Number of figures/tables/illustrations	1
High-res required	no
Will you be translating?	no
Circulation/distribution	5,001 to 10,000
Author of this Springer Nature content	no
Title	2D Colloidal Atomic-Thick Metal Chalcogenides: Synthesis, Growth Mechanisms and Applications
Institution name	Curtin University
Expected presentation date	Jul 2019
Portions	Figure 1

Requestor Location	Curtin University Kent Street, Bentley Perth, WA 6102 Australia Attn: Curtin University
Total	0.00 AUD

ORDER MORE CLOSE WINDOW

SPRINGER NATURE

Title:	Li–O2 and Li–S batteries with high energy storage
Author:	Peter G. Bruce, Stefan A. Freunberger, Laurence J. Hardwick, Jean-Marie Tarascon
Publication:	Nature Materials
Publisher:	Springer Nature
Date:	Dec 15, 2011

Logged in as:
Yingping Pang
Curtin University
Account #:
3001350177

Order Completed

Thank you for your order.

This Agreement between Curtin University -- Yingping Pang ("You") and Springer Nature ("Springer Nature") consists of your license details and the terms and conditions provided by Springer Nature and Copyright Clearance Center.

Your confirmation email will contain your order number for future reference.

printable details

License Number	4633410095756
License date	Jul 20, 2019
Licensed Content Publisher	Springer Nature
Licensed Content Publication	Nature Materials
Licensed Content Title	Li–O2 and Li–S batteries with high energy storage
Licensed Content Author	Peter G. Bruce, Stefan A. Freunberger, Laurence J. Hardwick, Jean-Marie Tarascon
Licensed Content Date	Dec 15, 2011
Licensed Content Volume	11
Licensed Content Issue	1
Type of Use	Thesis/Dissertation
Requestor type	academic/university or research institute
Format	print and electronic
Portion	figures/tables/illustrations
Number of figures/tables/illustrations	1
High-res required	no
Will you be translating?	no
Circulation/distribution	5,001 to 10,000
Author of this Springer Nature content	no
Title	2D Colloidal Atomic-Thick Metal Chalcogenides: Synthesis, Growth Mechanisms and Applications
Institution name	Curtin University
Expected presentation date	Jul 2019
Portions	Figure 1
Requestor Location	Curtin University

	Kent Street, Bentley Perth, WA 6102 Australia Attn: Curtin University
Total	0.00 AUD

ORDER MORE CLOSE WINDOW

Title:	Why Do Colloidal Wurtzite Semiconductor Nanoplatelets Have an Atomically Uniform Thickness of Eight Monolayers?
Author:	Yingping Pang, Minyi Zhang, Dechao Chen, et al
Publication:	Journal of Physical Chemistry Letters
Publisher:	American Chemical Society
Date:	Jun 1, 2019

PERMISSION/LICENSE IS GRANTED FOR YOUR ORDER AT NO CHARGE

This type of permission/license, instead of the standard Terms & Conditions, is sent to you because no fee is being charged for your order. Please note the following:

- Permission is granted for your request in both print and electronic formats, and translations.
- If figures and/or tables were requested, they may be adapted or used in part.
- Please print this page for your records and send a copy of it to your publisher/graduate school.
- Appropriate credit for the requested material should be given as follows: "Reprinted (adapted) with permission from (COMPLETE REFERENCE CITATION). Copyright (YEAR) American Chemical Society." Insert appropriate information in place of the capitalized words.
- One-time permission is granted only for the use specified in your request. No additional uses are granted (such as derivative works or other editions). For any other uses, please submit a new request.

BACK | CLOSE WINDOW

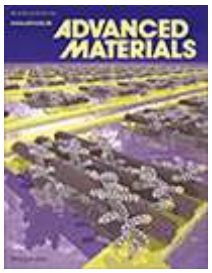

Title:	Colloidal Single-Layer Photocatalysts for Methanol-Storable Solar H2 Fuel
Author:	Yingping Pang, Md Nasir Uddin, Wei Chen, et al
Publication:	Advanced Materials
Publisher:	John Wiley and Sons
Date:	Oct 21, 2019

Order Completed

Thank you for your order.

This Agreement between Curtin University -- Yingping Pang ("You") and John Wiley and Sons ("John Wiley and Sons") consists of your license details and the terms and conditions provided by John Wiley and Sons and Copyright Clearance Center.

Your confirmation email will contain your order number for future reference.

printable details

License Number	4693941496070
License date	Oct 21, 2019
Licensed Content Publisher	John Wiley and Sons
Licensed Content Publication	Advanced Materials
Licensed Content Title	Colloidal Single-Layer Photocatalysts for Methanol-Storable Solar H2 Fuel
Licensed Content Author	Yingping Pang, Md Nasir Uddin, Wei Chen, et al
Licensed Content Date	Oct 21, 2019
Licensed Content Volume	0
Licensed Content Issue	0
Licensed Content Pages	11
Type of use	Dissertation/Thesis
Requestor type	Author of this Wiley article
Format	Print and electronic
Portion	Full article
Will you be translating?	No
Title of your thesis / dissertation	2D Colloidal Atomic-Thick Metal Chalcogenides: Synthesis, Growth Mechanisms and Applications
Expected completion date	Jul 2019
Expected size (number of pages)	1

Requestor Location	Curtin University Kent Street, Bentley Perth, WA 6102 Australia Attn: Curtin University
Publisher Tax ID	EU826007151
Total	0.00 AUD

Would you like to purchase the full text of this article? If so, please continue on to the content ordering system located here: Purchase PDF

If you click on the buttons below or close this window, you will not be able to return to the content ordering system.

ORDER MORE CLOSE WINDOW